



MONASH University

Fluorinated Ionic Liquid–Based Electrolytes with High Nitrogen Gas Solubility for Electrochemical Ammonia Synthesis

Colin Suk Mo Kang

BSc (Hons)

A thesis submitted for the degree of

Doctor of Philosophy

at Monash University

in 2019

Faculty of Science, School of Chemistry

Copyright notice

© Colin Suk Mo Kang (2019).

I certify that I have made all reasonable efforts to secure copyright permissions for third-party content included in this thesis and have not knowingly added copyright content to my work without the owner's permission.

“Everyone is a genius. But if a fish judges itself by its ability to climb a tree, it will live its whole life believing that it is stupid.

So my question for you is, what is your genius?”

-Adapted from Anonymous

Abstract

Ammonia is of growing interest as a carbon-free chemical fuel for the transportation and storage of renewable energy. The use of ammonia as an energy carrier can certainly absorb and alleviate the intermittency of renewable energy supplies and enable areas of the world, particularly those that have only limited renewable energy, access to this energy for electricity/fuel usage. Currently, ammonia is synthesised on an industrial scale for the production of fertilisers worldwide by the energy intensive Haber–Bosch process, generating millions of tonnes of CO₂ emissions per year.

Upon recent research, an attractive alternative is to electrochemically synthesise ammonia at ambient temperature and pressure, by the reduction reaction of N₂ to ammonia. Such a technology, should it be developed, has huge potential on a global scale to be more energetically favourable and environmentally friendly. However, due to the low Faradaic efficiency (i.e. the percentage of charge that is used to produce ammonia) and sluggish reaction rates, substantially better performance needs to be achieved before this can be carried out on a large scale.

One significant factor contributing to the low Faradaic Efficiency, is the occurrence of the hydrogen evolution reaction which is considerably more facile on many electrode materials, and which occurs at similar reduction potentials to the N₂ reduction reaction. Part of the reason for this stems from the low solubility of N₂ in aqueous electrolytes and many other solvents. As a result, this work involves an investigation of fluorinated ionic liquid–based electrolytes and their ability to dissolve higher amounts of N₂, for application in electrochemically reducing N₂ into ammonia. This is based in part on published papers along with additional chapters and sections detailing apparatus design and additional data.

Chapter 2 describes the design and construction of a custom–built isochoric pressure saturation apparatus to measure the N₂ solubility of synthesised fluorinated ionic liquids and

their co-solvent mixtures. More specifically, this chapter details the engineering requirements and specifications to ensure that a sufficiently leak-free system can be built. In addition, the thermodynamic controls that are essential for high precision measurements of N₂ solubility are established. Despite the inherently low solubility of N₂ in liquids, satisfactory agreement with literature data of N₂ solubility measurements is shown in various media (both ionic liquids and solvents), verifying the operation of the apparatus.

In chapter 3, the preparation of fluorinated ionic liquids and analysis of their transport properties and N₂ solubility are presented. Moreover, ionic liquids with an [eFAP]⁻ anion tend to display more ideal transport properties in terms of their ionicity, conductivity, viscosity and diffusivity. On the other hand, linear perfluorinated anions, such as the series of perfluorosulfonates and perfluorocarboxylates, display increased N₂ solubilities with increasing perfluoroalkyl chain length. This allows us to specifically design and tailor the N₂ solubility of ionic liquids for application in the electrochemical N₂ reduction reaction. This chapter is based on a paper published in *J. Phys. Chem. C* (Kang et al, 2018, 122, 24550—24558).

The next chapter delves into the fourth evolution of ionic liquids, where fluorinated ionic liquids are combined with fluorinated solvents with the advantage of enhancing their mass transport and N₂ solubility, if miscibility allows. The principle concepts of designing a fluorinated ionic liquid electrolyte, and their requirements for use in electrochemical ammonia synthesis are discussed. Novel phosphonium-based ionic liquids are synthesised, followed by the characterisation of their transport properties. N₂ solubility measurements are carried out with a number of ionic liquid + fluorinated solvent combinations, which allows us to establish rational design principles to achieve higher N₂ solubility in fluorinated ionic liquid-based electrolytes.

In chapter 5, the physical interactions of a fluorinated ionic liquid electrolyte system are investigated, in terms of their volumetric properties and transport properties, with a focus on [C₄mpyr][eFAP] – as the ionic liquid – dissolved in three fluorinated solvents: trifluorotoluene (TFT), 1H,1H,2H–heptafluorocyclopentane (HFCP) and 1H,1H,5H–octafluoropentyl 1,1,2,2–tetrafluoroethyl ether (FPPE). The thermodynamic properties of solvation are discussed in relation to the role of free volume and the effects of fluororous domains. An optimal composition in terms of conductivity is found for each system, for example ($\chi_2 \sim 0.20$) for [C₄mpyr][eFAP] in TFT. Finally, N₂ solubility in these fluorinated electrolytes displays an approximate linear trend as a function of ionic liquid composition with all of the fluorinated solvents. These studies reflect the importance in ionic liquid/fluorinated solvent composition in the design of fluorinated electrolytes for electrochemical N₂ reduction, both in terms of mass transport and N₂ solubility. This chapter is based on a paper published in *J. Phys. Chem. C* (Kang et al, *J. Phys. Chem. C* **2019**, 123, 21376—21385.)

Declaration

This thesis is an original work of my research and contains no material which has been accepted for the award of any other degree or diploma at any university or equivalent institution and that, to the best of my knowledge and belief, this thesis contains no material previously published or written by another person, except where due reference is made in the text of the thesis.

Signature:

Print Name: Colin Suk Mo Kang

Date: 3rd September 2019

Publications during enrolment

Kang, C. S. M.; Zhang, X.; MacFarlane, D. R., High Nitrogen Gas Solubility and Physicochemical Properties of [C₄mpyr][eFAP]–Fluorinated Solvent Mixtures. *J. Phys. Chem. C* **2019**, *123*, 21376—21385.

MacFarlane, D.; Zhang, X.; Zhou, F.; McDonnell-Worth, C. J.; **Kang, C. S. M.**; Kar, M. Method, Cell and Electrolyte for Conversion for Dinitrogen Conversion. PCT/AU2019/000122, 31 January, 2019.

Kang, C. S. M.; Zhang, X.; MacFarlane, D. R., Synthesis and Physicochemical Properties of Fluorinated Ionic Liquids with High Nitrogen Gas Solubility. *J. Phys. Chem. C* **2018**, *122*, 24550—24558.

Suryanto, B. H.; **Kang, C. S. M.**; Wang, D.; Xiao, C.; Zhou, F.; Azofra, L. M.; Cavallo, L.; Zhang, X.; MacFarlane, D. R., Rational Electrode–Electrolyte Design for Efficient Ammonia Electrosynthesis under Ambient Conditions. *ACS Energy Lett.* **2018**, *3*, 1219—1224.

MacFarlane, D.; Zhang, X.; Zhou, F.; McDonnell-Worth, C. J.; **Kang, C. S. M.**; Kar, M. Method and Cell for Conversion of Dinitrogen into Ammonia. PCT/AU2018/000036, 10 August, 2017.

Thesis including published works declaration

I hereby declare that this thesis contains no material which has been accepted for the award of any other degree or diploma at any university or equivalent institution and that, to the best of my knowledge and belief, this thesis contains no material previously published or written by another person, except where due reference is made in the text of the thesis.

This thesis includes two original papers published in peer reviewed journals and two thesis chapters. The core theme of the thesis is the N₂ solubility of fluorinated ionic liquid-based electrolytes. The ideas, development and writing up of all the papers in the thesis were the principal responsibility of myself, the student, working within the School of Chemistry under the supervision of Prof. Douglas R. MacFarlane.

In the case of chapters 2, 3, 4, 5 my contribution to the work involved the following:

Thesis Chapter	Publication Title	Status	Nature and % of student contribution	Co-author name(s) Nature and % of Co-author's contribution	Co-author(s), Monash student
Chapter 2	Engineering and Construction of N ₂ Solubility Apparatus	Not submitted	90%. Concept, experimental design and construction, collecting and analysing data and primary author	1) Douglas R. MacFarlane, input into manuscript 5% 2) Xinyi Zhang, input into manuscript 5%	No
Chapter 3	Synthesis and Physicochemical Properties of Fluorinated Ionic Liquids with High Nitrogen Gas Solubility	Published	90%. Concept, experimental design, collecting and analysing data and primary author	1) Douglas R. MacFarlane, input into manuscript 5% 2) Xinyi Zhang, input into manuscript 5%	No
Chapter 4	Design and Optimisation of Fluorinated Ionic Liquid-based Electrolytes to Achieve High Nitrogen Gas Solubility	Not submitted	90%. Concept, experimental design, collecting and analysing data and primary author	1) Douglas R. MacFarlane, input into manuscript 5% 2) Xinyi Zhang, input into manuscript 5%	No
Chapter 5	High Nitrogen Gas Solubility and Physicochemical Properties of [C ₄ mpyr][eFAP]–Fluorinated Solvent Mixtures	Published	90%. Concept, experimental design, collecting and analysing data and primary author	1) Douglas R. MacFarlane, input into manuscript 5% 2) Xinyi Zhang, input into manuscript 5%	No

I have not renumbered sections of submitted or published papers in order to generate a consistent presentation within the thesis.

Student name: Colin Suk Mo Kang

Student signature:

Date: 03/09/2019

I hereby certify that the above declaration correctly reflects the nature and extent of the student's and co-authors' contributions to this work.

Main Supervisor name: Douglas Robert MacFarlane

Main Supervisor signature:

Date: 03/09/2019

Acknowledgements

I would like to first express my enormous gratitude to my supervisor Doug for his mentorship and continuous support I have had throughout the course of my PhD. It has been a remarkable opportunity to learn from his approach to research work ranging from his wealth of technical knowledge and industry insight, to his interpersonal skills. It is my privilege to have shared several (non-)scientific discussions and having a supervisor to aspire to.

A big acknowledgement to Prof. Benny F. and Dr. Michelle D., who have both provided guidance and advice for my project in the construction of the gas solubility apparatus. There were an endless list of questions to which I am grateful for all of the answers. Furthermore, Dr. Peter N. has been great, as the laboratory support who can do everything, and as a fantastic buddy over the years. With the help of John, they have both assisted with building and assembling the bits and bobs, to which I am very appreciative of. I extend my thanks to the synthetic lab members, in particular to Mega who taught me the 'starting materials' toward synthesising ionic liquids, and the great lab chats that we shared.

Those that I have been fortunate to have met at conferences (overseas and the Deakin crew), for making those experiences great on a personal and technical level. I'm thankful to Prof. Margarida G. who provided some advice on a range of thermodynamic concepts regarding gas solubility. It might seem like general knowledge but to an aspiring student, it means a lot! That goes for all of the professors/researchers that I have met. And of course I am grateful for the funding opportunity where this research was supported by an Australian Government Research Training Program (RTP) Scholarship.

To previous group members and visitors, you have paved the way for which I have followed in your footsteps academically and socially with Alison, Ciaran, Diogo, Nieves, Seth, Vijay, Zheng to name a few. To all group members (2019), you have all been helpful with my scientific questions and cultural curiosities; this includes the numerous discussions with the Ammonia team (Beck, Long, Sam, Pavel). From, the Chitter Chatters (Mega, Jacinta, Karolina, Federico) to the Gold Club Crew (Tiago, Federico, Thomas, Tamas, the originals), the Westall Buffet Smashers (Manjunath, Cuong, Shuo) to the Elite Table Tennis Squad (Dabin, Jay, Bryan, Tiago, Jamie, Jonathan), you have all made this experience all the more pleasant, humorous and joyful to go through. A big mention to the coffee consumers of the previous era and of late, especially Bryan, Dabin and Jay (the Mala Crew) have all been 'problem sponges', who have helped 'soak up' some of the research problems and alleviate such issues.

I would like to thank my family, and friends (previous and new) for their support throughout my stay here in Melbourne, full of great experiences and travels. Lastly, I must thank my partner Sammi, who has been incredibly supportive and has kept me grounded (sane) during this whole experience. I am most fortunate to have you around and to hear out many of my research problems throughout these years.

It has been a journey, and a milestone to remember.

Table of Contents

LIST OF ABBREVIATIONS	xii
Chapter 1: Introduction.....	1
1.1 Energy Storage and Transportation	1
1.2 Ammonia	4
1.3 Electrochemical Ammonia Synthesis	6
1.3.1 Required Protocols.....	6
1.3.2 Improving Faradaic Efficiency	7
1.4 N ₂ Solubility	9
1.4.1 Methods of Measuring Gas Solubility	9
1.4.2 Literature Data of N ₂ Solubility	11
1.5 Ionic Liquids	15
1.5.1 Properties of Ionic Liquids.....	16
1.5.2 Fluorinated Ionic Liquids	17
1.6 Fluorinated Ionic Liquid–Based Electrolytes	20
1.6.1 Environmental Concerns	21
1.7 Research Objectives	21
1.8 References	22
Chapter 2: Engineering and Construction of N₂ Solubility Apparatus	31
2.1 Introduction	31
2.2 N ₂ Solubility Behaviour	32
2.2.1 Various Gases	32
2.2.2 Temperature Dependence in Water	33
2.2.3 Temperature Dependence in Organic Solvents	34
2.3 Isochoric Saturation Method	35
2.3.1 Data Analysis of N ₂ Solubility	36
2.3.2 Single–Transducer Mode	38
2.3.3 Dual–Transducer Mode.....	39
2.4 Mark I of N ₂ Solubility Apparatus.....	41
2.4.1 Experimental	42
2.4.2 Control Measurements	42
2.4.3 Tips for High Precision.....	47
2.5 Mark II of N ₂ Solubility Apparatus.....	48
2.5.1 Experimental	49
2.5.2 Step–by–step Measurement Procedure	51
2.5.3 Control Measurements	54

2.6	Conclusions	66
2.7	Supporting Information	66
2.8	References	68
Chapter 3: Synthesis and Physicochemical Properties of Fluorinated Ionic Liquids with High Nitrogen Gas Solubility		
3.1	Synopsis.....	70
3.2	Publication: Main Article.....	71
3.3	Publication: Supporting Information	80
Chapter 4: Design and Optimisation of Fluorinated Ionic Liquid–Based Electrolytes to Achieve High Nitrogen Gas Solubility		
4.1	Introduction	88
4.2	Experimental.....	89
4.2.1	Materials	89
4.2.2	Synthesis	89
4.2.3	Miscibility Experiments.....	90
4.2.4	Characterisation.....	90
4.1	Design of a Fluorinated Ionic Liquid–based Electrolyte.....	92
4.1.1	Fluorinated Solvent Selection	93
4.1.2	Ionic Liquid Criteria	95
4.2	Synthesis of Novel Phosphonium [eFAP] [−] –Based Ionic Liquids.....	98
4.2.1	Thermal Properties	99
4.3	N ₂ Solubility of Fluorinated Ionic Liquid–Based Electrolytes	100
4.3.1	N ₂ Solubility of Phosphonium [eFAP] [−] –based ILs.....	100
4.3.2	N ₂ Solubility of IL–TFT Mixtures	101
4.3.3	Rational Design Principles to Achieve Higher N ₂ Solubility.....	104
4.4	Phosphonium [eFAP] [−] –based ILs and Mixtures – Decreasing Cation Size.....	106
4.4.1	Transport Properties	106
4.4.2	Transport Properties in IL–TFT Mixtures	109
4.5	[P ₆₆₆₁₄] ⁺ –based IL Mixtures – Varying the Anion	112
4.5.1	Ionic Conductivity.....	112
4.5.2	Viscosity	115
4.5.3	Walden Plot.....	117
4.6	Conclusions	119
4.7	Supporting Information	120
4.7.1	Synthesis and Characterisation.....	120
4.7.2	Supporting Figures and Tables.....	122

4.8	References	136
Chapter 5: High Nitrogen Gas Solubility and Physicochemical Properties of [C₄mpyr][eFAP]– Fluorinated Solvent Mixtures		
		138
5.1	Synopsis.....	138
5.2	Publication: Main Article.....	139
5.3	Publication: Supporting Information	149
Chapter 6: Conclusions and Future Work.....		174
6.1	Conclusions	174
6.2	Future Work	176

LIST OF ABBREVIATIONS

[B(CN) ₄] ⁻	Tetracyanoborate
[BETI] ⁻	Bis(pentafluoroethanesulfonyl)imide
[BF ₂ (Ac) ₂] ⁻	Difluorobis(acetate)borate
[BF ₄] ⁻	Tetrafluoroborate
[B(otfe) ₄] ⁻	Tetrakis(trifluoroethoxy)borate
[C ₂ F ₅ BF ₃] ⁻	Pentafluoroethyltrifluoroborate
[C ₂ mim] ⁺	1-ethyl-3-methyl-imidazolium
[C ₄ F ₉ CO ₂] ⁻	Perfluoropentanoate
[C ₄ F ₉ SO ₃] ⁻	Perfluorobutanesulfonate
[C ₄ H ₄ F ₃ mim] ⁺	1-(4,4,4-trifluorobutyl)-3-methylimidazolium
[C ₄ H ₆ F ₃ mpip] ⁺	1-(4,4,4-trifluorobutyl)-1-methylpiperidinium
[C ₄ H ₆ F ₃ mpyr] ⁺	1-(4,4,4-trifluorobutyl)-1-methylpyrrolidinium
[C ₄ mim] ⁺	1-butyl-3-methyl-imidazolium
[C ₆ F ₁₃ SO ₃] ⁻	Perfluorohexanesulfonate
[C ₆ mim] ⁺	1-hexyl-3-methyl-imidazolium
[C ₇ mim] ⁺	1-heptyl-3-methyl-imidazolium
[C ₈ F ₁₇ CO ₂] ⁻	Perfluorononanoate
[C ₈ F ₁₇ SO ₃] ⁻	Perfluorooctanesulfonate
[C ₈ f _f mim] ⁺	1-(3,3,4,4,5,5,6,6,7,7,8,8,8-tridecafluorooctyl)-3-methylimidazolium
[CF ₃ CO ₂] ⁻	Trifluoroethanone
[CH ₃ CO ₂] ⁻	Ethanone
[DCA] ⁻	Dicyanamide
[DFOB] ⁻	Difluoro(oxalato)borate
[eFAP] ⁻	Tris(pentafluoroethyl) trifluorophosphate
[hmpy] ⁺	1-hexyl-3-methylpyridinium
[N ₁₁₄ (C ₇ H ₆ F ₉)] ⁺	Dimethylbutyl-(4,4,5,5,6,6,7,7,7-Heptadecafluoroundecyl)-ammonium
[N ₄₄₄ (11f)] ⁺	Tributyl (4,4,5,5,6,6,7,7,8,8,9,9,10,10,11,11,11-heptadecafluoroundecyl)-ammonium
[N ₄₄₄₄] ⁺	Tetrabutylammonium
[NC ₄ mim] ⁺	1-butanenitrile-3-methylimidazolium
[NTf ₂] ⁻	Bis(trifluoromethanesulfonyl)imide
[OTf] ⁻	Trifluorosulfonate
[P _{122i4}] ⁺	Diethylmethylisobutylphosphonium
[P ₁₄₄₄] ⁺	Tributylmethylphosphonium
[P ₁ mim] ⁺	1-(2-Methoxyethyl)-3-methylimidazolium
[P ₄₄₄ (C ₆ H ₄ F ₉)] ⁺	Tributyl-(3,3,4,4,5,5,6,6,6-nonafluorohexyl)-phosphonium
[P ₄₄₄₈] ⁺	Tributyloctylphosphonium
[P _{4448f}] ⁺	Tributyl-(3,3,4,4,5,5,6,6,7,7,8,8,8-Tridecafluorooctyl)-phosphonium
[P ₆₆₆₁₄] ⁺	Trihexyltetradecylphosphonium
[PF ₆] ⁻	Hexafluorophosphate
ADP	Adenosine Diphosphate
Ar	Argon
ATP	Adenosine Triphosphate
BC	Ballast Chamber
CH ₄	Methane

CO ₂	Carbon Dioxide
DMP	Dimethylphosphate
DSC	Differential Scanning Calorimetry
EC	Equilibrium Chamber
FPEE	1H,1H,5H-octafluoropentyl 1,1,2,2-tetrafluoroethyl ether
H ₂	Dihydrogen
HER	Hydrogen Evolution Reaction
HFCP	1H,1H,2H-heptafluorocyclopentane
IL	Ionic Liquid
K_H	Henry's Law Constant
MS	Methylsulfate
N ₂	Dinitrogen
NH ₃	Ammonia
NHE	Normal Hydrogen Electrode
NMR	Nuclear Magnetic Resonance
NO ₃ ⁻	Nitrate
NO _x	Nitrogen Oxides
NRR	Nitrogen Reduction Reaction
O ₂	Dioxygen
Pa	Pascal
PFAS	Polyfluoroalkyl Substances
PGSTE	Pulsed-Gradient Stimulated Echo
Pi	Phosphate
Pt	Platinum
S.D.	Standard Deviation
SO ₂	Sulfur Dioxide
TFT	Trifluorotoluene
TGA	Thermogravimetric Analysis
TG-IR	Thermogravimetric-Infrared Spectroscopy
Ts	Tosylate
VCR	Vacuum Coupled Radiation
V^E	Excess Molar Volume
VTF	Vogel-Tammann-Fulcher

Chapter 1: Introduction

1.1 Energy Storage and Transportation

With global energy consumption rising with the growing population and economy, the necessity for energy storage technologies becomes increasingly urgent. While several technologies exist to harness renewable energy sources such as solar, wind, hydro etc.,¹ the availability of such intermittent renewables in large quantities is often limited to specific parts of the world; Figure 1 shows the solar irradiation of the world, which differs in area within each continent. In the middle of Western Australia (and parts of Africa), the solar irradiation is intense enough such that a 250 km² array of solar panels can generate ~25 PWh/yr (based on an efficiency of ~16%);² this would sufficiently power the world's energy usage over a whole year.³⁻⁴ However, in order to utilise this energy as electricity and fuel, it must be exported worldwide to the countries in need. Thus, this puts an emphasis, not only on energy storage, but also on energy transportation to be effective on a global scale.

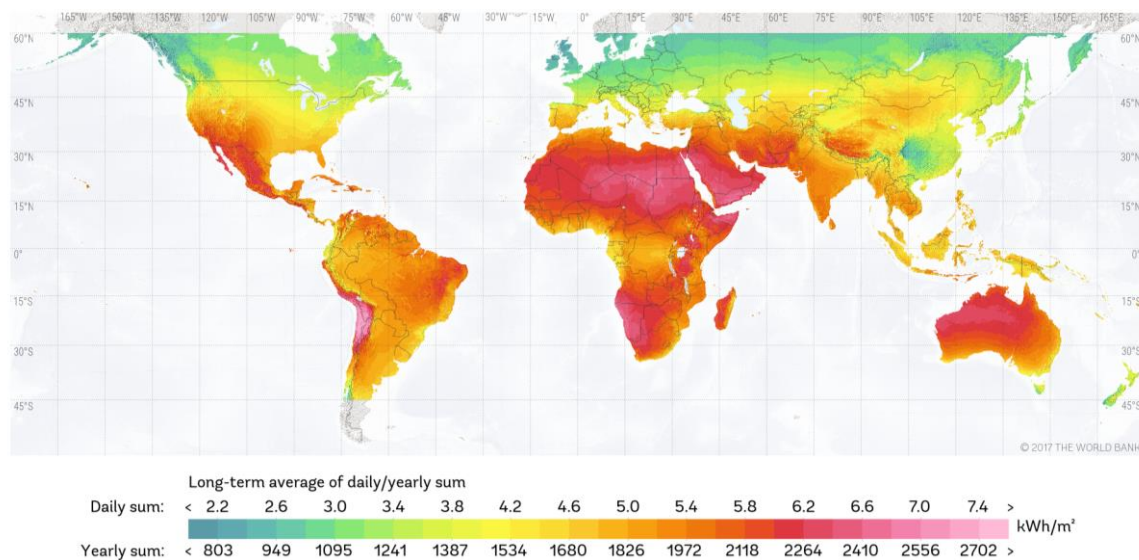


Figure 1: Long-term average solar irradiation on Earth. (Figure obtained from © 2017 The World Bank, Solar resource data: Solargis).⁵

The transmission of electricity through power lines is ideal for distributing power throughout cities and residential areas, but over long distances – a few thousand kilometres – this would result in substantial losses in efficiency; nor are they viable across the vast ocean space. Metal–

based batteries (such as Lithium–ion batteries) have dominated the world in portable devices⁶ (e.g. phones, laptops etc.) and stationary applications (e.g. South Australia’s Tesla battery); however, given the amount of energy that is used to power cities around the world, transporting this energy via batteries that are intrinsically heavy devices, offers little feasibility⁷⁻⁸ (especially if we consider the requirement to ship such batteries back to the point–of–origin to be charged again).

The use of chemical fuels such as hydrogen, methanol, or ammonia, particularly if they are produced from renewable energy sources, has been explored as potential energy carriers.⁹ Table 1 shows the gravimetric and volumetric energy densities of various chemical fuels. Methanol and other carbon–based fuels, whilst offering high energy density, can overly contribute to the carbon cycle and greenhouse gas emissions, leading to severe environmental effects (such as climate change and pollution) unless they are produced from a renewable source of carbon.¹⁰ Carbon capture technologies¹¹⁻¹² can synergise well with traditional fossil fuel based technologies through electrochemical/(photo)electrochemical carbon dioxide (CO₂) reduction to useful fuels such as methanol and ethylene¹³⁻¹⁶ (i.e. effectively acting as an artificial leaf, replicating photosynthesis).

Table 1. Gravimetric and volumetric energy densities of common chemical fuels. Adapted with permission from Mazloomi)^{8, 17-18} © Copyright 2019, Elsevier.

Material	Energy per kilogram /MJ kg⁻¹	Energy per litre /MJ L⁻¹
Hydrogen (liquid)	143	10.1
Ammonia (liquid)	22.5	15.6
Methanol	19.7	15.6
Natural gas (liquid)	53.6	22.2
LPG propane	49.6	25.3
LPG butane	49.1	27.7
Gasoline	46.4	34.2
Diesel	45.4	34.6

Hydrogen, if produced from renewable energy sources via water electrolysis, offers a practical solution as a clean chemical fuel, due to its lack of environmentally noxious

combustion products.¹⁹ Hence, the Tokyo 2020 Olympic Games aims to build a hydrogen-based demonstration by powering the Olympic village with hydrogen including mass-produced hydrogen-based fuel-cell vehicles and fuel stations.²⁰ On the other hand, to use this high energy density fuel throughout the world, hydrogen must be liquefied during long-distance transportation, requiring more than 30% of its energy content (without factoring in boil-off losses).¹⁷ Nevertheless, the production and application of hydrogen for domestic use alleviates such energy losses associated with overseas transportation.

In recent research, ammonia is increasingly recognised as a transport vector for renewable energy. Figure 2 shows a schematic of the diverse ways liquid ammonia can be utilised as a source of energy. Ammonia can be used directly in proton-exchange membrane fuel cells,²¹⁻²² as part of a fuel mixture in modified engines,²³ or cracked into hydrogen (releasing N₂ as the by-product) and subsequently used in the hydrogen economy in the aforementioned applications.²⁴

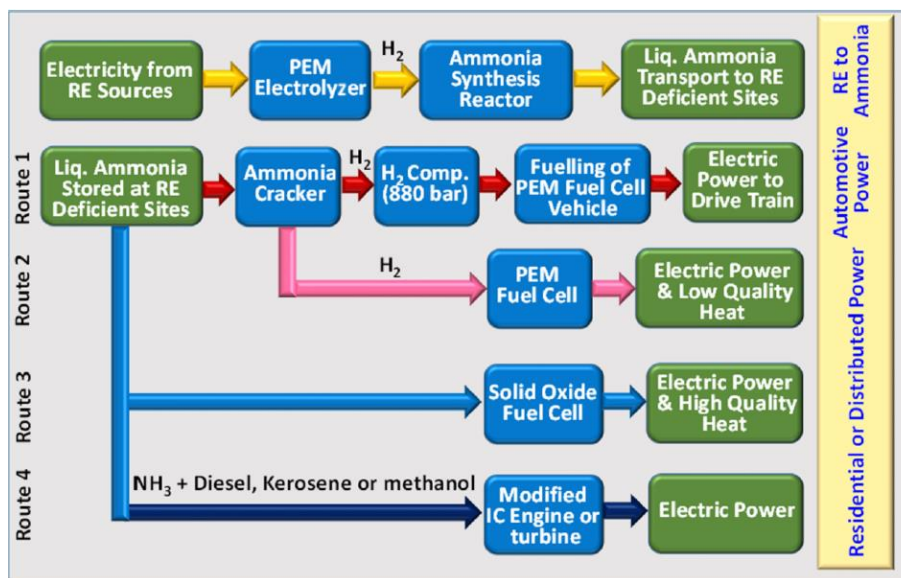


Figure 2: The different routes in which liquid ammonia can be used to generate power for residential/automotive applications. Reprinted with permission from Giddey et al.³ © Copyright 2019, American Chemical Society.

In terms of transportation, ammonia is much easier to liquefy than hydrogen due to the difference in their normal boiling temperatures of -33 °C and -253°C respectively.²⁵ Of course, pressurising these fuels can alleviate the burden of reaching these low temperatures (e.g.

ammonia is liquefied at room temperature under 10 atm), with the drawback of the energy requirements to pressurise such containments. Due to the worldwide use of ammonia in fertilisers over the last century, the technology for ammonia transportation already exists, from pipelines to trucks and shipping infrastructure, thus fast-tracking the techno-economic path for large-scale ammonia distribution. Hence, there lies immense potential in utilising ammonia as a carbon-free chemical fuel for energy storage and transportation, if ammonia can be derived from renewable energy sources by efficient and cost effective means.

1.2 Ammonia

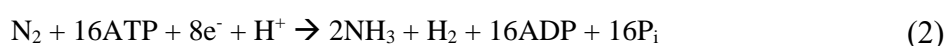
Ammonia is a colourless, alkaline gas with a pungent smell, and is the second most commonly produced chemical in the world.²⁶ Currently, the high demand of ammonia arises from its use as a starting precursor in the chemical synthesis of fertilisers. In 2018, approximately 140 million tonnes of ammonia was produced,²⁷ ~80% of which is used for agricultural fertilisers,²⁸⁻²⁹ responsible for feeding approximately half of the world's population.^{28, 30} Ammonia is also intensely used for the production of pharmaceuticals, explosives, cleaning agents, refrigerants etc. The bulk supply of ammonia, over the last century up to today, is produced via the industrial Haber-Bosch process. This process, developed by Fritz Haber in 1909, consists of mixing hydrogen and nitrogen gas together under a ruthenium or iron-based catalyst to yield ammonia³¹:



In 1913, Carl Bosch scaled this process up to the industrial level via which the process of synthesising ammonia was commercialised and large-scale production was made possible. However, the Haber-Bosch process requires intense energy consumption – the result of its high pressure (200 atm) and high temperature (500 °C) requirements.³² As a result, 1—2 % of the energy generated worldwide is devoted to the Haber-Bosch process.²⁹ In addition to this necessary usage of energy, which is all derived from fossil fuels, the steam reforming process

that is used to produce H₂ as feedstock generates over 240 million tonnes of CO₂ per annum.³ Of course, there is little feasibility in utilising ammonia as an energy carrier given such intense energy requirements, and the significant impact on the environment with the Haber–Bosch process. Given the conflicting issues of global warming and the large-scale production of ammonia being utterly crucial to sustain the growing human population worldwide, it is urgent that we seek sustainable methods of ammonia synthesis.

In nature, nitrogen can be converted to ammonia through biological nitrogen fixation via microorganisms³³ and biological enzymes³⁴, and also through naturally occurring lightning strikes.³⁵ The biological pathway for ammonia synthesis via the enzyme nitrogenase occurs through the reaction:

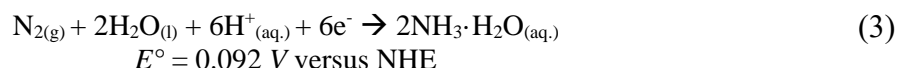


However, these pathways are not available on a reliable basis and cannot meet the substantial supply of ammonia required to sustain the current human population. Therefore, it is vital to find a scalable process of ammonia production that can simplify design, lower cost and operational requirements, compared to the standard Haber–Bosch process.³⁶ Replacing the current steam reforming process with the electrolysis of water to produce hydrogen is certainly an attractive option to alleviate the carbon dioxide emissions in the Haber–Bosch process.³⁷ Still, despite the advances in water splitting over the last few decades, several techno-economic considerations (e.g. catalyst poisoning, cost of materials, above ambient conditions required etc.) have slowed the progress of this development.³⁸⁻³⁹

This begs the important question; do we keep waiting for the perfect system (i.e. higher energy efficiencies and decreased costs until it becomes economically viable), or do we look for an alternative process that could directly produce ammonia at ambient conditions?

1.3 Electrochemical Ammonia Synthesis

Electrochemical ammonia synthesis, often referred to as the nitrogen reduction reaction (NRR), is the multi-step conversion of dinitrogen into ammonia by the half-reaction:⁴⁰



The potential for a green ammonia process has sparked huge interest in the field of electrocatalysis, where the electrocatalytic reaction of N_2 can be carried out via various methods, ranging from: photoelectrochemistry,⁴¹⁻⁴² homogenous catalysis such as transition metal complexes,⁴³⁻⁴⁴ lithium-mediated catalysis⁴⁵⁻⁴⁶, heterogeneous catalysis including metal⁴⁷⁻⁴⁸ and non-metal based⁴⁹⁻⁵⁰ catalysts, and the use of molten salts⁵¹ and solid electrolytes⁵²⁻⁵³. The references listed are merely examples and do not cover the respective research fields; should the reader be interested, the following review papers detail the extensive range of catalysts, conditions (e.g. pH, temperature, potential applied, catalyst loading etc.), and proposed reduction mechanisms, that have been studied.⁵⁴⁻⁵⁷

1.3.1 Required Protocols

Over the last few years, research groups have realised the necessity to establish meticulous protocols for the electrochemical NRR due to potential contamination issues associated with ammonia quantification.⁵⁸⁻⁶¹ Due to the small amount of ammonia that is electrochemically produced compared to the background, the following number of possible contamination sources should be addressed by carrying out:

- i) Rigorous scrubbing of Ar , $^{14}\text{N}_2$, and $^{15}\text{N}_2$ gas-streams and blank experiments at open circuit potential (for extended time periods) to ensure absolute high purity of each gas-stream.
- ii) Ar -flow experiments under the exact same $^{14}\text{N}_2$ experimental conditions to determine if there is a source of ammonia or (Nitrogen Oxide) NO_x species present in the catalyst/substrate or the electrode cell setup (since N_2 will not be present, ammonia should not be produced). These experiments also test for electrode stability during electrosynthesis at the same potential.

iii) Isotopically labelled $^{15}\text{N}_2$ gas–stream experiments in quantitative agreement with the $^{14}\text{N}_2$ experiments through NMR as a detection method (distinguished by the difference in NMR splitting patterns).

iv) Control experiments (cell/trap exposure to the atmosphere) and Berthelot and Griess tests (or ion chromatography) to determine if exogenous ammonia or NO_x can be derived from the atmosphere⁶² and enter the electrolyte, acid trap or adsorb onto the electrode surface (as NO_x species are known undergo electrochemical reduction to ammonia).⁶³

v) Careful handling of laboratory equipment such as gloves,⁶⁴ N–containing precursors, and even the human breath⁶⁵ which can all contribute to ammonia or NO_x species.

vi) Electrolyte compatibility with the detection method by spiking samples with a series of known concentrations followed by verification (with NMR, Berthelot, Griess, ion chromatography etc.).

While research groups exercise due diligence to address these contamination issues, they may not have foreseen every one of these issues. For example some groups have not considered possible NO_x contamination that may or may not be present in their system (even their $^{15}\text{N}_2$ supply),⁶⁶⁻⁶⁸ which can easily undergo electrochemical reduction into ammonia. As a result, one cannot know for sure if the obtained values are truly from electrochemical NRR or due to impurities. Given the questions of reliability makes it difficult to summarise the current state of the electrochemical NRR field, without complete confidence of the reported performance parameters. Hence, recent perspectives by Greenlee,⁶¹ MacFarlane,⁵⁹ and Chorkendorff⁵⁸ provide a series of protocols that should be followed in subsequent publications to allow reliable comparisons between different data sets, and allow the growth of this field.

1.3.2 Improving Faradaic Efficiency

With the current performance of the electrochemical NRR, the process of ambient ammonia synthesis is still far from being industrialised. Two simple, yet fundamental, reasons are i) the poor selectivity of ammonia formation (low Faradaic efficiencies of $< 20\%$)⁶⁹⁻⁷¹ and ii) the

substantially low yield rates ($\sim 10^{-11}$ mol s⁻¹ cm⁻²).^{70, 72-73} For electrochemical NRR to be commercially viable, Faradaic efficiencies (i.e. the percentage of current that is used to produce ammonia) would have to exceed 50% and yield rates faster than 1×10^{-7} mol s⁻¹ cm⁻².^{31, 74} In addition, these quantitative performance parameters must be considered along with catalyst stability, product separation, materials fabrication costs, limited usage of precious metals etc.

That being said, electrochemical ammonia synthesis is still in its infancy and much more is to be learned. One of the major challenges faced by research groups is the competing hydrogen evolution reaction (HER) that is considerably more facile than the NRR:⁷⁵



The reduction potential of the HER is lower than that of the NRR, leading to unfavourable thermodynamics. Thus, here lies the challenge of finding a highly selective NRR catalyst, capable of achieving high Faradaic efficiency. In addition, the low Faradaic efficiencies stem from the intrinsically low solubility of N₂ in aqueous-based electrolytes, limiting the kinetics of the NRR and resulting in such sluggish performance. In spite of this, the majority of the NRR field works in aqueous media and focuses on the electrocatalyst and substrate material in order to enhance Faradaic efficiency, whereas research into non-aqueous based electrolytes has received little attention. Hence, one relatively unexplored strategy is to move toward non-aqueous based solvents (with higher N₂ solubility) to minimise the degree of HER.

In terms of organic media, Koleli and co-workers investigated electrochemical ammonia synthesis using an electrolyte with LiClO₄/H⁺ in methanol, and achieved a Faradaic efficiency of 16%, albeit at a high pressure of 50 bar.⁷⁶ At ambient conditions, Kim and colleagues have studied electrochemical NRR on porous nickel catalysts in an acidic electrolyte containing 2-propanol/water (9:1) mixture, yet achieved a low Faradaic efficiency of 0.89% due to the co-formation of propoxide ions (C₃H₇O⁻) and H₂.⁷⁷ Pappenfus et al. encountered a similar problem using an electrolyte consisting of 0.2 M LiClO₄ and 0.18 M ethanol in [C₂mim][NTf₂],

obtaining a Faradaic efficiency of 5.1%, where control experiments indicated breakdown of the ionic liquid (IL). They also attempted to use the same electrolyte dissolved in [C₄mpyr][NTf₂]/tetrahydrofuran (1:1) with limited success, obtaining a Faradaic efficiency of 3.8%. This data from the literature demonstrates the difficulties associated with electrolyte breakdown when carrying out electrochemical NRR.

On the other hand, it was only very recently that electrochemical ammonia synthesis was deemed to be promising in IL media. MacFarlane and co-workers conducted electrochemical NRR using neat ILs with high N₂ solubility and hydrophobicity.⁷⁸ Through careful control of the water content (to ~100 ppm) Faradaic efficiencies as high as 60% were achieved. Thus, this demonstrates the suppression of the HER and the viability of utilising IL-based electrolytes, particularly if they exhibit high N₂ solubility. As a result, this led to the development of IL-fluorinated solvent mixtures that could dissolve high concentrations of N₂. Through the use of a fluorinated IL-based electrolyte (with high N₂ solubility) and an enhanced surface area α -Fe nanorod catalyst, the reaction rate was improved ten-fold whilst achieving a high Faradaic efficiency of 35%.⁷⁹ Hence, this provides scope to explore the N₂ solubility in ILs and various other media.

1.4 N₂ Solubility

1.4.1 Methods of Measuring Gas Solubility

The concentration of N₂ in the electrolyte may be a highly contributing factor for the performance of the electrochemical NRR. Hence, it is of significant value to be able to measure the value of N₂ solubility in such electrolytes. Several methods of measuring gas solubility exist in the literature, many of which have applications in CO₂ extraction and separation.⁸⁰⁻⁸¹ A brief summary of each method to measure the gas solubility in liquids is described:

- i) One common method to measure gas solubility involves the use of a gravimetric microbalance to measure the increase in weight after the gas is introduced. This method is

sufficient for measuring the solubility of gases such as CO₂ and NO₂, due to their inherent dipole and capability to chemically interact with the solvent such that a large amount of gas can be dissolved.⁸¹⁻⁸³ On the other hand, the low-polarisability, non-interacting nature of N₂ tends toward low gas dissolution in such solvents, resulting in large uncertainties in gravimetric measurements.⁸⁴

ii) During the 20th century, several researchers have determined gas solubility (based on the isobaric method of Bunsen's and Ostwald's apparatus) by carefully measuring the difference in the volume of gas, before and after the gas comes into contact with the liquid.⁸⁵⁻⁸⁶ However, these methods used reservoirs of mercury as part of their apparatus, which has well-known drawbacks due to its toxicity and safety concerns.⁸⁷

iii) Maurer and others utilise a static high-pressure apparatus to measure gas solubility.⁸⁸⁻⁹⁰ In this method, a known amount of solvent and gas is added after which the pressure is decreased stepwise; the point at which the first bubble/new phase appears indicates the point at which gas solubility can be determined. However, this apparatus is designed for high pressure measurements whereas our interests in N₂ solubility for electrochemical ammonia synthesis lie near ambient conditions.

iv) The time lag method involves injecting a known amount of gas into a feed chamber that passes through an IL membrane at which a steady increase in pressure is observed.⁹¹⁻⁹³ The pressure rise in the permeate chamber with respect to time allows the determination of diffusivity and solubility of the desired gas. However, in some cases the supporting membrane can interact either with the gas or solvent of interest. This is similar to the method of gas-liquid partition chromatography where an inert carrier gas instead passes through a liquid that is saturated with the desired gas, with the limitation of the need to use high-boiling liquids.⁹⁴⁻⁹⁵

v) Gas solubility can also be estimated by carrying out chronoamperometry on a macroelectrode and microelectrode and by the simultaneous fitting of two equations, the

concentration of gas and its diffusion coefficient can be determined.⁹⁶ However, the NRR and HER both occur at similar reduction potentials where the current cannot be merely attributed to nitrogen reduction.

vi) The isochoric saturation method (also known as pressure drop or pressure swing method) has been established by a number of research groups to measure gas solubility.⁹⁷⁻¹⁰⁰ In this method, a known amount of gas is added to a known amount of solvent sample at constant temperature and volume. Upon release of gas into the sample chamber, the decrease in pressure (which indicates absorption) is monitored until equilibrium is reached. Finally, the difference in pressure (before and after expansion) is related to the amount of gas dissolved within the sample.

Based on several factors including high precision requirements, safety concerns, and the desire to work at close to ambient pressures, solubility measurements in this dissertation will utilise the isochoric saturation method. This system to measure gas solubility is not commercially available and requires the construction of custom-designed apparatus to conduct measurements and obtain reliable data at low solubility levels. The details and procedures involved with constructing our high-precision apparatus are detailed in Chapter 2.

1.4.2 Literature Data of N₂ Solubility

Literature data of N₂ solubility in commonly used solvents are presented in Table 2. Should the reader be interested, the following review papers provide N₂ solubility values for an extensive list of solvents.^{95, 101-102} In the context of electrochemical ammonia synthesis, the reduction current density typically depends on the molar concentration of dissolved N₂ (rather than mole fraction or mass concentration);¹⁰³ hence, N₂ solubility data is presented primarily in terms of molar concentrations.

The nature of N₂ solubility in solvents of differing functionality will be explored in this thesis. A brief summary of the N₂ solubility database is as follows: The highest N₂ solubility is found with perfluorinated solvents, which decreases when polar functional groups are added.

Aliphatic organic solvents are observed to exhibit high N₂ solubility followed by aromatics and alcohols. Interestingly, increasing the chain length of the aliphatic alkyl chain results in lower N₂ solubility, likely associated with the increase in intermolecular dispersion forces. The same trend can be hypothesised with the presence of polar functional groups in these organic solvents, which adds intermolecular dipole–dipole forces and leads to lower N₂ solubility values. Next, ILs with a high degree of fluorination exhibit N₂ solubilities higher than ILs with low/no fluorination; this will be detailed further in the following section. Lastly, exceedingly low N₂ solubility is observed in water, which may be due to its extensive network of hydrogen bonds throughout the liquid structure and the exceedingly weak H–bond acceptor capability of N₂.¹⁰⁴

Here, the molecular compounds that display higher N₂ solubility values tend to exhibit relatively weak intermolecular interactions. However, one must consider the inherent properties of these solvents and recognise their advantages/drawbacks. For example, whilst perfluorinated solvents exhibit high N₂ solubility, they also have inherently low dielectric constants¹⁰⁵ such that ionic species do not dissolve into such media (which is obviously required in an electrolyte for the electrochemical NRR). On the other hand, ILs offer complexity in their molecular structure in which they could be specifically tailored to allow dissolution into perfluorinated solvents. An extensive study in the selection of an ideal solvent and ionic species, including their interactions with each other, is carried out in chapter 4 of this thesis.

Table 2. N_2 Solubility in various solvents expressed as molar concentration C_{N_2} , mass concentration γ_{N_2} , and mole fraction χ_2 near room temperature and atmospheric pressure ($p = 1 \text{ atm}$)

Sample	Temperature /K	C_{N_2} / $10^{-3} \text{ mol L}^{-1}$	γ_{N_2} /mg L ⁻¹	χ_2 / 10^{-3}
Caroxin-F (perfluoro-1-isopropoxy-hexane) ¹⁰⁶	298	17.7	497	5.1
Perfluoroheptane ^{*107}	298	17.4	487	3.9
Perfluoromethylcyclohexane ¹⁰⁸	298	16.7	469	3.3
Hexafluorobenzene ¹⁰⁸	298	15.6	436	1.8
Caroxin-D (perfluoro-1,4-diisopropoxybutane) ¹⁰⁶	298	15.4	431	5.0
Perfluoro-1-isopropoxy-hexane ¹⁰⁷	298	15.3	428	5.1
Perfluoro-1,3-dimethylcyclohexane ¹⁰⁷	298	15.2	427	3.3
Dipropyl ether ¹⁰¹	298	12.9	234	1.2
1H,1H,2H-heptafluorocyclopentane [*]	303	12.2	342	1.5
1H,1H,5H-octafluoropentyl 1,1,2,2-tetrafluoroethyl ether [*]	303	11.6	325	2.4
Diethyl ether ¹⁰¹	313	11.2	313	1.2
Perfluorotributylamine ¹⁰⁸	298	11.2	312	4.0
Hexane ^{*108}	298	10.7	301	1.4
FC-80 (perfluorobutyl perfluorotetrahydrofuran) ¹⁰⁶	298	10.4	291	4.3
Trifluorotoluene [*]	303	9.9	278	1.2
2,2,4-Trimethylpentane ¹⁰⁸	298	9.3	261	1.5
Heptane ¹⁰⁸	298	9.1	259	1.4
Octane ¹⁰⁸	298	8.0	225	1.3
Nonane ¹⁰⁸	298	7.7	215	1.3
Acetone ¹⁰⁸	298	7.4	206	0.5
Cyclohexane ¹⁰⁷	298	7.0	196	0.8
[P ₆₆₆₁₄][C ₈ F ₁₇ CO ₂] [*]	303	6.5	182	4.5
Acetonitrile ^{*109}	304	6.4	178	0.3
[P ₆₆₆₁₄][C ₈ F ₁₇ SO ₃] [*]	303	6.2	174	5.2
Ethanol ¹⁰⁸	298	6.2	172	0.4
Cyclohexene ¹⁰⁸	298	6.1	172	0.6
[P ₁₄₄₄][eFAP] [*]	303	5.9	164	2.7

[P ₆₆₆₁₄][C ₆ F ₁₃ SO ₃]*	303	5.8	162	4.5
[P _{4448f}][eFAP]*	303	5.7	160	3.8
[P _{122l4}][eFAP]*	303	5.5	154	2.2
[P ₄₄₄₈][eFAP]*	303	5.3	148	3.1
Toluene ¹⁰¹	298	5.1	143	0.5
Benzene ¹⁰¹	298	5.0	140	0.4
[P ₆₆₆₁₄][C ₄ F ₉ SO ₃]*	303	4.8	134	3.5
Pentadecane ¹⁰¹	298	4.8	134	1.3
[C ₄ mpyr][eFAP]*	303	4.8	133	1.8
[P ₆₆₆₁₄][C ₄ F ₉ CO ₂]*	303	4.6	129	3.2
[C _{8f} mim][NTf ₂] ¹¹⁰	303	4.5	125	1.9
[P ₆₆₆₁₄][eFAP]*	303	4.3	120	3.2
[C ₄ mim][BETI] ¹¹⁰	303	3.9	108	1.6
[C ₄ mim][PF ₆] ¹¹¹	303	3.7	104	0.8
[C ₄ mim][NTf ₂] ¹¹²	313	3.6	101	1.0
[C ₆ mim][NTf ₂] ¹¹²	313	3.4	96	1.1
[C ₂ mim][NTf ₂] ¹¹²	313	3.3	93	0.9
[C ₄ mim][BF ₄] ¹¹³	303	3.0	85	0.6
[C ₈ mim][NTf ₂] ¹¹⁰	303	3.0	83	1.2
[P ₁ mim][NTf ₂] ¹¹⁴	313	2.7	77	0.8
[C ₂ mim][NTf ₂] ¹¹²	298	2.5	69	0.7
[NC ₄ mim][NTf ₂] ¹¹²	313	2.2	61	0.6
[C ₂ mim][OTf] ¹¹⁵	313	2.0	57	0.4
[C ₄ mim][CH ₃ CO ₂] ¹¹⁶	333	1.9	54	0.4
[C ₂ mim][BF ₄] ¹¹²	313	1.7	47	0.3
[C ₂ mim][CH ₃ CO ₂] ¹¹⁶	333	1.7	46	0.3
[C ₂ mim][DCA] ¹¹²	313	1.3	35	0.2
[C ₂ mim][BF ₄] ¹¹²	298	0.9	26	0.1
[Hmpy][NTf ₂] ¹¹⁷	298	0.9	25	0.3
Water ¹⁰¹	303	0.6	17	0.01

*indicates the measurement of N₂ solubility in this thesis

1.5 Ionic Liquids

ILs are loosely defined as salts that have a melting point below 100 °C.¹¹⁸ As research into this field develops, ILs have later become broadly defined as ‘low melting salts’ or ‘a liquid comprised entirely of ions’.¹¹⁹⁻¹²⁰ To provide a brief history: The first ILs were discovered as early as 1914 with the synthesis of ethyl ammonium nitrate with a melting point of 12 °C.¹²¹ In the 1980s, chloroaluminate-based salts were developed with imidazolium and pyridinium cations that were liquid at ambient temperatures.¹²²⁻¹²³ In 1992, Wilkes and others discovered water-stable ILs by the combination of imidazolium cations with anions including [BF₄]⁻, [NO₃]⁻, [PF₆]⁻.¹²⁴⁻¹²⁵

One could argue when the first evolution of ILs actually began; whether it was the first discovery of an IL, the first time the scientific audience became interested, or when ILs were realised to be useful solvents for various applications. Nevertheless, the Rogers group identified the second evolution of ILs in which they were viewed as tuneable, multi-purpose materials with specific chemical and/or physical properties.¹²⁶ Subsequently, Rogers and co-workers recognised a third evolution of ILs by expanding the use of ILs into bio-active/pharmaceutical applications with targeted biological properties;¹²⁷ these ILs require a particularly different chemical nature and functionality than the inert ILs used in electrochemical (and other) applications.¹²⁸

More than a decade later, MacFarlane and co-workers offer the perspective of a fourth evolution of ILs.¹²⁰ As stated, even with the extensive applications of ILs as ‘a liquid comprised entirely of ions’, the utilisation of ILs should not be restricted to neat ILs and should certainly include their mixtures with molecular solvents¹²⁹ or gases.¹³⁰ Hence, the mixing of ILs with molecular solvents, gases, other IL/metal salts and even the combination of such gives rise to an overwhelming list of unique properties and applications. With this in mind, we can take advantage of this phenomenon to develop an ideal IL-solvent system for our application in electrochemical ammonia synthesis.

1.5.1 Properties of Ionic Liquids

ILs, which typically consist of bulky asymmetrical ions (to reduce electrostatic interactions and aid in lowering the melting point), have many beneficial properties over other classes of solvents.¹³¹ First, ILs are generally non-volatile, chemically and thermally stable such that they tend not to react or decompose over time.¹³² In the context of electrochemistry, they exhibit wide electrochemical potential limits of stability and are intrinsically conductive, thus removing the need for a supporting electrolyte.¹³³ This allows for a simpler electrolyte system for electrochemical applications.

Unlike the ~600 molecular solvents that are extensively used in industrial processes today, ILs offer a unique situation;¹³⁴ at least a million ILs exist (not to mention binary, ternary, or multi-component mixtures), allowing us to tailor these ‘designer solvents’, for instance to obtain maximum yield and purity of synthetic compounds.¹³⁵ This enables their versatility in a wide range of applications and allows us to target specific properties.¹³⁶ For example, a small change in the anion from [C₄mim][BF₄] to [C₄mim][PF₆] will lead to a difference in water solubility, the latter being water immiscible.¹³⁷

Another advantage of ILs is that they tend to exhibit high gas solubility (and solvent miscibility) with significant importance in gas capture and extraction applications.¹⁰² As described earlier, it is highly desirable to dissolve a high concentration of N₂ in the electrolyte for electrochemical NRR. By applying the trends that were observed from the database of N₂ solubility (Table 2), ILs can be tailored to incorporate a higher degree of fluorination as a possible strategy to further enhance N₂ solubility.

Fluorine is of great interest as a substituent in the IL cation/anion due to the inert nature of the C-F bond despite the high electronegativity of fluorine (when fluorine is bonded to carbon).¹³⁸⁻¹³⁹ This is further exemplified as fluorine substituents, which are electron-withdrawing, pull electron density away from the electrostatic charge of the anion (i.e. diluting the ionic character of the IL). As a result, fluorinated ILs tend to exhibit low overall cohesive

energies which may allow higher N₂ solubility in this class of solvents. This hypothesis of enhancing N₂ solubility by increasing the degree of fluorination on the IL, as well as other strategies to push the upper limit of N₂ solubility, are explored throughout this thesis.

1.5.2 Fluorinated Ionic Liquids

Research into fluorinated ILs has developed uses in many applications such as biomedical treatments,¹⁴⁰⁻¹⁴¹ metal extractions,¹⁴² thin-film surfaces¹⁴³ and lubricants.¹⁴⁴ Here, a fluorinated IL is defined as one or both of the ions containing fluorine. The first fluorinated ILs were synthesised in the search for a hydrophobic IL, by pairing imidazolium cations with fluorinated anions such as tetrafluoroborate [BF₄]⁻ and hexafluorophosphate [PF₆]⁻.^{125, 145} This research extended into examining various fluorinated anions such as trifluoroacetates, trifluorosulfonates and bis(trifluoromethylsulfonyl)imides.^{132, 146} It was later found that ILs that contain the [BF₄]⁻ and [PF₆]⁻ anion were hydrolytically unstable due to the loss of fluoride, resulting in the formation of hydrofluoric acid in water.¹⁴⁷⁻¹⁴⁸ Figure 3 shows the molecular structures of some fluorinated anions and cations that can be used as components to form a fluorinated IL.

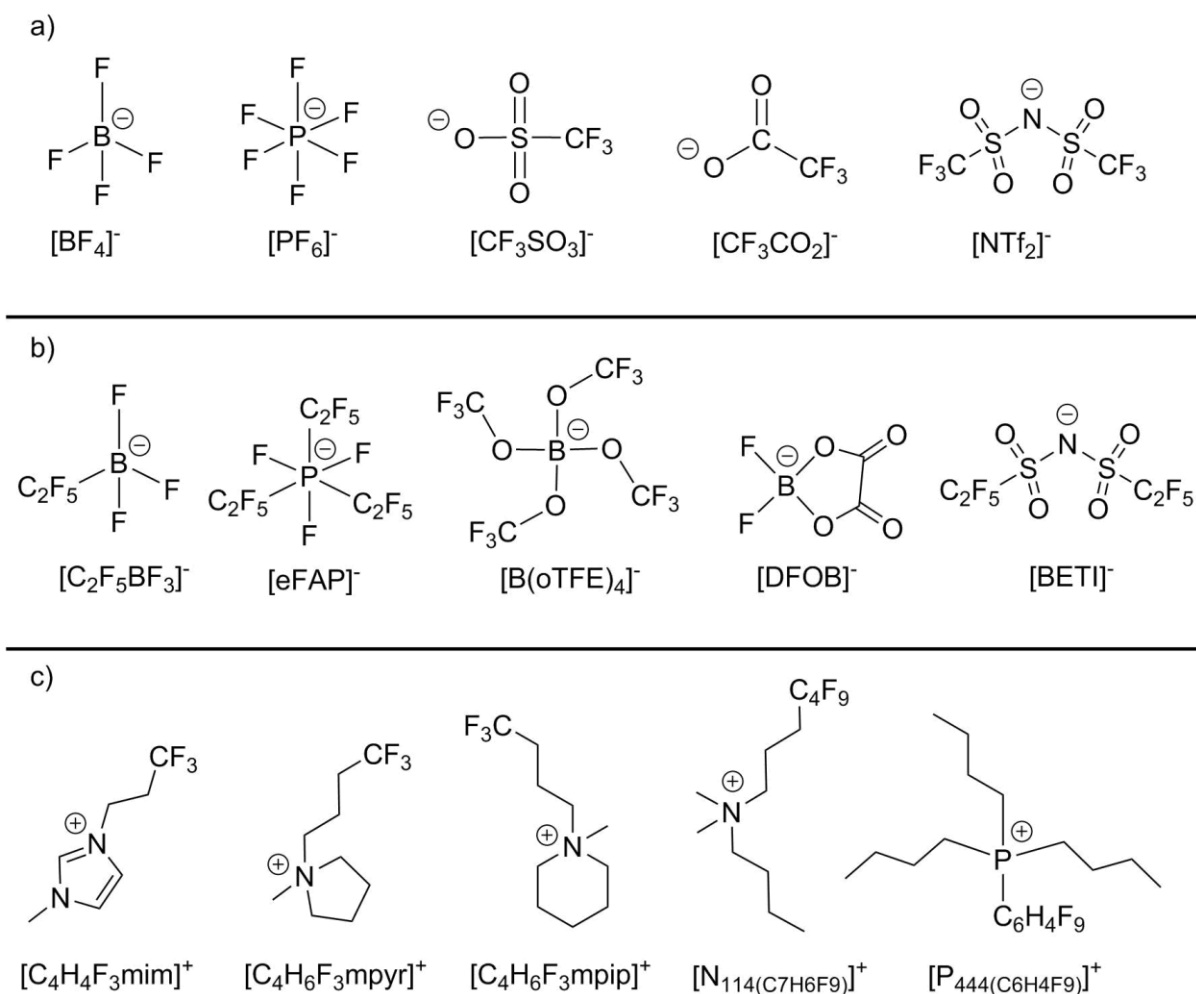


Figure 3: Molecular structures of fluorinated ionic liquid ions: a) first generation fluorinated IL anions, b) second generation fluorinated anions, and c) fluorinated cations.

Based on this first generation of fluorinated anions, a range of these anions had been modified to incorporate a higher degree of fluorination. For example, Ignatev et al., sought the addition of perfluoroethyl groups to the phosphate anion and produced the tris(pentafluoroethyl)trifluorophosphate $[eFAP]^-$ anion,¹⁴⁹ leading to better water stability than the $[PF_6]^-$ anion; Passerini et al. had synthesised bis(pentafluoroethanesulfonyl)imide $[BETI]^-$ and perfluorobutanesulfonyl (trifluoromethylsulfonyl)imide variants,¹⁵⁰ which were later observed by Russina et al., to exhibit mesoscopic fluorinated domains (due to its large perfluoroalkyl chains);¹⁵¹ Krossing et al. had synthesised fluoroalkyltrifluoroborates¹⁵² and tetrakis(fluoroethoxy)borates,¹⁵³⁻¹⁵⁴ derived from $[BF_4]^-$ and $[B(CN)_4]^-$ respectively. Further alternatives of fluoroborate-based ILs had been synthesised by Gore and others such as

difluoro(oxalato)borates [DFOB]⁻ and difluorobis(acetate)borates [BF₂(Ac)₂]⁻ for use in battery applications.¹⁵⁵⁻¹⁵⁶

Of course, these fluorinated anions have the potential to incorporate a higher degree of fluorination. However, one can expect that eventually, these fluorinated ILs will form solid salts at ambient temperature. For example, Forsyth et al. and Sundermeyer et al. have synthesised salts with a perfluorosulfonate anion (nonaflates) and highly fluorinated bistriflimide variants,¹⁵⁷⁻¹⁵⁸ yet they formed solid salts that would not be usable for the electrochemical NRR at ambient temperature. On the other hand, the melting point of an IL is certainly dependent on the paired cation, hence the potential utility of these fluorinated anions remains somewhat unexplored (see chapter 3).

In terms of the IL cation, several groups have synthesised phosphonium ILs with varying degrees of fluorination (from fluoroalkyl to tetrafluoroalkyl phosphoniums) for use as phase transfer catalysts.¹⁵⁹⁻¹⁶² In addition to trialkyl(fluoroalkyl) ammonium iodide salts,¹⁶³ common cations such as the imidazolium, pyrrolidinium and piperidinium also have been successfully partially fluorinated on the alkyl chain, for potential use as surfactants and lubricants.^{144, 163-166}

However, N₂ solubility measurements have not been carried out in most of these fluorinated ILs as they have sought applications elsewhere. The ILs which have measured values of N₂ solubility (shown in Table 2) are mostly limited to those with a low degree of fluorination such as [BF₄]⁻, [OTf]⁻, [NTf₂]⁻ etc. Gomes et al. have observed a 30% increase in N₂ solubility from [C₄mim][NTf₂] to [C₄mim][BETI], and a 50% increase by incorporating a high degree of fluorination in the imidazolium cation [C₈H₄F₁₃mim][NTf₂] (shown in Table 2). Thus, this demonstrates the effect on N₂ solubility of extending the fluorination on the [NTf₂]⁻ anion and fluorinating the alkyl chain on the imidazolium cation.

While a number of studies explore the effect of fluorination in regards to CO₂ solubility,¹⁶⁷⁻¹⁷⁰ these trends may vary compared to N₂ solubility due to the different nature of each gas.^{111,}

¹¹⁷ For example, CO₂ solubility decreases with the addition of acetonitrile to [C₂mim][NTf₂],¹⁷¹ likely due to the interaction of CO₂ with the cation and/or anion of the IL;¹⁶⁹ on the other hand, the non-polarisable nature of N₂ will lead to weak interactions with the IL, if any, and may in fact display the opposite trend.

1.6 Fluorinated Ionic Liquid–Based Electrolytes

As discussed earlier, highly fluorinated solvents, as well as highly fluorinated ILs, are observed to exhibit high N₂ solubility values. In this thesis (chapters 4 and 5), we explore the potential of mixing these two classes of solvents together to examine their effect on N₂ solubility. In the literature, fluorinated electrolytes are utilised in many applications of research such as lithium and lithium/sulfur batteries,¹⁷²⁻¹⁷⁵ electrochemical sensing¹⁷⁶⁻¹⁷⁷ and hydrofluorination applications.¹⁷⁸⁻¹⁷⁹ In these applications, the fluorinated electrolyte are quite dissimilar to each other in terms of properties and composition. For example, the commercialised lithium battery electrolyte consisting of 1 M LiPF₆ in ethylene carbonate/dimethyl carbonate¹⁸⁰ is different to the mixture of 80 mM [N₄₄₄₄][BArF₁₀₄] in perfluoro(methylcyclohexane), yet both would be classed as fluorinated electrolytes. There lies an implicit difference as whether or not the solvent itself (not to mention additives) is fluorinated, and if the charged species is not fluorinated given its dissolution into fluorinated solvent.¹⁸¹ Therefore, for the purpose of this thesis we must clarify this with the question; what defines a fluorinated electrolyte?

To put this in perspective, we explore the concept of the 4th evolution of ILs by using a fluorinated IL–based electrolyte mixture, containing a fluorinated IL and a fluorinated solvent, to further enhance properties such as N₂ solubility and ionic conductivity. In this case, a fluorinated IL consists of either the cation and/or anion being partially or completely fluorinated whereas a fluorinated solvent will be defined by containing at least one fluorine

atom. Of course, to maximise the N₂ solubility of a fluorinated IL-based electrolyte, a higher degree of fluorination on each component would likely be of greater interest.

Nevertheless, literature data for N₂ solubility in fluorinated IL-based electrolytes remains limited. The work in this thesis aims to fill this gap of knowledge by exploring the use of fluorinated IL-based electrolytes to achieve high N₂ solubility.

1.6.1 Environmental Concerns

Some of the fluorinated materials used in this work are members of the polyfluoroalkyl substances (PFAS) family of compounds. This may raise environmental concerns as they may accumulate over time in the environment and in the human body.¹⁸² In spite of this, PFAS are found in household products and surfactants, and continue to be used every day in these applications.¹⁸³ Nevertheless, it is important to recognise that the use of these PFAS in the electrochemical NRR involves an essentially closed system. Furthermore, ammonia, and its by-products, are free of fluorine-containing substituents. Throughout the work carried out in this thesis, all fluorinated materials were handled and disposed of with the required safety protocols.

1.7 Research Objectives

Based on the early research status of using fluorinated IL-based electrolytes for the electrochemical NRR, the research objectives of this dissertation are to establish the foundations for these electrolytes by:

- Engineering and construction of a custom-designed apparatus capable of measuring N₂ solubility to a high precision and accuracy (with verification by comparison to literature data). This work is detailed in chapter 2.
- Synthesising a library of ILs with a high degree of fluorination and identifying ideal moieties that lead to high N₂ solubility and optimal transport properties (shown in chapter 3).

- Rationalising design principles for fluorinated IL-based electrolytes to achieve high N₂ solubility by comprehensive analysis of each component and their physicochemical properties (shown in chapter 4).
- An in-depth study of fluorinated IL-based electrolyte systems by examining their volumetric properties and intermolecular interactions in correlation to their N₂ solubility (found in chapter 5).

1.8 References

1. Panwar, N. L.; Kaushik, S. C.; Kothari, S., Role of Renewable Energy Sources in Environmental Protection: A Review. *Renew. Sust. Energ. Rev.* **2011**, *15*, 1513—1524.
2. Gulagi, A.; Bogdanov, D.; Fasihi, M.; Breyer, C., Can Australia Power the Energy-Hungry Asia with Renewable Energy? *Sustainability* **2017**, *9*, 233—259.
3. Giddey, S.; Badwal, S. P. S.; Munnings, C.; Dolan, M., Ammonia as a Renewable Energy Transportation Media. *ACS Sustain. Chem. Eng.* **2017**, *5*, 10231—10239.
4. Department of the Environment and Energy, Australian Energy Update. *Australian Energy Statistics* **2018**.
5. 2017 the World Bank, Solar Resource Data: Solargis. Solar Resource Maps of the World, <https://solargis.com/maps-and-gis-data/download/world>. (accessed July 28, 2019).
6. Goodenough, J. B.; Park, K.-S., The Li-Ion Rechargeable Battery: A Perspective. *J. Am. Chem. Soc.* **2013**, *135*, 1167—1176.
7. Thomas, C. E., Fuel Cell and Battery Electric Vehicles Compared. *Int. J. Hydrogen Energy* **2009**, *34*, 6005—6020.
8. Shih, C. F.; Zhang, T.; Li, J.; Bai, C., Powering the Future with Liquid Sunshine. *Joule* **2018**, *2*, 1925—1949.
9. Bushuyev, O. S.; De Luna, P.; Dinh, C. T.; Tao, L.; Saur, G.; Van De Lagemaat, J.; Kelley, S. O.; Sargent, E. H., What Should We Make with CO₂ and How Can We Make It? *Joule* **2018**, *2*, 825—832.
10. Ramanathan, V.; Feng, Y., Air Pollution, Greenhouse Gases and Climate Change: Global and Regional Perspectives. *Atmos. Environ.* **2009**, *43*, 37—50.
11. Haszeldine, R. S., Carbon Capture and Storage: How Green Can Black Be? *Science* **2009**, *325*, 1647—1652.
12. Boot-Handford, M. E., et al., Carbon Capture and Storage Update. *Energy Environ. Sci.* **2014**, *7*, 130—189.
13. Qiao, J.; Liu, Y.; Hong, F.; Zhang, J., A Review of Catalysts for the Electroreduction of Carbon Dioxide to Produce Low-Carbon Fuels. *Chem. Soc. Rev.* **2014**, *43*, 631—675.
14. Costentin, C.; Robert, M.; Savéant, J.-M., Catalysis of the Electrochemical Reduction of Carbon Dioxide. *Chem. Soc. Rev.* **2013**, *42*, 2423—2436.
15. Morris, A. J.; Meyer, G. J.; Fujita, E., Molecular Approaches to the Photocatalytic Reduction of Carbon Dioxide for Solar Fuels. *Acc. Chem. Res.* **2009**, *42*, 1983—1994.
16. Kumar, B.; Llorente, M.; Froehlich, J.; Dang, T.; Sathrum, A.; Kubiak, C. P., Photochemical and Photoelectrochemical Reduction of CO₂. *Annu. Rev. Phys. Chem.* **2012**, *63*, 541—569.
17. Mazloomi, K.; Gomes, C., Hydrogen as an Energy Carrier: Prospects and Challenges. *Renew. Sust. Energ. Rev.* **2012**, *16*, 3024—3033.
18. Valera-Medina, A.; Xiao, H.; Owen-Jones, M.; David, W. I. F.; Bowen, P. J., Ammonia for Power. *Prog. Energy Combust. Sci.* **2018**, *69*, 63—102.

19. Carmo, M.; Fritz, D. L.; Mergel, J.; Stolten, D., A Comprehensive Review on PEM Water Electrolysis. *Int. J. Hydrogen Energy* **2013**, *38*, 4901—4934.
20. Harada, M.; Ichikawa, T.; Takagi, H.; Uchida, H., Building a Hydrogen Infrastructure in Japan. In *Compendium of Hydrogen Energy*, Ball, M.; Basile, A.; Veziroğlu, T. N., Eds. Woodhead Publishing: Oxford, 2016; Vol. 4, pp 321—335.
21. Afif, A.; Radenahmad, N.; Cheok, Q.; Shams, S.; Kim, J. H.; Azad, A. K., Ammonia-Fed Fuel Cells: A Comprehensive Review. *Renew. Sust. Energ. Rev.* **2016**, *60*, 822—835.
22. Baniyadi, E.; Dincer, I., Energy and Exergy Analyses of a Combined Ammonia-Fed Solid Oxide Fuel Cell System for Vehicular Applications. *Int. J. Hydrogen Energy* **2011**, *36*, 11128—11136.
23. Kobayashi, H.; Hayakawa, A.; Somaratne, K. D. Kunkuma A.; Okafor, Ekenechukwu C., Science and Technology of Ammonia Combustion. *P. Combust. Inst.* **2019**, *37*, 109—133.
24. CSIRO Cracks Barrier to Export Hydrogen Fuel to Power Cars, <https://reneweconomy.com.au/csiro-cracks-barrier-to-export-hydrogen-fuel-to-power-cars-79439/>, (accessed July 26, 2019).
25. Lide, D. R., 2005 Crc Handbook of Chemistry and Physics. CRC Press, New York: 2004.
26. Bartels, J. R., *A Feasibility Study of Implementing an Ammonia Economy*; ProQuest: Iowa, 2008.
27. Survey, U. G., Mineral Commodity Summaries. *Mineral Commodity Summaries, Geological Survey* **2016**.
28. Erisman, J. W.; Sutton, M. A.; Galloway, J.; Klimont, Z.; Winiwarter, W., How a Century of Ammonia Synthesis Changed the World. *Nat. Geosci.* **2008**, *1*, 636—639.
29. Smil, V., *Enriching the Earth: Fritz Haber, Carl Bosch, and the Transformation of World Food Production*; MIT press: Massachusetts, USA, 2004.
30. Smil, V., Nitrogen and Food Production: Proteins for Human Diets. *Ambio* **2002**, *31*, 126—131.
31. Giddey, S.; Badwal, S. P. S.; Kulkarni, A., Review of Electrochemical Ammonia Production Technologies and Materials. *Int. J. Hydrogen Energy* **2013**, *38*, 14576—14594.
32. Smil, V., Global Population and the Nitrogen Cycle. *Sci. Am.* **1997**, *1*, 76—81.
33. Frankow-Lindberg, B.; Dahlin, A., N₂ Fixation, N Transfer, and Yield in Grassland Communities Including a Deep-Rooted Legume or Non-Legume Species. *Plant Soil* **2013**, *370*, 567—581.
34. Hinnemann, B.; Nørskov, J. K., Catalysis by Enzymes: The Biological Ammonia Synthesis. *Top. Catal.* **2006**, *37*, 55—70.
35. Borucki, W. J.; Chameides, W. L., Lightning: Estimates of the Rates of Energy Dissipation and Nitrogen Fixation. *Rev. Geophys.* **1984**, *22*, 363—372.
36. Wang, L.; Xia, M.; Wang, H.; Huang, K.; Qian, C.; Maravelias, C. T.; Ozin, G. A., Greening Ammonia toward the Solar Ammonia Refinery. *Joule* **2018**, *2*, 1055—1074.
37. Walter, M. G.; Warren, E. L.; McKone, J. R.; Boettcher, S. W.; Mi, Q.; Santori, E. A.; Lewis, N. S., Solar Water Splitting Cells. *Chem. Rev.* **2010**, *110*, 6446—6473.
38. Jaramillo, T. F.; Jørgensen, K. P.; Bonde, J.; Nielsen, J. H.; Horch, S.; Chorkendorff, I., Identification of Active Edge Sites for Electrochemical H₂ Evolution from MoS₂ Nanocatalysts. *Science* **2007**, *317*, 100—102.
39. Kudo, A.; Miseki, Y., Heterogeneous Photocatalyst Materials for Water Splitting. *Chem. Soc. Rev.* **2009**, *38*, 253—278.
40. Deng, J.; Iñiguez, J. A.; Liu, C., Electrocatalytic Nitrogen Reduction at Low Temperature. *Joule* **2018**, *2*, 846—856.
41. Ali, M.; Zhou, F.; Chen, K.; Kotzur, C.; Xiao, C.; Bourgeois, L.; Zhang, X.; MacFarlane, D. R., Nanostructured Photoelectrochemical Solar Cell for Nitrogen Reduction Using Plasmon-Enhanced Black Silicon. *Nat. Commun.* **2016**, *7*, 1—5.
42. Banerjee, A.; Yuhas, B. D.; Margulies, E. A.; Zhang, Y.; Shim, Y.; Wasielewski, M. R.; Kanatzidis, M. G., Photochemical Nitrogen Conversion to Ammonia in Ambient Conditions with Femosecond Chalcogenides. *J. Am. Chem. Soc.* **2015**, *137*, 2030—2034.
43. Nishibayashi, Y., Recent Progress in Transition-Metal-Catalyzed Reduction of Molecular Dinitrogen under Ambient Reaction Conditions. *Inorg. Chem.* **2015**, *54*, 9234—9247.

44. Rittle, J.; Peters, J. C., An Fe–N₂ Complex That Generates Hydrazine and Ammonia Via Fe=NNH₂: Demonstrating a Hybrid Distal-to-Alternating Pathway for N₂ Reduction. *J. Am. Chem. Soc.* **2016**, *138*, 4243–4248.
45. Tsuneto, A.; Kudo, A.; Sakata, T., Lithium–Mediated Electrochemical Reduction of High Pressure N₂ to Nh₃. *J. Electroanal. Chem.* **1994**, *367*, 183–188.
46. Lazouski, N.; Schiffer, Z. J.; Williams, K.; Manthiram, K., Understanding Continuous Lithium-Mediated Electrochemical Nitrogen Reduction. *Joule* **2019**, *3*, 1–13.
47. Nazemi, M.; El-Sayed, M. A., The Role of Oxidation of Silver in Bimetallic Gold–Silver Nanocages on Electrocatalytic Activity of Nitrogen Reduction Reaction. *J. Phys. Chem. A* **2019**, *123*, 11422–11427.
48. Suryanto, B. H. R.; Wang, D.; Azofra, L. M.; Harb, M.; Cavallo, L.; Jalili, R.; Mitchell, D. R. G.; Chatti, M.; MacFarlane, D. R., MoS₂ Polymorphic Engineering Enhances Selectivity in the Electrochemical Reduction of Nitrogen to Ammonia. *ACS Energy Lett.* **2019**, *4*, 430–435.
49. Zhang, L.; Chen, G.-F.; Ding, L.-X.; Wang, H., Advanced Non-Metallic Catalysts for Electrochemical Nitrogen Reduction under Ambient Conditions. *Chem. Eur. J.* **2019**, 1–23.
50. Zhang, X.; Wu, T.; Wang, H.; Zhao, R.; Chen, H.; Wang, T.; Wei, P.; Luo, Y.; Zhang, Y.; Sun, X., Boron Nanosheet: An Elemental Two-Dimensional (2D) Material for Ambient Electrocatalytic N₂–to–NH₃ Fixation in Neutral Media. *ACS Catal.* **2019**, *9*, 4609–4615.
51. Licht, S.; Cui, B.; Wang, B.; Li, F.-F.; Lau, J.; Liu, S., Ammonia Synthesis by N₂ and Steam Electrolysis in Molten Hydroxide Suspensions of Nanoscale Fe₂O₃. *Science* **2014**, *345*, 637–640.
52. Kordali, V.; Kyriacou, G.; Lambrou, C., Electrochemical Synthesis of Ammonia at Atmospheric Pressure and Low Temperature in a Solid Polymer Electrolyte Cell. *Chem. Commun.* **2000**, *17*, 1673–1674.
53. Wang, W. B.; Cao, X. B.; Gao, W. J.; Zhang, F.; Wang, H. T.; Ma, G. L., Ammonia Synthesis at Atmospheric Pressure Using a Reactor with Thin Solid Electrolyte BaCe_{0.85}Y_{0.15}O_{3–a} Membrane. *J. Membrane Sci.* **2010**, *360*, 397–403.
54. Cui, X.; Tang, C.; Zhang, Q., A Review of Electrocatalytic Reduction of Dinitrogen to Ammonia under Ambient Conditions. *Adv. Energy Mater.* **2018**, *8*, 1800369, 1–25.
55. Kyriakou, V.; Garagounis, I.; Vasileiou, E.; Vourros, A.; Stoukides, M., Progress in the Electrochemical Synthesis of Ammonia. *Catal. Today* **2017**, *286*, 2–13.
56. Wang, K.; Smith, D.; Zheng, Y., Electron-Driven Heterogeneous Catalytic Synthesis of Ammonia: Current States and Perspective. *Carbon Resour. Convers.* **2018**, *1*, 2–31.
57. Zhao, R., et al., Recent Progress in the Electrochemical Ammonia Synthesis under Ambient Conditions. *EnergyChem* **2019**, *1*, 100011, 1–29.
58. Andersen, S. Z., et al., A Rigorous Electrochemical Ammonia Synthesis Protocol with Quantitative Isotope Measurements. *Nature* **2019**, *570*, 504–508.
59. Suryanto, B. H. R.; Du, H.-L.; Wang, D.; Chen, J.; Simonov, A. N.; MacFarlane, D. R., Challenges and Prospects in the Catalysis of Electroreduction of Nitrogen to Ammonia. *Nat. Catal.* **2019**, *2*, 290–296.
60. Tang, C.; Qiao, S.-Z., How to Explore Ambient Electrocatalytic Nitrogen Reduction Reliably and Insightfully. *Chem. Soc. Rev.* **2019**, *48*, 3166–3180.
61. Greenlee, L. F.; Renner, J. N.; Foster, S. L., The Use of Controls for Consistent and Accurate Measurements of Electrocatalytic Ammonia Synthesis from Dinitrogen. *ACS Catal.* **2018**, *8*, 7820–7827.
62. Warner, J. X.; Dickerson, R. R.; Wei, Z.; Strow, L. L.; Wang, Y.; Liang, Q., Increased Atmospheric Ammonia over the World's Major Agricultural Areas Detected from Space. *Geophys. Res. Lett.* **2017**, *44*, 2875–2884.
63. El-Deab, M. S., Electrochemical Reduction of Nitrate to Ammonia at Modified Gold Electrodes. *Electrochim. Acta* **2004**, *49*, 1639–1645.
64. Ishibashi, T.; Himeno, M.; Imaizumi, N.; Maejima, K.; Nakano, S.; Uchida, K.; Yoshida, J.; Nishio, M., NO_x Contamination in Laboratory Ware and Effect of Countermeasures. *Nitric Oxide* **2000**, *4*, 516–525.
65. Turner, C.; Španěl, P.; Smith, D., A Longitudinal Study of Ammonia, Acetone and Propanol in the Exhaled Breath of 30 Subjects Using Selected Ion Flow Tube Mass Spectrometry, SIFT–MS. *Physiol. Meas.* **2006**, *27*, 321–337.

66. Yu, J., et al., Structured Polyaniline: An Efficient and Durable Electrocatalyst for Nitrogen Reduction Reaction in Acidic Media. *ChemElectroChem* **2019**, 6, 2215—2218.
67. Hao, Y.-C., et al., Promoting Nitrogen Electroreduction to Ammonia with Bismuth Nanocrystals and Potassium Cations in Water. *Nat. Catal.* **2019**, 2, 448—456.
68. Wang, M.; Liu, S.; Qian, T.; Liu, J.; Zhou, J.; Ji, H.; Xiong, J.; Zhong, J.; Yan, C., Over 56.55% Faradaic Efficiency of Ambient Ammonia Synthesis Enabled by Positively Shifting the Reaction Potential. *Nat. Commun.* **2019**, 10, 341, 1—8
69. Ren, X., et al., High-Performance N₂-to-NH₃ Conversion Electrocatalyzed by Mo₂C Nanorod. *ACS Cent. Sci.* **2019**, 5, 116—121.
70. Huang, H.; Xia, L.; Shi, X.; Asiri, A. M.; Sun, X., Ag Nanosheets for Efficient Electrocatalytic N₂ Fixation to NH₃ under Ambient Conditions. *Chem. Commun.* **2018**, 54, 11427—11430
71. Hu, L.; Khaniya, A.; Wang, J.; Chen, G.; Kaden, W. E.; Feng, X., Ambient Electrochemical Ammonia Synthesis with High Selectivity on Fe/Fe Oxide Catalyst. *ACS Catal.* **2018**, 8, 9312—9319.
72. Chu, K.; Liu, Y.-p.; Wang, J.; Zhang, H., NiO Nanodots on Graphene for Efficient Electrochemical N₂ Reduction to NH₃. *ACS Appl. Energy Mater.* **2019**, 2, 2288—2295.
73. Chen, C.; Yan, D.; Wang, Y.; Zhou, Y.; Zou, Y.; Li, Y.; Wang, S., B–N Pairs Enriched Defective Carbon Nanosheets for Ammonia Synthesis with High Efficiency. *Small* **2019**, 15, 1805029, 1—9.
74. Soloveichik, G., Electrochemical Synthesis of Ammonia as a Potential Alternative to the Haber–Bosch Process. *Nat. Catal.* **2019**, 2, 377—380.
75. Abghoui, Y.; Garden, A. L.; Hlynsson, V. F.; Bjorgvinsdottir, S.; Olafsdottir, H.; Skulason, E., Enabling Electrochemical Reduction of Nitrogen to Ammonia at Ambient Conditions through Rational Catalyst Design. *PCCP* **2015**, 17, 4909—4918.
76. Köleli, F.; Röpke, T., Electrochemical Hydrogenation of Dinitrogen to Ammonia on a Polyaniline Electrode. *Appl. Catal. B-Environ.* **2006**, 62, 306—310.
77. Kim, K.; Lee, N.; Yoo, C.-Y.; Kim, J.-N.; Yoon, H. C.; Han, J.-I., Communication—Electrochemical Reduction of Nitrogen to Ammonia in 2-Propanol under Ambient Temperature and Pressure. *J. Electrochem. Soc.* **2016**, 163, F610—F612.
78. Zhou, F.; Azofra, L. M.; Al-Agele, M.; Kar, M.; Simonov, A. N.; McDonnell-Worth, C. J.; Sun, C.; Zhang, X.; MacFarlane, D., Electro-Synthesis of Ammonia from Nitrogen at Ambient Temperature and Pressure in Ionic Liquids. *Energy Environ. Sci.* **2017**, 10, 2516—2520.
79. Suryanto, B. H.; Kang, C. S. M.; Wang, D.; Xiao, C.; Zhou, F.; Azofra, L. M.; Cavallo, L.; Zhang, X.; MacFarlane, D. R., Rational Electrode–Electrolyte Design for Efficient Ammonia Electrosynthesis under Ambient Conditions. *ACS Energy Lett.* **2018**, 3, 1219—1224.
80. Liu, X.; He, M.; Lv, N.; Xu, H.; Bai, L., Selective Absorption of CO₂ from H₂, O₂ and N₂ by 1-Hexyl-3-Methylimidazolium Tris(Pentafluoroethyl)Trifluorophosphate. *J. Chem. Thermodyn.* **2016**, 97, 48—54.
81. Bahadur, I.; Osman, K.; Coquelet, C.; Naidoo, P.; Ramjugernath, D., Solubilities of Carbon Dioxide and Oxygen in the Ionic Liquids Methyl Trioctyl Ammonium Bis(Trifluoromethylsulfonyl)Imide, 1-Butyl-3-Methyl Imidazolium Bis(Trifluoromethylsulfonyl)Imide, and 1-Butyl-3-Methyl Imidazolium Methyl Sulfate. *J. Phys. Chem. B* **2015**, 119, 1503—1514.
82. Anthony, J. L.; Anderson, J. L.; Maginn, E. J.; Brennecke, J. F., Anion Effects on Gas Solubility in Ionic Liquids. *J. Phys. Chem. B* **2005**, 109, 6366—6374.
83. Anthony, J. L.; Maginn, E. J.; Brennecke, J. F., Solubilities and Thermodynamic Properties of Gases in the Ionic Liquid 1-N-Butyl-3-Methylimidazolium Hexafluorophosphate. *J. Phys. Chem. B* **2002**, 106, 7315—7320.
84. Zhan, C.-G.; Nichols, J. A.; Dixon, D. A., Ionization Potential, Electron Affinity, Electronegativity, Hardness, and Electron Excitation Energy: Molecular Properties from Density Functional Theory Orbital Energies. *J. Phys. Chem. A* **2003**, 107, 4184—4195.
85. Naim, A. B.; Baer, S., Method for Measuring Solubilities of Slightly Soluble Gases in Liquids. *T. Faraday Soc.* **1963**, 59, 2735—2738.
86. Markham, A. E.; Kobe, K. A., The Solubility of Gases in Liquids. *Chem. Rev.* **1941**, 28, 519—588.

87. Boening, D. W., Ecological Effects, Transport, and Fate of Mercury: A General Review. *Chemosphere* **2000**, *40*, 1335—1351.
88. Rumpf, B.; Maurer, G., Solubilities of Hydrogen Cyanide and Sulfur Dioxide in Water at Temperatures from 293.15 to 413.15 K and Pressures up to 2.5 MPa. *Fluid Phase Equilib.* **1992**, *81*, 241—260.
89. Xia, J.; Jödecke, M.; Pérez-Salado Kamps, Á.; Maurer, G., Solubility of CO₂ in (CH₃OH + H₂O). *J. Chem. Eng. Data* **2004**, *49*, 1756—1759.
90. Souza, A. T.; Corazza, M. L.; Cardozo-Filho, L.; Guirardello, R.; Meireles, M. A. A., Phase Equilibrium Measurements for the System Clove (*Eugenia Caryophyllus*) Oil + CO₂. *J. Chem. Eng. Data* **2004**, *49*, 352—356.
91. Bara, J. E.; Gabriel, C. J.; Carlisle, T. K.; Camper, D. E.; Finotello, A.; Gin, D. L.; Noble, R. D., Gas Separations in Fluoroalkyl-Functionalized Room-Temperature Ionic Liquids Using Supported Liquid Membranes. *Chem. Eng. J.* **2009**, *147*, 43—50.
92. Ferguson, L.; Scovazzo, P., Solubility, Diffusivity, and Permeability of Gases in Phosphonium-Based Room Temperature Ionic Liquids: Data and Correlations. *Ind. Eng. Chem. Res.* **2007**, *46*, 1369—1374.
93. Condemarin, R.; Scovazzo, P., Gas Permeabilities, Solubilities, Diffusivities, and Diffusivity Correlations for Ammonium-Based Room Temperature Ionic Liquids with Comparison to Imidazolium and Phosphonium Rtil Data. *Chem. Eng. J.* **2009**, *147*, 51—57.
94. Swinnerton, J. W.; Linnenbom, V. J.; Cheek, C. H., Revised Sampling Procedure for Determination of Dissolved Gases in Solution by Gas Chromatography. *Anal. Chem.* **1962**, *34*, 1509—1509.
95. Battino, R.; Clever, H. L., The Solubility of Gases in Liquids. *Chem. Rev.* **1966**, *66*, 395—463.
96. Pozo-Gonzalo, C.; Howlett, P. C.; Hodgson, J. L.; Madsen, L. A.; MacFarlane, D. R.; Forsyth, M., Insights into the Reversible Oxygen Reduction Reaction in a Series of Phosphonium-Based Ionic Liquids. *PCCP* **2014**, *16*, 25062—25070.
97. Bonifácio, R. P.; Costa Gomes, M. F.; Filipe, E. J. M., Solubility of Xenon in N-Hexane between 257 and 333 K. *Fluid Phase Equilib.* **2002**, *193*, 41—51.
98. Camper, D.; Becker, C.; Koval, C.; Noble, R., Diffusion and Solubility Measurements in Room Temperature Ionic Liquids. *Ind. Eng. Chem. Res.* **2006**, *45*, 445—450.
99. Bondar, V. I.; Freeman, B. D.; Pinnau, I., Gas Sorption and Characterization of Poly(Ether-B-Amide) Segmented Block Copolymers. *J. Polym. Sci., Part B: Polym. Phys.* **1999**, *37*, 2463—2475.
100. Koros, W. J.; Paul, D. R., Design Considerations for Measurement of Gas Sorption in Polymers by Pressure Decay. *J. Polym. Sci. Pol. Phys.* **1976**, *14*, 1903—1907.
101. Battino, R.; Rettich, T. R.; Tominaga, T., The Solubility of Nitrogen and Air in Liquids. *J. Phys. Chem. Ref. Data* **1984**, *13*, 563—600.
102. Lei, Z.; Dai, C.; Chen, B., Gas Solubility in Ionic Liquids. *Chem. Rev.* **2014**, *114*, 1289—1326.
103. Bard, A. J.; Faulkner, L. R.; Leddy, J.; Zoski, C. G., *Electrochemical Methods: Fundamentals and Applications*; Wiley: New York, 1980; Vol. 2.
104. Kumar, R.; Schmidt, J. R.; Skinner, J. L., Hydrogen Bonding Definitions and Dynamics in Liquid Water. *J. Chem. Phys.* **2007**, *126*, 204107, 1—12
105. Hird, M., Fluorinated Liquid Crystals - Properties and Applications. *Chem. Soc. Rev.* **2007**, *36*, 2070—2095.
106. Tham, M. K.; Walker, R. D.; Modell, J. H., Physical Properties and Gas Solubilities in Selected Fluorinated Ethers. *J. Chem. Eng. Data* **1973**, *18*, 385—386.
107. Gjaldbaek, J. C.; Hildebrand, J. H., The Solubility of Nitrogen in Carbon Disulfide, Benzene, Normal- and Cyclo-Hexane, and in Three Fluorocarbons. *J. Am. Chem. Soc.* **1949**, *71*, 3147—3150.
108. Wilhelm, E.; Battino, R., Thermodynamic Functions of the Solubilities of Gases in Liquids at 25.Deg. *Chem. Rev.* **1973**, *73*, 1—9.
109. Jabłonic, A.; Horstmann, S.; Gmehling, J., Experimental Determination and Calculation of Gas Solubility Data for Nitrogen in Different Solvents. *Ind. Eng. Chem. Res.* **2007**, *46*, 4654—4659.
110. Almantariotis, D.; Pensado, A. S.; Gunaratne, H. Q. N.; Hardacre, C.; Pádua, A. A. H.; Coxam, J. Y.; Costa Gomes, M. F., Influence of Fluorination on the Solubilities of Carbon Dioxide, Ethane, and Nitrogen in 1-N-Fluoro-Alkyl-3-Methylimidazolium Bis(N-Fluoroalkylsulfonyl)Amide Ionic Liquids. *J. Phys. Chem. B* **2017**, *121*, 426—436.

111. Jacquemin, J.; Husson, P.; Majer, V.; Gomes, M. F. C., Low-Pressure Solubilities and Thermodynamics of Solvation of Eight Gases in 1-Butyl-3-Methylimidazolium Hexafluorophosphate. *Fluid Phase Equilib.* **2006**, *240*, 87—95.
112. Carlisle, T. K.; Bara, J. E.; Gabriel, C. J.; Noble, R. D.; Gin, D. L., Interpretation of CO₂ Solubility and Selectivity in Nitrile-Functionalized Room-Temperature Ionic Liquids Using a Group Contribution Approach. *Ind. Eng. Chem. Res.* **2008**, *47*, 7005—7012.
113. Jacquemin, J.; Costa Gomes, M. F.; Husson, P.; Majer, V., Solubility of Carbon Dioxide, Ethane, Methane, Oxygen, Nitrogen, Hydrogen, Argon, and Carbon Monoxide in 1-Butyl-3-Methylimidazolium Tetrafluoroborate between Temperatures 283 K and 343 K and at Pressures Close to Atmospheric. *J. Chem. Thermodyn.* **2006**, *38*, 490—502.
114. Bara, J. E.; Gabriel, C. J.; Lessmann, S.; Carlisle, T. K.; Finotello, A.; Gin, D. L.; Noble, R. D., Enhanced CO₂ Separation Selectivity in Oligo(Ethylene Glycol) Functionalized Room-Temperature Ionic Liquids. *Ind. Eng. Chem. Res.* **2007**, *46*, 5380—5386.
115. Camper, D.; Bara, J.; Koval, C.; Noble, R., Bulk-Fluid Solubility and Membrane Feasibility of Rmim-Based Room-Temperature Ionic Liquids. *Ind. Eng. Chem. Res.* **2006**, *45*, 6279—6283.
116. Blath, J.; Deubler, N.; Hirth, T.; Schiestel, T., Chemisorption of Carbon Dioxide in Imidazolium Based Ionic Liquids with Carboxylic Anions. *Chem. Eng. J.* **2012**, *181*, 152—158.
117. Anderson, J. L.; Dixon, J. K.; Brennecke, J. F., Solubility of CO₂, CH₄, C₂H₆, C₂H₄, O₂, and N₂ in 1-Hexyl-3-Methylpyridinium Bis(Trifluoromethylsulfonyl)Imide: Comparison to Other Ionic Liquids. *Acc. Chem. Res.* **2007**, *40*, 1208—1216.
118. Rogers, R. D.; Seddon, K. R., Ionic Liquids--Solvents of the Future? *Science* **2003**, *302*, 792—793.
119. MacFarlane, D. R.; Kar, M.; Pringle, J. M., *Fundamentals of Ionic Liquids: From Chemistry to Applications*; John Wiley & Sons, 2017.
120. MacFarlane, D. R.; Chong, A. L.; Forsyth, M.; Kar, M.; Vijayaraghavan, R.; Somers, A.; Pringle, J. M., New Dimensions in Salt-Solvent Mixtures: A 4th Evolution of Ionic Liquids. *Faraday Discuss.* **2017**, *206*, 9—28.
121. Walden, P., Molecular Weights and Electrical Conductivity of Several Fused Salts. *Bull. Acad. Imper. Sci. St. Petersburg* **1914**, *1800*, 405—422.
122. Gale, R. J.; Gilbert, B.; Osteryoung, R. A., Raman Spectra of Molten Aluminum Chloride: 1-Butylpyridinium Chloride Systems at Ambient Temperatures. *Inorg. Chem.* **1978**, *17*, 2728—2729.
123. Wilkes, J. S.; Levisky, J. A.; Wilson, R. A.; Hussey, C. L., Dialkylimidazolium Chloroaluminate Melts: A New Class of Room-Temperature Ionic Liquids for Electrochemistry, Spectroscopy and Synthesis. *Inorg. Chem.* **1982**, *21*, 1263—1264.
124. Wilkes, J. S.; Zaworotko, M. J., Air and Water Stable 1-Ethyl-3-Methylimidazolium Based Ionic Liquids. *J. Chem. Soc., Chem. Commun.* **1992**, 965—967.
125. Fuller, J.; Carlin, R. T.; Osteryoung, R. A., The Room Temperature Ionic Liquid 1-Ethyl-3-Methylimidazolium Tetrafluoroborate: Electrochemical Couples and Physical Properties. *J. Electrochem. Soc.* **1997**, *144*, 3881—3886.
126. Smiglak, M.; Metlen, A.; Rogers, R. D., The Second Evolution of Ionic Liquids: From Solvents and Separations to Advanced Materials—Energetic Examples from the Ionic Liquid Cookbook. *Acc. Chem. Res.* **2007**, *40*, 1182—1192.
127. Hough, W. L., et al., The Third Evolution of Ionic Liquids: Active Pharmaceutical Ingredients. *New J. Chem.* **2007**, *31*, 1429-1436.
128. Pernak, J.; Sobaszekiewicz, K.; Mirska, I., Anti-Microbial Activities of Ionic Liquids. *Green Chem.* **2003**, *5*, 52—56.
129. Canongia Lopes, J. N.; Costa Gomes, M. F.; Husson, P.; Pádua, A. A. H.; Rebelo, L. P. N.; Sarraute, S.; Tariq, M., Polarity, Viscosity, and Ionic Conductivity of Liquid Mixtures Containing [C₄C₁im][NTf₂] and a Molecular Component. *J. Phys. Chem. B* **2011**, *115*, 6088—6099.
130. Bates, E. D.; Mayton, R. D.; Ntai, I.; Davis, J. H., CO₂ Capture by a Task-Specific Ionic Liquid. *J. Am. Chem. Soc.* **2002**, *124*, 926—927.
131. Welton, T., Room-Temperature Ionic Liquids. Solvents for Synthesis and Catalysis. *Chem. Rev.* **1999**, *99*, 2071—2084.
132. Buzzeo, M. C.; Evans, R. G.; Compton, R. G., Non-Haloaluminate Room-Temperature Ionic Liquids in Electrochemistry—a Review. *ChemPhysChem* **2004**, *5*, 1106—1120.

133. O'Mahony, A. M.; Silvester, D. S.; Aldous, L.; Hardacre, C.; Compton, R. G., Effect of Water on the Electrochemical Window and Potential Limits of Room-Temperature Ionic Liquids. *J. Chem. Eng. Data* **2008**, *53*, 2884—2891.
134. Plechkova, N. V.; Seddon, K. R., Applications of Ionic Liquids in the Chemical Industry. *Chem. Soc. Rev.* **2008**, *37*, 123—150.
135. Mallakpour, S.; Dinari, M., Ionic Liquids as Green Solvents: Progress and Prospects. In *Green Solvents II: Properties and Applications of Ionic Liquids*, Mohammad, A.; Inamuddin, D., Eds. Springer Netherlands: Dordrecht, 2012; pp 1—32.
136. Davis Jr, J. H.; Gordon, C. M.; Hilgers, C.; Wasserscheid, P., Synthesis and Purification of Ionic Liquids. Wiley-VCH Verlag GmbH & Co. KGaA: Weinheim, Germany: 2002; pp 7—40.
137. Davis, J. J. H.; Fox, P. A., From Curiosities to Commodities: Ionic Liquids Begin the Transition. *Chem. Commun.* **2003**, 1209—1212.
138. Dunitz, J. D.; Taylor, R., Organic Fluorine Hardly Ever Accepts Hydrogen Bonds. *Chem. Eur. J.* **1997**, *3*, 89—98.
139. Dunitz, J. D., Organic Fluorine: Odd Man Out. *ChemBioChem* **2004**, *5*, 614—621.
140. Alves, M.; Vieira, N. S. M.; Rebelo, L. P. N.; Araújo, J. M. M.; Pereiro, A. B.; Archer, M., Fluorinated Ionic Liquids for Protein Drug Delivery Systems: Investigating Their Impact on the Structure and Function of Lysozyme. *Int. J. Pharm.* **2017**, *526*, 309—320.
141. Vieira, N. S. M.; Bastos, J. C.; Rebelo, L. P. N.; Matias, A.; Araújo, J. M. M.; Pereiro, A. B., Human Cytotoxicity and Octanol/Water Partition Coefficients of Fluorinated Ionic Liquids. *Chemosphere* **2019**, *216*, 576—586.
142. Heitzman, H.; Young, B. A.; Rausch, D. J.; Rickert, P.; Stepinski, D. C.; Dietz, M. L., Fluorous Ionic Liquids as Solvents for the Liquid–Liquid Extraction of Metal Ions by Macrocyclic Polyethers. *Talanta* **2006**, *69*, 527—531.
143. Wang, B.; Moran, C.; Lin, D.; Tang, H.; Gage, E.; Li, L., Nanometer-Thick Fluorinated Ionic Liquids (ILs) as Media Lubricants for Data Storage Devices. *ACS appl. Nano Mater.* **2019**, *8*, 5260—5265
144. Pereiro, A. B.; Araújo, J. M. M.; Martinho, S.; Alves, F.; Nunes, S.; Matias, A.; Duarte, C. M. M.; Rebelo, L. P. N.; Marrucho, I. M., Fluorinated Ionic Liquids: Properties and Applications. *ACS Sustain. Chem. Eng.* **2013**, *1*, 427—439.
145. M. Gordon, C.; D. Holbrey, J.; R. Kennedy, A.; R. Seddon, K., Ionic Liquid Crystals: Hexafluorophosphate Salts. *J. Mater. Chem.* **1998**, *8*, 2627—2636.
146. Bonhote, P.; Dias, A.-P.; Papageorgiou, N.; Kalyanasundaram, K.; Grätzel, M., Hydrophobic, Highly Conductive Ambient-Temperature Molten Salts. *Inorg. Chem.* **1996**, *35*, 1168—1178.
147. Freire, M. G.; Neves, C. M. S. S.; Marrucho, I. M.; Coutinho, J. A. P.; Fernandes, A. M., Hydrolysis of Tetrafluoroborate and Hexafluorophosphate Counter Ions in Imidazolium-Based Ionic Liquids. *J. Phys. Chem. A* **2010**, *114*, 3744—3749.
148. Swatoski, R. P.; Holbrey, J. D.; Rogers, R. D., Ionic Liquids Are Not Always Green: Hydrolysis of 1-Butyl-3-Methylimidazolium Hexafluorophosphate. *Green Chem.* **2003**, *5*, 361—363.
149. Ignat'ev, N. V.; Welz-Biermann, U.; Kucheryna, A.; Bissky, G.; Willner, H., New Ionic Liquids with Tris(Perfluoroalkyl)Trifluorophosphate (FAP) Anions. *J. Fluorine Chem.* **2005**, *126*, 1150—1159.
150. Castiglione, F.; Moreno, M.; Raos, G.; Famulari, A.; Mele, A.; Appetecchi, G. B.; Passerini, S., Structural Organization and Transport Properties of Novel Pyrrolidinium-Based Ionic Liquids with Perfluoroalkyl Sulfonylimide Anions. *J. Phys. Chem. B* **2009**, *113*, 10750—10759.
151. Lo Celso, F.; Yoshida, Y.; Castiglione, F.; Ferro, M.; Mele, A.; Jafta, C. J.; Triolo, A.; Russina, O., Direct Experimental Observation of Mesoscopic Fluorous Domains in Fluorinated Room Temperature Ionic Liquids. *PCCP* **2017**, *19*, 13101—13110.
152. Zhou, Z. B.; Matsumoto, H.; Tatsumi, K., Cyclic Quaternary Ammonium Ionic Liquids with Perfluoroalkyltrifluoroborates: Synthesis, Characterization, and Properties. *Chemistry—A European Journal* **2006**, *12*, 2196—2212.
153. Rupp, A. B. A.; Klose, P.; Scherer, H.; Krossing, I., New Water-Stable Ionic Liquids Based on Tetrakis-(2,2,2-Trifluoroethoxy)Borate. *ChemPhysChem* **2014**, *15*, 3729—3731.
154. Rupp, A. B. A.; Krossing, I., Ionic Liquids with Weakly Coordinating $[M^{III}(OR^F)_4]^-$ Anions. *Acc. Chem. Res.* **2015**, *48*, 2537—2546.

155. Schreiner, C.; Zugmann, S.; Hartl, R.; Gores, H. J., Temperature Dependence of Viscosity and Specific Conductivity of Fluoroborate-Based Ionic Liquids in Light of the Fractional Walden Rule and Angell's Fragility Concept. *J. Chem. Eng. Data* **2010**, *55*, 4372—4377.
156. Allen, J. L.; McOwen, D. W.; Delp, S. A.; Fox, E. T.; Dickmann, J. S.; Han, S.-D.; Zhou, Z.-B.; Jow, T. R.; Henderson, W. A., N-Alkyl-N-Methylpyrrolidinium Difluoro(Oxalato)Borate Ionic Liquids: Physical/Electrochemical Properties and Al Corrosion. *J. Power Sources* **2013**, *237*, 104—111.
157. Forsyth, S. A.; Fraser, K. J.; Howlett, P. C.; MacFarlane, D. R.; Forsyth, M., N-Methyl-N-Alkylpyrrolidinium Nonafluoro-1-Butanesulfonate Salts: Ionic Liquid Properties and Plastic Crystal Behaviour. *Green Chem.* **2006**, *8*, 256—261.
158. Linder, T.; Sundermeyer, J., Three Novel Anions Based on Pentafluorophenyl Amine Combined with Two New Synthetic Strategies for the Synthesis of Highly Lipophilic Ionic Liquids. *Chem. Commun.* **2009**, *20*, 2914—2916.
159. Emnet, C.; Weber, K. M.; Vidal, J. A.; Consorti, C. S.; Stuart, A. M.; Gladysz, J. A., Syntheses and Properties of Fluorous Quaternary Phosphonium Salts That Bear Four Ponytails; New Candidates for Phase Transfer Catalysts and Ionic Liquids. *Adv. Synth. Catal.* **2006**, *348*, 1625—1634.
160. Tindale, J. J.; Na, C.; Jennings, M. C.; Ragogna, P. J., Synthesis and Characterization of Fluorinated Phosphonium Ionic Liquids. *Can. J. Chem.* **2007**, *85*, 660—667.
161. Guterman, R.; Berven, B. M.; Chris Corkery, T.; Nie, H.-Y.; Idacavage, M.; Gillies, E. R.; Ragogna, P. J., Fluorinated Polymerizable Phosphonium Salts from PH₃: Surface Properties of Photopolymerized Films. *J. Polym. Sci., Part A: Polym. Chem.* **2013**, *51*, 2782—2792.
162. Vlád, G.; Richter, F. U.; Horváth, I. T., Synthesis of Fluorous Trialkyl Phosphines with the Complete Exclusion of PH₃. *Tetrahedron Lett.* **2005**, *46*, 8605—8608.
163. Alhanash, H. B.; Brisdon, A. K., Quaternary Ammonium Ionic Liquids Containing Fluorous Ponytails: Competitive Alkylation and Elimination Reactions of I(CH₂)_nRf (N = 2, 3) with Tertiary Amines. *J. Fluorine Chem.* **2013**, *156*, 152—157.
164. Singh, R. P.; Manandhar, S.; Shreeve, J. n. M., New Dense Fluoroalkyl-Substituted Imidazolium Ionic Liquids. *Tetrahedron Lett.* **2002**, *43*, 9497—9499.
165. Le, M.-L.-P.; Alloin, F.; Strobel, P.; Leprêtre, J.-C.; Cointeaux, L.; del Valle, C. P., Electrolyte Based on Fluorinated Cyclic Quaternary Ammonium Ionic Liquids. *Ionics* **2012**, *18*, 817—827.
166. Merrigan, T. L.; Bates, E. D.; Dorman, S. C.; Davis Jr, J. H., New Fluorous Ionic Liquids Function as Surfactants in Conventional Room-Temperature Ionic Liquids. *Chem. Commun.* **2000**, 2051—2052.
167. Pereira, A. B.; Tomé, L. C.; Martinho, S.; Rebelo, L. P. N.; Marrucho, I. M., Gas Permeation Properties of Fluorinated Ionic Liquids. *Ind. Eng. Chem. Res.* **2013**, *52*, 4994—5001.
168. Umecky, T.; Abe, M.; Takamuku, T.; Makino, T.; Kanakubo, M., CO₂ Absorption Features of 1-Ethyl-3-Methylimidazolium Ionic Liquids with 2,4-Pentanedionate and Its Fluorine Derivatives. *J. CO₂ Util.* **2019**, *31*, 75—84.
169. Cadena, C.; Anthony, J. L.; Shah, J. K.; Morrow, T. I.; Brennecke, J. F.; Maginn, E. J., Why Is CO₂ So Soluble in Imidazolium-Based Ionic Liquids? *J. Am. Chem. Soc.* **2004**, *126*, 5300—5308.
170. Muldoon, M. J.; Aki, S. N. V. K.; Anderson, J. L.; Dixon, J. K.; Brennecke, J. F., Improving Carbon Dioxide Solubility in Ionic Liquids. *J. Phys. Chem. B* **2007**, *111*, 9001—9009.
171. Hong, G.; Jacquemin, J.; Husson, P.; Costa Gomes, M. F.; Deetlefs, M.; Nieuwenhuyzen, M.; Sheppard, O.; Hardacre, C., Effect of Acetonitrile on the Solubility of Carbon Dioxide in 1-Ethyl-3-Methylimidazolium Bis(Trifluoromethylsulfonyl)Amide. *Ind. Eng. Chem. Res.* **2006**, *45*, 8180—8188.
172. Zhang, Z.; Hu, L.; Wu, H.; Weng, W.; Koh, M.; Redfern, P. C.; Curtiss, L. A.; Amine, K., Fluorinated Electrolytes for 5 V Lithium-Ion Battery Chemistry. *Energy Environ. Sci.* **2013**, *6*, 1806—1810.
173. Tarascon, J. M.; Armand, M., Issues and Challenges Facing Rechargeable Lithium Batteries. *Nature* **2001**, *414*, 359—367.
174. Fan, X., et al., Non-Flammable Electrolyte Enables Li-Metal Batteries with Aggressive Cathode Chemistries. *Nat. Nanotechnol.* **2018**, *13*, 715—722.
175. Dokko, K., et al., Solvate Ionic Liquid Electrolyte for Li-S Batteries. *J. Electrochem. Soc.* **2013**, *160*, A1304—A1310.

176. Olson, E. J.; Boswell, P. G.; Givot, B. L.; Yao, L. J.; Bühlmann, P., Electrochemistry in Media of Exceptionally Low Polarity: Voltammetry with a Fluorous Solvent. *J. Electroanal. Chem.* **2010**, *639*, 154—160.
177. Boswell, P. G.; Lugert, E. C.; Rábai, J.; Amin, E. A.; Bühlmann, P., Coordinative Properties of Highly Fluorinated Solvents with Amino and Ether Groups. *J. Am. Chem. Soc.* **2005**, *127*, 16976—16984.
178. Lu, Z.; Zeng, X.; Hammond, G. B.; Xu, B., Widely Applicable Hydrofluorination of Alkenes Via Bifunctional Activation of Hydrogen Fluoride. *J. Am. Chem. Soc.* **2017**, *139*, 18202—18205.
179. Tang, X., et al., Fluorinated Phosphorene: Electrochemical Synthesis, Atomistic Fluorination, and Enhanced Stability. *Small* **2017**, *13*, 1702739, 1—10
180. Armand, M.; Tarascon, J. M., Building Better Batteries. *Nature* **2008**, *451*, 652—657
181. Mogi, R.; Inaba, M.; Jeong, S.-K.; Iriyama, Y.; Abe, T.; Ogumi, Z., Effects of Some Organic Additives on Lithium Deposition in Propylene Carbonate. *J. Electrochem. Soc.* **2002**, *149*, A1578—A1583.
182. Prevedouros, K.; Cousins, I. T.; Buck, R. C.; Korzeniowski, S. H., Sources, Fate and Transport of Perfluorocarboxylates. *Environ. Sci. Technol.* **2006**, *40*, 32—44.
183. Herzke, D.; Olsson, E.; Posner, S., Perfluoroalkyl and Polyfluoroalkyl Substances (PFAS) in Consumer Products in Norway – a Pilot Study. *Chemosphere* **2012**, *88*, 980—987.

Chapter 2: Engineering and Construction of N₂ Solubility Apparatus

2.1 Introduction

The solubility of N₂ in many liquids has been measured by a number of research groups through various techniques. However, the instruments that have been used to measure N₂ solubility are not commercially available and involve custom-designed apparatus to conduct such measurements. Due to the significance of N₂ solubility in electrochemical ammonia synthesis, we strive to construct such an apparatus based on the isochoric saturation method. In this chapter, we describe the design of our N₂ solubility apparatus and the engineering concepts involved with its construction.

First, the trends of N₂ solubility in common solvents and their temperature dependence are introduced to provide the basis for comparison to ILs. The isochoric saturation method is described in detail in both single-transducer and dual-transducer modes, along with their different measurement procedures. The components involved with Mark I of the N₂ solubility apparatus are described in addition to the discussion of various control measurements such as pressure stability and temperature control.

The experience and knowledge obtained from the development process of Mark I of the N₂ solubility apparatus allowed us to identify previously unforeseen challenges/issues, enabling the construction of a more robust Mark II of the N₂ solubility apparatus. Such an apparatus requires an isolated leak-free system, and strict controls that are imperative for high-precision measurements of N₂ solubility. A comprehensive description of this second experimental setup is specified, followed by a step-by-step procedure to conduct N₂ solubility measurements, from degasification to N₂ dissolution. After a thorough description of control measurements, N₂ solubility values are presented for common solvents and are benchmarked to literature data to determine the accuracy of our apparatus. Furthermore, due to the difficult nature of achieving

a gas–tight N₂ solubility apparatus that provides reliable measurements, some potential pitfalls and their solutions are outlined.

This chapter also serves as a walkthrough to any reader who aims to construct an isochoric saturation method where some recommendations and troubleshooting solutions are provided.

2.2 N₂ Solubility Behaviour

The solubility of common gases in liquids are briefly examined in terms of the type of solvent medium, and the temperature dependence trends from the literature. This puts the solubility of N₂ in liquids into context with other gases, various solvents, and temperature ranges.

2.2.1 Various Gases

Figure 1a–b shows the solubility of various gases in water and hexane respectively from literature data. The solubility of non–polar gases are much lower than the polar gases such as CO₂ and SO₂, which both exhibit hydrogen bonding interactions with water. On the other hand, polar gases do not undertake hydrogen bonding interactions with hexane, thus showing smaller values of gas solubility. These polar gases still exhibit higher gas solubility in hexane, likely due to the intermolecular dipole–dipole forces that CO₂ and SO₂ offer to overcome some of the intermolecular interactions between hexane itself. On the contrary, the non–polarisable nature of N₂ offers little interaction, resulting in its inherently low gas solubility. This allows us to approximately estimate the solubility of gases based on the strength of their intermolecular forces, and the intermolecular interactions within the solvent medium.

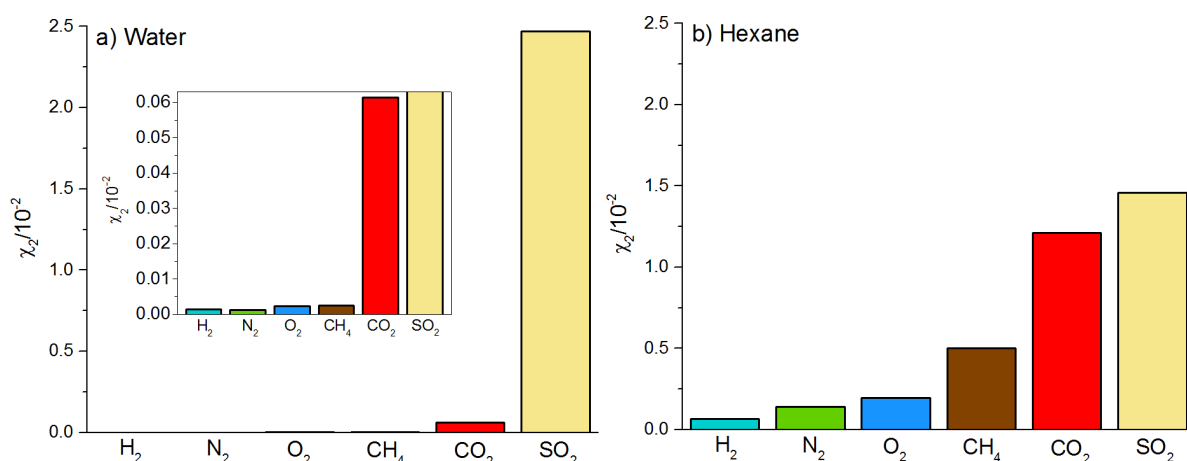


Figure 1a–b: Gas solubility (χ_2) of H₂, N₂, O₂, CH₄, CO₂, and SO₂ in a) water and b) hexane at $p = 1$ atm and 25°C. Inset of a) shows the zoomed in plot of gas solubility. Data obtained from Gerrard et al.¹⁸⁴

In Figure 1a, the solubility of SO₂ in water is more than three orders of magnitude larger than the solubility of N₂. By contrast, the solubility of SO₂ in hexane is only one order magnitude larger than the solubility of N₂. This demonstrates the change in SO₂ solubility through hydrogen bonding interactions with the solvent in comparison to intermolecular dispersion interactions. With regard to the non-polar gases, H₂, N₂, and O₂ display relatively similar levels of gas dissolution (within uncertainty error). In terms of intermolecular forces, H₂ offers little dispersion forces as it contains only two electrons; O₂ has a double bond where its electrons will contribute more to dispersion forces compared to the triple bond contained in N₂. Lastly, the single bonds within CH₄ may allow larger dispersion forces (compared to O₂ and N₂) and result in higher solubility values.

2.2.2 Temperature Dependence in Water

Figure 2 shows the temperature dependence of various gases in water from literature data. Each of these gases show an initial decrease in gas solubility with temperature until it reaches a minimum at which gas solubility then starts to increase. This point lies close to the boiling point of water, and the trend of solubility changes. For electrochemical ammonia synthesis, it is unlikely that temperature conditions will exceed 373 K; however, this trend must be considered if low-boiling solvents are to be used. Given the likely temperature range between 293–333 K, gas solubility would decrease in aqueous electrolytes with increasing

temperature. Moreover, the gas solubility would be lower in an electrolyte compared to pure water, even more so with increasing concentration of salt/acid/base.^{101, 185}

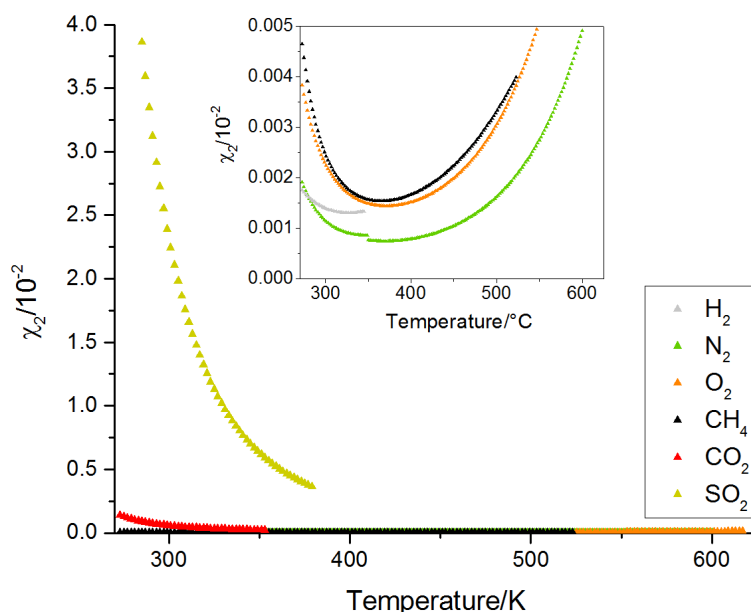


Figure 2: Temperature dependence plot of the solubility of gases in water at $p = 1 \text{ atm}$. Data obtained from Gerrard et al.¹⁸⁴

2.2.3 Temperature Dependence in Organic Solvents

The following temperature dependence plot of N_2 solubility in various organic solvents is displayed in Figure 3, where N_2 solubility is shown to be higher in organic solvents compared to water. In organic solvents, N_2 solubility is shown to increase with higher temperature, contrary to N_2 solubility in water where it is observed to decrease. This observation demonstrates that the nature of the solvent medium will affect the temperature dependence trends. Additionally, various organic solvents are shown to display different temperature dependence slopes of N_2 solubility (i.e. different Gibbs free energy of solvation for each solvent). For example, the change in N_2 solubility with temperature for hexane/butanol is smaller than that of cyclohexane. Gerrard et al. speculate that the ability of the solute gas molecule to break short-range ordering of within the solvent medium becomes less significant at higher temperatures, and becomes more a matter of gas solvation that causes favourable/unfavourable energy changes of the solvent-solute system.¹⁸⁴

Nevertheless, we can examine the temperature dependence of cyclohexane in Figure 3, which appears to have the greatest change in N₂ solubility. Here, the N₂ solubility observed to be $\chi_2 = 8.8 \times 10^{-4}$ and $\chi_2 = 7.2 \times 10^{-4}$ (7.9 mmol L⁻¹ and 6.8 mmol L⁻¹) at a temperature of 323 and 283 K respectively. The difference in N₂ solubility is not large over this temperature range, less than 19%, and would be even smaller for other organic solvents. This data puts N₂ solubility into perspective with other gases, liquids and temperature ranges and provides a general understanding of gas solubility behaviour.

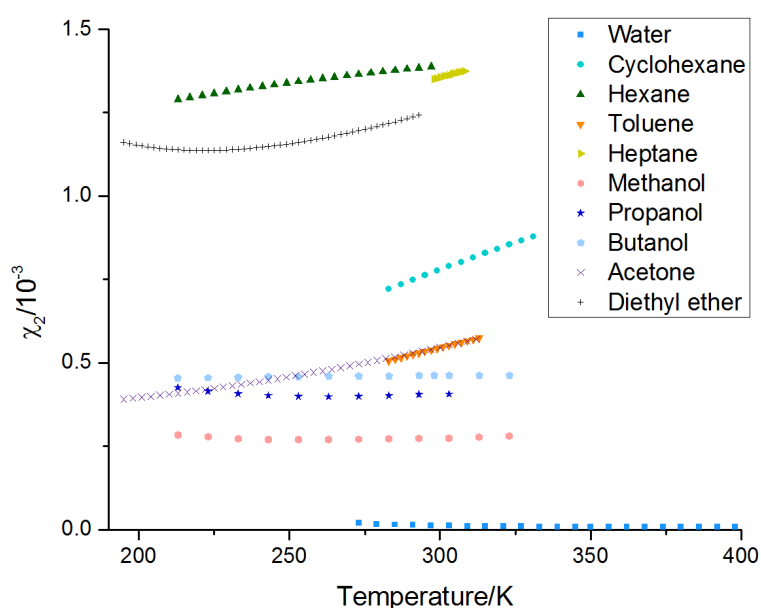


Figure 3: Temperature dependence of N₂ solubility in several organic solvents at atmospheric pressure. Data obtained from Gerrard et al.¹⁸⁴ and Tominaga et al.¹⁰¹

2.3 Isochoric Saturation Method

The N₂ solubility in ILs and co-solvent mixtures are measured using the isochoric saturation method. This method utilises a specific pressure drop apparatus in a closed system at constant temperature, where pressure is the variable being measured. In the literature, a number of research groups measure gas solubility through this method through the construction of their own gas solubility apparatus.^{97, 99, 186-187} Each measurement begins by admitting a known amount of gas to the EC that contains the degassed liquid medium. As the pressure decreases, the gas undergoes absorption into the liquid until the pressure reaches equilibrium (see Figure 11), at which the gas solubility value is calculated. Due to Henry's law, which states that gas

solubility in the liquid is proportional to the partial pressure of gas within the headspace, obtained data can be normalised to atmospheric pressure (partial pressure of N₂ at $p = 1$ atm).

The challenging aspect of this work derives from the inherently low solubility of N₂. This will result in smaller changes in pressure due to N₂ dissolution and may potentially lead to high uncertainties. The following section allows perspective into data handling and provides a mathematical description of how N₂ solubility is calculated, and how precision can be improved.

2.3.1 Data Analysis of N₂ Solubility

This section details the arithmetic involved in calculating N₂ solubility, which can be used to determine the solubility of other gases as well, given the respective values of the compressibility factor. If we consider the simple ideal gas equation:

$$n = \frac{pV}{RT} \quad (1)$$

where p is the pressure (Pa), V is the volume (L), n is the number of moles of gas (mol), R is the universal gas constant (Pa L mol⁻¹ K⁻¹), and T is the temperature (K). Given that the temperature and volume are controlled to be constant, the measured variable is the pressure change upon gas dissolution. Of course, one must consider the non-ideality of gases through the compressibility factor $Z(p, T)$, which is a measure of deviation from ideal gas behaviour at a given temperature and pressure:

$$n = \frac{pV}{RTZ(p, T)} \quad (2)$$

Shown in Figure 4 is the diagram of the compressibility factor for N₂ with pressure and temperature. The effect of non-ideality arises from attractive and repulsive intermolecular forces of N₂ that become more significant at each extreme of temperature and pressure, particularly near the critical point of N₂.¹⁸⁸ On the other hand, one can notice that at temperatures near 300 K, the compressibility factor does not change by much, even up to a pressure of 80 atm. Although the electrochemical ammonia synthesis process aims to be carried

out at near-ambient conditions, it is still important to consider the effect of non-ideality given the low solubility of N₂.

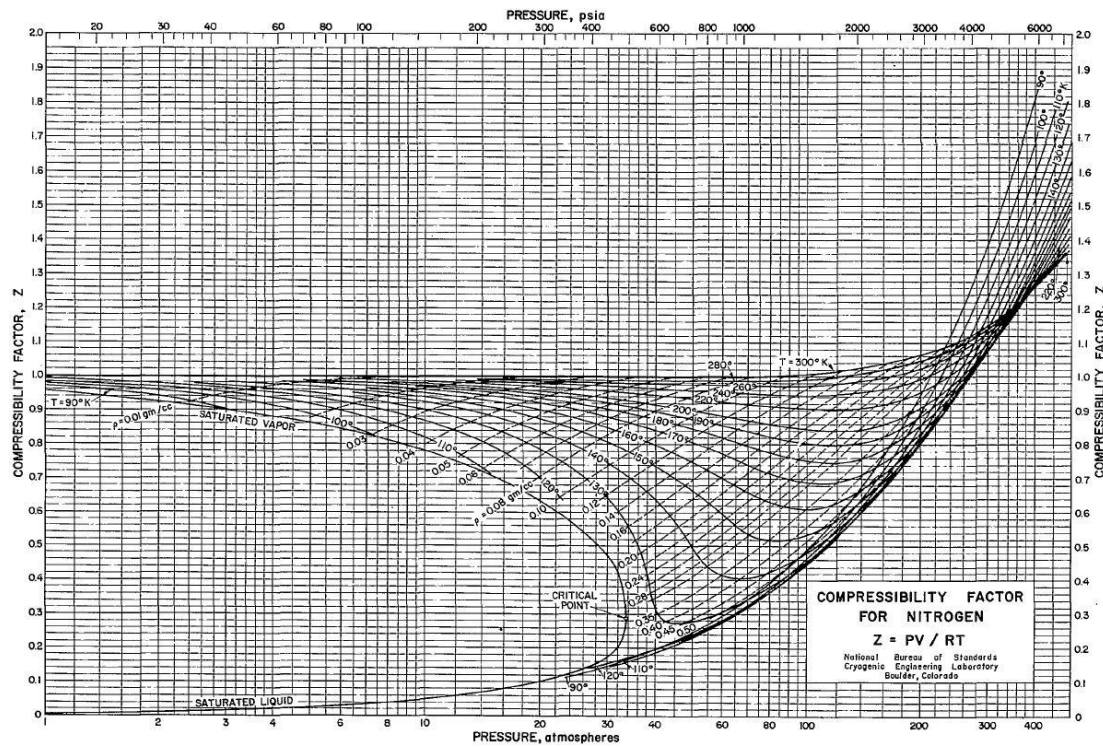


Figure 4: Compressibility diagram for N₂ with increasing pressure. Reprinted from *Fundamentals of Classical Thermodynamics* with permission from Wylen et al.¹⁸⁹ Copyright 1985 John Wiley & Sons.

Quantitative compressibility factors for N₂ near ambient conditions can be calculated by following the equation:

$$Z = 1 + \frac{PB_{22}}{RT} \quad (3)$$

where B_{22} is the second virial coefficient of N₂. The second virial coefficients of N₂ at various temperatures can be found in a valuable compilation by Dymond and Smith.¹⁹⁰ Should the desired data delve into higher pressure experiments, compressibility factors can be calculated using the Peng–Robinson equation of state.¹⁹¹ In the case of measuring N₂ solubility in solvents, that exerts an amount of vapour pressure, the compressibility factor is calculated by the equation:

$$Z_{12} = 1 + \frac{P}{RT} (y_1 B_{22} + y_2 B_{33} + y_1 y_2 \delta_{23}) \quad (4)$$

where y_1 and y_2 are the mole fraction of N_2 and the mole fraction of solvent contained in the vapour phase respectively, B_{22} and B_{33} are the second virial coefficients of N_2 and the respective solvent. δ_{23} is calculated using the second virial coefficient of each pure component and the crossed virial coefficient B_{23} , taken as the average between B_{22} and B_{33} ($\delta_{23} = 2B_{22} - B_{33} - B_{23}$).

Depending on the construction setup of the N_2 solubility apparatus, N_2 solubility can be experimentally measured in two different modes: single and dual-transducer mode.

2.3.2 Single-Transducer Mode

Single-transducer mode of the isochoric saturation method relies on the use of one transducer to measure the pressure of N_2 before and after equilibrium. The advantage is that only one precise pressure transducer is required in this setup. Schematics of various gas solubility apparatus by several research groups are shown in the figures below:

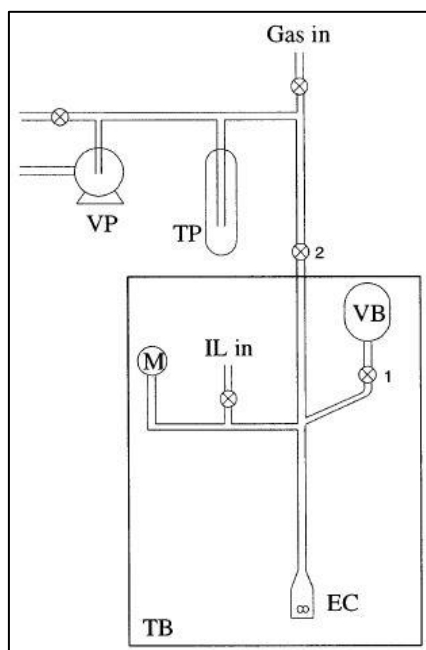


Figure 5: Schematic of the isochoric saturation apparatus that utilises one pressure transducer, developed by Gomes and co-workers. This apparatus consists of: an equilibrium chamber EC, manometer M, vapour phase bulb VB, ionic liquid IL, trap TP, vacuum pump VP, and thermostated bath TB. Reprinted with permission from Gomes et al.¹⁹² Copyright 2003 American Chemical Society.

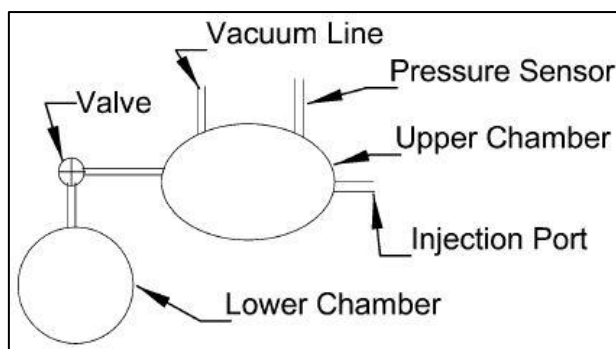


Figure 6: Schematic of the isochoric saturation apparatus that utilises one pressure transducer, developed by Noble et al. Reprinted with permission from Noble et al.¹⁸⁷ Copyright 2004 American Chemical Society.

Both of these schematics consist of a ballast chamber (BC) and equilibrium chamber (EC): one to hold a ballast volume of N₂ and other to hold the degassed liquid sample. The known amount of N₂ in the BC is delivered to the EC by opening a valve. Here, the solubility of N₂ is calculated on the basis of two measurements:

$$n_{N_2} = \frac{p_1 V_{BC}}{RT_1 Z_1} - \frac{p_2 (V_{total} - V_{EC})}{RT_2 Z_2} \quad (5)$$

where, n_{N_2} is the moles of N₂ dissolved in the liquid sample, p_1 and p_2 are the pressure before and after the valve is opened respectively, T_1 and T_2 are the temperature before and after the valve is opened respectively, V_{BC} is the volume of the BC, V_{EC} is the volume of the EC, V_{total} is the total volume of $V_{BC} + V_{EC}$, Z_1 and Z_2 are the compressibility factors (at the given temperature and pressure) before and after the valve is opened respectively, and R is the universal gas constant. Mark I of our N₂ solubility apparatus consists of using a single pressure transducer to conduct measurements of N₂ solubility.

2.3.3 Dual-Transducer Mode

Dual-transducer mode is similar in design to single-transducer mode except that it utilises two pressure transducers to measure N₂ solubility. The major difference is that the valve that connects both of these chambers is subsequently closed after admitting N₂ into the EC. The advantage is that the volume of headspace ($V_{EC} - V_{sample}$) is significantly reduced, allowing for greater changes in pressure due to the absorption of N₂. The following schematics detail dual-transducer mode:

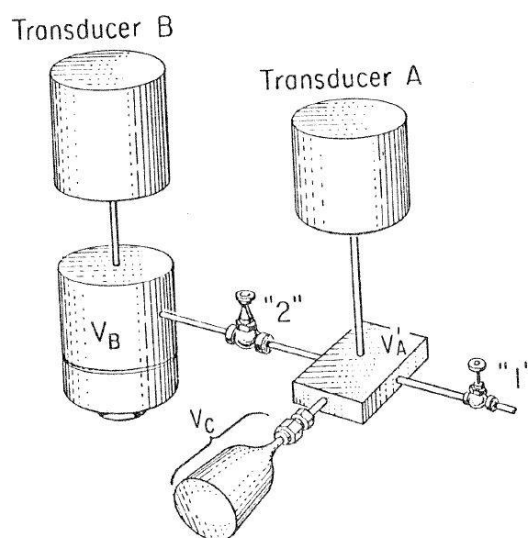


Figure 7: Schematic of the dual-transducer isochoric saturation apparatus, developed by Koros and co-workers. Reprinted with permission from Koros et al.¹⁰⁰ Copyright 1976 John Wiley and Sons.

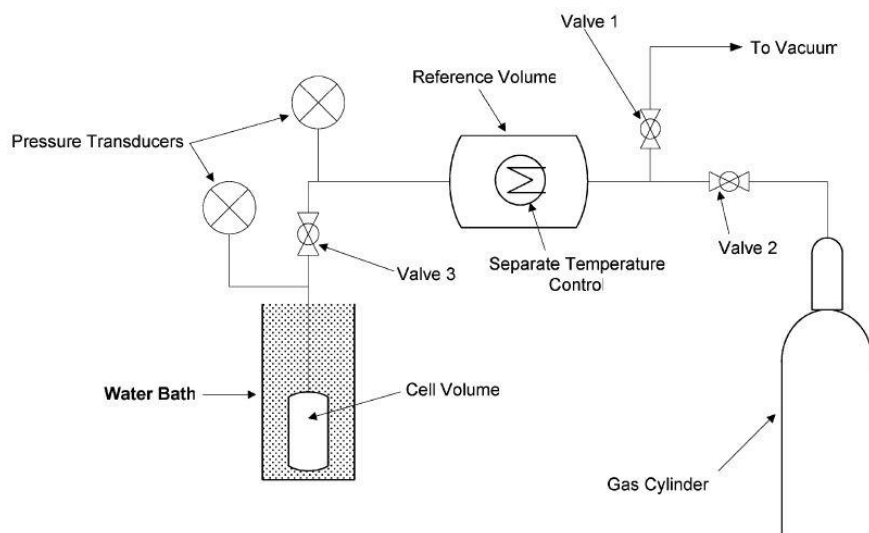


Figure 8: Schematic of the dual-transducer isochoric saturation apparatus, developed by Noble and colleagues. Reprinted with permission from Noble et al.⁹⁸ Copyright 2006 American Chemical Society.

The N₂ solubility in liquids is measured by the same principle as single-transducer mode, through a different series of equations. In dual-transducer mode, a known number of moles of N₂ is admitted from the BC into the EC that contains the degassed liquid:

$$n_{N_2}^{admitted} = \frac{p_1 V_{BC}}{RT_1 Z_1} - \frac{p_2 V_{BC}}{RT_2 Z_2} \quad (6)$$

Where p is the pressure, T is the temperature, Z is the compressibility factor and V_{BC} is the volume of the BC. Subscript 1 indicates the measurement before admitting N₂ and subscript 2

denotes the measurement after admitting N₂ into the EC. Next, the number of moles of N₂ in the headspace of the EC, after N₂ dissolution, is determined by equation 7:

$$n_{N_2}^{headspace} = \frac{(p_3 - p_{sample})(V_{EC} - V_{sample})}{RT_3 Z_{12}} \quad (7)$$

Here, p_{sample} is the vapour pressure exerted by the sample (which is usually negligible in a neat IL), V_{sample} is the volume of the liquid sample, V_{EC} is the volume of the EC, Z_{12} is the compressibility factor of the vapour phase (described in equation 4). Subscript 3 denotes the measurement of the respective variable after the vapour–liquid equilibrium is established between N₂ and the liquid sample. The volume of the sample is determined by knowing the exact mass of sample and measurement of its density. Additionally, in the case with volatile solvent samples, the amount that is present in the vapour phase is subtracted from the total sample volume albeit such values are substantially lower than the volume of the sample, hardly affecting measurement accuracy. Lastly, the moles of N₂ that has been absorbed by the liquid sample is calculated by the difference of N₂ admitted, and N₂ in the headspace:

$$n_{N_2}^{absorbed} = n_{N_2}^{admitted} - n_{N_2}^{headspace} \quad (8)$$

Mark II of the N₂ solubility apparatus utilises the dual–transducer method to measure N₂ solubility. Both single–transducer and dual–transducer have their advantages, where the following sections go into detail about the construction and control measurements that have been undertaken.

2.4 Mark I of N₂ Solubility Apparatus

The first design of the N₂ solubility apparatus utilised the single–transducer approach to measure N₂ solubility. The approach to conducting significant control experiments for this apparatus are shown.

2.4.1 Experimental

The Swagelok fittings and tubing were adapted from previous work within the MacFarlane group. The experimental setup, shown in Figure 9, consists of common Swagelok components such as unions and tube fittings to connect the system together. The total internal volume of the BC consisted of a custom-welded BC and stainless steel tubing whereas EC was made up of a custom-design cylindrical cell attached to ¼ inch elbow union. Also connected to the BC were the vacuum and N₂ lines, where a Swagelok needle valve separated the BC and EC apart. The volume of the BC and EC were determined to be 90.30 cm³ and 6.03 ± 0.02 cm³ (see Table 2—4). Specialised equipment consisted of a MKS Baratron 622C as the pressure transducer, Binder BF115 oven ± 0.3 °C, RTD Pt100 probe ± 0.03 °C, Edwards class 3 vacuum pump, and Edwards Pirani PRM 10 interfaced with a Pirani Penning 1005.

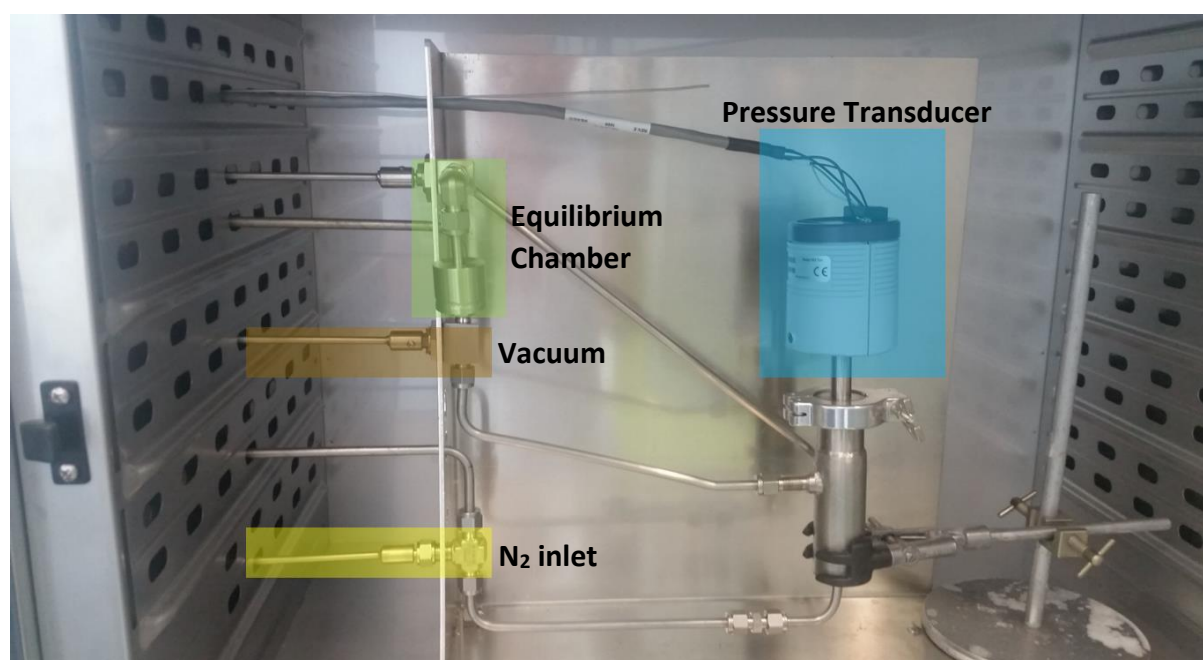


Figure 9: Photograph of the single-transducer Mark I of the N₂ solubility apparatus contained inside a thermostated oven based the isochoric saturation method.

2.4.2 Control Measurements

Several measurements were carried out to ensure the apparatus was suitable for N₂ solubility measurements. Factors such as temperature control, internal volume measurements and leak stability were examined.

2.4.2.1 Temperature Control

Due to the sensitive nature of Gay–Lussac’s law which states that the pressure of a given amount of gas varies directly with the absolute temperature of the gas,¹⁹³ the temperature stability was monitored over an extended time period. Figure 10 demonstrates that the temperature was relatively stable through the use of heated air–flow within an oven with an uncertainty of ± 0.3 °C.

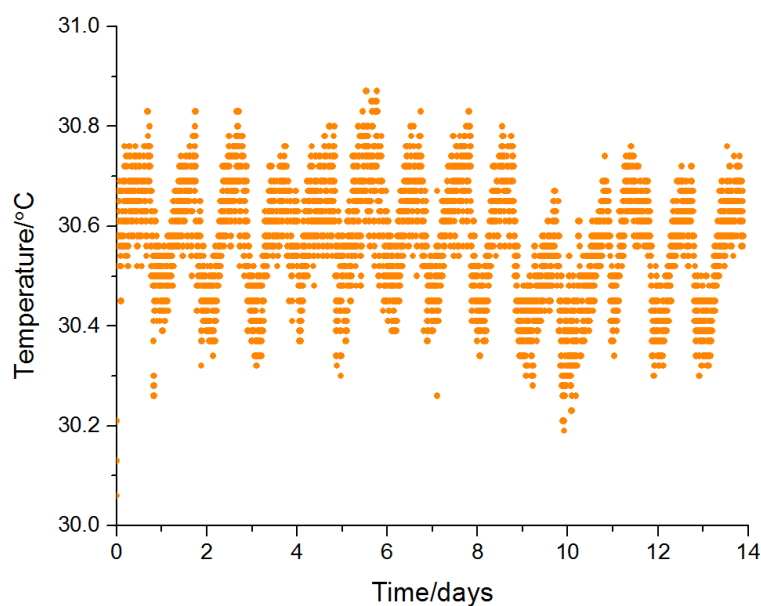


Figure 10: Temperature stability of the thermostated oven over two weeks.

2.4.2.2 Internal Volume Calculations

The measurement of the correct internal volume of the N₂ solubility apparatus (BC and EC) is absolutely critical for accurate N₂ solubility measurements; incorrectly determined internal volumes would lead to subpar accuracy of calculated N₂ solubility values. Shown in Table 1, the internal volume is determined by filling and weighing the EC with/without water (at a known temperature) and using the density to calculate volume. However, discrepancies in weight measurements had been obtained where this may be attributed to unforeseen air bubbles trapped within the components. Hence, Table 2 shows the internal volume measurements that are conducted using methanol as the solvent, due to its higher fluidity, where higher precision is observed (note the lower standard deviation, S.D.)

After the internal volume of the EC was established, the internal volume of the BC (including tubing/fitting volume) was then determined by a series of pressure expansion tests. However, once pressure expansion tests were cross-checked (i.e. by performing the reverse pressure expansion and evaluating data) it was discovered that the internal volume of the valve was contributing to the experiment. Thus, it is imperative that one is aware of the internal volume of any valves (note the difference in volume between Table 1 and Table 2).

Table 1. Numerical data of the mass of the EC, before and after filling with water, to calculate the internal volume of the EC.

Experiment #	1	2	3	4
Total mass of components	249.61	249.59	249.71	249.53
Total mass of components + water	295.82	295.77	295.79	295.68
Mass of water/g	5.81	5.77	5.68	5.75
Temperature/°C	20.2	21.5	24.0	22.0
Density of water/g cm ⁻³	0.9982	0.9979	0.9973	0.9978
Volume of EC/cm ³	5.82	5.78	5.70	5.76
			Average	5.77
			S.D.	0.046

Table 2. Numerical data of the mass of the EC, before and after filling with methanol, including the internal volume of the valve, to calculate the internal volume of the EC.

Experiment #	1	2	3
Total mass of components	249.62	249.61	249.61
Total mass of components + methanol	254.39	254.39	254.39
Mass of methanol/g	4.77	4.78	4.78
Temperature/°C	20.0	20.0	20.0
Density of methanol/g cm ⁻³	0.7923	0.7923	0.7923
Volume of EC/cm ³	6.02	6.04	6.03
		Average	6.03
		S.D.	0.005

After including the internal volume of the valve to calculate the internal volume of the EC, pressure expansion tests following the series of steps are performed as follows: i) fill the whole system with N₂ ii) close the valve to EC and apply vacuum, iii) close vacuum and open valve at the EC, iv) once pressure is stabilised, the pressure reading is used to calculate the volume of BC. The data for these experiments are shown in Table 3.

The internal volume of the BC is calculated through pV calculations with the measured internal volume of the EC. In Table 4, subsequent pressure expansion tests using the calculated EC volume is carried out to verify previous calculations. In these experiments, vacuum is first applied to the whole system after which the valve to the EC was closed. Next, the BC is filled with N₂ at a recorded pressure. After stabilisation of initial pressure, the valve is opened and the internal volume of the EC is determined with the final pressure.

Table 3. Pressure and volume data calculate the volume of the BC.

Experiment #	1	2	3	4	5	6
Pressure in EC/torr	965.3	966.9	968.9	950.4	816.9	876.7
Volume of EC/cm ³	6.03	6.03	6.03	6.03	6.03	6.03
Total pressure (EC + BC)/torr	60.5	60.5	60.6	59.5	51.2	54.9
Total volume (EC + BC)/cm ³	96.23	96.38	96.34	96.36	96.13	96.28
Volume of BC/cm ³	90.20	90.35	90.31	90.33	90.10	90.26
					Average	90.26
					S.D.	0.086

Table 4. Pressure and volume data to calculate the volume of the EC.

Experiment #	1	2	3
Pressure in BC/torr	940.1	951.3	933.6
Volume of BC/cm ³	90.26	90.26	90.26
Total pressure (EC + BC)/torr	881.2	891.8	875.3
Total volume (EC + BC)/cm ³	96.23	96.38	96.34
Volume of EC/cm ³	6.03	6.02	6.01
		Average	6.02
		S.D.	0.009

In summary, the internal volume of the EC was measured to be 6.03 ± 0.02 cm³, using methanol as the solvent. Through pressure expansion tests, the internal volume of the BC was calculated to be 90.26 ± 0.02 cm³. These calculations were cross-checked via reverse pressure expansion tests, where the internal volume of the EC was recalculated to a value of 6.02 ± 0.02 cm³. Through the series of these measurements, the internal volume of the N₂ solubility apparatus was calculated and verified.

2.4.2.3 Pressure Stability

Overpressure Stability

One significant factor that must be controlled is any N_2 that may be leaking within the N_2 solubility apparatus. Any N_2 that leaks out of the apparatus will lead to overestimated decreases in pressure and greatly affect calculations. Shown in Figure 11 below is the plot of absorption of N_2 into an IL. Over time, N_2 dissolved into the IL until saturation occurred. After which the pressure was shown to be stable over a long time period of 30 hours, this indicated that N_2 gas did not leak from the system over time.

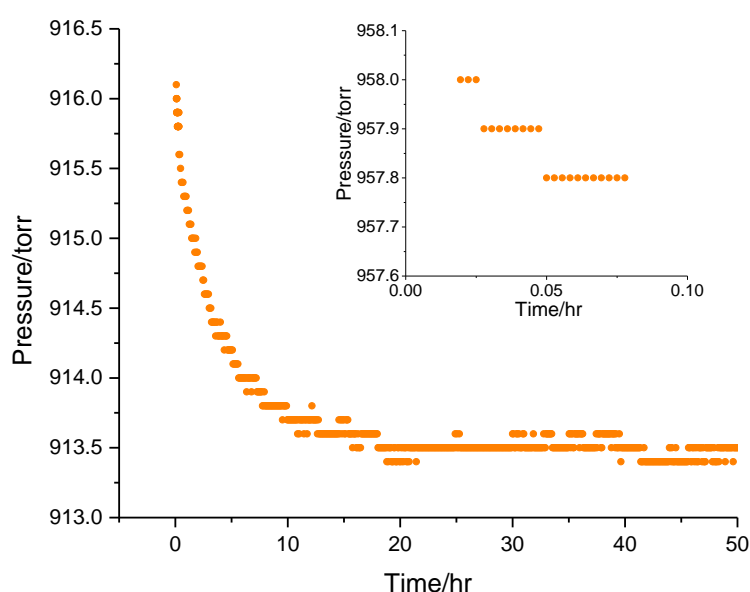


Figure 11: Plot of N_2 absorption over time into an IL at above atmospheric pressures. Inset shows the initial pressure before N_2 is admitted into the EC.

Vacuum Pressure Stability

The following experiment, shown in Figure 12, was carried out to determine if the system was vacuum-tight (i.e. if any gas from the atmosphere would enter into the system). However, it was observed that apparatus undergoes a leak rate of ~ 0.03 torr/hr. Attempts to identify the source of the leak was investigated by replacing certain Swagelok parts but inevitably, a leak-free apparatus was not be achieved. This may be due to Swagelok tube fittings, which were not usually designed to sustain vacuum pressure conditions.

While it is only required to keep the EC under vacuum pressure, which would contain the degassed liquid sample, the EC would still be susceptible to leaking. Additionally, there is a time period required for N_2 in the BC to reach thermal equilibrium where the pressure would take time to stabilise, allowing time for gases to enter the EC. Moreover, due to the use of a single pressure transducer, the actual pressure inside the EC is unknown, or the amount of air that would have entered into the liquid sample is not known. This issue would result in an underestimated solubility of N_2 that would be unavoidable. Furthermore, the amount of gas that could enter into the apparatus in an experiment (~ 1 torr) is a huge fraction of the pressure absorbed by the liquid sample in Figure 11 (~ 3 torr).

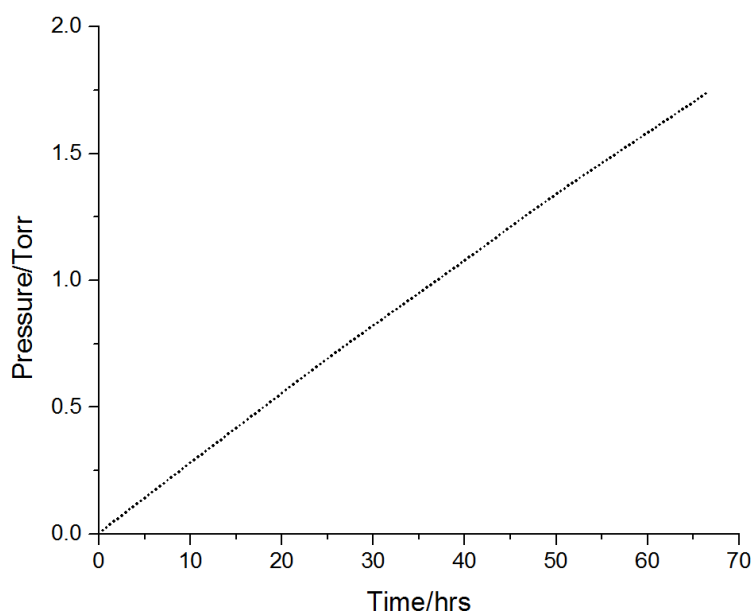


Figure 12: Pressure monitoring of the N_2 solubility apparatus, showing an increase in pressure over time under vacuum conditions.

2.4.3 Tips for High Precision

Through the construction of Mark I of the N_2 solubility apparatus, many issues and challenges were encountered. The following summarises the outcomes:

- The pressure difference was not large upon N_2 expansion from the BC to the EC. The internal volume of the BC was far too large compared to the EC, which resulted in small pressure differences due to N_2 absorption.

- The internal volume of the BC was too large compared to the EC whereby the pressure did not decrease as much upon expansion, nor due to N₂ that dissolved into the liquid sample.
- The sample size was small which led to small decreases in pressure due to N₂ absorption. A larger sample volume (and smaller headspace volume) would allow more N₂ to enter the sample, and result in larger pressure differences.
- Standard Swagelok fittings were not holding vacuum pressure and resulted in a leak in the system. Swagelok VCR parts would be ideal as they would be stable above atmospheric pressure, and under vacuum conditions.
- Water was used to fill the internal volume which resulted in incomplete filling of such parts due to the formation of air bubbles. Therefore the use of a fluid solvent would have prevented this problem.
- An air–flow oven for temperature control displayed a larger uncertainty than standard water baths.

2.5 Mark II of N₂ Solubility Apparatus

The use of a dual–volume apparatus allows the ability to monitor pressure in both the BC and EC during all times of the experiment. Moreover, higher precision can be achieved with a second pressure transducer as the amount of headspace volume will be reduced by subsequently closing the valve to the EC; during N₂ dissolution, the pressure change will be greater in a smaller headspace volume compared to the total volume of the whole apparatus (in the case of single–transducer mode). In Mark I of our N₂ solubility apparatus, we had discovered that the volume of the BC was far too large compared to the EC. Therefore, the use of a smaller volume for the BC allows for a greater difference in pressure upon N₂ dissolution, and greater precision.

Additionally, it was found that the use of similar volumes for the BC and EC was important to maintain precision and reliability of results. This concept was examined by Koros and co-workers¹⁰⁰ in Figure 13a—b where the effect of scattering for gas absorption was highly prominent when volume BC:EC ratio is ~10:1. Mark I of our N₂ solubility apparatus had a BC:EC ratio of ~15:1. As a result, the concept of using similar internal volumes of the BC and EC are incorporated into Mark II N₂ solubility apparatus.

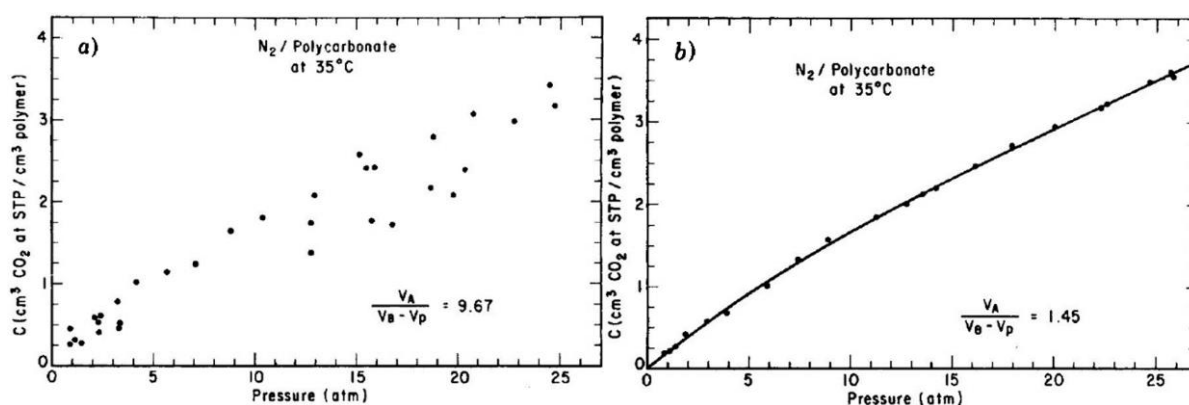


Figure 13a—b: Sorption isotherms for N₂/polycarbonate at 35 °C at a volume ratio of a) 9.7 compared to b) 1.5. Consistent results were obtained in the latter case. V_A and V_B is the volume of section A and B respectively, V_p is the volume of the polymer sample. Reprinted with permission from Koros et al.¹⁰⁰ Copyright 1976 John Wiley and Sons.

2.5.1 Experimental

Once the overall design was established, each section was constructed and connected together in various setups. After several iterations, the complete Mark II of the N₂ solubility apparatus is shown in Figure 14 with further details of each component described in Supporting Figure S1. A simplified schematic of the N₂ solubility apparatus is displayed in Figure 15.

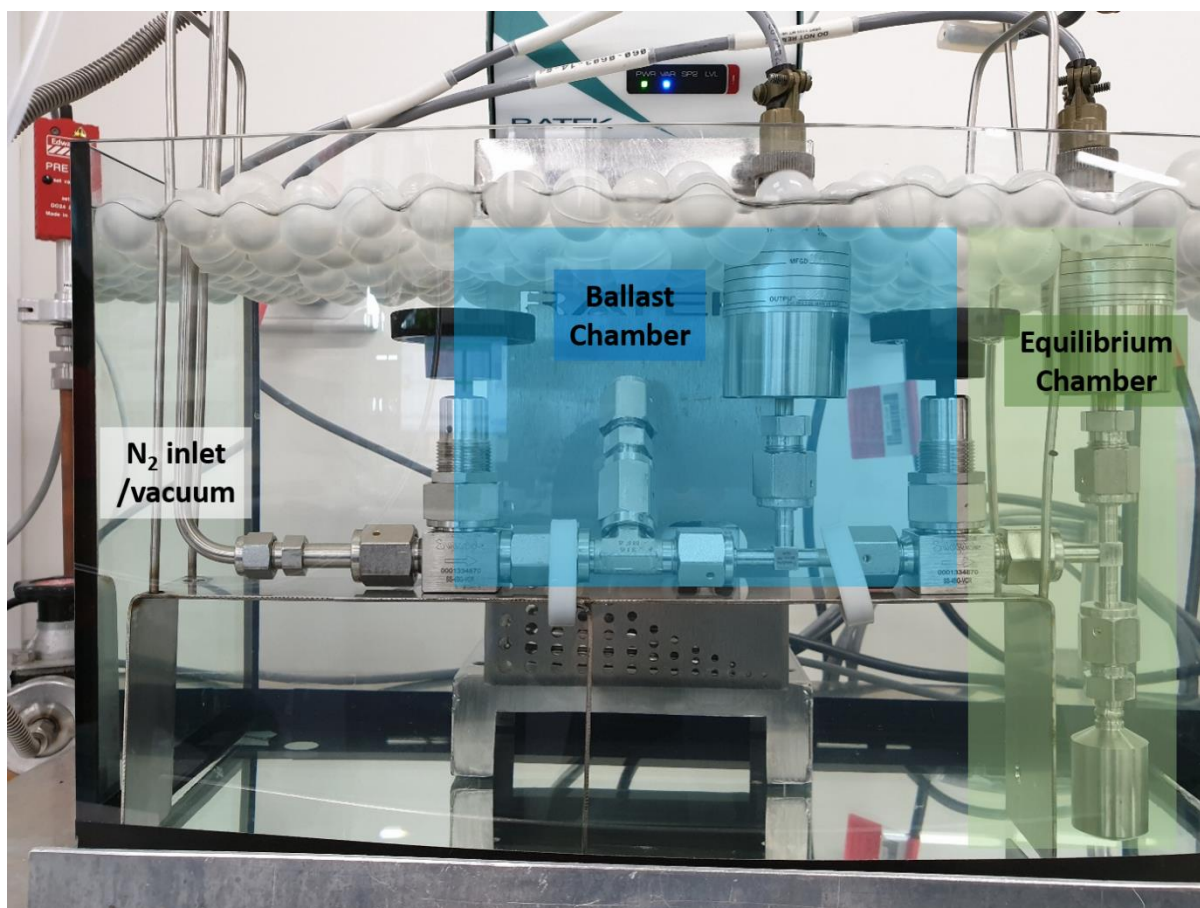


Figure 14: Photograph of the dual-transducer Mark II of the N_2 solubility apparatus contained inside a water bath, based on the isochoric saturation method.

The N_2 solubility apparatus setup consisted of several 316L Stainless Steel VCR Swagelok components such as $\frac{1}{4}$ inch VCR unions, VCR bellow valves and a VCR fitted sample cylinder. VCR stands for Vacuum Coupling Radiation fittings, where two ‘male’ fittings formed a gas leak-tight connection onto VCR Ag-plated stainless steel gasket fittings. VCR fittings were designed to withstand both overpressure and ultra-high vacuum due to the perfect contact between the gasket and fitting. Gaskets were replaced after each use and were tightened to the same degree to ensure replicated internal volume upon assembly. Gaskets and fittings were polymer free, as polymer materials had the tendency to absorb some amount of gas. N_2 lines and the vacuum pump were connected at the end and controlled via a three way valve. The volume of the BC and EC were determined (see Table 5—6) to be $7.29 \pm 0.02 \text{ cm}^3$ and $15.38 \pm 0.02 \text{ cm}^3$; depending on the volume of liquid sample, the volume ratio (BC:EC) was usually close to unity.

Specialised equipment included two Super-TJE ultra-precision pressure transducers (75, 150 bar; Honeywell Test & Measurement) interfaced to a Model SC2000 Transducer Display and Signal Conditioning Unit and subsequently connected to a computer where pressure data was processed using Sensocom software. The temperature of the water bath was controlled using a Ratek TH8000 precision immersion heating circulator ± 0.04 °C and measured with a RTD Pt100 probe ± 0.03 C. Other components consisted of an Edwards class 3 vacuum pump, Edwards Pirani PRM 10 interfaced with a Pirani Penning 1005, Ratek MS8 Compact Magnetic Stirrer and VWR anti-evaporation spheres to reduce water evaporation. The water bath stand, apparatus stand and heating circulator platforms were custom built and welded. Specific part listings are shown in Supporting Table S1 and Supporting Table S2.

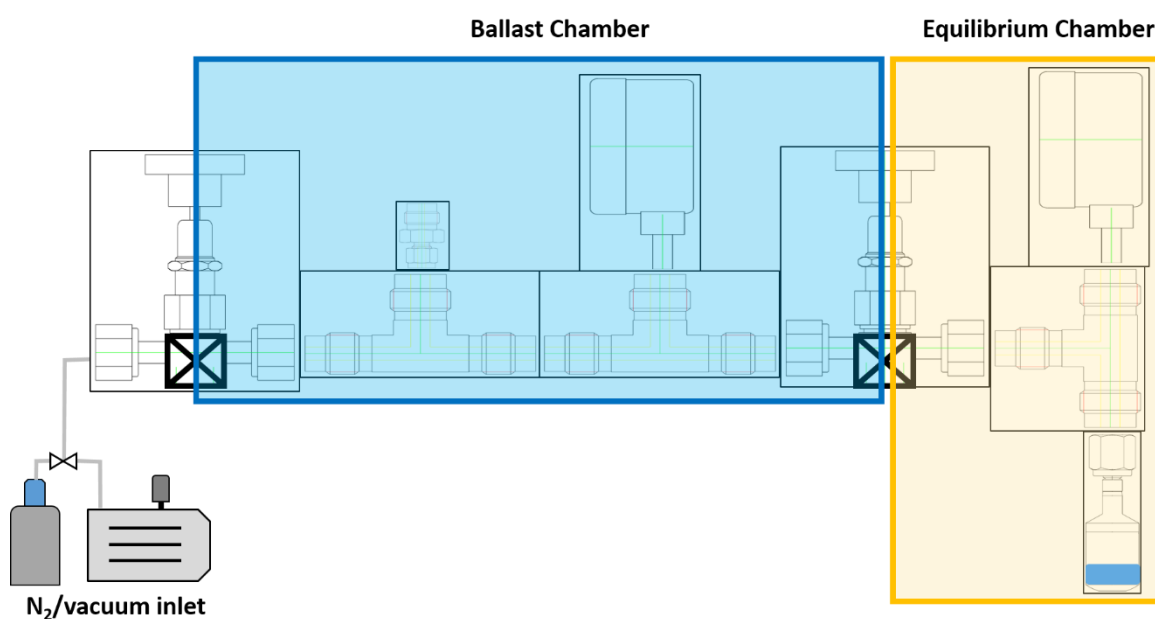


Figure 15: Schematic of the dual-transducer Mark II of the N_2 solubility apparatus based on the isochoric saturation method.

2.5.2 Step-by-step Measurement Procedure

Through the isochoric saturation method, each measurement during the operation of the N_2 solubility apparatus proceeded through three main stages: i) degassing of liquid sample, ii) delivery of known amount of N_2 into the EC, and iii) N_2 dissolution into the liquid sample.

2.5.2.1 Degasification Procedure

It was essential for all N₂ solubility measurements that the liquid sample was completely degassed, as any leftover dissolved gas would have led to underestimated solubility values. The degasification procedure for ILs was simply to vacuum-dry the IL for over 24 hours (or longer than the time required for complete gas absorption). Given the ideal sample size of ~8 mL, highly viscous ILs may require longer time under vacuum to degas. In the case of solvents (or IL-solvent mixtures), freeze-thaw cycles were required to degas liquid samples. In this work, at least six freeze-thaw cycles were performed per liquid sample.

To recap the degasification procedure: the liquid sample was first cooled under liquid N₂ for a certain time period, ~7 minutes (this varied between different melting points of various solvents). Next, vacuum was applied by opening the valve to the frozen sample for 10—120 seconds such that gases were removed from the headspace. After the valve was closed to vacuum, the sample was placed into a water bath (~25 °C) and allowed to warm. As the sample melted, dissolved gases in the liquid outgassed into the headspace of the sample, which was facilitated by stirring. This procedure was repeated at least six times until the vacuum gauge did not move upon opening the valve to vacuum (i.e. no change in pressure when vacuum was applied). Care was taken to ensure the liquid sample was not heated too high, as this resulted in the loss of sample upon applied vacuum.

Figure 16 shows an example of the freeze/thaw cycles performed with water. One might notice the decrease in pressures prior to applied vacuum with subsequent freeze-thaw cycles such that dissolved gases were still being removed at cycle five. This reflects the importance of repeated freeze-thaw cycles, where in some samples up to nine freeze-thaw cycles were performed. In this particular experiment, the vapour pressure of water was measured to be 4320 Pa at 30 °C, compared to the literature data of 4246 Pa.²⁵ This shows satisfactory agreement to within 2%.

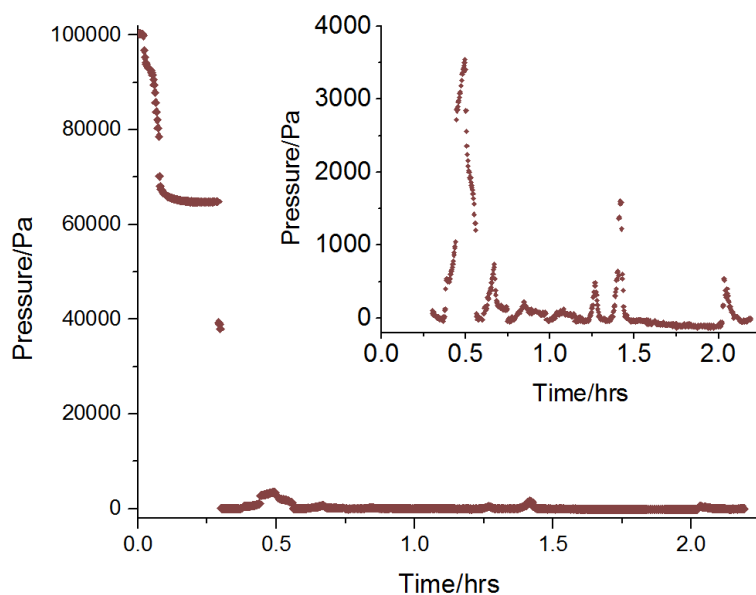


Figure 16: The plot of pressure during freeze–thaw cycles. The inset shows the zoomed in plot of pressure.

2.5.2.2 Delivering N_2 to the Equilibrium Chamber

Once the liquid sample was degassed, N_2 was admitted to the BC and allowed to reach thermal equilibrium. Shown in Figure 17, approximately two hours was required for N_2 to reach thermal equilibrium and the pressure to stabilise within the BC. The initial pressure of N_2 was targeted such that after N_2 dissolution, the final pressure in the headspace was close to atmospheric pressure (or above atmospheric if N_2 solubility at higher pressure was desired). Once the pressure was constant, the valve was opened for a very brief moment and subsequently closed to allow N_2 into the EC. Here, Joule–Thomson effects were observed in both the BC and EC (described later in this chapter).

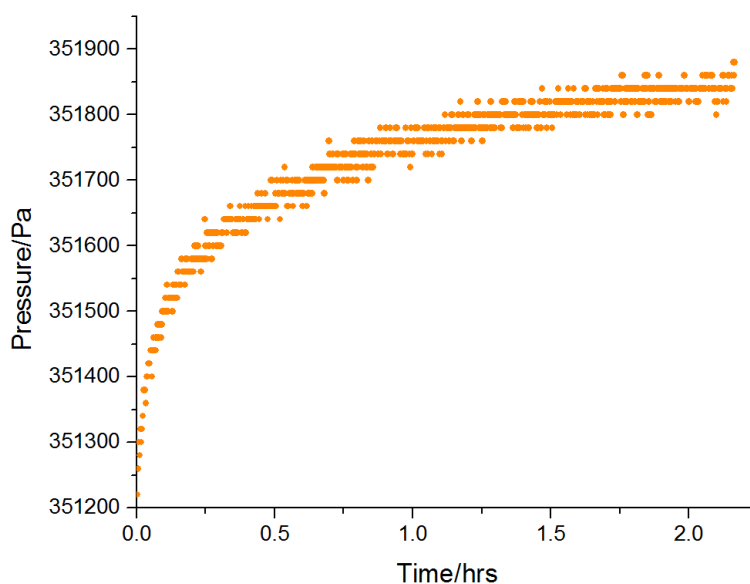


Figure 17: Pressure increase due to N_2 reaching thermal equilibrium with the water bath over two hours.

2.5.2.3 N_2 Dissolution

Once N_2 was admitted into the EC, the pressure in the headspace decreased as N_2 dissolved into the liquid sample. The same was stirred to facilitate the equilibrium process of gas dissolving in the liquid versus the converse of N_2 outgassing into the headspace. After some time (less than two hours for volatile solvents and more than ten hours for ILs), the pressure in the EC reached a constant value. During the experiment, we ensured that the level of the water bath remained high enough to cover the pressure transducers due to pressure fluctuations that were caused by changes in ambient temperature. After the experiment, these pressure values were used to calculate N_2 solubility. An example of a spreadsheet used to perform such calculations is shown in Supporting Figure S2.

2.5.3 Control Measurements

In the same way for Mark I of the N_2 solubility apparatus, a series of control experiments were conducted to ensure applicability of the apparatus to perform high-precision measurements.

2.5.3.1 Temperature Control

The temperature stability of the water bath showed higher precision compared to the temperature control of the fan-controlled oven. Comparison of Figure 18 to Figure 10, shows

approximately an order of magnitude in difference in temperature uncertainty, $\pm 0.4\text{ }^{\circ}\text{C}$ and $\pm 0.03\text{ }^{\circ}\text{C}$ respectively.

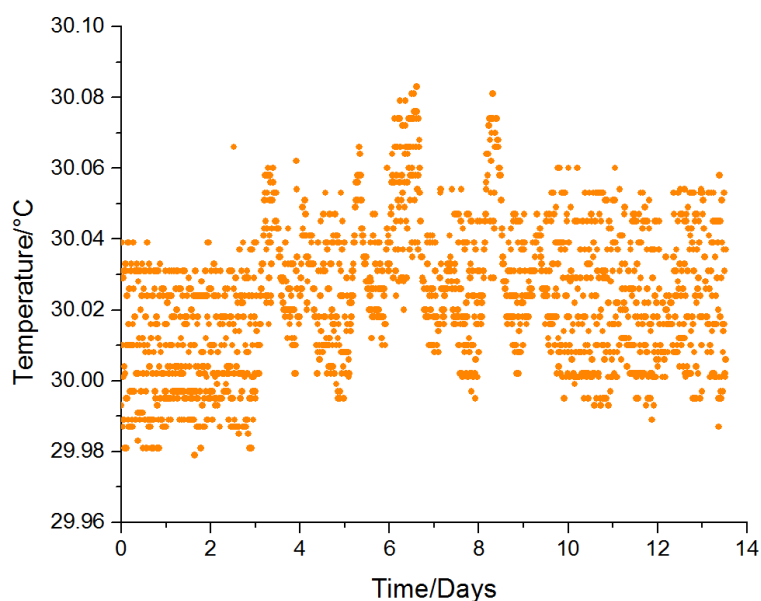


Figure 18: Temperature stability of the water bath over two weeks.

2.5.3.2 Joule–Thomson Effect

The Joule–Thomson effect describes the temperature change when a gas expands from high pressure to low pressure as an isoenthalpic process.¹⁹⁴ A positive value of the Joule–Thomson coefficient μ_{JT} results in the cooling of gas (or liquid) upon expansion, which is the usual case at ambient conditions. Figure 19 shows the inversion curve of N_2 as a function of temperature and pressure that determines whether cooling or heating occurs upon gas expansion. This phenomenon is utilised in refrigeration processes, air conditioners, heat pumps etc.,¹⁹⁵ and also has an effect on our N_2 solubility apparatus.

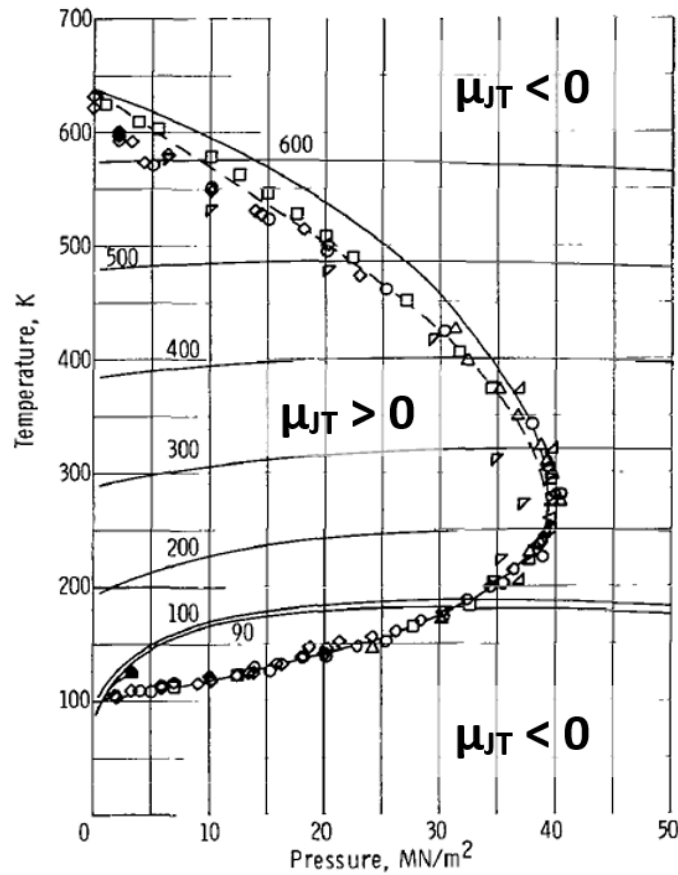


Figure 19: Joule–Thomson inversion curve for N_2 as a function of temperature (K) and pressure (MN/m^2). Inside the curve, where the Joule–Thomson coefficient $\mu_{JT} > 0$, cooling occurs upon expansion from high to low pressure. The converse occurs outside of this inversion curve. Figure reproduced from Hendricks et al.¹⁹⁶ and used with permission of NASA.

In Figure 20, the Joule–Thomson effects are shown through a blank experiment that is conducted by admitting a large amount of N_2 from the BC into the empty EC. After the valve was opened and closed, the EC displayed a slight increase in pressure whereas the BC displayed a decrease in pressure. These pressure changes were caused by the temperature compensation by the isothermal water bath since the EC undergoes cooling whilst the BC undergoes heating. Due to the Joule–Thomson effect, approximately 2 hours was required to stabilise the temperature; hence this stabilisation time must be considered in the time scale of experiments.

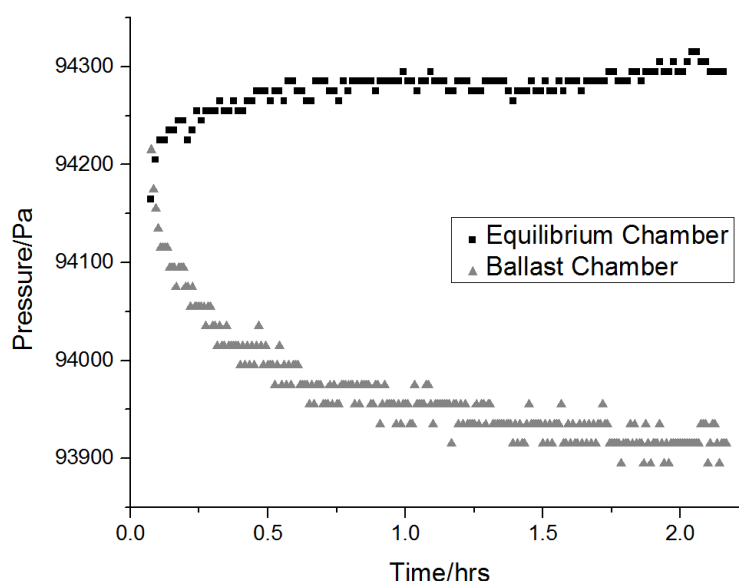


Figure 20: The Joule–Thomson effect on pressure after N_2 was admitted into the EC. The EC undergoes cooling whilst the temperature of the BC increased; both are ultimately compensated by the water bath.

2.5.3.3 Internal Volume Calculations

As discussed in Mark I of the N_2 solubility apparatus, it is critical to accurately determine the internal volume of the system. The internal volume was measured in two separate sections; the BC, and the EC whilst also including internal volume of metal gaskets and valves. Moreover, the system was dry and free from any particulates prior to weight measurements. The weight of each component is summarised in Table 5 and Table 6 below.

Table 5. Tabulated internal volume data based on the weight and density of methanol to calculate the volume of the BC.

Experiment #	1	2	3	4	5	Average
BC/cm ³	4.94	4.93	4.94	-	-	4.93
Transducer 1/cm ³	1.89	1.87	1.87	-	-	1.88
Inner valve/cm ³	0.52	0.53	0.52	0.52	0.52	0.52
Swagelok cap/cm ³	0.04	0.05	0.04	0.05	0.05	0.05
Total/cm ³						7.29

*Weighing measurements were conducted on a 4 d.p. weighing balance

**Swagelok cap volume is subtracted from the total

Table 6. Tabulated internal volume data based on the weight and density of methanol to calculate the volume of the EC.

Experiment #	1	2	3	4	Average
EC/cm ³	13.57	13.57	13.55	-	13.56
Transducer 2/cm ³	1.82	1.81	1.81	1.81	1.81
Total/cm ³					15.38

Additionally, pressure expansion tests were carried out to cross-check measurements of the internal volume of the BC and EC. The moles of N₂ in the EC (n_3) was calculated by the following equation:

$$n_3 = \frac{p_1 V_{BC}}{RT_1 Z_1} - \frac{p_2 V_{BC}}{RT_2 Z_2} \quad (9)$$

Based on the moles of N₂, and the pressure contained in the EC, the internal volume was determined:

$$V_{EC} = \frac{n_3 RT Z_3}{p_3} \quad (10)$$

Table 7 summarises the pressure values and calculations involved in these measurements. The calculated volume of the EC via pressure expansion tests falls within uncertainty of the measured value by methanol filling. Thus, the internal volume was established.

Table 7. Tabulated pressure data and calculations for the moles of N₂ and volume of the EC based on a BC volume 7.29 cm³ and temperature 303.3 K through three N₂ pressure expansion tests.

Experiment #	1	2	3
Before Expansion			
p_1 in BC/Pa	300160	282640	243780
n_1 in BC/mmol	0.868	0.817	0.705
After Expansion			
p_2 in BC/Pa	96880	90820	79540
n_2 in BC/mmol	0.280	0.263	0.230
n_3 in EC ($= n_1 - n_2$)/mmol	0.588	0.554	0.475
p_3 in EC/Pa	96440	91100	77980
V_{EC}/cm^3	15.37	15.36	15.37

2.5.3.4 Pressure Stability of N₂ Solubility Apparatus

The pressure stability of the N₂ solubility apparatus was examined at above-ambient and under vacuum pressures. Standard Swagelok fittings and unions were previously shown to be ideal at above ambient pressure but were not able to sustain vacuum pressure. Therefore, the use of VCR Swagelok fittings was critical to ensure a leak-free apparatus.

Overpressure Stability

Figure 21a—b shows the pressure stability of each chamber of the N₂ solubility apparatus. Both of these plots demonstrate the stability of pressure over 12 hours after performing a blank experiment (a pressure expansion test into an empty EC), and also demonstrates the aforementioned Joule–Thomson effects.

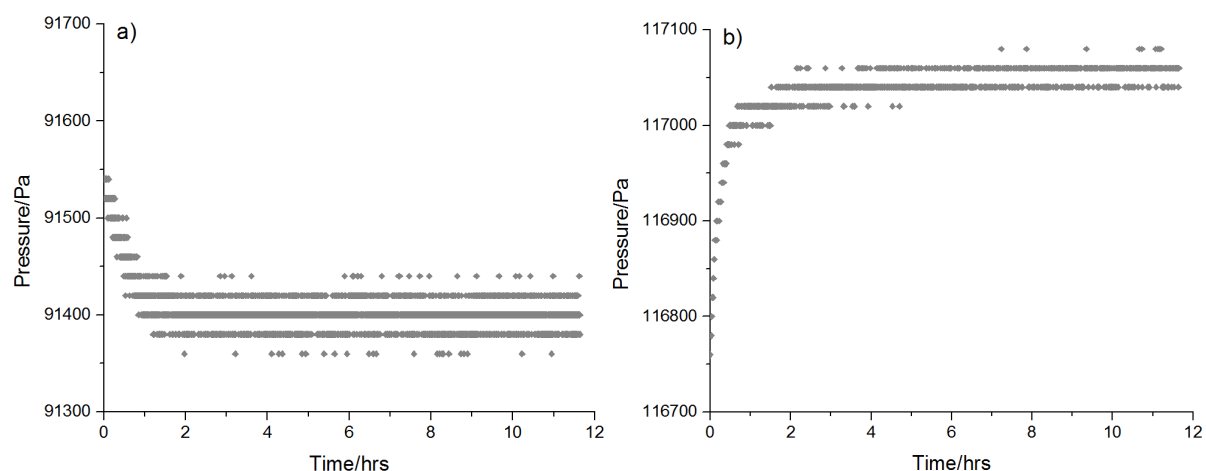


Figure 21a—b. Pressure stability in the a) BC and b) EC after N₂ was admitted into the EC.

Vacuum pressure stability

Shown in Figure 22—b, the BC and EC within the N₂ solubility apparatus were observed to be stable over a long period of time under vacuum pressure.

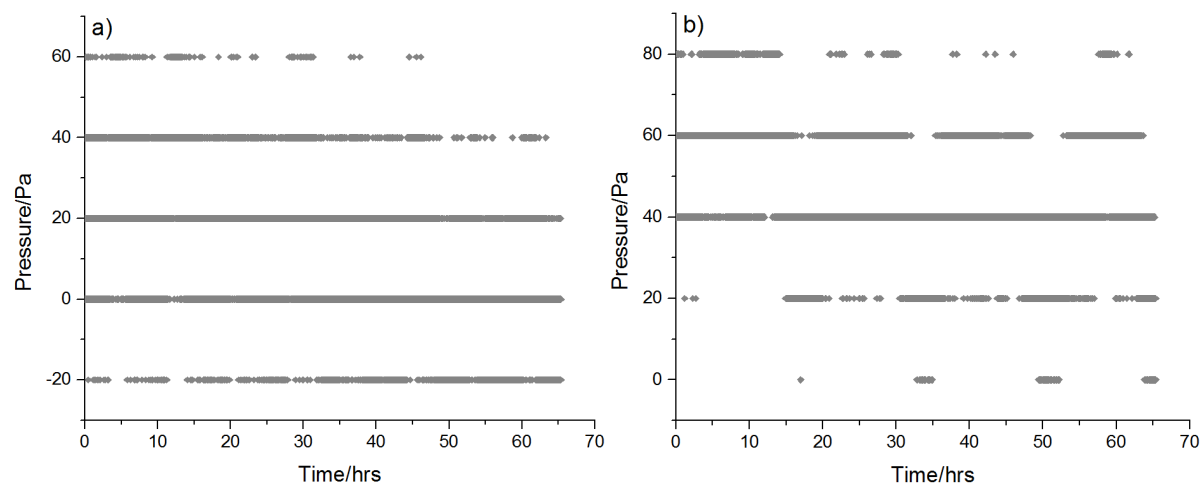


Figure 22a—b. Pressure stability in the a) BC and b) EC under vacuum pressure over an extended time period.

Pressure Fluctuations

An issue that was encountered was the highly erratic pressure data from one of the pressure transducers shown in Figure 23. This scattered pattern does not represent gas leaking, noise or atmospheric changes. It was eventually discovered that the pressure transducer wires connected to the back of the display must be electrically grounded.

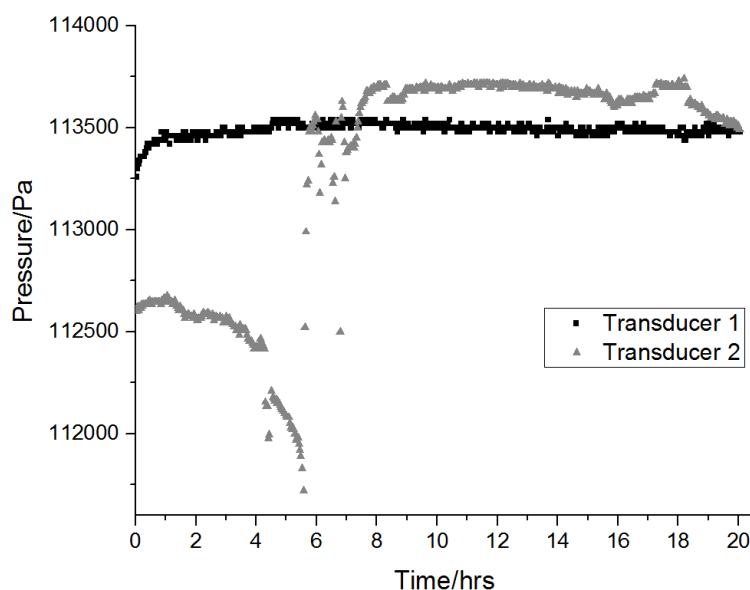


Figure 23: Erratic pressure data for one of the transducers in the closed system over time.

2.5.3.5 Data Validation

After control experiments were performed to ensure stability of the N₂ solubility apparatus, N₂ solubility measurements were performed to benchmark data to literature. Due to the intrinsic low solubility of N₂ compared with other gases, it can be difficult to measure such data on a reliable basis. For example, two different research groups had measured CO₂ and N₂ solubility in [P₆₆₆₁₄][eFAP] at 60 °C using the isochoric saturation method,^{186, 197} where comparison of the measured N₂ solubility value showed a 43% greater discrepancy between groups compared to CO₂. Therefore, it is important to compare our apparatus with literature N₂ solubility data, as shown in Table 8.

Table 8. Data comparison of N₂ solubility values to literature expressed as mole fraction χ_2 and molar concentration C_{N_2} , corrected to a partial pressure of $p = 1$ atm, for various solvents and ILs at 303 K.

Sample	Measured χ_2 / 10^{-3}	Literature χ_2 / 10^{-3}	% deviation /%	C_{N_2} /mmol L ⁻¹
--------	----------------------------------	------------------------------------	-------------------	------------------------------------

	$\pm 2\%$			$\pm 2\%$
Hexane	1.4(2)	1.39 ¹⁰¹	+2.2	10.7
Perfluoroheptane	4.0(4)	3.88 ¹⁰⁷	+3.9	17.9
Perfluorotributylamine	4.2(3)	4.17 ¹⁹⁸	+1.5	11.8
Acetonitrile	0.3(4)	0.33 ¹⁰⁹	+3.0	6.4
[C ₄ mim][BF ₄]	0.5(0)	0.57 ¹¹³	-12.6	2.6
[C ₄ mim][NTf ₂] ^a	1.2(4)	1.04 ¹¹²	+19.0	4.2(2)
[P ₆₆₆₁₄][eFAP]	3.2(0)	$\sim 3^b$	-	4.1(4)

^aConducted at 313 K

^bN₂ solubility for [P₆₆₆₁₄][eFAP], measured by Blath et al.¹⁸⁶ at 333K was adjusted to 303 K by using the enthalpy of solvation of [P₆₆₆₁₄][eFAP].¹⁹⁷

The N₂ solubility data that we measured for organic solvents is highly comparable to literature data, within 4%. The agreement for some ILs is within 19%, which likely reflects greater variation in IL purity across different laboratories.

2.5.3.6 Maintenance of N₂ Solubility Apparatus

The N₂ solubility apparatus was maintained and cleaned regularly to prevent us from obtaining irregular data points with the same sample. For example, Table 9 describes a series of experiments that we conducted in attempt to resolve the sporadic variations of N₂ solubility (i.e. poor accuracy in results). Since the N₂ solubility in [C₄mpyr][eFAP] and TFT (TFT) were both previously measured to be 4.7 and 10.0 mmol L⁻¹ respectively, it was expected that a 1:4 mixture would have yielded a N₂ solubility value less than that of neat TFT. On the contrary, the measured N₂ solubility in the 1:4 mixture of [C₄mpyr][eFAP]/TFT was observed to be ~ 11 mmol L⁻¹, larger than that of neat TFT. To investigate this behaviour, the experiment was repeated several times yet resulted in overestimation of solubility values despite after thoroughly double-checking calculations and resetting instrumental software. Next, the N₂ solubility in neat TFT was measured, where it was found to be larger than determined previously. The pressure transducers were recalibrated and their hysteresis determined to be similar as before. Although additional freeze/thaw degassing cycles were performed in the case that gas impurities may have been present in TFT, the solubility values were still being overestimated. To confirm that TFT was not the source of the error, due to impurities, the N₂

solubility of perfluoroheptane was also measured to be 15% larger than previously measured (which had been previously verified to literature). Thus, N₂ solubility measurements in both TFT and perfluoroheptane led to significant errors, which suggested that the problem was not related to the solvent itself.

At this stage, the internal volume of the pressure transducer and other sections of the apparatus were measured for any potential corrosion of Swagelok components/chambers. Still the internal volume was measured to be the same as before. However, upon reassembly of the apparatus, moisture and particulates were found to be present within specific components of the apparatus. Finally, after all parts of the system were cleaned (including the water bath and heating circulator), the N₂ solubility in TFT was measured to be similar to that of previous values followed by a reliable measurement in the 1:4 mixture of [C₄mpyr][eFAP]/TFT. Thus, the cleaning and maintenance of the N₂ solubility apparatus was imperative for reliable results.

Table 9. Series of experiments undertaken to troubleshoot irregular results of N₂ solubility.

Experiment #	Experiment	Result	Previous Result	Error/%
1.1	N ₂ solubility in 20% [C ₄ mpyr][eFAP]/TFT	10.8 mmol L ⁻¹	-	-
1.2	N ₂ solubility in 20% [C ₄ mpyr][eFAP]/TFT	11.0 mmol L ⁻¹	-	-
2.1	N ₂ solubility in TFT	12.2 mmol L ⁻¹	10.0 mmol L ⁻¹	22
2.2	N ₂ solubility in TFT	12.5 mmol L ⁻¹	10.0 mmol L ⁻¹	25
2.3	N ₂ solubility in TFT	12.9 mmol L ⁻¹	10.0 mmol L ⁻¹	29
3.1	N ₂ solubility in Perfluoroheptane	20.6 mmol L ⁻¹	17.9 mmol L ⁻¹	15
4.1	Internal volume of Transducer 1	1.88 cm ³	1.88 cm ³	0
5.1	Reconstruct apparatus Clean moisture/dirt	-	-	-
6.1	N ₂ solubility in TFT	10.2 mmol L ⁻¹	10.0 mmol L ⁻¹	2
7.1	N ₂ solubility in 20% [C ₄ mpyr][eFAP]/TFT	8.8 mmol L ⁻¹	-	-

2.5.3.7 Temperature Study of Pressure Transducers

A number of N₂ solubility experiments were conducted at temperatures above 30 °C. In some cases, instead of a constant decrease/increase in N₂ solubility with temperature as shown in literature, fluctuating results were obtained. Therefore, a series of blank pressure experiments were conducted on a closed system (after vacuum was applied for 48 hours), where the final pressure was monitored at each temperature step. Figure 24a—f displays the initial and final pressure at the given temperature steps. The initial heating occurred due to heating the water bath followed by the adjustment to temperature, where the pressure values do not return back to ‘zero’ after thermal equilibrium. Table 10 displays the final pressure values after thermal equilibrium after each temperature step.

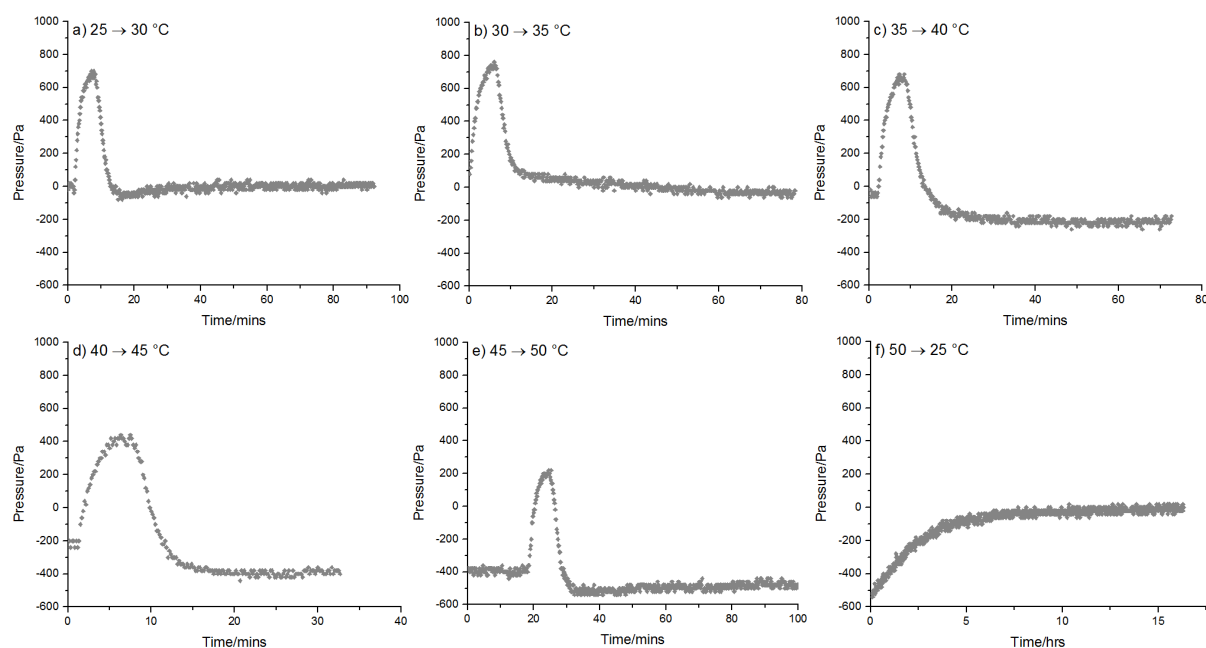


Figure 24a—f: Monitoring pressure under closed vacuum at temperature intervals from a) 25 → 30 °C, b) 30 → 35 °C, c) 35 → 40 °C, d) 40 → 45 °C, e) 45 → 50 °C, and f) 50 → 25 °C.

Table 10. Final pressure values after thermal equilibrium at each temperature step, in a closed system under vacuum pressure.

Temperature/°C	Transducer 1/Pa	Transducer 2/Pa
25	0	0
30	10	300
35	-40	600
40	-220	820
45	-380	1020
50	-480	1180
25	0	160

The increases/decreases in pressure between each temperature step are not consistent, which may suggest that the sensitivity of the pressure transducers change at different temperatures. Since the pressure differences cannot be estimated, it would not be ideal to merely subtract this from the final pressure. Therefore, when N₂ solubility measurements are to be carried out at a different temperature, both pressure transducers are calibrated after thermal equilibrium at the given temperature. This involves applying vacuum to the whole system and once the pressure has stabilised, calibration is conducted using the Model SC2000 display unit. Through this calibration procedure, temperature dependence studies can be carried out, as shown in Chapter 5.

2.5.3.8 *Potential Pitfalls/Solutions*

In the design and construction of a N₂ solubility apparatus, the ultimate goal was the accurate measurement of N₂ solubility in liquids to a high degree of precision. However, in many occasions, these measurements did not yield such reliable results. Here, we describe some of the potential pitfalls that we encountered and provide some resolutions that we adopted to tackle such issues:

- Inaccurate N₂ solubility values were calculated due to incorrect determination of the internal volume of the apparatus. The use of water to fill the internal volume led to unforeseen air bubbles and resulted in a smaller calculated volume. Hence, methanol was used to fill the internal volume of the apparatus (including any internal volume of the valves), due to its higher fluidity than water. In addition, measurements were repeated a number of times, preferably with most of the apparatus components already constructed, to ensure reliable determination of the internal volume.

Blank pressure expansion tests were carried out to cross-check the determined volumes of the BC and EC. In addition, helium can be used to conduct pressure expansion tests through the Burnett expansion process,¹⁹⁹ at multiple temperatures.

- As the pressure was very susceptible to temperature, the temperature was controlled using a water bath as it was found to be more stable than an air-based oven.
- The super-TJE pressure transducers were found to be very temperature sensitive which led to pressure differences due to the change in atmospheric temperature. To reduce the effect of ambient temperature fluctuations, the pressure transducers were submerged into the water bath at least $\frac{3}{4}$ of their height. In addition, pressure transducers were calibrated at the given temperature of the water bath.
- In Mark I of the N₂ solubility apparatus, an air leak was found in the system under vacuum pressure. In Mark II of the N₂ solubility apparatus, we utilised Swagelok VCR components that were able to sustain overpressure and applied vacuum. This pressure stability was confirmed by long-term stability experiments.
- Underestimated N₂ solubility values were obtained due to incomplete degassing of the liquid sample. During the degassing procedure, at least six freeze/thaw cycles were conducted (usually eight). Repeat cycles were performed until the pressure did not change upon applied vacuum (to the frozen sample).
- The internal volume of the apparatus consisted of stainless steel, rather than any high gas-absorbing polymeric based materials (e.g. polymer stem tip valves), which would have led to the gas being partially absorbed.
- Irregular N₂ solubility measurements were obtained due to particulates that were present in the system. After the internal volume of the N₂ solubility apparatus was cleaned and dried, the measured results were the same as previously measured. Additionally, irregular results can also be caused by impurities within the sample.

After resolving these issues associated with the N₂ solubility apparatus, we were able to achieve a stable instrument, capable of high precision measurements. This chapter would be highly

beneficial to a reader who would undertake the construction of a gas solubility apparatus based on the isochoric saturation method.

2.6 Conclusions

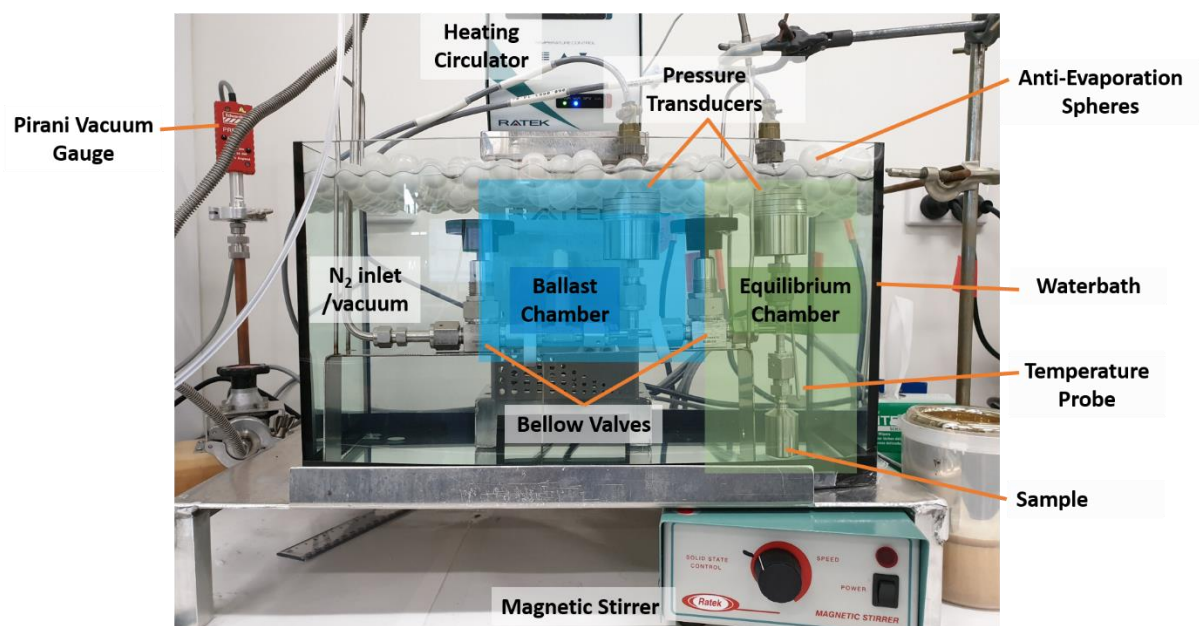
This chapter provided an in-depth discussion and guide to the construction of a custom-designed N₂ solubility apparatus based on the isochoric saturation method. The trends of N₂ solubility in liquids were put into perspective where N₂ solubility was observed to increase slightly with temperature in organic solvents. Mark I of the N₂ solubility apparatus was constructed and control measurements were carried out to determine applicability of the N₂ solubility apparatus. Through this process, numerous requirements were discovered and then utilised for the construction of Mark II of the N₂ solubility apparatus.

Several control protocols were established and final measurements of N₂ solubility were carried out with high precision followed by data verification to literature, where highly satisfactory agreement was achieved despite the inherently low solubility of N₂ in liquids.

A step-by-step process of conducting N₂ solubility measurements, from the degassing of liquid to N₂ absorption, was provided followed by general guidelines and tips for the construction of a N₂ solubility apparatus. This method of measuring N₂ solubility underpins the themes of this dissertation for the investigation of N₂ solubility in fluorinated ILs and their fluorinated co-solvent mixtures.

2.7 Supporting Information

The following supporting information shows additional details of the custom-designed N₂ solubility apparatus that was constructed using Swagelok components and high-precision pressure transducers, as detailed below.



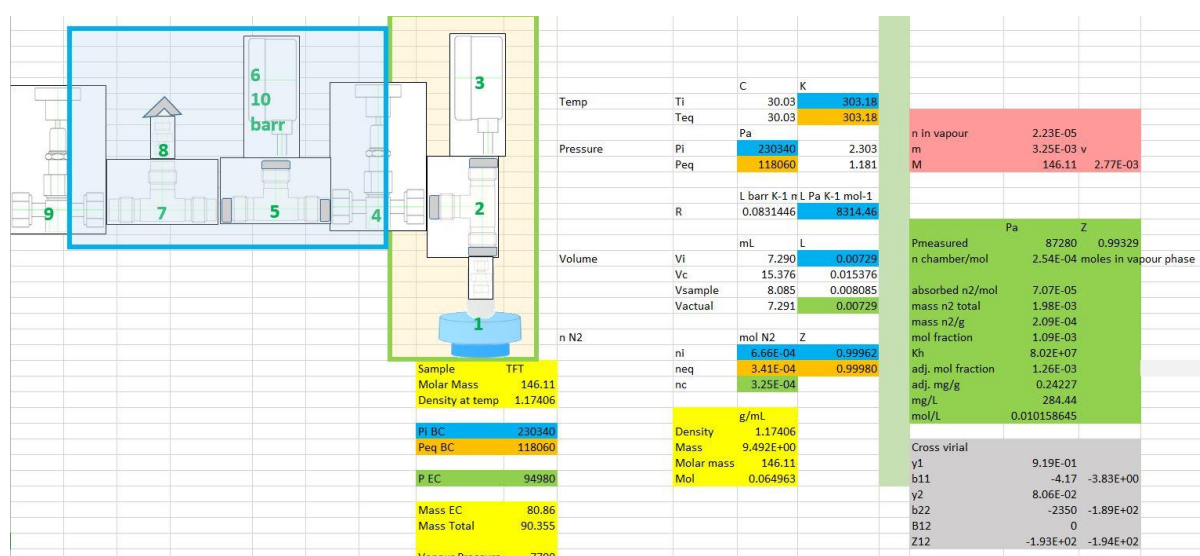
Supporting Figure S1: Photograph of the dual-transducer Mark II of the N_2 solubility apparatus with each component labelled.

Supporting Table S1. Specific Swagelok components used to construct the N_2 solubility apparatus

Swagelok Components	Part Number
316L VAR Welded VCR Face Seal Fitting, Female Tee, 1/4 in. WVCR	6LV-4-WVCR-T-FFF
316 Stainless Steel VCR Face Seal Fitting, 1/4 in. Union Tee	SS-4-VCR-T
Stainless Steel Bellows Sealed Valve, Gasketed, Spherical Stem Tip, 1/4 in.	SS-4BG-VCR
Male Swagelok VCR Face Seal Fitting, SC-11 Cleaned	
316L VAR High Flow VCR Fitting, Tube Butt Weld Body, 1/4 in. HVCR x 3/8 in. TBW, 0.75 in. (19.1 mm) Ext	6LV-4-HVCR-1-6TB7P
316 Stainless Steel Single Ended Miniature Sample Cylinder, 10 cm ³ , 1000 psig (68.9 bar)	SS-4CS-TW-10
316 Stainless Steel Welded VCR Face Seal Fitting, Swagelok Tube Fitting Connector, 1/4 in. WVCR x 1/4 in. Tube Fitting	SS-4-WVCR-6-400
316 Stainless Steel VCR Face Seal Fitting, 1/4 in. Female VCR Coupling Body	SS-4-VCR-CG
316L Stainless Steel VCR Face Seal Fitting, 1/4 in. Silver Plated Gasket, Non-Retained Style	SS-4-VCR-2
316L Stainless Steel VCR Face Seal Fitting, 1/4 in. Silver Plated Snubber Gasket, Non-Retained Style 0.5 Micron	SS-4-VCR-2-.5M
316 Stainless Steel VCR Face Seal Fitting, 1/4 in. Double Male Union Body	SS-4-VCR-6-DM
316 Stainless Steel VCR Face Seal Fitting, Reducing Bushing Body, 1/2 in. VCR x 1/4 in. Female VCR	SS-8-VCR-7-4VCRF
316 Stainless Steel VCR Face Seal Fitting, Socket Weld Gland, 1/2 in. VCR x 1/2 in. Tube Socket	SS-8-VCR-3
316 Stainless Steel VCR Face Seal Fitting, 1/4 in. Cap	SS-4-VCR-CP
316 Stainless Steel VCR Face Seal Fitting, 1/4 in. Plug	SS-4-VCR-P

Supporting Table S2: Specialised equipment used as part of the N₂ solubility apparatus.

Equipment	Brand
Super-TJE Pressure transducers (75, 150 bar)	Honeywell Test & Measurement
Model SC2000 Display	Honeywell Test & Measurement
TH8000 liquid thermostat	Ratek
MS8 Compact Magnetic Stirrer	Ratek
Pirani Vacuum Gauge	Edwards
Anti-Evaporation Spheres	VWR
Waterbath	Yi Ding Bay (Coburg Aquarium)



Supporting Figure S2: Spreadsheet of the calculations involved for calculating the solubility of N₂ in TFT. Yellow = pre-experimental values. Pink = amount of N₂ in headspace. Blue = Initial calculation of N₂. Orange = Calculation of N₂ after admission of gas. Green = After N₂ dissolution calculations. Grey = Values of compressibility factors.

2.8 References

1. P. G. T. Fogg, W. G., *Solubility of Gases in Liquids*; John Wiley & Sons Ltd.: Chichester, 1991; Vol. 63.
2. Weiss, R. F., The Solubility of Nitrogen, Oxygen and Argon in Water and Seawater. *Deep-Sea Res. Oceanogr. Abstr.* **1970**, 17, 721—735.
3. Battino, R.; Rettich, T. R.; Tominaga, T., The Solubility of Nitrogen and Air in Liquids. *J. Phys. Chem. Ref. Data* **1984**, 13, 563—600.
4. Bondar, V. I.; Freeman, B. D.; Pinnau, I., Gas Sorption and Characterization of Poly(Ether-B-Amide) Segmented Block Copolymers. *J. Polym. Sci., Part B: Polym. Phys.* **1999**, 37, 2463—2475.
5. Blath, J.; Christ, M.; Deubler, N.; Hirth, T.; Schiestel, T., Gas Solubilities in Room Temperature Ionic Liquids – Correlation between R_{til}-Molar Mass and Henry's Law Constant. *Chem. Eng. J.* **2011**, 172, 167—176.
6. Bonifácio, R. P.; Costa Gomes, M. F.; Filipe, E. J. M., Solubility of Xenon in N-Hexane between 257 and 333 K. *Fluid Phase Equilib.* **2002**, 193, 41—51.
7. Camper, D.; Scovazzo, P.; Koval, C.; Noble, R., Gas Solubilities in Room-Temperature Ionic Liquids. *Ind. Eng. Chem. Res.* **2004**, 43, 3049—3054.
8. Look, D. C.; Sauer, H. J., Gases. In *Engineering Thermodynamics: Si Edition*, Look, D. C.; Sauer, H. J., Eds. Springer Netherlands: Dordrecht, 1988.

9. Van Wylen, G. J.; Sonntag, R. E., *Fundamentals of Classical Thermodynamics*; John Wiley & Sons: United States of America, 1985.
10. Dymond, J. H., *The Virial Coefficients of Gases: A Critical Compilation*; Clarendon Press: Oxford, 1969; Vol. 2.
11. Peng, D.-Y.; Robinson, D. B., A New Two-Constant Equation of State. *Ind. Eng. Chem. Fundam.* **1976**, *15*, 59—64.
12. Husson-Borg, P.; Majer, V.; Costa Gomes, M. F., Solubilities of Oxygen and Carbon Dioxide in Butyl Methyl Imidazolium Tetrafluoroborate as a Function of Temperature and at Pressures Close to Atmospheric Pressure. *J. Chem. Eng. Data* **2003**, *48*, 480—485.
13. Koros, W. J.; Paul, D. R., Design Considerations for Measurement of Gas Sorption in Polymers by Pressure Decay. *J. Polym. Sci. Pol. Phys.* **1976**, *14*, 1903—1907.
14. Camper, D.; Becker, C.; Koval, C.; Noble, R., Diffusion and Solubility Measurements in Room Temperature Ionic Liquids. *Ind. Eng. Chem. Res.* **2006**, *45*, 445—450.
15. Benedict, R. P., *Fundamentals of Temperature, Pressure, and Flow Measurements*; John Wiley & Sons: United States of America, 1984.
16. Lide, D. R., 2005 Crc Handbook of Chemistry and Physics. CRC Press, New York: 2004.
17. Atkins, P.; dePaula, J., *Physical Chemistry: Thermodynamics, Structure, and Change*; W. H. Freeman and Company: New York, 2014.
18. Peiyi, W.; Little, W. A., Measurement of Friction Factors for the Flow of Gases in Very Fine Channels Used for Microminiature Joule–Thomson Refrigerators. *Cryogenics* **1983**, *23*, 273—277.
19. Hendricks, R. C.; Peller, I. C.; Baron, A. K., *Joule–Thomson Inversion Curves and Related Coefficients for Several Simple Fluids*; National Aeronautics and Space Administration: Washington, 1972.
20. Stevanovic, S.; Costa Gomes, M. F., Solubility of Carbon Dioxide, Nitrous Oxide, Ethane, and Nitrogen in 1-butyl-1-methylpyrrolidinium and Trihexyl(tetradecyl)phosphonium Tris(pentafluoroethyl)trifluorophosphate (eFAP) Ionic Liquids. *J. Chem. Thermodyn.* **2013**, *59*, 65—71.
21. Gjaldbaek, J. C.; Hildebrand, J. H., The Solubility of Nitrogen in Carbon Disulfide, Benzene, Normal- and Cyclo-Hexane, and in Three Fluorocarbons. *J. Am. Chem. Soc.* **1949**, *71*, 3147—3150.
22. Sargent, J. W.; Seffl, R. J., Properties of Perfluorinated Liquids. *Fed. Proc.* **1970**, *29*, 1699—1703.
23. Jabłoniec, A.; Horstmann, S.; Gmehling, J., Experimental Determination and Calculation of Gas Solubility Data for Nitrogen in Different Solvents. *Ind. Eng. Chem. Res.* **2007**, *46*, 4654—4659.
24. Jacquemin, J.; Costa Gomes, M. F.; Husson, P.; Majer, V., Solubility of Carbon Dioxide, Ethane, Methane, Oxygen, Nitrogen, Hydrogen, Argon, and Carbon Monoxide in 1-Butyl-3-Methylimidazolium Tetrafluoroborate between Temperatures 283 K and 343 K and at Pressures Close to Atmospheric. *J. Chem. Thermodyn.* **2006**, *38*, 490—502.
25. Carlisle, T. K.; Bara, J. E.; Gabriel, C. J.; Noble, R. D.; Gin, D. L., Interpretation of CO₂ Solubility and Selectivity in Nitrile-Functionalized Room-Temperature Ionic Liquids Using a Group Contribution Approach. *Ind. Eng. Chem. Res.* **2008**, *47*, 7005—7012.
26. Czichos, H.; Saito, T.; Smith, L., *Springer Handbook of Materials Measurement Methods*; Springer: Germany, 2006; Vol. 978.

Chapter 3: Synthesis and Physicochemical Properties of Fluorinated Ionic Liquids with High Nitrogen Gas Solubility

3.1 Synopsis

As chapter 2 involved the construction of the N₂ solubility apparatus, chapter 3 utilises this instrument to explore the core theme of the N₂ solubility in highly fluorinated ILs. For the application of electrolytes in electrochemical ammonia synthesis, a hypothesis in this thesis explores the effect of increasing the degree of fluorination on the IL in enhancing its N₂ solubility, and can we specifically tailor the synthesis of these fluorinated ILs to do so?


In this publication, a range of fluorinated ILs are synthesised and studied in terms of their N₂ solubility and physicochemical properties. This chapter focusses on phosphonium-based ILs due to their ability to reduce electrostatic interactions and reduce the melting point through their long alkyl chains. Since these ILs are to serve as a liquid electrolyte to conduct ions for the electrochemical nitrogen reduction reaction, they must be electrochemically stable in a wide range of potentials to prevent breakdown during the reaction.

The phosphonium-based ILs that contain the [eFAP]⁻ anion display faster transport properties whereas the ILs that contain perfluorosulfonate and perfluorocarboxylate anions exhibit higher N₂ solubility values. Nevertheless, all of these fluorinated ILs show much higher N₂ solubility compared to water (and standard ILs), where longer perfluoroalkyl chains correlate with a higher dissolution of N₂. Furthermore, a detailed study of the thermal behaviour and transport properties of these ILs is carried out to examine their use as viable electrolytes for the electrochemical NRR.

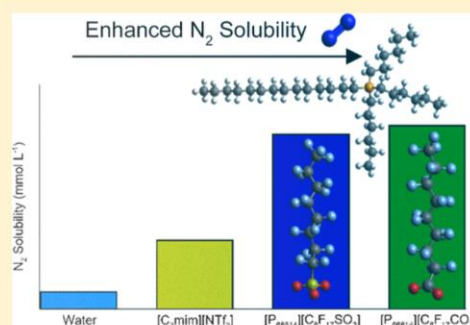
Synthesis and Physicochemical Properties of Fluorinated Ionic Liquids with High Nitrogen Gas Solubility

Colin S. M. Kang,¹ Xinyi Zhang, and Douglas R. MacFarlane*

ARC Centre of Excellence for Electromaterials Science, School of Chemistry, Monash University, Clayton, Victoria 3800, Australia

 Supporting Information

ABSTRACT: Electrosynthesis of ammonia, especially at ambient temperature and pressure, could provide a facile and efficient renewable energy transportation and storage process. However, the nitrogen reduction reaction (NRR) often exhibits low faradaic efficiencies due to (i) the low solubility of nitrogen gas (N_2) in water and (ii) the hydrogen evolution reaction that is prominent in the same range of potentials in aqueous systems. Ionic liquids (ILs) have been shown to overcome these issues to some extent. In this work, we describe the synthesis and characterization of a family of phosphonium-based ILs with highly fluorinated anions, which are shown to display high N_2 solubilities. Their thermal properties were examined, with perfluorosulfonate-based ILs showing high decomposition temperatures in comparison to a low, two-step decomposition process found with perfluorocarboxylate-based ILs. Their transport properties, including viscosity and ionic conductivity, were fitted to the Vogel–Tammann–Fulcher (VTF) equation over a wide temperature range, and the VTF parameters are described. The electrochemical window for all of the synthesized ILs extend past the reduction potentials required for N_2 reduction. Thus, these high N_2 solubility ILs show scope as nonaqueous electrolytes for the electrochemical NRR.



INTRODUCTION

Ammonia is of growing interest as a carbon-free fuel for transporting (and storing) renewable energy and as means of alleviating the intermittency of renewable energy supply. At present, ammonia is produced using fossil fuels by the industrial Haber–Bosch process, generating intense energy requirements and CO_2 emissions.¹ An attractive alternative that is based on renewable energy involves the electrochemical reduction of N_2 to ammonia, especially if it can take place efficiently under ambient conditions.^{2–7} However, recent reports of the electrochemical nitrogen reduction reaction (NRR) require significant improvements in faradaic efficiency (FE), to be a scalable industrial process. The low FE stems from the highly competitive water or proton reduction to hydrogen gas reaction, which is considerably more facile on most electrode materials and occurs in a similar reduction potential range to that of nitrogen reduction. Part of the reason for this stems from the intrinsically low N_2 solubility in water and many other solvents.⁸ By moving away from aqueous media and exploring ionic liquids (ILs) that offer unusually high N_2 solubility,⁹ N_2 availability to the reaction can be enhanced while at the same time suppressing the hydrogen evolution reaction. On this basis, we have recently reported FE values for N_2 reduction of up to 60%, using a stable hydrophobic IL [P₆₆₆₁₄][eFAP].¹⁰

ILs, as electrolyte media, have other advantageous properties in this context, including their nonvolatility, which would allow facile separation of products from the electrolyte, as well as

their chemical and electrochemical stability.¹¹ Mixtures of ILs with aprotic solvents have also been shown to be viable in the NRR.¹² Furthermore, the N_2 solubility and hydrophobicity of these ILs can be tailored to enhance the efficiency of the electrochemical NRR. One approach to IL design to further enhance N_2 solubility is functionalization of one or both of the ions. Gomes et al.¹³ observed up to 50% increase in N_2 solubility by partial fluorination of the octyl-imidazolium cation compared to the nonfluorinated analogue. On the other hand, Noble et al.¹⁴ examined the influence of nitrile functionality on the imidazolium cation and found that the N_2 solubility decreased by approximately 36% and attributed this effect to the polar nature of the nitrile group. Gomes et al.¹³ also explored the influence of the anion and showed a 30% increase in N_2 solubility from [C₈mim][NTf₂] ([NTf₂] is the bis(trifluoromethanesulfonyl)imide ion) to [C₈mim][BETI] ([BETI] is the bis(pentafluoroethanesulfonyl)imide).¹³ Other ILs with low fluorine content were generally found to display lower N_2 solubilities,^{14–21} so it may appear that higher fluorine content leads to high N_2 solubility.

Fluorinated ILs have been investigated for a number of applications, such as lubricants, surfactants, artificial blood substitutes, and biomedical applications; a useful review has been provided by Pereiro and co-workers.²² A number of

Received: August 9, 2018

Revised: October 1, 2018

Published: October 5, 2018

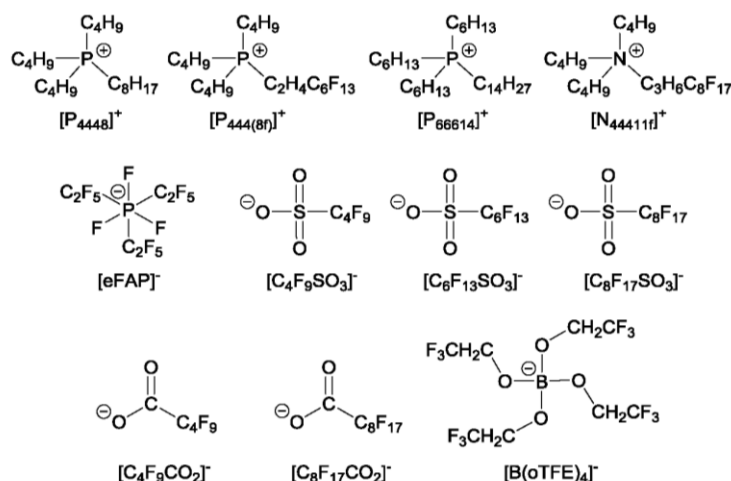


Figure 1. IL structures and acronyms used in this study.

fluorinated ILs have been described,^{23–29} although some tend to form solids upon a large degree of fluorination. However, N₂ solubility studies of these highly fluorinated ILs are relatively limited, and the underlying physicochemical relationships need to be investigated further.^{13,30}

Triolo and co-workers³¹ identified the appearance of “fluorous domains” in some fluorinated ILs. Given the known high N₂ solubility in fluorous solvents such as perfluoroheptane and perfluorotributylamine, we hypothesize that such domains may support high N₂ solubility in such ILs. In this work, we explore a range of novel fluorinated ILs with various fluoroalkyl moieties to investigate the effect of these moieties on N₂ solubility. Herein, we describe the synthesis and characterization of a series of phosphonium-based ILs with fluorinated anions and examine their solubility and transport properties. Initial investigation of electrochemical stability indicates their applicability in the electrochemical NRR.

EXPERIMENTAL SECTION

Materials. The chemical structures and abbreviations of ILs investigated in this work are shown in Figure 1. Potassium nonafluorobutane-sulfonate (98%, Fluka), potassium tridecafluorohexane-sulfonate (>98%, Sigma-Aldrich), potassium heptafluorooctane-sulfonate (>98%, Sigma-Aldrich), nonafluoropentanoic acid (97%, Sigma-Aldrich), heptafluorooctanoic acid (97%, Sigma-Aldrich), tributylphosphine (99%, Sigma-Aldrich), tributyl(octyl)phosphonium chloride (>98%, CYPHOS), trifluoroethanol (>99%, Sigma-Aldrich), *N*-butyl-*N*-methyl-pyrrolidinium bromide (99%, Sigma-Aldrich), tributylamine (99%, Sigma-Aldrich), 3,3,4,4,5,5,6,6,7,7,8,8,8-tridecafluorooctyl iodide (>96%, Sigma-Aldrich), 4,4,5,5,6,6,7,7,8,8,9,9,10,10,11,11,11-heptafluoroundecyl iodide (>97%, Synquest), and 1-butyl-1-methylpyrrolidinium tris(pentafluoroethyl)trifluorophosphate (99%, [C₄mpyr][eFAP], Merck) were used without further purification. Nitrogen gas (99%, Alphagaz) was supplied by Air Liquide. Trihexyltetradecylphosphonium chloride (>95%, [P₆₆₆₁₄][Cl], CYPHOS) was purified with activated charcoal and alumina (basic, Sigma-Aldrich) using dichloromethane as an eluent according to a published procedure.³²

Synthesis. A series of phosphonium-based ILs paired with highly fluorinated anions were synthesized via metathesis

reactions in water and dichloromethane.¹¹ Potassium salts of the desired anion were added with water and dichloromethane, and after several extractions, afford the desired IL. The acid precursors of fluorinated anions were added in the same manner and extracted until a neutral pH was obtained in the water wash. In both procedures, the organic layer was washed with water until the silver nitrate test produced no precipitation, indicating a halide of content <5 ppm. Further details and characterization are included in the [Supporting Information](#).

Characterization. Proton (¹H), fluorine (¹⁹F), and phosphorus (³¹P) NMR spectroscopies were conducted using a Bruker DRX400 spectrometer operating at 400, 376, 162 MHz, respectively. Electrospray ionization mass spectrometry was conducted using a Micromass Platform II QMS instrument (cone voltage, 35 V), with methanol as the solvent. Density measurements were carried out using an Anton Paar DMA 5000 density meter that utilizes the “oscillating U-tube principle”. Viscosity measurements were undertaken on an Anton Paar Lovis 2000 M microviscometer via the falling ball technique. A Hewlett Packard 4284 LCR meter was used to measure conductivity by using alternating current impedance spectroscopy over a range of 0.1 Hz to 10 MHz with a two-electrode platinum wire dip cell, calibrated using a 0.01 mol/L aq KCl solution. By taking the data point closest to the *x* axis on the impedance plot, the resistance was then used to calculate the conductivity.

Thermogravimetric analysis (TGA) was performed using a Mettler Toledo TGA/DSC 1 STARe System over a range of 25–550 °C under N₂ (30 mL/min), at a heating rate of 10 °C/min. Thermogravimetric-infrared (TG-IR) spectroscopy experiments were conducted using PerkinElmer STA8000 and Frontier Fourier transform infrared spectrometer instruments at a heating rate of 10 °C/min. Differential scanning calorimetry (DSC) was performed on a DSC Q100 instrument at 10 °C/min. Water content was measured using a Metrohm 831 KF coulometer.

The electrochemical windows of the ILs, as determined by the onset potentials, were measured using a Princeton Applied Research VMP2 instrument, and the data were analyzed with EC-Lab software (Bio-Logic Science Instruments). Cyclic voltammetry was performed using a three-electrode cell setup:

a glassy carbon disk with 1 mm diameter as the working electrode, coiled platinum (Pt) wire as the counter electrode, and a mixture of silver trifluoromethanesulfonate (10 mM) dissolved in [C₄mpyr][eFAP] as the reference electrode.

Diffusion NMR Measurements. The self-diffusion coefficients of ILs were measured using a pulsed-gradient stimulated echo (PGSTE) pulse sequence. These experiments were performed using a Bruker DRX600 spectrometer for ¹H nuclei exclusive to the cation, and a Bruker DRX400 spectrometer was used for ¹⁹F nuclei contained on the anion. Dimethyl sulfoxide-*d*₆ was used as the external solvent reference, surrounding the inner sample tube to minimize any convection effects. The diffusion coefficient was calculated by fitting data to the Stejskal–Tanner equation³³

$$\ln\left(\frac{S}{S_{g=0}}\right) = -\gamma^2 g^2 D \delta^2 \left(\Delta - \frac{\delta}{3}\right) \quad (1)$$

where *S* is the spin–echo signal intensity, γ is the gyromagnetic ratio of the nucleus being observed, *g* is the strength of the gradient, *D* is the self-diffusion coefficient, δ is the duration of the field gradient, and Δ is the time between two gradient pulses.

The self-diffusion coefficient of Milli-Q water was measured to be 2.3×10^{-9} m²/s at 25 °C, within 1% of the literature value.³⁴ The uncertainty of self-diffusion coefficient measurements is $\pm 5\%$.

N₂ Solubility Measurements. N₂ solubility was measured using a dual-volume apparatus based on the isochoric saturation method, similar to that used by other groups.^{18,35,36} In this method, a ballast chamber (Bc) was used to deliver a known amount of N₂ to the equilibrium chamber (Ec) containing the degassed liquid sample. Once pressure equilibrium was established between the sample and its headspace, the solubility of N₂ can be determined as described below.

Our pressure apparatus, constructed in stainless steel, consists of a ballast chamber (Bc), equilibrium chamber (Ec), and bellow-sealed valves (V₁, V₂) to control the flow of gas between chambers (see Figure S1 in the Supporting Information). The pressure in each chamber that determines the number of moles of N₂ was recorded by Super-TJE pressure transducers (Honeywell Test & Measurement, 0.05% accuracy). The transducers connect to a digital meter and subsequently to the computer where pressure data was processed using Sensocom software.

The internal volumes of the Bc and Ec were measured to be 7.29 ± 0.02 and 15.38 ± 0.02 cm³, respectively. These volumes were obtained by filling and weighing each chamber with methanol (at constant temperature) and using the density to calculate volume; furthermore, these volumes were cross-checked via pressure expansion tests with (and without) nonabsorbing stainless steel balls of known volume. The temperature of the dual-volume apparatus was maintained within a water bath ± 0.04 °C and monitored using an RTD Pt100 probe ± 0.03 °C. Stirring was maintained throughout each experiment to enhance the mass transport of gas into the liquid sample. ILs were degassed by directly applying vacuum (0.5 mbar) overnight to the sample while stirring.

A typical experiment consisted of adding a known volume of sample, between 4 and 9 cm³, to the Ec, which was degassed overnight. The Ec was isolated by closing valve 2 (refer to Figure S1 in the Supporting Information). Then, valve 1 was

opened to allow a desired amount of N₂ into the Bc. After valve 1 was closed and thermal equilibrium was established, the number of moles of N₂ (initial) in Bc was calculated from pressure *P*₁ (using transducer 1). After opening and immediately closing valve 2, the number of moles of N₂ (after) was calculated from pressure *P*₂ (using transducer 1). The number of moles of N₂ admitted to the Ec can then be determined from eq 2, using the second virial coefficient to account for nonideality.³⁷

$$n_{N_2}^{\text{admitted}} = \frac{P_1 V_{Bc}}{RT_1 Z_1} - \frac{P_2 V_{Bc}}{RT_2 Z_2} \quad (2)$$

where *V*_{Bc} is the volume of Bc, *R* is the universal gas constant, *T* is the temperature at any point of measurement, and *Z* is the compressibility factor of N₂ at a given temperature and pressure.

Once equilibrium with the liquid sample was attained, the number of moles of N₂ in the headspace of the Ec can be determined from pressure *P*₃ (using transducer 2) using eq 3.

$$n_{N_2}^{\text{headspace Ec}} = \frac{P_3 (V_{Ec} - V_{\text{sample}})}{RT_3 Z_3} \quad (3)$$

where *V*_{Ec} is the volume of Ec, and *V*_{sample} is the volume of IL sample. The difference between the number of moles that entered the Ec and the number of moles of N₂ in the headspace allows calculation of the solubility of N₂ in the sample (eq 4).

$$n_{N_2}^{\text{absorbed}} = n_{N_2}^{\text{admitted}} - n_{N_2}^{\text{headspace Ec}} \quad (4)$$

The solubility of N₂ in IL at the obtained equilibrium pressure can then be expressed as a molar concentration value *C*_{N₂} (calculated via the known density), mole fraction χ_2 value, Henry's law constant *K*_H, or the molal concentration value *b*_{N₂}. See Tables S1 and S2 in the Supporting Information for further information.

RESULTS AND DISCUSSION

Thermal Properties. The thermal properties of the synthesized fluorinated ILs are shown in Table 1. To enhance the N₂ solubility, a range of highly fluorinated anions are

Table 1. Thermal Properties of Fluorinated ILs Investigated in This Study^a

fluorinated IL	<i>T</i> _g (°C)	<i>T</i> _{ss} (°C)	<i>T</i> _m (°C)	<i>T</i> _{dec} (°C)
[P ₄₄₄₈][eFAP]	−82			299
[P _{444(8f)}][eFAP]	−72			257
[P ₆₆₆₁₄][eFAP] ⁴⁰	−85		−71	353
[P ₆₆₆₁₄][C ₄ F ₉ SO ₃] ⁴¹	−78			416
[P ₆₆₆₁₄][C ₆ F ₁₃ SO ₃]	−74	−61		410
[P ₆₆₆₁₄][C ₈ F ₁₇ SO ₃] ⁴²	−61	−32	−19	415
[P ₆₆₆₁₄][C ₄ F ₉ CO ₂] ⁴³	−80			151
[P ₆₆₆₁₄][C ₈ F ₁₇ CO ₂]	−71			154
[C ₄ mpyr][C ₈ F ₁₇ SO ₃] ⁴⁴	−68		102	397
[C ₄ mpyr][B(oTFE) ₄]			119	204
[P ₆₆₆₁₄][B(oTFE) ₄]			15 ^b	200
[N _{444(11f)}][C ₄ F ₉ SO ₃]	−22		65 ^{b,c}	314

^aReferences therein indicate prior synthesis. ^bForms a waxy solid upon cooling to room temperature. ^cDid not crystallize after initial melt.

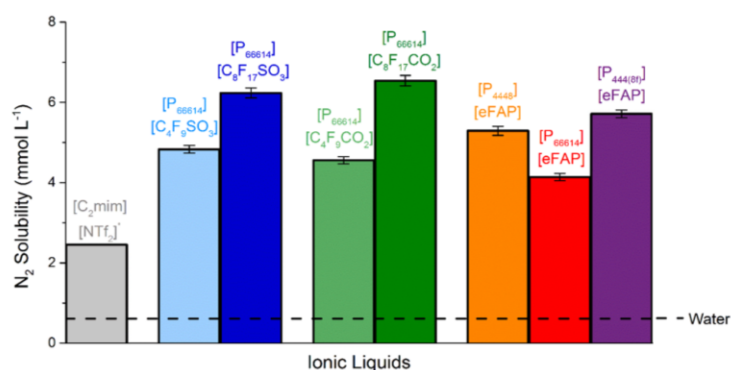


Figure 2. N₂ solubilities of fluorinated ILs at 30 °C and $P = 1$ atm, expressed as molar concentration (mmol/L). Data for water⁸ and [C₂mim][NTf₂]¹⁴ (at 25 °C) are shown for comparison.

chosen on the basis of the hypothesis that $-\text{CF}_2-$ functionality supports N₂ dissolution.¹³ These anions are paired with large tetraalkylphosphonium cations to maintain liquid state since a high degree of fluorination on both the cation and anion tend to form solids at room temperature.²² As a result, most of these salts are liquid at room temperature with the exception of some waxy solids and some high-melting [C₄mpyr]⁺-based solids. The glass-transition temperature of the ILs varies depending on their anion, where tris(pentafluoroethyl)trifluorophosphate ([eFAP][−])-based ILs tend to show slightly lower T_g values. This suggests that a smaller amount of energy is required for diffusion and rotation of the [eFAP][−] anion at lower temperatures; this may also reflect a lower total cohesive energy within these ILs due to charge delocalization within the [eFAP][−] anion.³⁸ ILs that contain long perfluorosulfonate anions, such as [P₆₆₆₁₄][C₈F₁₃SO₃][−] and [P₆₆₆₁₄][C₈F₁₇SO₃][−], show an additional DSC transition below melting that is often associated with solid–solid transitions. Interestingly, such solid–solid transitions were not observed with long perfluorocarboxylate anions. This difference may be attributed to the increase in conformational flexibility with perfluorosulfonate anions, not only from extending the linear perfluoroalkyl chain, but also from changing a carboxylate group to a sulfonate group (i.e., trigonal planar compared to tetrahedral geometry).³⁹ Comparing the cations, changing the alkyl chain length on the phosphonium cation from [P₆₆₆₁₄][eFAP] to [P₄₄₄₈][eFAP] does not appear to change the T_g significantly. On the other hand, [P_{444(8f)}][eFAP] displays a more positive T_g by ~ 10 °C than [P₄₄₄₈][eFAP], which shows the effect of a more rigid fluoroalkyl chain compared to a simple alkyl chain.

The decomposition temperature as determined by TGA experiments on the phosphonium-based ILs is usually highly dependent on the IL anion. The perfluorosulfonate-based ILs show high thermal stabilities, up to 416 °C, with no apparent effect in increasing perfluoroalkyl chain length. On the other hand, the perfluorocarboxylate-based ILs show relatively low thermal stabilities with a two-step decomposition process that begins at ~ 150 °C. Further investigation using TG-IR spectroscopy shows decomposition of the perfluorocarboxylate anion in the first step, evident from the CO₂ and C–F signals at 2400 and 1200 cm^{−1}, respectively (Figure S2). The second decomposition step shows C–H peaks found at ~ 2900 cm^{−1}, consistent with the breakdown of the phosphonium cation. Typically, phosphonium-based ILs with nonfluorinated carboxylate anions show a single decomposition step from

250 °C onward.⁴⁵ It is interesting to note that perfluorosulfonate anions, although similar to perfluorocarboxylate anions, exhibit a single decomposition step above 400 °C, which highlights the differing reactivity of the $-\text{SO}_3^-$ and $-\text{CO}_2^-$ functionalities of the anion.

N₂ Solubility. Data Validation. It is critical to benchmark the solubility data for N₂ due to its intrinsic low solubility;³⁹ this makes N₂ solubility difficult to measure accurately compared to other gases.^{14,15,21,46} For example, both Gomes et al.⁹ and Blath et al.¹⁹ measured the solubility of CO₂ and N₂ in [P₆₆₆₁₄][eFAP] at 60 °C, where it was found that the obtained Henry's law constants of CO₂ are in much closer agreement between the two laboratories than comparable data for N₂. Therefore, we compared data from our apparatus to literature data for a range of different solvents, including hexane, perfluoroheptane, perfluorotributylamine, and ILs [C₄mim][BF₄][−] and [C₄mim][NTf₂][−] (see Table S1 in the Supporting Information). In addition, repeated measurements to establish the precision of our solubility data indicated repeatability to better than 2%. The N₂ solubility data for the solvents in Table S1 display agreement with literature data within 4%, which is satisfactory given the precision of the measurements. The agreement for the ILs is within 19%, which likely reflects greater variation in IL sample purity across different laboratories.

N₂ Solubility of Fluorinated ILs. The N₂ solubilities for the fluorinated ILs prepared in this work are presented in Figure 2 and Table S2 in the Supporting Information. Although it is common to report gas solubility in terms of Henry's law constant K_H or mole fraction χ_2 , electrochemical current density is typically dependent on the molar concentration of dissolved species.⁴⁷ Hence, solubility data are reported in this unit system in Figure 2.

Gas solubility is typically a result of (i) physical mixing of the molecules, reflecting the thermodynamics of transferring a gas molecule into the liquid solvent and to some extent the availability of unoccupied or “free” volume in the solvent and (ii) interaction effects between the gas molecule and the solvent molecules or parts of them. Therefore, the range of IL structures synthesized here allows some discussion of the nature of N₂ dissolution in these ILs. N₂ tends to be of very low solubility in many solvents because of its nonpolar, strongly internally bonded, low polarizability nature that results in very weak interactions with other molecules. Thus, the highest solubilities for N₂ tend to be exhibited by solvents that

can be characterized as displaying only weak van der Waals intermolecular interactions (e.g., the perfluorocarbons listed in Table S1 in the Supporting Information). Indeed, all of the highly fluorinated ILs in Figure 2 display higher N_2 solubilities compared to common ILs, as shown in Table S3 in the Supporting Information, such as $[C_2mim][NTf_2]$ (2.5 mmol/L at 25 °C)¹⁴ and $[C_2mim][OTf]$ (2.0 mmol/L at 40 °C).⁴⁸

Focusing on comparisons on a molar concentration basis, $[P_{4448}][eFAP]$ was found to dissolve a higher concentration of N_2 than $[P_{66614}][eFAP]$ (see Figure 2). Thus, significantly extending the length of the alkyl chains seems to disfavor N_2 dissolution. This may be the result of van der Waals interactions between long alkyl chains that tend to increase cohesive energy density in these regions and thereby decrease free volume⁴⁹ or increase the energy required to create cavities for gas dissolution. Further studies of varied alkyl chain lengths on the phosphonium cation would be useful in elucidating this trend.

Comparing ILs of the phosphonium cation and its fluorinated analogue ($[P_{444(8f)}][eFAP]$ vs $[P_{4448}][eFAP]$) shows only a slight increase in N_2 solubility with the fluorinated cation, as found by other groups with CO_2 solubility when they incorporate a fluorinated chain onto an imidazolium cation.^{30,50} On the other hand, the series of perfluorosulfonate-based ILs show an increase in N_2 solubility compared to the $[eFAP]^-$ -based ILs, and also with increasing perfluoroalkyl chain length. For example, extending this chain on the anion from $[C_4F_9SO_3]^-$ to $[C_8F_{17}SO_3]^-$ produces a 29% increase in N_2 solubility. This trend is also observed with the perfluorocarboxylate-based ILs, which suggests a similar change in interactions related to the perfluoroalkyl chain length. Triolo and co-workers³¹ observed the formation of distinct fluorine domains in ILs with a high degree of fluorination, and these domains may represent favorable sites for N_2 dissolution. Gomes et al.⁵¹ also pointed to an effect of rigidity of the fluoroalkyl chain increasing overall free volume. The nanostructure of the IL (e.g., the appearance of fluorine domains) may also have an effect on its ionicity, as discussed further below.

Transport Properties. Viscosity. Figure 3 shows an Arrhenius plot of viscosity for the fluorinated ILs prepared in

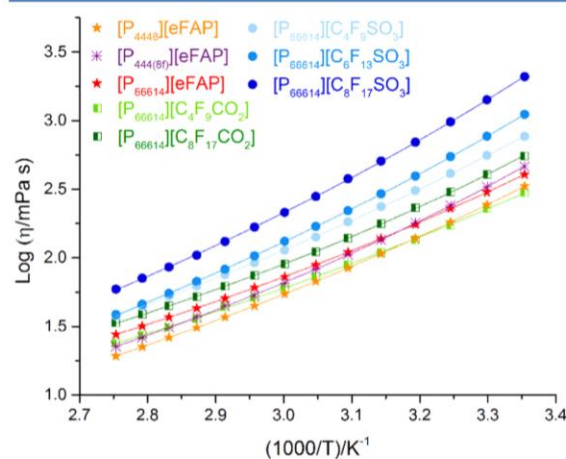


Figure 3. Arrhenius plot of viscosity vs inverse absolute temperature for the fluorinated ILs in this study.

this study. The viscosity of $[P_{66614}][eFAP]$, obtained by Fernández et al.,⁵² was found to be 347 mPa s at 25 °C, within error of our measured value of 375 mPa s at 25 °C. Examining the effect of extending the perfluoroalkyl chain length, an increase from a perfluorobutyl to a perfluorooctyl alkyl chain produces an almost 3-fold increase in viscosity (~ 2.7 times increase from $[P_{66614}][C_4F_9SO_3]$ to $[P_{66614}][C_8F_{17}SO_3]$ at 25 °C); this is probably due to decreased motional freedom with the larger molecule. However, the effect of extending the phosphonium cation alkyl chains from $[P_{4448}]^+$ to $[P_{66614}]^+$, when paired with the $[eFAP]^-$ anion, does not impact the viscosity as much. For example, there is only $\sim 12\%$ increase in viscosity (333–375 mPa s respectively at 25 °C). Fluorination of a cation side chain in $[P_{444(8f)}][eFAP]$ produces a 40% increase in viscosity (465 mPa s at 25 °C) compared to the nonfluorinated analogue $[P_{4448}][eFAP]$, suggesting increased frictional forces when a fluoroalkyl chain is present on the cation.

Additionally, the type of anion in the IL significantly affects its viscosity. $[P_{66614}][C_8F_{17}SO_3]$ is ~ 5 times more viscous than $[P_{66614}][eFAP]$ (2090 and 375 mPa s, respectively, at 25 °C), which may highlight the effect of anion geometry on its viscosity (a linear rodlike anion compared to an approximately spherical anion). Interestingly, $[P_{66614}][C_4F_9SO_3]$ is ~ 2.5 times more viscous than the perfluorocarboxylate analogue $[P_{66614}][C_4F_9CO_2]$, showing the influence of the SO_3^- and CO_2^- anions, and their differences in molecular geometry and electron-withdrawing nature. In addition, the temperature dependence is well described by the Vogel–Tammann–Fulcher (VTF) equation⁵³ (eq 5) with fitted parameters shown in Table S4 in the Supporting Information.

$$\eta = \eta_0 \exp \left[\frac{B_\eta}{T - T_0} \right] \quad (5)$$

Here, η_0 is the viscosity at infinite temperature (in mPa s), B_η is the pseudoactivation energy that is related to the energy required for ions to move past each other (K), and T_0 is the ideal glass-transition temperature (in K). The pseudoactivation energy B_η was found to increase with different classes of anions in the order of perfluorosulfonates > perfluorocarboxylates > $[eFAP]^-$. This suggests that ILs with perfluorosulfonate anions require a larger amount of energy to diffuse past each other, and this is related to their inherently high viscosities. The ideal glass-transition T_0 values appear to correlate well with the glass transitions of the ILs, typically lying 10–45 K below T_g .

Ionic Conductivity. Ionic conductivity plays a significant role in electrochemical applications, particularly for the NRR. The Arrhenius plot of ionic conductivity for the fluorinated ILs is shown in Figure 4. The perfluorosulfonate-based ILs display the lowest conductivities, as expected from their high viscosities. The $[eFAP]^-$ -based ILs display higher ionic conductivities than perfluorocarboxylates, despite their similar viscosities; this shows an influence from other effects, as discussed further below. As expected, $[P_{4448}][eFAP]$, with a smaller phosphonium cation, displays a higher ionic conductivity than $[P_{66614}][eFAP]$. While the ionic conductivity of $[P_{444(8f)}][eFAP]$ is slightly larger than $[P_{66614}][eFAP]$ at 25 °C, this difference becomes increasingly larger at higher temperatures. The temperature dependencies are well described by eq 6, where the fitted parameters are shown in Table S5 in the Supporting Information.

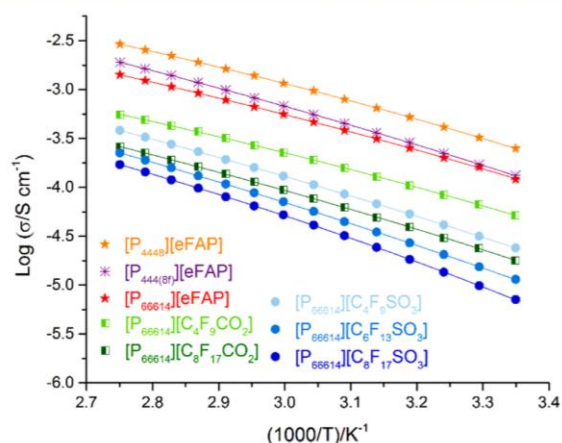


Figure 4. Arrhenius plot of ionic conductivity vs inverse absolute temperature for the fluorinated ILs in this study.

$$\sigma = \sigma_0 \exp \left[\frac{-B_\sigma}{T - T_0} \right] \quad (6)$$

Here, σ_0 is the ionic conductivity at infinite temperature (S/cm) and B_σ is the pseudoactivation energy that is related to the critical free volume for ion transport (K).

Walden Plot, Self-Diffusion Coefficients, and Ionicity. The Walden plot of the transport data is shown in Figure 5, which

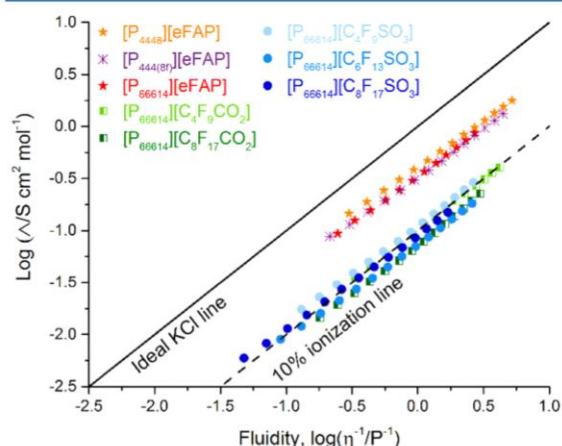


Figure 5. Walden plot of the fluorinated ILs in this study.

combines the density (see Figure S3 in the Supporting Information), viscosity, and conductivity to show the relationship between molar conductivity (Λ) and fluidity ($1/\eta$) and to qualitatively assess the ionicity of the ILs.⁵⁴ This relationship, as described by Angell et al.,⁵⁵ compares the data to an ideal reference electrolyte of aq KCl (0.01 mol/L), where ions are considered to be completely dissociated. ILs that lie within an order of magnitude, as denoted by the 10% ionization line, are generally classed as “good” ILs.

While ILs containing the $[eFAP]^-$ anion fall within this region, ILs with perfluorosulfonate and perfluorocarboxylate anions lie similarly close to the 10% ionization line. ILs based on the large phosphonium cations are often observed to sit near or below this line.⁵⁶ The perfluoroalkyl chain on the anions here may support the formation of fluorous domains. Such domains will hinder the independent movement of cations and anions and thus may result in a low ionicity for the perfluorocarboxylate- and perfluorosulfonate-based ILs.

As the Walden plot is only a qualitative approach to assessing ionicity, a more quantitative approach was adopted by measuring the self-diffusion coefficients of these ILs.⁵⁷ Using PGSTE NMR, the self-diffusion coefficients were measured via 1H and ^{19}F nuclei to differentiate between the cation and anion, respectively. As expected from the trends of conductivity and viscosity, $[eFAP]^-$ anions display larger self-diffusion coefficients, followed by the perfluorocarboxylate and perfluorosulfonate anions (see Table 2). For the perfluorocarboxylate- and perfluorosulfonate-based ILs, extending the perfluoroalkyl chain length on the anion produces a decrease in the self-diffusion coefficients of both the cation and anion in all cases, as expected from the viscosity and conductivity data.

The ionicity values are determined⁵⁸ by calculating the molar conductivity ratio $\Lambda_{imp}/\Lambda_{NMR}$ where Λ_{imp} is the molar conductivity obtained experimentally from impedance measurements of ionic conductivity and Λ_{NMR} is the molar conductivity calculated using the self-diffusion coefficients of the cation and anion ($D_{cation} + D_{anion}$) via the Nernst–Einstein equation

$$\Lambda_{NMR} = \frac{F^2(D_{cation} + D_{anion})}{RT} \quad (7)$$

where F is the Faraday constant and R is the universal gas constant.

This equation assumes that all diffusive motions contribute to the molar conductivity, whereas Λ_{imp} only reflects the response of charged species to an electric field. Therefore, any ratio less than unity can indicate that there are some diffusing species present, e.g., ion pairs or neutral aggregates, which are

Table 2. Self-Diffusion Coefficients (m^2/s) and the Degree of Ionicity ($\Lambda_{imp}/\Lambda_{NMR}$) for the Fluorinated ILs in This Study at 25 °C

fluorinated IL	D_{cation} ($10^{-12} m^2/s \pm 5\%$)	D_{anion} ($10^{-12} m^2/s \pm 5\%$)	$\Lambda_{imp}/\Lambda_{NMR} \pm 10\%$
$[P_{444}][eFAP]$	2.4	2.6	0.79
$[P_{444(8f)}][eFAP]$	1.8	1.7	0.67
$[P_{666}][eFAP]$	2.2	2.2	0.56
$[P_{666}][C_4F_9SO_3]$	1.1	0.87	0.23
$[P_{666}][C_6F_{13}SO_3]$	0.83	0.50	0.18
$[P_{666}][C_8F_{17}SO_3]$	0.47	0.30 ^a	0.21
$[P_{666}][C_4F_9CO_2]$	2.5	1.8	0.22
$[P_{666}][C_8F_{17}CO_2]$	1.2	0.87	0.19

^aData point was extrapolated from five temperature points.

not contributing to Λ_{imp} on the time scale of the measurement.⁵⁹ This provides a measure of the “ionicity” of the IL.⁶⁰

All of the fluorinated ILs in this work display ionicity values less than 1 (see Table 2), as usually observed for ILs due to their strong cation–anion interactions. Both the perfluorosulfonate- and perfluorocarboxylate-based ILs were found to have similarly low ionicity values, suggesting similar interactions with the $[P_{66614}]^+$ cation. As discussed above, highly fluorinated anions that contain perfluoroalkyl chain lengths greater than 4 can form fluorine domains within the IL³¹ (or at least create more ordering of fluorine counterparts), and this is likely to result in low ionicity values due to the ion–ion correlations that such domains represent.

Examination of the cation effect shows a significant rise in ionicity with $[P_{4448}][\text{eFAP}]$ compared to $[P_{66614}][\text{eFAP}]$, which reflects the increased ion aggregation with the larger phosphonium cation.⁵⁶ The influence of a fluoroalkyl chain on the cation of $[P_{444(8f)}][\text{eFAP}]$, compared to $[P_{4448}][\text{eFAP}]$, results in lower self-diffusion coefficients and a corresponding decrease in ionicity (i.e., $\sim 3/4$ of the nonfluorinated analogue). Again, this may arise from associations between the fluoroalkyl chain on the cation and the perfluorinated anion.

Electrochemical Stability. The electrochemical limits of stability of the fluorinated ILs were examined to determine their stability in the electric potential range, in which the NRR would usually be conducted, i.e., between -0.5 and -1.5 V versus Ag/Ag^+ . Electrochemical stabilities for the neat ILs are shown in Table 3, and cyclic voltammograms are shown in

Table 3. Anodic and Cathodic Limiting Potentials (vs Ag/Ag^+) and the Electrochemical Potential Ranges of Fluorinated ILs Investigated in This Study

fluorinated IL	E cathodic (V)	E anodic (V)	ΔE total (V)
$[P_{4448}][\text{eFAP}]$	-3.2	0.6	3.8
$[P_{444(8f)}][\text{eFAP}]$	-2.4	-0.2	2.6
$[P_{66614}][\text{eFAP}]$	-3.2	0.8	4.0
$[P_{66614}][\text{C}_8\text{F}_9\text{SO}_3]$	-3.8	1.1	4.9
$[P_{66614}][\text{C}_6\text{F}_{13}\text{SO}_3]$	-3.8	1.2	5.0
$[P_{66614}][\text{C}_8\text{F}_{17}\text{SO}_3]$	-3.7	1.4	5.1
$[P_{66614}][\text{C}_4\text{F}_9\text{CO}_2]$	-3.1	0.6	3.7
$[P_{66614}][\text{C}_8\text{F}_{17}\text{CO}_2]$	-3.0	0.8	3.8

Figure S4 in the Supporting Information. The perfluorosulfonate-based ILs display the highest electrochemical stabilities with a potential range of up to -3.7 to $+1.4$ V versus Ag/Ag^+ in $[P_{66614}][\text{C}_8\text{F}_{17}\text{SO}_3]$. Perfluorocarboxylate-based ILs show reduced stability, with both reductive and oxidative limits lower than that of perfluorosulfonate-based ILs. This reflects both the stronger electron-withdrawing nature of the perfluorosulfonate functionality and the more facile reductive chemistry of the carboxylate group.

As expected, incorporating an electron-withdrawing fluoroalkyl chain into the phosphonium cation significantly decreases the reductive stability such that $[P_{444(8f)}][\text{eFAP}]$ displays a reductive onset at -2.4 V versus Ag/Ag^+ compared to the onset of -3.2 V versus Ag/Ag^+ for $[P_{4448}][\text{eFAP}]$. On the other hand, the oxidative limit around -0.2 V versus Ag/Ag^+ for $[P_{444(8f)}][\text{eFAP}]$ compared to the nonfluorinated analogue is unexpectedly low since this limit is usually associated with the anion. This is the subject of further

investigation in our laboratories as to the chemical nature of this process.

These studies indicate that all of the fluorinated ILs are sufficiently reductively stable to be viable media in which to carry out the NRR. However, the reduced oxidative stability of the $[P_{444(8f)}]^+$ cation indicates that such structures may not represent a fruitful direction in further developing ILs for this purpose. Detailed NRR studies of these ILs are underway and will be reported in a future publication.

CONCLUSIONS

A series of phosphonium-based ILs with highly fluorinated anions were synthesized and studied in terms of their physicochemical properties. The N_2 solubility of these FILs have been measured using the isochoric saturation technique. Although there are difficulties associated with measuring N_2 solubility, due to its inherently low solubility in liquids, comparisons conducted across a range of solvents and ILs show satisfactory agreement to literature data. All of these fluorinated ILs display high N_2 solubility, whereby increasing the perfluoroalkyl chain on the anion produces an increase in N_2 solubility. The highest N_2 solubility observed was 6.5 mmol/L in $[P_{66614}][\text{C}_8\text{F}_{17}\text{CO}_2]$. The perfluorocarboxylate- and perfluorosulfonate-based ILs tend to also exhibit low ionicity. Introduction of a fluorine chain into the $[P_{4448}]^+$ cation was also found to slightly increase N_2 solubility and lower ionicity. The perfluorosulfonate-based ILs show high thermal stability, whereas the perfluorocarboxylate-based ILs undergo a two-step thermal decomposition process at relatively low temperatures.

All of the fluorinated ILs in this study display sufficient electrochemical stability within the reduction potential range for the electrochemical NRR. Thus, this study exemplifies a number of new ILs that offer high N_2 solubility and illustrates their potential in the context of the electrochemical NRR, either as pure IL electrolytes or mixed aprotic solvents.

ASSOCIATED CONTENT

Supporting Information

The Supporting Information is available free of charge on the ACS Publications website at DOI: 10.1021/acs.jpcc.8b07752.

Synthesis and characterization of ionic liquids, N_2 solubility schematic, thermogravimetric-infrared spectrum, density plot, additional N_2 solubility data and comparison to the literature, VTF fitting parameters of viscosity and conductivity, and electrochemical potential ranges (PDF)

AUTHOR INFORMATION

Corresponding Author

*E-mail: douglas.macfarlane@monash.edu. Tel: +61 3 9905 4540.

ORCID

Colin S. M. Kang: 0000-0002-7697-3330

Author Contributions

C.S.M.K. carried out all of the experiments. All authors contributed to the writing of the manuscript.

Notes

The authors declare no competing financial interest.

■ ACKNOWLEDGMENTS

C.S.M.K. acknowledges the Australian Postgraduate Award for funding, and Prof. D.R.M. acknowledges the ARC for funding through Discovery Project DP170102267 and his Australian Laureate Fellowship (FL120100019). Additionally, the authors thank Prof. Benny D. Freeman and his research group for their help and guidance in constructing the N₂ solubility apparatus.

■ REFERENCES

- (1) Smil, V. Global Population and the Nitrogen Cycle. *Sci. Am.* **1997**, *1*, 76–81.
- (2) Lan, R.; Irvine, J. T. S.; Tao, S. Synthesis of Ammonia Directly from Air and Water at Ambient Temperature and Pressure. *Sci. Rep.* **2013**, *3*, No. 1145.
- (3) Guo, C.; Ran, J.; Vasileff, A.; Qiao, S.-Z. Rational Design of Electrocatalysts and Photo(Electro)Catalysts for Nitrogen Reduction to Ammonia (NH₃) under Ambient Conditions. *Energy Environ. Sci.* **2018**, *11*, 45–56.
- (4) Zhang, L.; Ji, X.; Ren, X.; Ma, Y.; Shi, X.; Tian, Z.; Asiri, A. M.; Chen, L.; Tang, B.; Sun, X. Electrochemical Ammonia Synthesis Via Nitrogen Reduction Reaction on a MoS₂ Catalyst: Theoretical and Experimental Studies. *Adv. Mater.* **2018**, No. 1800191.
- (5) Cao, N.; Zheng, G. Aqueous Electrocatalytic N₂ Reduction under Ambient Conditions. *Nano Res.* **2018**, *11*, 2992–3008.
- (6) Manjunatha, R.; Schechter, A. Electrochemical Synthesis of Ammonia Using Ruthenium–Platinum Alloy at Ambient Pressure and Low Temperature. *Electrochem. Commun.* **2018**, *90*, 96–100.
- (7) Deng, J.; Iniguez, J. A.; Liu, C. Electrocatalytic Nitrogen Reduction at Low Temperature. *Joule* **2018**, *2*, 846–856.
- (8) Battino, R.; Rettich, T. R.; Tominaga, T. The Solubility of Nitrogen and Air in Liquids. *J. Phys. Chem. Ref. Data* **1984**, *13*, 563–600.
- (9) Stevanovic, S.; Gomes, M. F. C. Solubility of Carbon Dioxide, Nitrous Oxide, Ethane, and Nitrogen in 1-Butyl-1-Methylpyrrolidinium and Trihexyl(Tetradecyl)Phosphonium Tris(Pentafluoroethyl)-Trifluorophosphate (eFAP) Ionic Liquids. *J. Chem. Thermodyn.* **2013**, *59*, 65–71.
- (10) Zhou, F.; Azofra, L. M.; Ali, M.; Kar, M.; Simonov, A. N.; McDonnell-Worth, C.; Sun, C.; Zhang, X.; MacFarlane, D. R. Electro-Synthesis of Ammonia from Nitrogen at Ambient Temperature and Pressure in Ionic Liquids. *Energy Environ. Sci.* **2017**, *10*, 2516–2520.
- (11) Welton, T. Room-Temperature Ionic Liquids. Solvents for Synthesis and Catalysis. *Chem. Rev.* **1999**, *99*, 2071–2084.
- (12) Suryanto, B. H.; Kang, C. S.; Wang, D.; Xiao, C.; Zhou, F.; Azofra, L. M.; Cavallo, L.; Zhang, X.; MacFarlane, D. R. Rational Electrode–Electrolyte Design for Efficient Ammonia Electrosynthesis under Ambient Conditions. *ACS Energy Lett.* **2018**, *3*, 1219–1224.
- (13) Almantariotis, D.; Pensado, A. S.; Gunaratne, H. Q. N.; Hardacre, C.; Pádua, A. A. H.; Coxam, J. Y.; Gomes, M. F. C. Influence of Fluorination on the Solubilities of Carbon Dioxide, Ethane, and Nitrogen in 1-N-Fluoro-Alkyl-3-Methylimidazolium Bis(N-Fluoroalkylsulfonyl)Amide Ionic Liquids. *J. Phys. Chem. B* **2017**, *121*, 426–436.
- (14) Carlisle, T. K.; Bara, J. E.; Gabriel, C. J.; Noble, R. D.; Gin, D. L. Interpretation of CO₂ Solubility and Selectivity in Nitrile-Functionalized Room-Temperature Ionic Liquids Using a Group Contribution Approach. *Ind. Eng. Chem. Res.* **2008**, *47*, 7005–7012.
- (15) Anderson, J. L.; Dixon, J. K.; Brennecke, J. F. Solubility of CO₂, CH₄, C₂H₆, C₃H₈, O₂, and N₂ in 1-Hexyl-3-Methylpyridinium Bis(Trifluoromethylsulfonyl)Imide: Comparison to Other Ionic Liquids. *Acc. Chem. Res.* **2007**, *40*, 1208–1216.
- (16) Seo, S.; DeSilva, M. A.; Xia, H.; Brennecke, J. F. Effect of Cation on Physical Properties and CO₂ Solubility for Phosphonium-Based Ionic Liquids with 2-Cyanopyrrolide Anions. *J. Phys. Chem. B* **2015**, *119*, 11807–11814.
- (17) Jacquemin, J.; Husson, P.; Majer, V.; Gomes, M. F. C. Low-Pressure Solubilities and Thermodynamics of Solvation of Eight Gases in 1-Butyl-3-Methylimidazolium Hexafluorophosphate. *Fluid Phase Equilib.* **2006**, *240*, 87–95.
- (18) Jacquemin, J.; Gomes, M. F. C.; Husson, P.; Majer, V. Solubility of Carbon Dioxide, Ethane, Methane, Oxygen, Nitrogen, Hydrogen, Argon, and Carbon Monoxide in 1-Butyl-3-Methylimidazolium Tetrafluoroborate between Temperatures 283 K and 343 K and at Pressures Close to Atmospheric. *J. Chem. Thermodyn.* **2006**, *38*, 490–502.
- (19) Blath, J.; Christ, M.; Deubler, N.; Hirth, T.; Schiestel, T. Gas Solubilities in Room Temperature Based Ionic Liquids – Correlation between Rtil-Molar Mass and Henry's Law Constant. *Chem. Eng. J.* **2011**, *172*, 167–176.
- (20) Anthony, J. L.; Maginn, E. J.; Brennecke, J. F. Solubilities and Thermodynamic Properties of Gases in the Ionic Liquid 1-N-Butyl-3-Methylimidazolium Hexafluorophosphate. *J. Phys. Chem. B* **2002**, *106*, 7315–7320.
- (21) Blath, J.; Deubler, N.; Hirth, T.; Schiestel, T. Chemisorption of Carbon Dioxide in Imidazolium Based Ionic Liquids with Carboxylic Anions. *Chem. Eng. J.* **2012**, *181–182*, 152–158.
- (22) Pereira, A. B.; Araújo, J. M. M.; Martinho, S.; Alves, F.; Nunes, S.; Matias, A.; Duarte, C. M. M.; Rebelo, L. P. N.; Marrucho, I. M. Fluorinated Ionic Liquids: Properties and Applications. *ACS Sustainable Chem. Eng.* **2013**, *1*, 427–439.
- (23) Tindale, J. J.; Na, C.; Jennings, M. C.; Ragogna, P. J. Synthesis and Characterization of Fluorinated Phosphonium Ionic Liquids. *Can. J. Chem.* **2007**, *85*, 660–667.
- (24) Merrigan, T. L.; Bates, E. D.; Dorman, S. C.; Davis, J. H., Jr. New Fluorous Ionic Liquids Function as Surfactants in Conventional Room-Temperature Ionic Liquids. *Chem. Commun.* **2000**, 2051–2052.
- (25) Tsukada, Y.; Iwamoto, K.; Furutani, H.; Matsushita, Y.; Abe, Y.; Matsumoto, K.; Monda, K.; Hayase, S.; Kawatsura, M.; Itoh, T. Preparation of Novel Hydrophobic Fluorine-Substituted-Alkyl Sulfate Ionic Liquids and Application as an Efficient Reaction Medium for Lipase-Catalyzed Reaction. *Tetrahedron Lett.* **2006**, *47*, 1801–1804.
- (26) Xue, H.; Verma, R.; Shreeve, J. M. Review of Ionic Liquids with Fluorine-Containing Anions. *J. Fluorine Chem.* **2006**, *127*, 159–176.
- (27) Lo Celso, F.; Pibiri, I.; Triolo, A.; Triolo, R.; Pace, A.; Buscemi, S.; Vivona, N. Study on the Thermotropic Properties of Highly Fluorinated 1,2,4-Oxadiazolylpyridinium Salts and Their Perspective Applications as Ionic Liquid Crystals. *J. Mater. Chem.* **2007**, *17*, 1201–1208.
- (28) Linder, T.; Sundermeyer, J. Three Novel Anions Based on Pentafluorophenyl Amine Combined with Two New Synthetic Strategies for the Synthesis of Highly Lipophilic Ionic Liquids. *Chem. Commun.* **2009**, 2914–2916.
- (29) Gladysz, J. A.; Emnet, C. Fluorous Solvents and Related Media. *Handbook of Fluorous Chemistry*; Wiley-VCH Verlag GmbH & Co. KGaA, 2005; pp 11–23.
- (30) Almantariotis, D.; Gefflaut, T.; Pádua, A. A. H.; Coxam, J. Y.; Gomes, M. F. C. Effect of Fluorination and Size of the Alkyl Side-Chain on the Solubility of Carbon Dioxide in 1-Alkyl-3-Methylimidazolium Bis(Trifluoromethylsulfonyl)Amide Ionic Liquids. *J. Phys. Chem. B* **2010**, *114*, 3608–3617.
- (31) Lo Celso, F.; Yoshida, Y.; Castiglione, F.; Ferro, M.; Mele, A.; Jaffa, C. J.; Triolo, A.; Russina, O. Direct Experimental Observation of Mesoscopic Fluorous Domains in Fluorinated Room Temperature Ionic Liquids. *Phys. Chem. Chem. Phys.* **2017**, *19*, 13101–13110.
- (32) Earle, M. J.; Gordon, C. M.; Plechkova, N. V.; Seddon, K. R.; Welton, T. Decolorization of Ionic Liquids for Spectroscopy. *Anal. Chem.* **2007**, *79*, 758–764.
- (33) Stejskal, E. O.; Tanner, J. E. Spin Diffusion Measurements: Spin Echoes in the Presence of a Time-Dependent Field Gradient. *J. Chem. Phys.* **1965**, *42*, 288–292.
- (34) Holz, M.; Heil, S. R.; Sacco, A. Temperature-Dependent Self-Diffusion Coefficients of Water and Six Selected Molecular Liquids for Calibration in Accurate 1h Nmr Pfg Measurements. *Phys. Chem. Chem. Phys.* **2000**, *2*, 4740–4742.

- (35) Bondar, V. I.; Freeman, B. D.; Pinnau, I. Gas Sorption and Characterization of Poly(Ether-B-Amide) Segmented Block Copolymers. *J. Polym. Sci., Part B: Polym. Phys.* **1999**, *37*, 2463–2475.
- (36) Camper, D.; Scovazzo, P.; Koval, C.; Noble, R. Gas Solubilities in Room-Temperature Ionic Liquids. *Ind. Eng. Chem. Res.* **2004**, *43*, 3049–3054.
- (37) Dymond, J. H. *The Virial Coefficients of Gases: A Critical Compilation*; Clarendon Press, 1969; Vol. 2.
- (38) MacFarlane, D. R.; Kar, M.; Pringle, J. M. *Fundamentals of Ionic Liquids: From Chemistry to Applications*; John Wiley & Sons, 2017.
- (39) Wasserscheid, P.; Welton, T. *Ionic Liquids in Synthesis*; John Wiley & Sons, 2008.
- (40) Ignat'ev, N. V.; Welz-Biermann, U.; Kucheryna, A.; Bissky, G.; Willner, H. New Ionic Liquids with Tris(Perfluoroalkyl)-Trifluorophosphate (Fap) Anions. *J. Fluorine Chem.* **2005**, *126*, 1150–1159.
- (41) Del Sesto, R. E.; Corley, C.; Robertson, A.; Wilkes, J. S. Tetraalkylphosphonium-Based Ionic Liquids. *J. Organomet. Chem.* **2005**, *690*, 2536–2542.
- (42) MacFarlane, D.; Zhang, X.; Zhou, F.; McDonnell-Worth, C. J.; Kang, C. S. M.; Kar, M. Method and Cell for Conversion of Dinitrogen into Ammonia. WO20171327212017.
- (43) Zhao, H.; Baker, G. A.; Wagle, D. V.; Ravula, S.; Zhang, Q. Tuning Task-Specific Ionic Liquids for the Extractive Desulfurization of Liquid Fuel. *ACS Sustainable Chem. Eng.* **2016**, *4*, 4771–4780.
- (44) Lueckmann, M.; Schuster, R. H.; Dehnke, V.; Rosenplaenter, A. Effects of Ionic Liquids on Fluorinated Rubber. *Kautsch. Gummi Kunstst.* **2012**, *65*, 26–32.
- (45) Oster, K.; Goodrich, P.; Jacquemin, J.; Hardacre, C.; Ribeiro, A. P. C.; Elsinawi, A. A New Insight into Pure and Water-Saturated Quaternary Phosphonium-Based Carboxylate Ionic Liquids: Density, Heat Capacity, Ionic Conductivity, Thermogravimetric Analysis, Thermal Conductivity and Viscosity. *J. Chem. Thermodyn.* **2018**, *121*, 97–111.
- (46) Finotello, A.; Bara, J. E.; Camper, D.; Noble, R. D. Room-Temperature Ionic Liquids: Temperature Dependence of Gas Solubility Selectivity. *Ind. Eng. Chem. Res.* **2008**, *47*, 3453–3459.
- (47) Bard, A. J.; Faulkner, L. R.; Leddy, J.; Zoski, C. G. *Electrochemical Methods: Fundamentals and Applications*; Wiley: New York, 1980; Vol. 2.
- (48) Camper, D.; Bara, J.; Koval, C.; Noble, R. Bulk-Fluid Solubility and Membrane Feasibility of Rmim-Based Room-Temperature Ionic Liquids. *Ind. Eng. Chem. Res.* **2006**, *45*, 6279–6283.
- (49) Shannon, M. S.; Tedstone, J. M.; Danielsen, S. P. O.; Bara, J. E. Evaluation of Alkylimidazoles as Physical Solvents for CO₂/CH₄ Separation. *Ind. Eng. Chem. Res.* **2012**, *51*, 515–522.
- (50) Muldoon, M. J.; Aki, S. N. V. K.; Anderson, J. L.; Dixon, J. K.; Brennecke, J. F. Improving Carbon Dioxide Solubility in Ionic Liquids. *J. Phys. Chem. B* **2007**, *111*, 9001–9009.
- (51) Dias, A. M. A.; Bonifacio, R. P.; Marrucho, I. M.; Padua, A. A. H.; Gomes, M. F. C. Solubility of Oxygen in N-Hexane and in N-Perfluorohexane. Experimental Determination and Prediction by Molecular Simulation. *Phys. Chem. Chem. Phys.* **2003**, *5*, 543–549.
- (52) Gaciño, F. M.; Regueira, T.; Lugo, L.; Comuñas, M. J. P.; Fernández, J. Influence of Molecular Structure on Densities and Viscosities of Several Ionic Liquids. *J. Chem. Eng. Data* **2011**, *56*, 4984–4999.
- (53) Vogel, H. The Law of the Relation between the Viscosity of Liquids and the Temperature. *Phys. Z.* **1921**, *22*, 645–646.
- (54) Walden, P. Organic Solutions and Ionisation Means. III. Chapter: Internal Friction and Its Connection with Conductivity. *Z. Phys. Chem.* **1906**, *55*, 207–249.
- (55) Yoshizawa, M.; Xu, W.; Angell, C. A. Ionic Liquids by Proton Transfer: Vapor Pressure, Conductivity, and the Relevance of Δp_{ka} from Aqueous Solutions. *J. Am. Chem. Soc.* **2003**, *125*, 15411–15419.
- (56) Fraser, K. J.; Izgorodina, E. I.; Forsyth, M.; Scott, J. L.; MacFarlane, D. R. Liquids Intermediate between “Molecular” and “Ionic” Liquids: Liquid Ion Pairs? *Chem. Commun.* **2007**, 3817–3819.
- (57) Damodaran, K. Recent NMR Studies of Ionic Liquids. *Annual Reports on NMR Spectroscopy*; Academic Press, 2016; Vol. 88, pp 215–244.
- (58) Ueno, K.; Tokuda, H.; Watanabe, M. Ionicity in Ionic Liquids: Correlation with Ionic Structure and Physicochemical Properties. *Phys. Chem. Chem. Phys.* **2010**, *12*, 1649–1658.
- (59) Tokuda, H.; Tsuzuki, S.; Susan, M. A. B. H.; Hayamizu, K.; Watanabe, M. How Ionic Are Room-Temperature Ionic Liquids? An Indicator of the Physicochemical Properties. *J. Phys. Chem. B* **2006**, *110*, 19593–19600.
- (60) Noda, A.; Hayamizu, K.; Watanabe, M. Pulsed-Gradient Spin-Echo ¹H and ¹⁹F NMR Ionic Diffusion Coefficient, Viscosity, and Ionic Conductivity of Non-Chloroaluminate Room-Temperature Ionic Liquids. *J. Phys. Chem. B* **2001**, *105*, 4603–4610.

Synthesis and Physicochemical Properties of Fluorinated Ionic Liquids with High Nitrogen Gas Solubility

*Colin S. M. Kang, Xinyi Zhang and Douglas R. MacFarlane**

ARC Centre of Excellence for Electromaterials Science, School of Chemistry, Monash
University, Clayton, Victoria 3800, Australia

SUPPORTING INFORMATION

1. Synthesis and characterisation

Trihexyltetradecylphosphonium nonafluorobutanesulfonate [P₆₆₆₁₄][C₄F₉SO₃]

¹H NMR (400 MHz, CDCl₃) δppm: 0.84-0.88 (12H, t), 1.25 (20H, m), 1.29-1.32 (12H, m), 1.46-1.52 (16H, m), 2.17-2.24 (8H, m). ¹⁹F NMR (376 MHz, CDCl₃) δppm: -81.0-(-80.9) (3F, m), -114.7-(-114.6) (2F, t), -121.6-(-121.5) (2F, m), -126.0-(-125.9) (2F, t). ³¹P NMR (162 MHz, CDCl₃) δppm: 32.7 (1P, s). ES-MS: ES+ m/z 483 P₆₆₆₁₄⁺, ES- m/z 299 C₄F₉SO₃⁻

Water content after 48 hours vacuum: 37 ppm

Trihexyltetradecylphosphonium tridecafluorohexanesulfonate [P₆₆₆₁₄][C₆F₁₃SO₃]

¹H NMR (400 MHz, CDCl₃) δppm: 0.87-0.92 (12H, t), 1.25 (20H, m), 1.29-1.35 (12H, m), 1.43-1.56 (16H, m), 2.16-2.26 (8H, m). ¹⁹F NMR (376 MHz, CDCl₃) δppm: -81.4-(-81.3) (3F, t), -115.0-(-114.9) (2F, t), -121.1-(-121.0) (2F, m), -122.3-(-122.2) (2F, m), -123.3 (2F, m), -126.7-(-126.6) (2F, m). ³¹P NMR (162 MHz, CDCl₃) δppm: 32.7 (1P, s). ES-MS: ES+ m/z 483 P₆₆₆₁₄⁺, ES- m/z 399 C₆F₁₃SO₃⁻.

Water content after 48 hours vacuum: 19 ppm

Trihexyltetradecylphosphonium heptadecafluorooctanesulfonate [P₆₆₆₁₄][C₈F₁₇SO₃]

¹H NMR (400 MHz, CDCl₃) δppm: 0.86-0.91 (12H, t), 1.25 (20H, m), 1.29-1.33 (12H, m), 1.45-1.55 (16H, m), 2.17-2.25 (8H, m). ¹⁹F NMR (376 MHz, CDCl₃) δppm: -80.8-(-80.7) (3F, m), -114.5-(-114.4) (2F, t), -120.6-(-120.5) (2F, m), -121.6-(-121.5) (2F, m), -122.0-(-121.7) (4F, m), -122.8-(-122.6) (2F, m), -126.1-(-126.0) (2F, m). ³¹P NMR (162 MHz, CDCl₃) δppm: 32.7 (1P, s). ES-MS: ES+ m/z 483 P₆₆₆₁₄⁺, ES- m/z 499 C₈F₁₇SO₃⁻

Water content after 48 hours vacuum: 17 ppm

Trihexyltetradecylphosphonium nonafluoropentanoate [P₆₆₆₁₄][C₄F₉CO₂]

¹H NMR (400 MHz, CDCl₃) δppm: 0.85-0.93 (12H, t), 1.25 (20H, m), 1.27-1.35 (12H, m), 1.39-1.55 (16H, m), 2.12-2.24 (8H, m). ¹⁹F NMR (376 MHz, CDCl₃) δppm: -81.5 (3F, m), -115.1 (2F, t), -122.0 (2F, m), -126.5 (2F, t). ³¹P NMR (162 MHz, CDCl₃) δppm: 33.0 (1P, s). ES-MS: ES+ m/z 483 P₆₆₆₁₄⁺, ES- m/z 263 C₅F₉O₂⁻, 219 C₄F₉⁻.

Water content after 48 hours vacuum: 211 ppm

Trihexyltetradecylphosphonium heptadecafluorononanoate [P₆₆₆₁₄][C₈F₁₇CO₂]

¹H NMR (400 MHz, CDCl₃) δppm: 0.85-0.92 (12H, t), 1.25 (20H, m), 1.28-1.35 (12H, m), 1.42-1.56 (16H, m), 2.26-2.36 (8H, m). ¹⁹F NMR (376 MHz, CDCl₃) δppm: -81.3 (3F, t), -116.7 (2F, t), -122.1 (2F, m), -122.4 (4F, m), -122.6 (2F, m), -123.2 (2F, m), -126.6 (2F, m). ³¹P NMR (162 MHz, CDCl₃) δppm: 33.0 (1P, s). ES-MS: ES+ m/z 483 P₆₆₆₁₄⁺, ES- m/z 463 C₈F₁₇CO₂⁻, 419 C₈F₁₇⁻, 269 C₅F₁₁⁻, 219 C₄F₉⁻, 169 C₃F₇⁻.

Water content after 48 hours vacuum: 148 ppm

Tributyloctylphosphonium tris(pentafluoroethyl)trifluorophosphate [P₄₄₄₈][eFAP]

¹H NMR (400 MHz, CDCl₃) δppm: 0.86-0.89 (3H, t), 0.95-0.99 (9H, t), 1.27-1.31 (8H, m), 1.48-1.54 (16H, m), 2.16-2.25 (8H, m). ¹⁹F NMR (376 MHz, CDCl₃) δppm: -46.5-(-44.9) (1F, m), -80.8-(-80.5) (3F, m), -82.34-(-81.2) (6F, m), -87.4-(-87.2) (F, m), -89.8-(-89.6) (F, m), -116.6-(-116.0) (6F, m). ³¹P NMR (162 MHz, CDCl₃) δppm: 33.0 (1P, s), -155.8-(-137.4) (1P, (q)m). ES-MS: ES+ m/z 483 P₆₆₆₁₄⁺, ES- m/z 445 eFAP⁻

Water content after 48 hours vacuum: 26 ppm

Tributyl-(3,3,4,4,5,5,6,6,7,7,8,8,8-tridecafluorooctyl)-phosphonium tris(perfluoroethyl)trifluorophosphate [P_{444(8f)}][eFAP]

[P_{444(8f)}][I] was synthesised according to published literature.¹⁶⁰ Briefly, 1H,1H,2H,2H-Perfluorooctyl iodide was added to tributylphosphine and stirred under N₂ for 72 hours. Any residual starting material was removed in vacuo at 40°C. 1-(2-Methoxyethyl)-1-methylpyrrolidinium tris(pentafluoroethyl)trifluorophosphate was added to [P_{444(8f)}][I] in water and dichloromethane (DCM), and after purification, afforded a light yellow liquid.

¹H NMR (400 MHz, CDCl₃) δppm: 0.86-1.01 (9H, t), 1.36-1.56 (12H, m), 1.63-1.71 (2H, m), 1.98-2.40 (8H, m). ¹⁹F NMR (376 MHz, CDCl₃) δppm: [P_{444(8f)}]⁺ -80.4 (3F, m), -113.9 (2F, m), -121.8 (2F, m), -122.4 (4F, m), -122.7 (2F, m), -125.9 (2F, m). [eFAP]⁻ -43.5-(-45.0) (1F, m, PF), -79.6 (3F, m), -81.1 (6F, m), -88.7-(-86.2) (2F, m), -113.8 (4F, m), -115.7 (2F, m). ³¹P NMR (162 MHz, CDCl₃) δppm: 33.0 (1P, s), -155.9-(-138.0) (1P, (q)m). ES-MS: ES⁺ m/z 483 P₆₆₆₁₄⁺, ES⁻ m/z 445 eFAP⁻.

Trihexyltetradecylphosphonium tris(pentafluoroethyl)trifluorophosphate [P₆₆₆₁₄][eFAP]

¹H NMR (400 MHz, CDCl₃) δppm: 0.86-0.92 (12H, t), 1.26 (20H, m), 1.29-1.33 (12H, m), 1.45-1.49 (16H, m), 1.98-2.04 (8H, m). ¹⁹F NMR (376 MHz, CDCl₃) δppm: -44.0-(-46.4) (1F, m, PF), -80.7-(-80.5) (3F, m), -81.3-(-81.2) (6F, m), -87.4-(-87.2) (F, m), -89.8-(-89.6) (F, m), -116.5-(-115.9) (6F, m). ³¹P NMR (162 MHz, CDCl₃) δppm: 32.9 (1P, s), -156.5-(-138.0) (1P, (q)m). ES-MS: ES⁺ m/z 483 P₆₆₆₁₄⁺, ES⁻ m/z 445 eFAP⁻.

Water content after 48 hours vacuum: 13 ppm

N-butyl-N-methyl-pyrrolidinium heptadecafluorooctanesulfonate [C₄mpyr][C₈F₁₇SO₃]

¹H NMR (400 MHz, (CD₃)₂SO) δppm: 0.86-0.91 (3H, m), 1.26-1.35 (2H, m), 1.63-1.70 (2H, m), 2.05-2.09, (4H, m), 2.95 (3H, s), 3.24-3.28 (2H, m), 3.58-3.59 (4H, m). ¹⁹F NMR (376 MHz, (CD₃)₂SO) δppm: -80.2-(-80.1) (2F, t), -114.6-(-114.5) (2F, t), -114.6-(-114.5) (2F, t), -120.5-(-120.4) (2F, m), -121.5-(-121.4) (2F, m), -121.7-(-121.5) (4F, m), -122.5-(-122.3) (2F, m), -125.7-(-125.6) (3F, t). ES-MS: ES⁺ m/z 142 C₄mpyr⁺, ES⁻ m/z 499 C₈F₁₇SO₃⁻.

Trihexyltetradecylphosphonium tetrakis(2,2,2-trifluoroethoxy)borate [P₆₆₆₁₄][B(oTfE)₄]

[Na][B(oTfE)₄] was synthesised according to published literature.¹⁵³ Briefly, NaBH₄ was added to dimethoxyethane and toluene. Trifluoroethanol was added dropwise over one hour under an acetone/dry ice bath and then heated to reflux overnight under N₂. After purification, afforded a white powder. [Na][B(oTfE)₄] was added to trihexyltetradecylphosphonium chloride and dry acetonitrile. The reaction mixture was stirred for 72 hr. Acetonitrile was removed in vacuo and DCM was added to the white solid and allowed to stir for 1 hr. The white solid was filtered under N₂ and dried in vacuo to afford an opaque waxy solid.

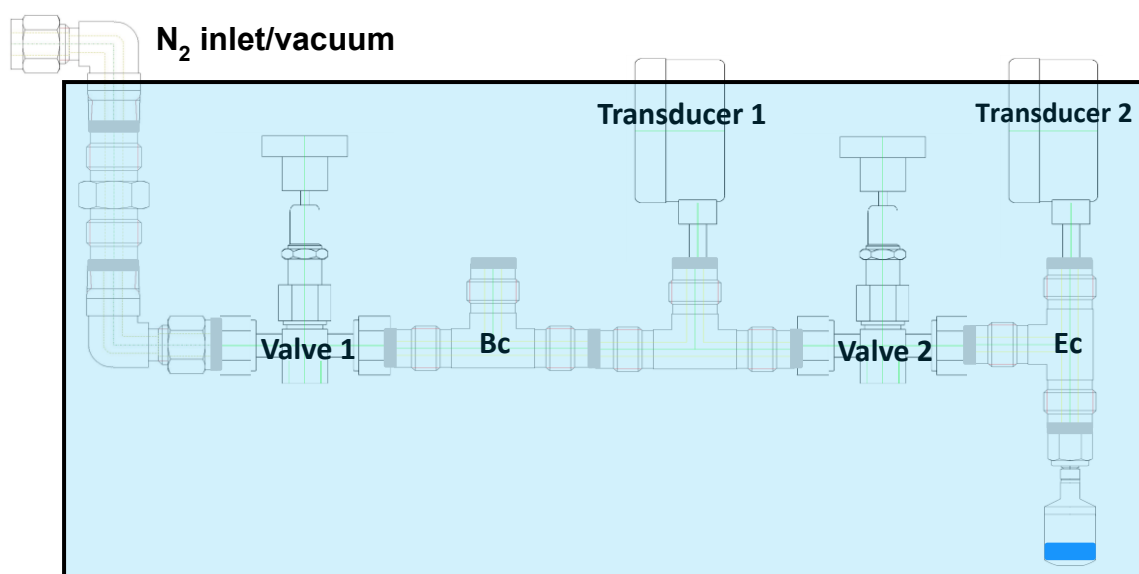
¹H NMR (400 MHz, CDCl₃) δppm: [P₆₆₆₁₄]⁺ 0.85-0.93 (12H, t), 1.26 (20H, m), 1.29-1.35 (12H, m), 1.41-1.55 (16H, m), 2.17-2.29 (8H, m). [B(oTfE)₄]⁻ 3.71-3.86, (8H, m). ¹⁹F NMR (376 MHz, CDCl₃) δppm: -77.0 (12F, t). ¹¹B NMR (128 MHz, CD₃CN) δppm: 2.28 (1B, m). ES-MS: ES⁺ m/z 483 P₆₆₆₁₄⁺, ES⁻ anion not observed.

Tributyl (4,4,5,5,6,6,7,7,8,8,9,9,10,10,11,11,11-heptadecafluoroundecyl)-ammonium nonafluorobutanesulfonate [N_{444(11f)}][C₄F₉SO₃]

[N_{444(11f)}][I] was synthesised according to published literature.¹⁶³ Briefly, 4,4,5,5,6,6,7,7,8,8,9,9,10,10,11,11,11-heptadecafluoroundecyl iodide was added to tributylamine and acetonitrile and stirred under N₂. The mixture was heated to reflux overnight. After washing with hexane and drying in vacuo, afforded a white solid. [N_{444(11f)}][I] was added to potassium nonafluorobutanesulfonate, water and DCM, and after purification afforded a white cream solid.

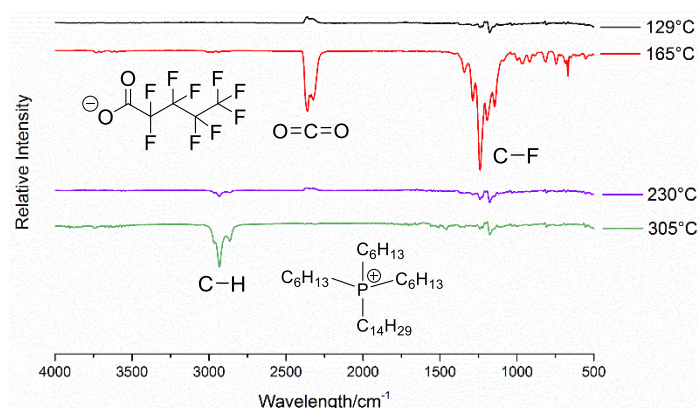
^1H NMR (400 MHz, CDCl_3) δ ppm: 0.96-1.05 (9H, t), 1.39-1.48 (6H, m), 1.63-1.71 (6H, m), 1.97-2.08 (2H, p), 2.25-2.40 (2H, (t)t), 3.19-3.30 (6H, m), 3.46-3.54 (2H, m). ^{19}F NMR (376 MHz, CDCl_3) δ ppm: $[\text{N}_{444(11\text{f})}]^+$ -81.1 (3F, t), -113.6 (2F, t), -121.7 (2F, m) -121.9 (4F, m), -122.7 (2F, m), -123.4 (2F, m), -126.1 (2F, m). $[\text{C}_4\text{F}_9\text{SO}_3]^-$ -80.8 (3F, t), -114.7 (2F, m), -121.7 (2F, m), -126.1 (2F, m). ES-MS: ES+ m/z 646 $[\text{N}_{444(11\text{f})}]^+$, ES- m/z 299 $\text{C}_4\text{F}_9\text{SO}_3^-$

2. N_2 Solubility Apparatus

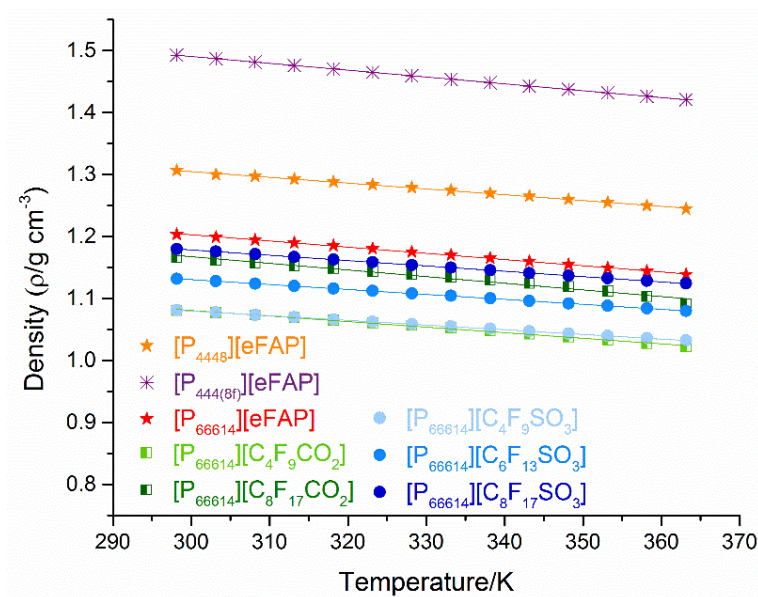


Supporting Figure S1: Schematic of N_2 solubility apparatus: Valve 1, Valve 2, Bc Ballast chamber, Ec Equilibrium chamber are all contained within a thermostated water bath, and connected to a N_2 inlet, vacuum pump, and gauge. Schematic drawings are obtained from swagelok.com

3. Thermal and Physical Properties



Supporting Figure S2: Thermogravimetric-Infrared spectrum showing the decomposition process of $[\text{P}_{66614}][\text{C}_4\text{F}_9\text{CO}_2]$ at increasing temperature



Supporting Figure S3: Plot of density versus temperature for the fluorinated ionic liquids used in this study

Supporting Table S1: Comparison with N_2 solubility literature data, expressed in mole fraction χ_2 and molar concentration C_{N_2} , for various solvents/ILs at 30°C.

Sample	Measured χ_2 / 10^{-3} $\pm 2\%$	Literature χ_2 / 10^{-3}	% deviation /%	C_{N_2} /mmol L $^{-1}$ $\pm 2\%$
Hexane	1.4(2)	1.39 ¹⁰¹	+2.2	10.7
Perfluoroheptane	4.0(4)	3.88 ¹⁰⁷	+3.9	17.9
Perfluorotributylamine	4.2(3)	4.17 ¹⁹⁸	+1.5	11.8
[C ₄ mim][BF ₄]	0.5(0)	0.57 ¹¹³	-12.6	2.6(3)
[C ₄ mim][NTf ₂]	1.2(4) ^b	1.04 ^{112,b}	+19.0	4.2(2)
[P ₆₆₆₁₄][eFAP]	3.2(0)	$\sim 3^c$	-	4.1(4)

^aAll data is adjusted to a partial pressure of $p = 1$ atm

^bConducted at 40°C

^c N_2 solubility for [P₆₆₆₁₄][eFAP], measured by Blath et al.¹⁸⁶ at 333K was adjusted to 303 K by using the enthalpy of solvation of [P₆₆₆₁₄][eFAP]¹⁹⁷ in the following equation:²⁰⁰

$$\Delta_{\text{sol}}H^\infty = -RT^2 \frac{\partial}{\partial T} \left[\ln \left(\frac{K_H}{p^0} \right) \right] \quad (1)$$

Where $\Delta_{\text{sol}}H^\infty$ is the enthalpy of solvation, T is the temperature, R is the universal gas constant, K_H is the Henry's law constant and p^0 is the standard state pressure.

Supporting Table S2: Experimental values of N_2 solubility in fluorinated ILs at 30°C, adjusted to a partial pressure of $p = 1$ atm, expressed as mole fraction (χ_2), Henry's law constant K_H , molar concentration C_{N_2} and molal concentration b_{N_2} . p_{eq} is the experimental equilibrium pressure and ρ is the density used to calculate N_2 solubility.

Fluorinated IL	p_{eq} / 10^4 Pa	ρ /g cm $^{-3}$	χ_2 / 10^{-3} $\pm 2\%$	K_H / 10^7 Pa $\pm 2\%$	C_{N_2} /mmol L $^{-1}$ $\pm 2\%$	b_{N_2} /mmol kg $^{-1}$ $\pm 2\%$
[P ₄₄₄₈][eFAP]	8.34	1.3021	3.1	3.3	5.3	4.1

[P ₄₄₄ (8f)][eFAP]	10.34	1.4873	3.8	2.7	5.7	3.8
[P ₆₆₆ 14][eFAP]	9.64	1.1991	3.2	3.2	4.1	3.5
[P ₆₆₆ 14][C ₄ F ₉ SO ₃]	9.93	1.1653	3.5	2.9	4.8	4.5
[P ₆₆₆ 14][C ₆ F ₁₃ SO ₃]	9.69	1.1280	4.5	2.2	5.8	5.2
[P ₆₆₆ 14][C ₈ F ₁₇ SO ₃]	9.70	1.1760	5.2	2.0	6.2	5.3
[P ₆₆₆ 14][C ₄ F ₉ CO ₂]	10.69	1.0770	3.2	3.2	4.6	4.2
[P ₆₆₆ 14][C ₈ F ₁₇ CO ₂]	9.35	1.1620	4.5	2.2	6.5	5.6

Supporting Table S3: Literature N₂ solubility values expressed as molar concentration, C_{N_2} of some common ILs at the indicated temperature, T .

IL	T /K	C_{N_2} /mmol L ⁻¹
[C ₂ mim][NTf ₂] ¹¹²	298	2.5
[C ₂ mim][OTf] ¹¹⁵	313	2.0
[C ₂ mim][DCA] ¹¹⁵	313	1.3
[C ₁ mim][MeSO ₄] ²⁰¹	298	0.4
[hmpy][NTf ₂] ¹¹⁷	298	0.9
[C ₂ mim][OAc] ¹¹⁶	333	1.7
[C ₄ mim][OAc] ¹¹⁶	333	1.9
[HC-C ₁ mim][NTf ₂] ¹¹²	313	2.5

Supporting Table S4: VTF fitting parameters for viscosity data.

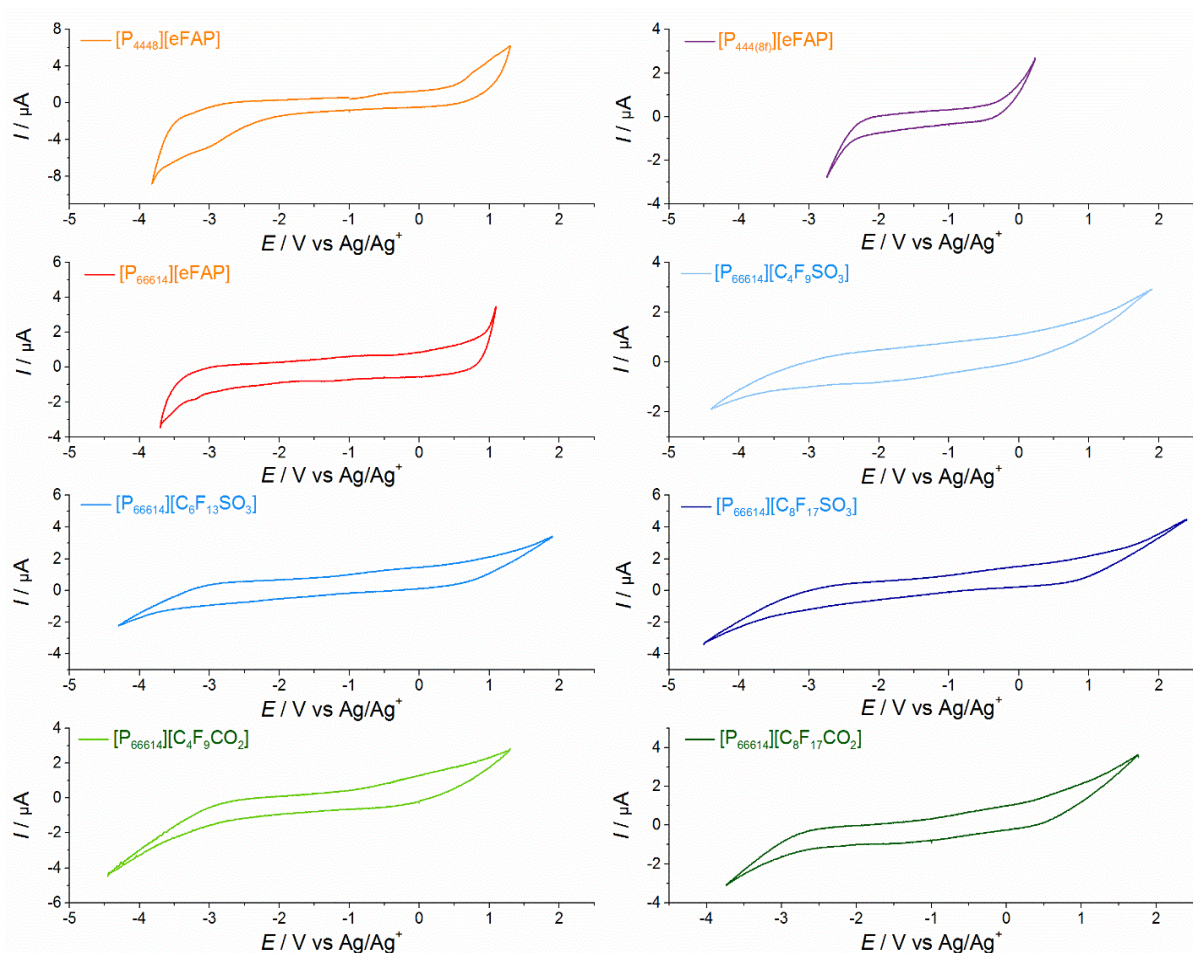
Fluorinated IL	η_0 /10 ⁻¹ mPa S	B_η /10 ² K	T_0 /K	R^2
[P ₄₄₄ 8][eFAP]	0.5 ± 0.1	11.7 ± 0.2	164 ± 1	1.0000
[P ₄₄₄ (8f)][eFAP]	0.9 ± 0.2	10.0 ± 0.7	181 ± 5	0.9999
[P ₆₆₆ 14][eFAP]	1.5 ± 0.2	10.0 ± 0.4	172 ± 3	1.0000
[P ₆₆₆ 14][C ₄ F ₉ SO ₃]	0.6 ± 0.2	12.9 ± 1.1	161 ± 7	1.0000
[P ₆₆₆ 14][C ₆ F ₁₃ SO ₃]	0.3 ± 0.1	14.0 ± 0.7	163 ± 4	1.0000
[P ₆₆₆ 14][C ₈ F ₁₇ SO ₃]	0.4 ± 0.2	14.2 ± 1.2	167 ± 7	0.9999
[P ₆₆₆ 14][C ₄ F ₉ CO ₂]	1.0 ± 0.7	11.1 ± 2.0	158 ± 15	0.9997
[P ₆₆₆ 14][C ₈ F ₁₇ CO ₂]	2.3 ± 0.7	9.0 ± 0.8	183 ± 6	0.9999

*Errors are denoted as 2 times the standard deviation in the fitted parameter.

Supporting Table S5: VTF fitting parameters for conductivity data.

Fluorinated IL	σ_0 /10 ⁻¹ S cm ⁻¹	B_σ /10 ² K	T_0 /K	R^2
[P ₄₄₄ 8][eFAP]	8.7 ± 1.3	12.3 ± 0.5	148 ± 4	1.0000
[P ₄₄₄ (8f)][eFAP]	25.6 ± 8.2	17.3 ± 1.2	123 ± 7	1.0000
[P ₆₆₆ 14][eFAP]	6.9 ± 3.2	14.2 ± 1.6	134 ± 11	0.9999
[P ₆₆₆ 14][C ₄ F ₉ SO ₃]	9.5 ± 1.4	19.4 ± 0.6	115 ± 3	1.0000
[P ₆₆₆ 14][C ₆ F ₁₃ SO ₃]	10.7 ± 2.9	21.1 ± 1.1	114 ± 5	1.0000
[P ₆₆₆ 14][C ₈ F ₁₇ SO ₃]	2.8 ± 0.9	16.0 ± 1.1	147 ± 6	1.0000
[P ₆₆₆ 14][C ₄ F ₉ CO ₂]	1.8 ± 0.4	12.8 ± 0.9	142 ± 6	1.0000
[P ₆₆₆ 14][C ₈ F ₁₇ CO ₂]	2.8 ± 0.6	16.3 ± 0.8	130 ± 5	1.0000

*Errors are denoted by 2 times the standard deviation in the fitted parameter



Supporting Figure S4: Electrochemical potential ranges vs. Ag/Ag⁺ for the fluorinated ILs used in this study. Cyclic voltammetry was conducted on a 1 mm glassy carbon working electrode at a scan rate of 100 mV/s.

Supporting References

1. Tindale, J. J.; Na, C.; Jennings, M. C.; Ragona, P. J., Synthesis and Characterization of Fluorinated Phosphonium Ionic Liquids. *Can. J. Chem.* **2007**, *85*, 660—667.
2. Rupp, A. B. A.; Klose, P.; Scherer, H.; Krossing, I., New Water-Stable Ionic Liquids Based on Tetrakis-(2,2,2-Trifluoroethoxy)Borate. *ChemPhysChem* **2014**, *15*, 3729—3731.
3. Alhanash, H. B.; Brisdon, A. K., Quaternary Ammonium Ionic Liquids Containing Fluorous Ponytails: Competitive Alkylation and Elimination Reactions of I(CH₂)_nRf (N = 2, 3) with Tertiary Amines. *J. Fluorine Chem.* **2013**, *156*, 152—157.
4. Battino, R.; Rettich, T. R.; Tominaga, T., The Solubility of Nitrogen and Air in Liquids. *J. Phys. Chem. Ref. Data* **1984**, *13*, 563—600.
5. Gjaldbaek, J. C.; Hildebrand, J. H., The Solubility of Nitrogen in Carbon Disulfide, Benzene, Normal- and Cyclo-Hexane, and in Three Fluorocarbons. *J. Am. Chem. Soc.* **1949**, *71*, 3147—3150.
6. Sargent, J. W.; Seffl, R. J., Properties of Perfluorinated Liquids. *Fed. Proc.* **1970**, *29*, 1699—1703.
7. Jacquemin, J.; Costa Gomes, M. F.; Husson, P.; Majer, V., Solubility of Carbon Dioxide, Ethane, Methane, Oxygen, Nitrogen, Hydrogen, Argon, and Carbon Monoxide in 1-Butyl-3-

Methylimidazolium Tetrafluoroborate between Temperatures 283 K and 343 K and at Pressures Close to Atmospheric. *J. Chem. Thermodyn.* **2006**, 38, 490—502.

8. Carlisle, T. K.; Bara, J. E.; Gabriel, C. J.; Noble, R. D.; Gin, D. L., Interpretation of CO₂ Solubility and Selectivity in Nitrile-Functionalized Room-Temperature Ionic Liquids Using a Group Contribution Approach. *Ind. Eng. Chem. Res.* **2008**, 47, 7005—7012.

9. Blath, J.; Christ, M.; Deubler, N.; Hirth, T.; Schiestel, T., Gas Solubilities in Room Temperature Ionic Liquids – Correlation between RTIL-Molar Mass and Henry's Law Constant. *Chem. Eng. J.* **2011**, 172, 167—176.

10. Stevanovic, S.; Costa Gomes, M. F., Solubility of Carbon Dioxide, Nitrous Oxide, Ethane, and Nitrogen in 1-Butyl-1-Methylpyrrolidinium and Trihexyl(Tetradecyl)Phosphonium Tris(Pentafluoroethyl)Trifluorophosphate (eFAP) Ionic Liquids. *J. Chem. Thermodyn.* **2013**, 59, 65—71.

11. Hildebrand, J. H.; Prausnitz, J. M.; Scott, R. L., *Regular and Related Solutions: The Solubility of Gases, Liquids, and Solids*; Van Nostrand Reinhold Co., 1970.

12. Camper, D.; Bara, J.; Koval, C.; Noble, R., Bulk-Fluid Solubility and Membrane Feasibility of Rmim-Based Room-Temperature Ionic Liquids. *Ind. Eng. Chem. Res.* **2006**, 45, 6279—6283.

13. Finotello, A.; Bara, J. E.; Camper, D.; Noble, R. D., Room-Temperature Ionic Liquids: Temperature Dependence of Gas Solubility Selectivity. *Ind. Eng. Chem. Res.* **2008**, 47, 3453—3459.

14. Anderson, J. L.; Dixon, J. K.; Brennecke, J. F., Solubility of CO₂, CH₄, C₂H₆, C₂H₆, O₂, and N₂ in 1-Hexyl-3-Methylpyridinium Bis(Trifluoromethylsulfonyl)Imide: Comparison to Other Ionic Liquids. *Acc. Chem. Res.* **2007**, 40, 1208—1216.

15. Blath, J.; Deubler, N.; Hirth, T.; Schiestel, T., Chemisorption of Carbon Dioxide in Imidazolium Based Ionic Liquids with Carboxylic Anions. *Chem. Eng. J.* **2012**, 181, 152—158.

Chapter 4: Design and Optimisation of Fluorinated Ionic Liquid–Based Electrolytes to Achieve High Nitrogen Gas Solubility

4.1 Introduction

This chapter delves into the design and optimisation of fluorinated IL–based electrolytes based on their physicochemical properties. These fluorinated IL–based electrolytes fall into the category of the “4th evolution of ILs”, described by MacFarlane et al.,¹²⁰ whereby fluorinated ILs are mixed with fluorinated solvents to offer unique and improved properties. As discovered previously in chapter 3, highly fluorinated ILs were shown to exhibit increased N₂ solubility. In addition, literature data shows that fluorinated solvents can exhibit very high N₂ solubility (as high as 17.9 mmol L⁻¹ for perfluoroheptane).¹⁰⁸ Based on this data, our aim is to enhance N₂ solubility even further by using fluorinated IL–based electrolytes and also explore the effects on the transport behaviour of these mixtures.

This study investigates the miscibility of several fluorinated ILs (including aprotic and protic ILs, waxy/amorphous salts etc.) with fluorinated solvents (of varying functionality). The process of dissolution between an IL and fluorinated solvent is briefly described in thermodynamic terms; generally, ILs that tend to display a lower overall energy density are likely to be miscible in fluorinated solvents. As a result, a range of new phosphonium [eFAP]⁻–based ILs are synthesised and characterised, in terms of their thermal behaviour and transport properties, and then analysed for their N₂ solubility. Moreover, these phosphonium [eFAP]⁻–based ILs are dissolved into mixtures with TFT to explore the increase in N₂ solubility. From these solubility experiments, we are able to define some rational design principles to achieve higher N₂ solubility in these fluorinated IL–based electrolytes.

The transport properties of [P₆₆₆₁₄]⁺–based ILs, described in chapter 3, are also studied as fluorinated IL–based electrolytes by the dissolution of these ILs into three fluorinated solvents:

TFT, HFCEP, and FPCE. The ionicity of a given electrolyte mixture is shown to differ depending on the IL, fluorinated solvent, and the composition of these two components. The work presented in this chapter describes the design and optimisation of fluorinated IL-based electrolytes, suitable for the electrochemical NRR.

4.2 Experimental

4.2.1 Materials

Triisobutyl(methyl)phosphonium tosylate ($[P_{141414}][Ts]$, CYPHOS 106), Tributyl(methyl)phosphonium methylsulfate ($[P_{1444}][MS]$, CYPHOS 108), Methyl(diethyl)isobutylphosphonium tosylate ($[P_{122i4}][Ts]$ CYPHOS 322) and Triethyl(methyl)phosphonium dimethylphosphate ($[P_{122i4}][DMP]$) were supplied by Cytec Industries. 1-ethyl-3-methylimidazolium tris(pentafluoroethyl)trifluorophosphate (> 98%, $[C_2mim][eFAP]$, Merck), σ , σ , σ -trifluorotoluene (> 99%, TFT, Synquest Laboratories), 1H,1H,2H-heptafluorocyclopentane (> 99%, HFCEP, Synquest Laboratories), 1H,1H,5H-octafluoropentyl 1,1,2,2-tetrafluoroethyl ether (> 97%, FPCE, Synquest Laboratories), 1,3-bis(trifluoromethyl)benzene (99%, Synquest Laboratories), 1,2,4,5-tetrafluorobenzene (98%, Synquest Laboratories), 1,3,5-tris(trifluoromethyl)benzene (98%, Synquest Laboratories), 1-fluoro-4-(trifluoromethoxy)benzene (99%, Synquest Laboratories), 2-fluorobenzotrifluoride (99%, Synquest Laboratories), pentafluorobenzene (98%, Synquest Laboratories), octafluorotoluene (98%, Synquest Laboratories) were used without further purification. Nitrogen gas (N_2 , ALPHAGAZ) was used as received from Air Liquide.

4.2.2 Synthesis

The synthesis of $[P_{66614}]$ -based ILs, $[C_4mpyr][C_8F_{17}SO_3]$ and $[N_{444(11f)}][C_4F_9SO_3]$ were described previously in chapter 3. The new phosphonium $[eFAP]$ -based ILs $[P_{141414}][eFAP]$, $[P_{1444}][eFAP]$, $[P_{122i4}][eFAP]$ and $[P_{1222}][eFAP]$ were synthesised via metathesis reactions in water, dichloromethane with the corresponding phosphonium-based starting material and

[C₂mim][eFAP].¹³¹ The water soluble phosphonium salts were added in molar excess of ~1.2 times. After several extractions with water (usually five), the IL was dried in vacuo to afford the desired IL/salt. The purity was checked by the absence of starting materials (the [C₂mim]⁺ cation and the respective phosphonium anion) in the NMR and MS spectra. Some reactions required repeated metathesis steps to ensure that the reaction reached completion. Characterisation data is provided in the supporting information.

4.2.3 Miscibility Experiments

To determine if a fluorinated IL was miscible with a fluorinated solvent, the following procedure was followed:

Several aliquots of IL was added (~0.1 g), in steps, to a known mass of solvent (~1 g). After each aliquot addition, the mixture was shaken in a vortex mixer (~15 seconds) and allowed to settle. Miscibility of the IL in the given solvent was determined by the appearance of a single phase, and the lack of any liquid/solid particles in this phase. Since the optimum composition of IL to solvent lies closer toward the solvent-rich region (based on ionic conductivity), the concentration at saturation was not determined in all cases.

4.2.4 Characterisation

Proton (¹H), fluorine (¹⁹F) and phosphorus (³¹P) NMR was carried out with a Bruker DRX400 spectrometer operating at 400 MHz, 376 MHz, 162 MHz respectively. The molecular mass of cations and anions were determined using electrospray ionisation mass spectrometry via a Micromass Platform II QMS instrument (cone voltage 35 V), with methanol as the solvent. The density of IL/IL-mixtures were measured with an Anton Paar DMA 5000 Density Meter via the “oscillating U-tube principle”. Viscosity measurements were conducted on an Anton Paar Lovis 2000M micro-viscometer with the falling ball technique. A Hewlett Packard 4284 LCR meter measured the conductivity through AC impedance spectroscopy over a range of 0.1 Hz to 10 MHz using a 2-electrode platinum wire dip cell, calibrated with an a. solution of 0.01

mol L⁻¹ KCl. Using the data point closest to the x-axis on the impedance plot, the resistance value was then used to calculate the conductivity.

Thermogravimetric analysis (TGA) was conducted with a Mettler Toledo TGA/DSC 1 STARe System over a range of 25 – 550 °C under a flow of N₂ at 30 mL/min, with a heating rate of 10 °C/min. Differential scanning calorimetry (DSC) experiments were performed on a DSC Q 100 instrument at 10 °C/min.

Diffusion NMR Measurements: The self-diffusion coefficient measurements were carried out with a pulsed-gradient stimulated echo (PGSTE) pulse sequence. Experiments were performed with a Bruker DRX600 spectrometer for ¹H nuclei for the cation, and a Bruker DRX400 spectrometer was used for ¹⁹F nuclei for the anion. D₂O was used as the external solvent reference, to surround the inner sample tube to minimise any convection effects. The diffusion coefficient was calculated by fitting data to the Stejskal–Tanner equation:²⁰²

$$\ln\left(\frac{S}{S_{g=0}}\right) = -\gamma^2 g^2 D \delta^2 \left(\Delta - \frac{\delta}{3}\right) \quad (1)$$

where S is the spin-echo signal intensity, γ is the gyromagnetic ratio of the nucleus being observed, g is the strength of the gradient, D is the self-diffusion coefficient, δ is the duration of the field gradient, and Δ is the time between two gradient pulses.

The self-diffusion coefficient of Milli-Q water was measured to be $2.3 \times 10^{-9} \text{ m}^2 \text{ s}^{-1}$ at 25 °C, within 1% of literature.²⁰³ The uncertainty of self-diffusion coefficient measurements is $\pm 5\%$

N₂ Solubility Measurements

N₂ solubility measurements were conducted near atmospheric pressure via the isochoric saturation method using a dual-volume apparatus, as described in previous publications (and Chapter 2) which are included in this thesis.²⁰⁴⁻²⁰⁵ N₂ solubility measurements were repeated

to ensure reproducible results, with a repeatability estimated to be within $\pm 0.2 \text{ mmol L}^{-1}$. Numerical data can be found in Supporting Table S2.

4.1 Design of a Fluorinated Ionic Liquid–based Electrolyte

The addition of an IL to a fluorinated solvent can range in various compositions, from one extreme of the salt at infinite dilution to the other of a slightly diluted network of ions. For the design of a fluorinated electrolyte, it is critical that a certain amount of IL is miscible in the fluorinated solvent ($>10\%$ wt) for the ionic conductivity to be sufficiently high enough. Therefore, the dissolution step is key for a usable electrolyte, as ion mobility is required for electrochemical applications. To briefly describe this dissolution step, we refer to the thermodynamic terms of mixing a fluorinated IL into a fluorinated solvent:

$$\Delta G = \Delta H - T\Delta S \quad (2)$$

Where ΔG is the Gibbs free energy change such that dissolution proceeds favourably when $\Delta G < 0$. H , T and S refer to the enthalpy, temperature and entropy respectively. Generally, the entropy of mixing the fluorinated IL and fluorinated solvent favours dissolution (unless strong interactions between species induce order and result in a lower entropy). On the other hand, the enthalpy term can be large and positive, and this would not be unexpected if we consider the electrostatic interactions within the IL versus the weaker dipole/dispersion interactions of the fluorinated solvent. Expanding the enthalpy term into:

$$\Delta H = H_{\text{reactants}} - H_{\text{products}} \quad (3)$$

describes the difference in interactions before and after mixing; a ΔH that is large and positive, and results in $\Delta G_s > 0$, will lead to sparingly soluble mixtures. ILs, if they are liquid at room temperature, are already at an advantage since the electrostatic interactions have already been weakened. This stems from the asymmetric organic side chains on the ions that do not allow tight packing, in contrast to the efficient packing of crystalline sodium chloride. In the

context of fluorinated ILs, it is certainly possible that the fluorinated section of the IL may interact favourably with the fluorinated solvent such that $\Delta G_s < 0$.²⁰⁵

4.1.1 Fluorinated Solvent Selection

Fluorinated solvents are a class of solvents that are hydrophobic, chemically inert, non-toxic, highly fluid, and highly dense.²⁰⁶ They also have unique properties, different to the extent such that they generally do not dissolve in aqueous or organic solvents. These distinct properties arise from their inert nature as they rarely act as proton acceptors to form hydrogen bonds, when bonded to carbon or phosphorus, despite the high electronegativity of fluorine.¹³⁹ This stems from the tightly bound outer-electron shell, resulting in the low polarisability of these fluorinated moieties. Moreover, the polarisability of perfluorinated solvents versus hydrogenated solvents can be very similar despite the extra nine electrons contained in fluorine, compared to a hydrogen atom. In fact, the dielectric constant of perfluorohexane is lower than hexane (1.69 cf. 1.89 respectively) and this is also reflected in its lower boiling point (57 °C cf. 69 °C respectively).¹⁰⁵ Since the boiling point of a molecular compound can be approximately related to the strength of its intermolecular forces, one can argue that fluorinated solvents display the lowest intermolecular forces compared to aqueous and organic solvents. In terms of gas solubility, a solvent that exhibits a low overall cohesive energy – in terms of solute-solute interaction energies – tend to favour the enthalpy of gas dissolution, and lead to a higher N₂ solubility. Hence, this interesting family of solvents were investigated with ILs to further enhance N₂ solubility. Following the procedure described in the experimental, the miscibility of a standard fluorinated IL, [C₄mpyr][eFAP], with highly fluorinated solvents is shown in Table 1.

Table 1: Table of fluorinated solvents miscible or immiscible in [C₄mpyr][eFAP].

Miscible	Immiscible
1H,1H,5H–octafluoropentyl 1,1,2,2–tetrafluoroethyl ether	Perfluoromethyldecalin
Bis(2,2,2–trifluoroethyl) ether	Perfluorooctane
1,1,1,3,3,3–Hexafluoro–2– (fluoromethoxy)propane	Perfluorohexane
Heptafluorocyclopentane	Heptacosafuorotributylamine
Trifluorotoluene	Perfluoro–1–butanesulfonyl fluoride
Fluorobenzenes*	Perfluoro–1–octanesulfonyl fluoride
	1,1,1,5,5,6,6,6–Octafluoro–2,4–hexanedione
	2–(Trifluoromethyl)–3– ethoxydodecafluorohexane

*Fluorobenzenes include: 1–Fluoro–4–(trifluoromethoxy)benzene, 1,3,5–Tris(trifluoromethyl)benzene, Pentafluorobenzene, 1,2,4,5–Tetrafluorobenzene, 2–Fluorobenzotrifluoride, 1,3–Bis(trifluoromethyl)benzene, 1,3–Bis(1,1,2,2–tetrafluoroethoxy)benzene, (2,2,2–Trifluoroethoxy)pentafluorobenzene

Examination of the solvents that were not miscible in [C₄mpyr][eFAP] showed that perfluorinated alkanes were not capable of dissolving [C₄mpyr][eFAP], likely due to their low polarisability and dipole.²⁰⁷ The effect of adding some functional groups to the fluorinated solvents was tested in order to slightly enhance the strength of their intermolecular forces (and polarisability). First, perfluorinated solvents that contained polar functional groups such as a sulfonyl and dione group were examined, although these were both observed to be immiscible with [C₄mpyr][eFAP]. On the other hand, small ether–based solvents such as bis(2,2,2–trifluoroethyl) ether, 1,1,1,3,3,3–hexafluoro–2–(fluoromethoxy)propane, and FPPE were found to be miscible in [C₄mpyr][eFAP]. However, a highly fluorinated ether, 2–(trifluoromethyl)–3–ethoxydodecafluorohexane was found to not produce miscibility. Further studies showed that [C₄mpyr][eFAP] was miscible in HFCEP and a range of fluorobenzene related solvents. As a result, partial hydrogenation of the fluorinated solvent appeared to contribute to IL miscibility.

It should be noted that this table of fluorinated solvents that are found to dissolve in [C₄mpyr][eFAP] is not exhaustive and several other classes of molecular compounds have the potential to show miscibility. However, to narrow down possible fluorinated solvent candidates, it is essential to consider the applicability of the chosen solvent to be used in an electrolyte. For example, it would not be feasible to use perfluoropentane as a solvent in reactions at ambient conditions, since its boiling point is 29 °C. Furthermore, the solvent should be electrochemically stable within the potential range where the electrochemical NRR is conducted (usually between -1.1 and 0 *V* versus NHE). This can limit the usage of alcohols (proton abstraction), degrees of saturation (double bond cleavage), acids, halogens, etc.

To summarise, we provide a brief list of parameters to consider for the choice of fluorinated solvent: miscibility of an IL in the fluorinated solvent, a relatively high boiling point (>80 °C), high fluidity, relatively high dielectric constant (within this family of solvents) and high electrochemically (and chemical) stability. As a result, a selection of various fluorinated solvents, that are found to be miscible in an IL, are studied in terms of their boiling point, density, and viscosity (shown in Supporting Table S1). Based on these properties, three different fluorinated solvents TFT, FPEE and HFCP are used throughout this study.

4.1.2 Ionic Liquid Criteria

In the field of electrochemical NRR, significant issues and challenges are prominent, that mostly arise from product contamination due to the small quantities of ammonia produced.⁵⁸⁻⁵⁹ Therefore, research groups must follow stringent protocols to demonstrate that ammonia has been electrochemically reduced from N₂, and not from any other potential sources (e.g. NH₄ itself or any NO_x species present) that may come from the N₂ gas supply, the atmosphere, or even the electrochemical cell setup. This also includes the electrolyte, catalyst and substrate material, all of which can breakdown and contribute to the final amount of ammonia produced. Therefore it is highly beneficial to utilise materials that are free of nitrogen groups; this removes any doubt of false positives due to the breakdown of the materials themselves. Some

authors have carefully identified the breakdown of nitrogen-based materials that have contributed to the total amount of ammonia produced,²⁰⁸⁻²⁰⁹ however this may not have been accounted for in other studies in the literature. Hence, in the next section we aim to design and synthesise new ILs (and use any fluorinated solvents) that are free of any nitrogen functionality.

In terms of miscibility, the IL itself certainly plays a role in its miscibility with the fluorinated solvent. Although [C₄mpyr][eFAP] is not miscible with the perfluorinated solvents used in this chapter, it is possible that an IL can be sufficiently fluorinated to permit dissolution. For example, Boswell et al. synthesised an extremely fluorinated salt, tri(4,4,5,5,6,6,7,7,8,8,9,9,10,10,11,11,11-heptafluoroundecyl)-methyllummonium ([CF₃(CF₂)₇(CH₂)₃]₃CH₃N⁺) tetrakis[3,5-bis(perfluorohexyl)phenyl], which was found to be miscible in perfluoroperhydrophenanthrene and perfluorohexane.²¹⁰ Although N₂ solubility would potentially be high for this electrolyte, such a bulky structure would likely exhibit sluggish mass transport properties.

The phosphonium [eFAP]⁻-based ILs, and fluorinated ILs that were described in chapter 3, all show miscibility in TFT, HFCEP, and FPEE. Even some of the IL salts that were solid at room temperature were found to be miscible in these solvents (see Table 2). For example, [C₄mpyr][C₈F₁₇SO₃] was miscible in HFCEP, and FPEE. On the other hand, [C₄mpyr][C₈F₁₇SO₃] did not dissolve in TFT. TFT has three fluorine atoms as a trifluoromethyl group (compared to seven and twelve fluorine atoms on HFCEP and FPEE respectively), suggesting that a sufficient degree of fluorination on the solvent may be required for miscibility with [C₄mpyr][C₈F₁₇SO₃]. Moreover, [C₄mpyr][C₄F₉SO₃], which contains a shorter fluoroalkyl chain, was not miscible in any of these fluorinated solvents. This demonstrates the effect of increasing the degree of fluorination on the anion to enable miscibility.

Table 2. Table of IL salts that are found to be miscible or immiscible in TFT, HFCE, and FPEE.

Miscible Solid ILs	Immiscible Solid ILs
[C ₄ mpyr][C ₈ F ₁₇ SO ₃]	[C ₄ mpyr][C ₄ F ₉ SO ₃]
[P ₁₄₁₄₁₄][eFAP]	[C ₄ mpyr][B(otfe) ₄]
[P ₁₂₂₂][eFAP]	[P ₆₆₆₁₄][B(otfe) ₄]
	[N _{44411f}][C ₄ F ₉ SO ₃]
	[Hmpyr][C ₇ F ₁₅ CO ₂]
	[Hmpyr][C ₂ H ₂ F ₄ SO ₃]
	[C ₄ H ₂ F ₇ NH ₃][NTf ₂]

Other IL salts that were examined, such as the highly fluorinated borates or fluorinated ammonium cations, were also not miscible in these fluorinated solvents. This likely stems from a large $H_{\text{reactants}}$ term, in equation 3, due to the greater extent of intermolecular forces within the solid, and relatively low H_{products} term upon dissolution into a fluorinated solvent.¹²⁰ This also appears to be the case for the protic ILs studied, whether they exist in solid or liquid phase. The $H_{\text{reactants}}$ term, based on equation 3, would likely be large due to the availability of hydrogen bonding such that that these salts are found to be water soluble. As a result, they were found to be immiscible with fluorinated solvents. This extends into solid salts (with high electrostatic interactions), where lithium bistriflimide/triflate may require the addition of additives, such as dimethoxyethane, which may allow miscibility compared to the pure fluorinated solvent (with limited miscibility). However in preliminary work, lithium triflate was added to a mixture of HFCE and DME, and still yielded an immiscible mixture. Hence, these salts may not be viable candidates for use as fluorinated electrolytes. On the other hand, using ILs as additives may allow miscibility, e.g. a combination of IL, lithium salt and fluorinated solvent may yield a highly conductive electrolyte.

To summarise, several of our fluorinated ILs, that are liquid at room temperature, are miscible in the fluorinated solvents TFT, HFCE, and FPEE. On the other hand, many of the IL salts that are solid at room temperature do not dissolve in the above mentioned solvents. These

trends can be attributed to the difference in the enthalpic term ΔH , since $H_{\text{reactants}}$ for solid ILs and protic ILs are often much larger than $\Delta H_{\text{products}}$. Thus, it is important to consider the choice of IL as the conducting ionic species, for the design of an electrolyte.

4.2 Synthesis of Novel Phosphonium [eFAP][−]-Based Ionic Liquids

While a series of [P₆₆₆₁₄]⁺-based ILs have been described in chapter 3, which all were found to exhibit high N₂ solubility, different phosphonium cations with shorter alkyl chain lengths are studied. Since ILs, that contain the [eFAP][−] anion, were found to exhibit better transport properties,²⁰⁴ we aim to synthesise a range of phosphonium [eFAP][−]-based ILs and describe the properties of these new ILs. In addition to the favourable ionic conductivity of an [eFAP][−]-based IL, the N₂ solubility may also reveal interesting trends due to a smaller presence of alkyl chains on the cation compared to the highly fluorinated anion. After physical characterisation of the neat ILs, their properties are then examined as IL-TFT mixtures. The molecular structures of these phosphonium [eFAP][−]-based ILs are shown in Figure 1.

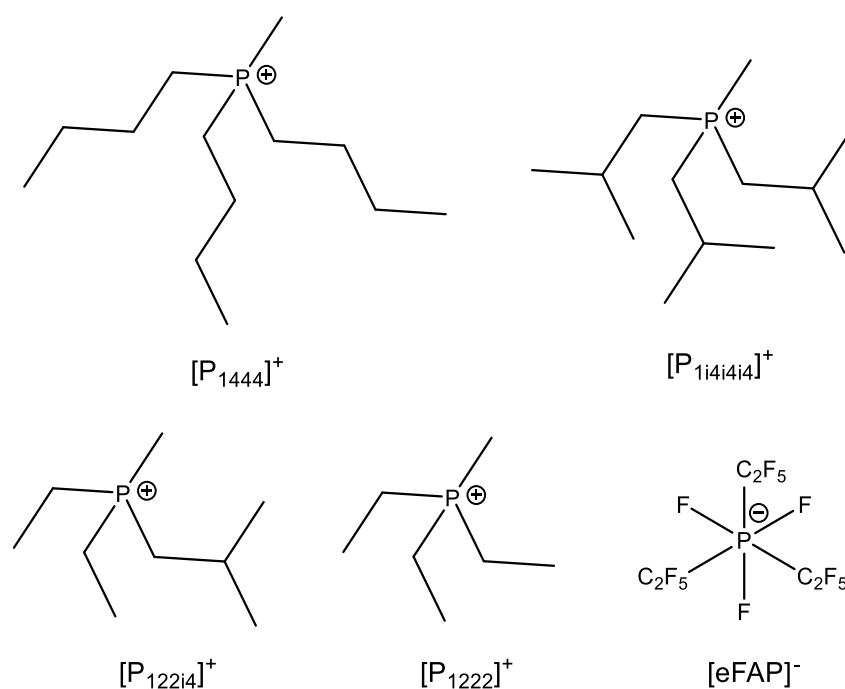


Figure 1: Molecular structures of various phosphonium cations and the tris(pentafluoroethyl)trifluorophosphate anion used in this study.

4.2.1 Thermal Properties

The thermal properties of phosphonium [eFAP][−]-based ILs are shown in Table 3. Two of these ILs are observed to be liquid at room temperature whereas the other two are relatively low-melting solids. In the case of [P₁₄₄₄][eFAP] and [P_{1i4i4i4}][eFAP], where their molecular weights are identical, the change in melting point is likely attributed to the differences in structural arrangement. Here, branched triisobutyl alkyl chains, compared to linear tributyl alkyl chains, reduce the long-range disorder of the IL, and also allow more efficient packing.²⁰⁶ Hence, this leads to increased electrostatic ion attractions in [P_{1i4i4i4}][eFAP], and thus, results in an increase in melting point. In the case with [P_{122i4}][eFAP], the presence of the isobutyl alkyl chain may disrupt the structural arrangement and symmetry that is likely to exist with [P₁₂₂₂][eFAP]. As a result, [P₁₂₂₂][eFAP] exists as a solid at room temperature, which may reflect the increase in electrostatic ion interactions compared to [P_{122i4}][eFAP]. For [P₆₆₆₁₄][eFAP] and [P₄₄₄₈][eFAP], the long alkyl chains on the phosphonium cation are sufficiently long enough to disrupt electrostatic interactions, where these ILs tend to form a glassy state upon cooling²⁰⁴ as solidification kinetics are slow.²⁰⁶ [P₁₂₂₂][eFAP] displays features of organic ionic plastic crystal behaviour, due to its prominent solid–solid transition with a low entropy of fusion $\Delta S_f = 23 \text{ J mol}^{-1} \text{ K}^{-1}$ (similar to its entropy of melting $\Delta S_f = 24 \text{ J mol}^{-1} \text{ K}^{-1}$).²¹¹

Table 3: Thermal properties of phosphonium [eFAP][−]-based ILs investigated in this study.

IL	T _g (°C)	T _{ss} (°C)	T _m (°C)	T _{dec} (°C)
[P ₆₆₆₁₄][eFAP] ²⁰⁴	-85			353
[P ₄₄₄₈][eFAP]	-82			355
[P ₁₄₄₄][eFAP]		3	19	353
[P _{1i4i4i4}][eFAP]			44	354
[P _{122i4}][eFAP]		-51, -43	-14	352
[P ₁₂₂₂][eFAP]	-78	14	71	354

The thermal stability of phosphonium [eFAP][−]-based ILs all show similarly high decomposition temperatures near ~350 °C. This suggests that the size of the alkyl chains on

the phosphonium cation do not affect the mechanism of decomposition, which may occur via nucleophilic substitution or the Hoffmann elimination.²¹²

4.3 N₂ Solubility of Fluorinated Ionic Liquid–Based Electrolytes

N₂ solubility can be described as the concentration of N₂ that dissolves in a given liquid. In the electrolyte, it is desirable to have a high concentration of N₂ in order to maximise the current density from electrochemical reduction of N₂ to NH₃. Previously in chapter 3, it was found that increasing degree of fluorination in a series of ILs produced an increase in N₂ solubility. Here, we focus on increasing the N₂ solubility in a series of phosphonium [eFAP][−]-based ILs, and explore a number of factors: shorter alkyl chains on the phosphonium cation, the effect of adding a fluorinated solvent, the composition of IL to solvent, and the interplay between these parameters on the solubility of N₂.

4.3.1 N₂ Solubility of Phosphonium [eFAP][−]-based ILs

The N₂ solubility data of phosphonium [eFAP][−]-based ILs are shown in Figure 2 and Supporting Table S2. The N₂ solubility of these ILs follow the order of [P₁₄₄₄][eFAP] > [P_{122i4}][eFAP] > [P₄₄₄₈][eFAP] > [P₆₆₆₁₄][eFAP]. Initially, decreasing the size of the alkyl chains on the phosphonium cation shows a constant rise in N₂ solubility; this is likely related to the contribution of van der Waals interactions, from long alkyl chains, which may lead to an increase in energy required to create cavities for N₂ dissolution. On the other hand, [P₁₄₄₄][eFAP] displays a higher N₂ solubility than [P_{122i4}][eFAP]. This likely reflects the effect of electrostatic ion attractions (between the cation and anion of the IL), that become the dominating intermolecular interaction in terms of the overall cohesive energy density of the IL. ILs with a lower overall cohesive energy density is likely to be a contributing factor in the solubility of N₂ in these electrolytes.

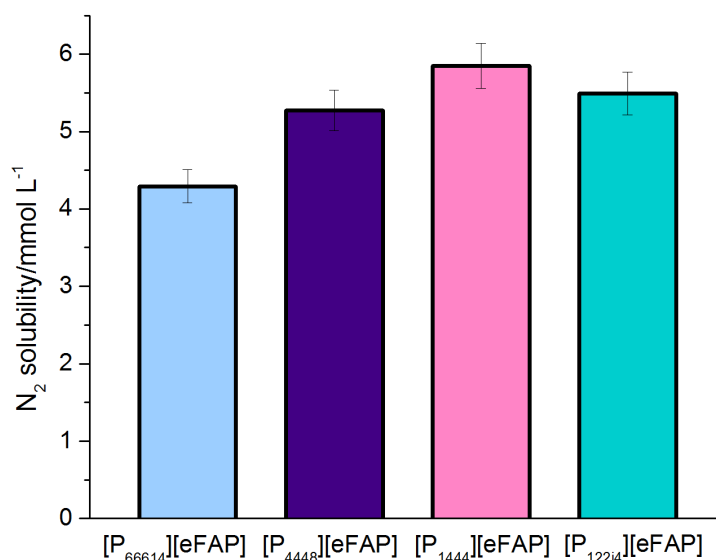


Figure 2: N_2 solubility of phosphonium [eFAP]⁻-based ILs at 30 °C and $p = 1$ atm, expressed as molar concentration (mmol L⁻¹).

Another possible mechanism of N_2 solubility is the dissolution into the free volume of these IL electrolytes. Triolo and co-workers have experimentally observed the formation of distinct fluorinated domains in highly fluorinated ILs, where such domains may represent favourable sites for N_2 dissolution.^{151, 213-214} Moreover, Gomes and colleagues have calculated the radial distribution functions for fluorinated ILs and show that non-interacting gases are likely to occupy these areas of fluorinated domains due to the larger available free volume that may exist in these regions.²¹⁵

The combination of large fluorinated domains (by increasing the degree of fluorination on the IL) and decreasing the size of the phosphonium cation (resulting in an increase in the fluorinated portion of the IL) have been shown to further enhance N_2 solubility. We can extend this concept by the addition of a fluorinated solvent to the IL to i) reduce electrostatic ion attractions and reduce the overall cohesive energy density, and ii) expand the regions of fluorinated domains and thus, increase the free volume.

4.3.2 N_2 Solubility of IL-TFT Mixtures

The N_2 solubility of an IL can be expected to change with the addition of a fluorinated solvent. Here, we explore the increase in N_2 solubility by adding TFT to each of the phosphonium [eFAP]⁻-based ILs in a 1:1 volumetric mixture. Moreover, the solid salts

$[P_{1i4i4i4}][eFAP]$ and $[P_{1222}][eFAP]$ were miscibility with TFT, which allowed the measurement of N_2 solubility in these IL–TFT mixtures. The N_2 solubility of the IL, TFT, and their mixture ($\Phi = 0.5$) are shown in Figure 3a–f. Volumetric fractions are estimated based on the densities of the pure IL (extrapolated in the case of solid salts), and TFT. This data, along with the exact weight and χ_2 composition are shown in Supporting Table S2.

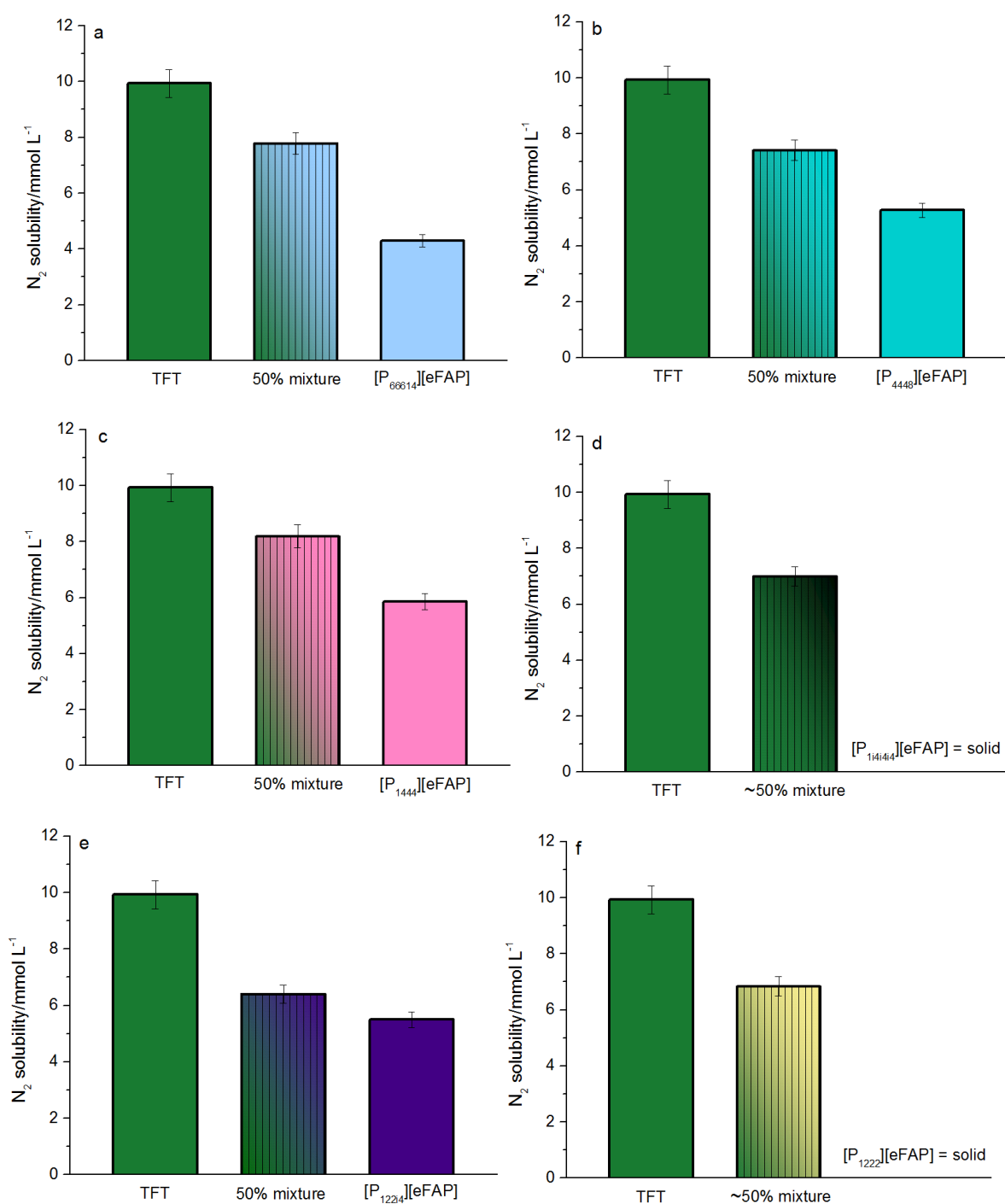


Figure 3a–f: N_2 solubility (mmol L^{-1}) of IL–TFT mixtures: a) $[P_{66614}][eFAP]$, b) $[P_{4448}][eFAP]$, c) $[P_{1444}][eFAP]$, d) $[P_{1i4i4i4}][eFAP]$, e) $[P_{122i4}][eFAP]$, and f) $[P_{1222}][eFAP]$ at a volume fraction (Φ) of 0, 0.5, and 1, at 30 °C and $p = 1$ atm.

TFT exhibits a higher N₂ solubility than the neat IL on the basis of concentration (mmol L⁻¹). This is likely related to the higher overall cohesive energy density in ILs due to the electrostatic ion interactions, that are absent in the neat fluorinated solvent. The addition of TFT to each of the ILs all show a marked increase in N₂ solubility, revealing the advantage of using IL–TFT mixtures (fluorinated IL–based electrolytes). In many cases, the N₂ solubility of the IL–TFT mixture ($\Phi = 0.5$) lies approximately between the IL, and TFT. This could suggest a dependence on total free volume in a given mixture. This concept is further explored and discussed in chapter 5.

A comparison of N₂ solubility in IL–TFT mixtures ($\Phi = 0.5$) are shown in Figure 4. IL–TFT mixtures that have a larger phosphonium cation display slight increases in N₂ solubility than those with a smaller phosphonium cation. However, a higher composition of IL (e.g. $\Phi = 0.8$) in these IL–TFT mixtures would probably yield larger variations in N₂ solubility due to the greater influence of the IL, and approach the values shown in Figure 2. On the other hand, moving towards lower concentrations of IL in these mixtures would result in smaller differences as the solubility of N₂ approaches that of neat TFT; hence, this therefore emphasises the impact on the fluorinated solvent to be used in fluorinated IL–based electrolytes.

Furthermore, the solid salts ([P_{1i4i4i4}][eFAP] and [P₁₂₂₂][eFAP]) that were dispersed into TFT as a 1:1 mixture displayed slightly lower levels of N₂ solubility (~20%) compared to mixtures with ILs that were liquid at room temperature. A comparison of [P_{1i4i4i4}][eFAP]–TFT and [P₁₄₄₄][eFAP]–TFT show that the branched chains of the triisobutyl(methyl)phosphonium cation (and its interaction with the solvent) led to a decrease in N₂ solubility of ~17%. These trends reflect the importance of the IL structure and its composition in a given mixture for the design of an electrolyte, those structures that tend to have higher lattice energies (higher T_m) produced lower N₂ solubility.

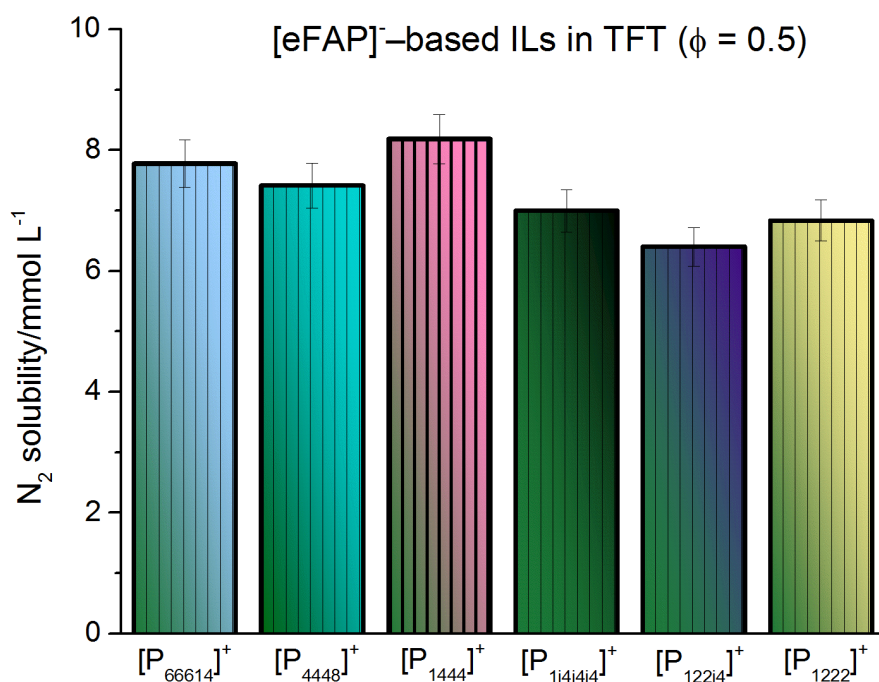


Figure 4: N₂ solubility (mmol L⁻¹) of phosphonium [eFAP]⁻-TFT mixtures at a volume fraction $\Phi = 0.5$, at 30 °C and $p = 1$ atm.

4.3.3 Rational Design Principles to Achieve Higher N₂ Solubility

Based on the previous section, the N₂ solubility of the neat IL can have an effect on the final solubility of its mixture. Here, we aim for the highest fluorinated IL-based mixture (at $\Phi = 0.5$) by selecting [P₆₆₆₁₄][C₈F₁₇CO₂] and [P₆₆₆₁₄][C₈F₁₇SO₃] as these ILs displayed the highest N₂ solubility out of all the ILs investigated in this thesis (see chapter 3). Furthermore, the fluorinated solvent HFCEP is selected due to its higher N₂ solubility than TFT.²⁰⁵ Figure 5a—b show the N₂ solubility of these ILs, HFCEP, and their mixture ($\Phi = 0.5$). Here [P₆₆₆₁₄][C₈F₁₇CO₂]-HFCEP displays a N₂ solubility of 9.3 mmol L⁻¹, up to 40% higher than some of the phosphonium [eFAP]⁻-based TFT mixtures shown in Figure 4.

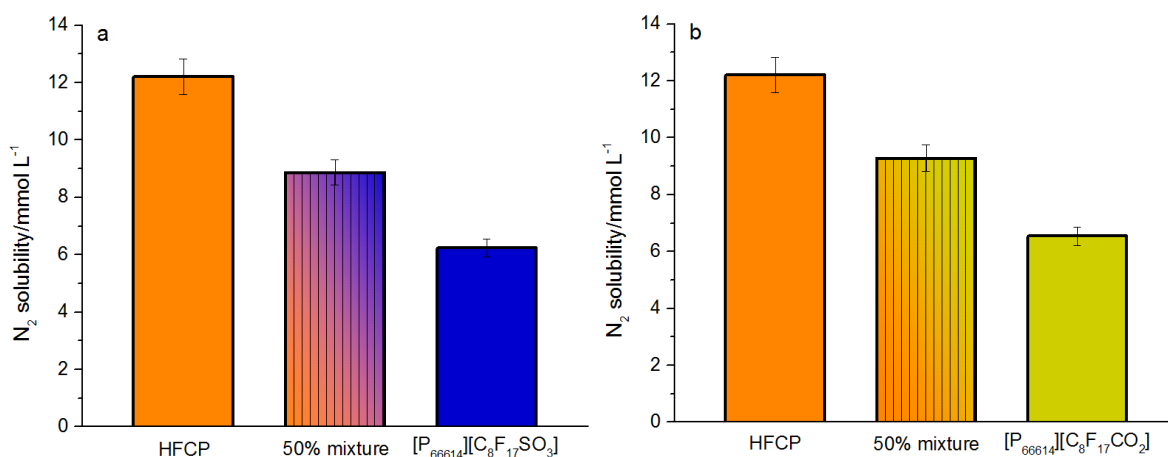


Figure 5a—b: N_2 solubility ($mmol\ L^{-1}$) of IL–HFCP mixtures: a) $[P_{66614}][C_8F_{17}SO_3]$ and b) $[P_{66614}][C_8F_{17}CO_2]$ at a volume fraction (Φ) of 0, 0.5, and 1, at 30 °C and $p = 1\ atm$.

To provide an overall summary, the N_2 solubility of all fluorinated IL–based electrolytes and their compositions studied in this chapter are plotted in Figure 6. The series of phosphonium $[eFAP]^+$ –based mixtures with TFT showed promising levels of dissolved N_2 , more than ten times higher than aqueous–based systems. The highest values of N_2 solubility were found with $[P_{66614}][C_8F_{17}CO_2]$ –HFCP and $[P_{66614}][C_8F_{17}SO_3]$ –HFCP mixtures. Thus, we have demonstrated here some rational design principles in achieving high N_2 solubility by the selection of an ideal fluorinated solvent, cation, and anion of the IL.

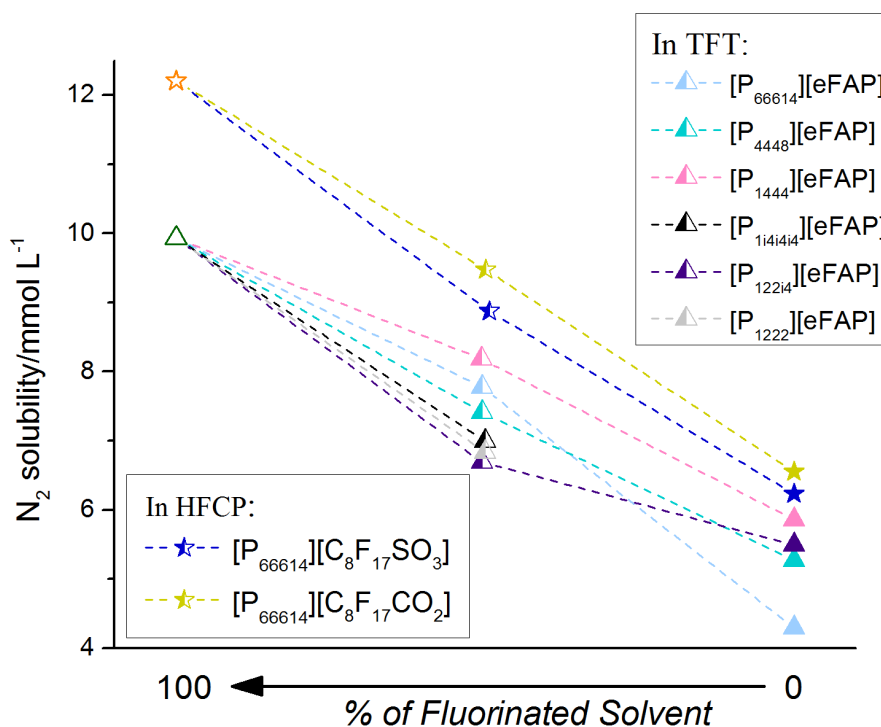


Figure 6: N_2 solubility ($mmol\ L^{-1}$) of all IL–fluorinated solvent mixtures at a volume fraction (Φ) of 0, 0.5, and 1, at 30 °C and $p = 1\ atm$.

4.4 Phosphonium $[eFAP]^-$ –based ILs and Mixtures – Decreasing Cation Size

In addition to N_2 solubility, it is important to consider the transport behaviour of these fluorinated IL–based electrolytes. First, the new phosphonium $[eFAP]^-$ –based ILs are studied in terms of their transport properties. The subsequent section then delves into the physicochemical properties of the IL–TFT mixtures over a range of compositions. TFT is chosen as an exemplar fluorinated solvent due to its low viscosity, and thus, potential to produce an IL–mixture with high fluidity.

4.4.1 Transport Properties

4.4.1.1 Ionic Conductivity and Viscosity

In the electrochemical NRR, it is important to incorporate highly conductive electrolytes that are capable of facilitating high current densities and fast reaction rates. Figure 7a shows the Arrhenius plot of ionic conductivity of the phosphonium $[eFAP]^-$ –based ILs (with the temperature dependence plots shown in the supporting information). $[P_{122i4}][eFAP]$ displays

much higher ionic conductivities (up to one order of magnitude higher) compared to the other ILs across the whole temperature range. For example, $[P_{122i4}][eFAP]$ shows a substantial increase in ionic conductivity of ~ 11.6 times higher than $[P_{66614}][eFAP]$, and ~ 3.5 times compared to $[P_{1444}][eFAP]$. This shows the effect of decreasing the alkyl chain on the phosphonium cation in terms of ionic conductivity. Furthermore, all of these $[eFAP]^-$ -based ILs show much higher ionic conductivity in comparison with the perfluorosulfonate and perfluorocarboxylate-based ILs from chapter 3.

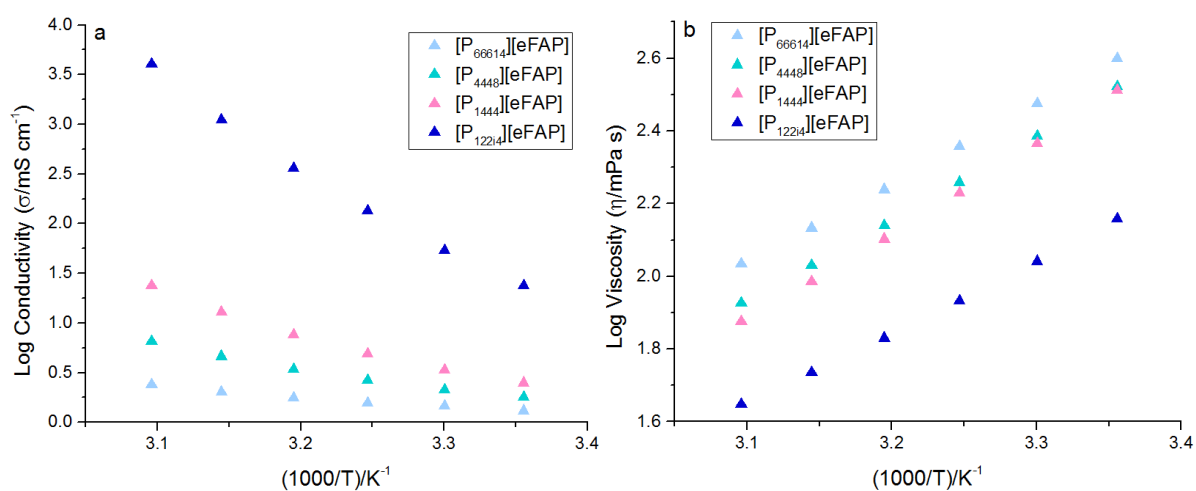


Figure 7a–b: Arrhenius plot of a) ionic conductivity, and b) viscosity vs inverse absolute temperature for the ILs in this study.

The viscosity of an electrolyte certainly plays a role in the performance of electrochemical devices as it is related to the mobility of ions in solution. The Arrhenius plot of viscosity for the phosphonium $[eFAP]^-$ -based ILs are shown in Figure 7b. As expected, a decrease in size of the alkyl chains on the phosphonium cation results in a lower viscosity, with a particularly large decrease when comparing $[P_{122i4}][eFAP]$ to the other ILs. This suggests that the frictional forces between alkyl chains become more prominent at a certain alkyl chain length on the phosphonium cation, and result in a marked increase in viscosity. Similarly to the ionic conductivity, all of these ILs exhibit lower viscosities than the aforementioned series of perfluorosulfonate and perfluorocarboxylate-based ILs studied in chapter 3.

4.4.1.2 *Walden Plot*

The Walden plot is a qualitative measure of assessing the ionicity of an electrolyte by combining the ionic conductivity, viscosity and density data to show the relationship between molar conductivity (Λ) and fluidity ($1/\eta$).²¹⁶ This relationship compares the data to an ideal reference electrolyte of aqueous KCl (0.01 mol L⁻¹), where the ions are considered to be completely dissociated.²¹⁷ Comparison to an ideal KCl line and the 10% ionisation line allows the examination of any interactions and trends with our fluorinated ILs.

The Walden plot of phosphonium [eFAP]⁻-based ILs synthesised in this study are shown in Figure 8. Also shown in Table 4, the degree of ionicity is quantitatively calculated at 25 °C via diffusion ordered spectroscopy (as described in chapter 3). The degree of ionicity with phosphonium [eFAP]⁻-based ILs decreases as the size of the phosphonium cation becomes larger, suggesting that formation of ion pairing/neutral clusters in these ILs stems from the aggregation of long alkyl chains. On the Walden plot, [P_{122i4}][eFAP] lies only slightly below the ideal line and exhibits a high ionicity of $\Lambda_{\text{IMP}}/\Lambda_{\text{NMR}} = 0.82$. Such high ionicity values are also observed in other [P_{122i4}][eFAP]-based ILs with different anions (e.g. [TFSI]⁻, [FSI]⁻, [DCA]⁻ etc.),²¹⁸ that were found to be viable electrolytes for lithium battery applications. In terms of the electrochemical NRR, [P_{122i4}][eFAP] displays ideal transport properties, demonstrating the potential of an alternative, nitrogen-free IL to be used as an electrolyte. Furthermore, the series of phosphonium [eFAP]⁻-based ILs display much better ion dissociation compared to the series of perfluorosulfonate and perfluorocarboxylate-based ILs. The increase in the self-diffusion coefficients of these ILs, up to 3 times higher from [P_{122i4}][eFAP] to [P₁₄₄₄][eFAP], reflect the same trends as found with the ionic conductivity and viscosity.

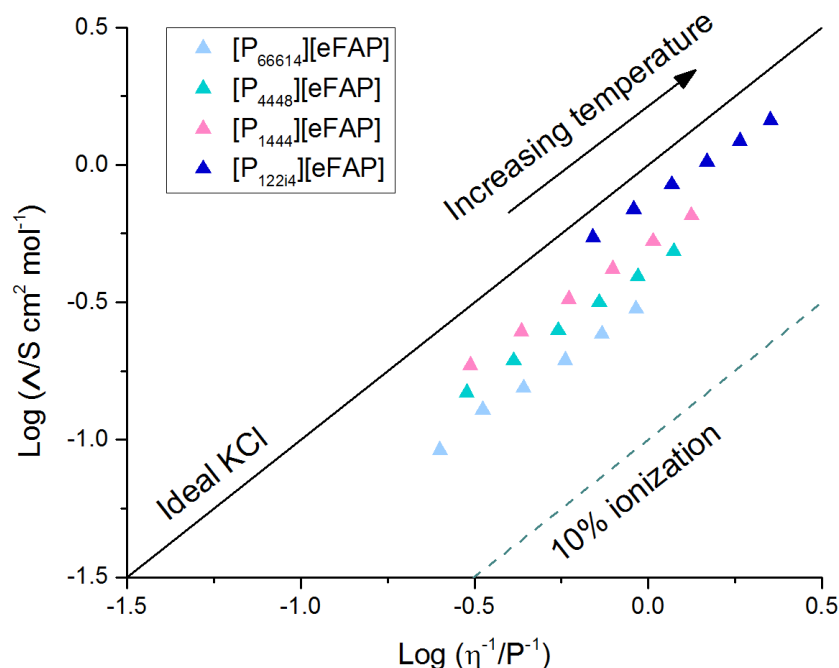


Figure 8: Walden plot of the phosphonium [eFAP][−]–based ILs in this study at 25 °C, 30 °C, 35 °C, 40 °C, 45 °C, 50 °C.

Table 4: Self-diffusion coefficients ($m^2 s^{-1}$) and the degree of ionicity ($\Lambda_{IMP}/\Lambda_{NMR}$) for the phosphonium [eFAP][−]–based ILs in this study at 25 °C.

IL	D_{cation} / $10^{-12} m^2 s^{-1}$ ± 5%	D_{anion} / $10^{-12} m^2 s^{-1}$ ± 5%	$\Lambda_{IMP}/\Lambda_{NMR}$ ± 10%
[P ₆₆₆₁₄][eFAP] ²⁰⁴	2.2	2.2	0.56
[P ₄₄₄₈][eFAP]	2.6	3.1	0.69
[P ₁₄₄₄][eFAP]	3.1	3.5	0.75
[P _{122i4}][eFAP]	9.2	8.5	0.82

4.4.2 Transport Properties in IL–TFT Mixtures

4.4.2.1 Ionic Conductivity and Viscosity

Exploration into the 4th evolution of ILs, allows us to study fluorinated salts that are solid at room temperature through their dissolution into a fluorinated solvent. For example, the dissolution of [P_{1i4i4i4}][eFAP], and [P₁₂₂₂][eFAP] with TFT produces a miscible salt–solvent mixture that can be used as an electrolyte. Here, the fluorinated solvent can play a role in disrupting electrostatic interactions between ions such that the salt can then dissolve in solution. The aim of this section is to study the enhanced transport properties with phosphonium [eFAP][−]

–TFT mixtures, over the range of IL compositions near the maxima of ionic conductivity (see Figure 9a). The temperature dependence plots for all of the transport properties, although they do not reveal any unexpected trends, are shown in the supporting information.

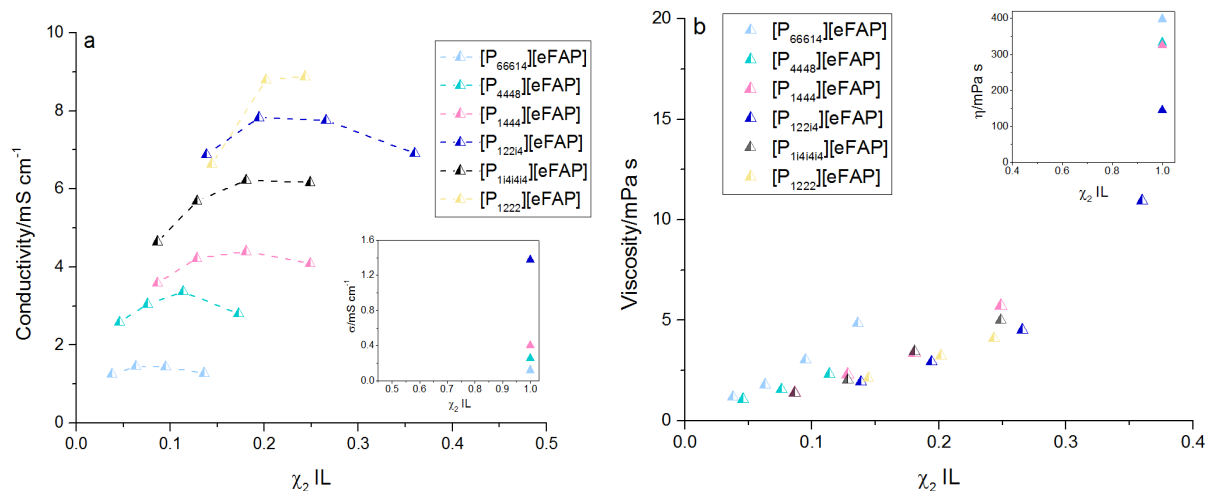


Figure 9a—b: Plot of a) ionic conductivity and b) viscosity of IL–TFT mixtures, as a function of mole fraction, χ_2 , at 25 °C. Insets shows the ionic conductivity and viscosity of the neat IL respectively.

The ILs, that are liquid at room temperature, exhibit miscibility with TFT across a wide range of IL compositions whereas the solid salts reach saturation at $\chi_2 > 0.25$. While ionic conductivity rises with the addition of fluorinated solvent (by reducing the viscosity), the value of conductivity will eventually decline toward zero due to the absence of charge carriers. Interestingly, the χ_2 of IL, near the maximum in ionic conductivity, is found to increase with molecular weight of the IL. To see if this trend is skewed by the molecular weight, the ionic conductivity is plotted against the mass fraction of IL in Supporting Figure S1; however this trend remains the same, suggesting that this peak in ionic conductivity may be a function of concentration that differs for each IL–solvent system. Thus, the composition of IL at the optimum of ionic conductivity cannot be assumed to be the same for all IL–solvent systems.

The ionic conductivity of the IL–TFT mixtures increases as the size of the phosphonium cation on the IL becomes smaller. For example, the $[P_{1222}][eFAP]$ –TFT mixture displays an ionic conductivity ~ 6 times higher than $[P_{66614}][eFAP]$ –TFT which reflects an advantage of moving toward a smaller IL structure. In the comparison of two ILs with identical molecular

weight, $[P_{1i4i4i4}][eFAP]$ displays approximately 30% higher ionic conductivity than $[P_{1444}][eFAP]$. This shows the impact of cation structure, in a given mixture of TFT, where the branched isobutyl alkyl chains lead to this increase in ionic conductivity compared to the linear butyl alkyl chains. As a result, the choice in the molecular structure of the IL is also relevant when considering an electrolyte to achieve high ionic conductivity.

Figure 9b shows the plot of viscosity of IL–TFT mixtures versus the χ_2 composition of IL. As observed with $[P_{66614}]^+$ –based mixtures, the addition of solvent to the neat IL results in the decrease in viscosity toward the neat fluorinated solvent. Furthermore, IL–TFT mixtures that contain a smaller phosphonium cation tend to show lower viscosities at a given χ_2 of IL. In comparing the structure of a branched isobutyl alkyl chain versus a linear alkyl chain on the phosphonium cation, the viscosity of $[P_{1i4i4i4}][eFAP]$ –TFT displays similar viscosity values to $[P_{1444}][eFAP]$ –TFT at low IL concentrations.

4.4.2.2 *Walden Plot*

The qualitative analysis of the ionicity of IL–TFT mixtures are shown via the Walden plot in Figure 10. Decreasing the concentration of IL in these mixtures leads to lower degrees of ionicity; this behaviour often reflects unusual electrolyte behaviour where the solvent exhibits a low dielectric constant.¹²⁰ Since TFT exhibits a dielectric constant of 9.2 at 25 °C,²⁵ ion pairing and aggregation in these mixtures are likely to occur at lower IL concentrations. Aside from this fact, solvents that exhibit high dielectric constants often exhibit very poor N_2 solubility. For example, water exhibits a dielectric constant of 80.1 at 20°C²⁵ yet displays a N_2 solubility of 0.7 mmol L⁻¹ at 20 °C.¹⁰¹ Therefore, it is essential to consider both of these properties when exploring suitable solvents for the NRR. Lastly, if we consider the structures of $[P_{1i4i4i4}][eFAP]$ –TFT and $[P_{1444}][eFAP]$ –TFT mixtures, a higher degree of ionicity is observed in the case of branched alkyl chains. Since the viscosity of these two mixtures are similar at the same concentration, a higher ionicity may describe the higher ionic conductivity that is observed with $[P_{1i4i4i4}][eFAP]$ –TFT.

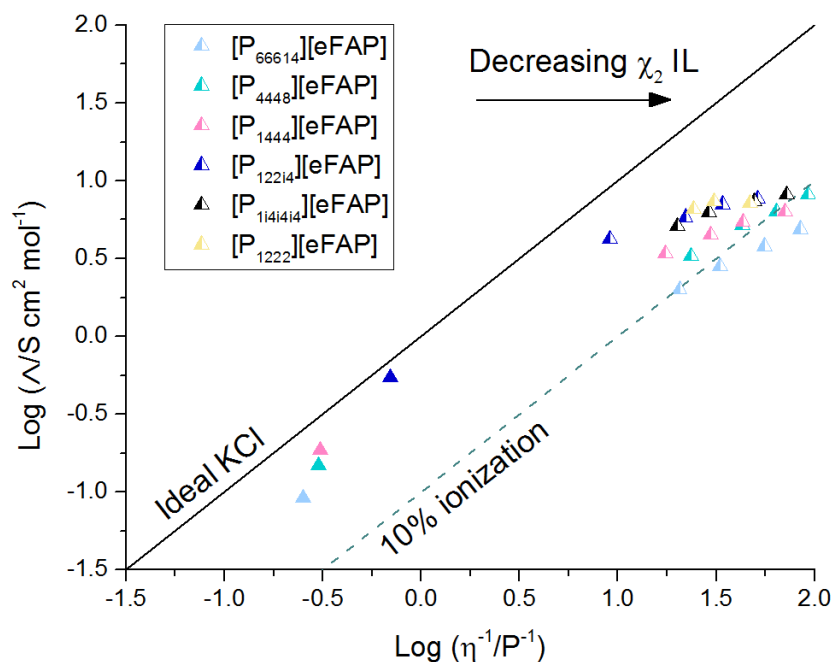


Figure 10: Walden plot of IL-TFT mixtures in various compositions at 25 °C.

4.5 $[\text{P}_{66614}]^+$ -based IL Mixtures – Varying the Anion

$[\text{P}_{66614}]^+$ -based IL mixtures are investigated as they are found to be miscible with the fluorinated solvents used in this study. This may result from weakened electrostatic interactions within these ILs due to their long alkyl chains that may prevent efficient structural packing. Therefore, a range of $[\text{P}_{66614}]^+$ -based IL mixtures are investigated in terms of their ionic conductivity, viscosity and ionicity. Furthermore, the concentration of IL in a given mixture will certainly affect the transport properties, where we aim to explore any trends with IL composition. Temperature dependence data for all of the transport properties and ionicity values are presented in the supporting information; however analysis of this data did not reveal unexpected trends that add significant insight to this chapter.

4.5.1 Ionic Conductivity

The transport properties of $[\text{P}_{66614}]^+$ -based IL mixtures with differing IL composition are studied for the advantage of lowering viscosity and enhancing ionic conductivity. Figure 11a—f shows the plot of the ionic conductivity in $[\text{P}_{66614}]^+$ -based mixtures, with TFT, HFCEP, and FPPE.

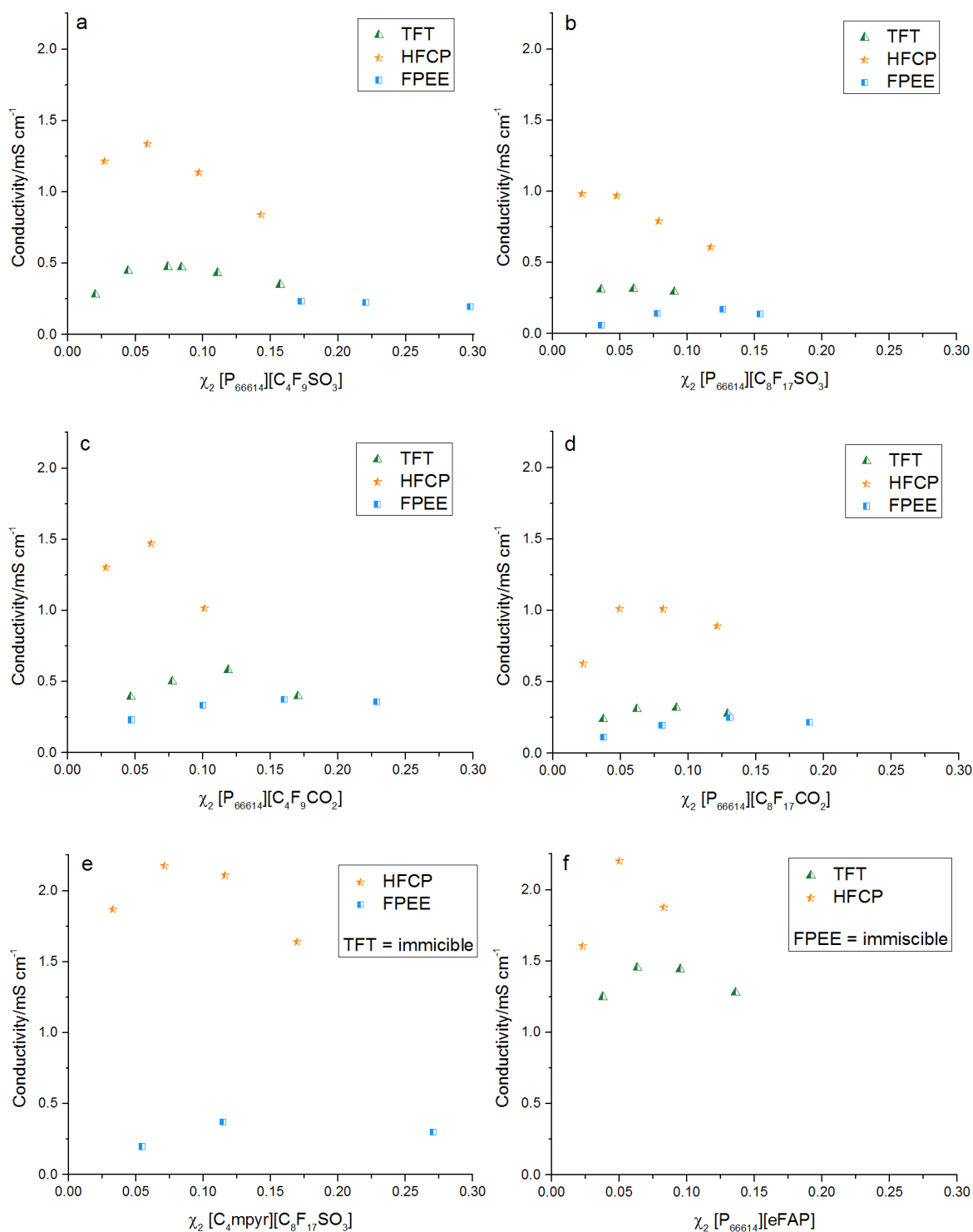


Figure 11a–f: Plot of ionic conductivity of IL–fluorinated solvent mixtures: a) $[P_{66614}][C_4F_9SO_3]$, b) $[P_{66614}][C_8F_{17}SO_3]$, c) $[P_{66614}][C_4F_9CO_2]$, d) $[P_{66614}][C_8F_{17}CO_2]$, e) $[C_4mpyr][C_8F_{17}SO_3]$, and f) $[P_{66614}][eFAP]$, as a function of mole fraction, χ_2 , with TFT (\blacktriangle), HFCP (\star), and FPEE (\blacksquare) at 25 °C.

All ILs are found to be miscible with HFCP whilst $[C_4mpyr][C_8F_{17}SO_3]$ and $[P_{66614}][eFAP]$ are not miscible in TFT and FPEE respectively. Interestingly, the $[P_{66614}][C_4F_9SO_3]$ –FPEE mixture shows limited miscibility at $\chi_2 < 0.17$ whereas the $[P_{66614}][C_4F_9CO_2]$ –FPEE mixture is

miscible across all low χ_2 compositions. This suggests an effect due to the structural arrangement of the anion (e.g. tetrahedral versus trigonal planar for the sulfonate and carboxylate anion respectively) since the fluoroalkyl chain is the same in both of these anions. All $[P_{66614}]^+$ -based mixtures with HFCP are found to exhibit the highest ionic conductivities, followed by mixtures with TFT, and then FPEE. Approximate values of the near-optimum ionic conductivity of each IL–fluorinated solvent mixture are shown in Figure 12, where “near-optimum” indicates the highest value observed in the concentrations studied. As a result, this value does not indicate the highest value of ionic conductivity nor the absolute χ_2 IL composition; nevertheless, further optimization to find the absolute maximum would no doubt produce higher values (although not by more than 10%).

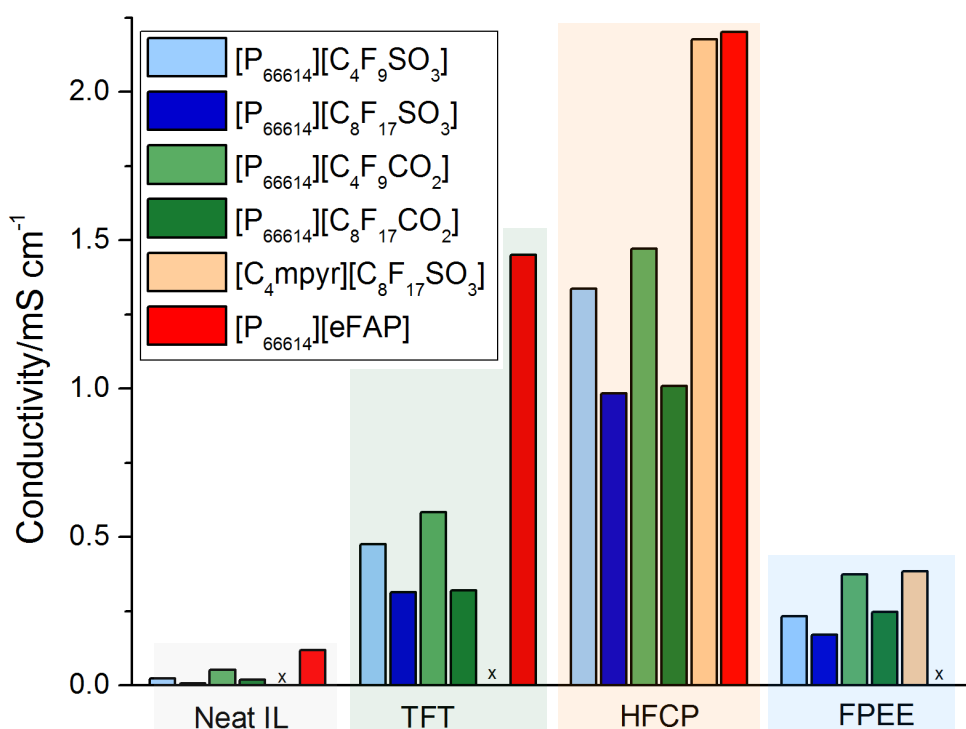


Figure 12: Near-optimum ionic conductivity of each IL–fluorinated solvent mixture system. The symbol X indicates immiscibility at the concentration range studied.

The ionic conductivity of $[C_4mpyr][C_8F_{17}SO_3]$ -fluorinated solvent mixtures are ~2 times higher compared to $[P_{66614}][C_8F_{17}SO_3]$ -fluorinated solvent mixtures likely due to the smaller size of the pyrrolidinium cation. In addition, when the perfluoroalkyl chain on the anion is shorter, these mixtures show higher near-optimum ionic conductivities (e.g. 1.3 mS cm⁻¹ and

1.0 mS cm⁻¹ with [P₆₆₆₁₄][C₄F₉SO₃] and [P₆₆₆₁₄][C₈F₁₇SO₃] respectively). In terms of the [eFAP]⁻ anion, [P₆₆₆₁₄][eFAP]–fluorinated solvent mixtures exhibit ionic conductivities approximately 1.5–2 times higher than the perfluorosulfonate and perfluorocarboxylate–based fluorinated solvent mixtures.

In all cases, each of the IL mixtures that consist of HFCP as the fluorinated solvent, show the largest improvement in ionic conductivity. This is unexpected since the viscosity of HFCP is almost three times larger than TFT (1.59 mPa s versus 0.58 mPa s respectively, at 25 °C).⁷ Usually, one would expect that a solvent with a lower viscosity produce a mixture with a higher ionic conductivity; therefore, this suggests differing ion dissociation effects with IL–HFCP versus IL–TFT mixtures. FPPE on the other hand, exhibits a larger viscosity of 2.36 mPa s at 25 °C, where IL–FPPE mixtures exhibit the lowest ionic conductivities. Further discussion is presented with the Walden plot in Figure 14a–f below.

4.5.2 Viscosity

Figure 13a–f shows the plot of viscosity versus the χ_2 composition of IL–fluorinated solvent mixtures. Upon addition of the fluorinated solvent to the neat IL, the viscosity declines as χ_2 approaches 0, toward the neat fluorinated solvent. Although large differences are observed in the viscosity of the neat ILs, these differences become much smaller when dissolved into a fluorinated solvent. The viscosity of the neat solvents ($\chi_2 = 0$) follow the order of highest viscosity FPPE > HFCP > TFT. The viscosity of these mixtures do not always follow the order of neat solvent viscosity on the basis of χ_2 . For example in Figure 13c, the [P₆₆₆₁₄][C₄F₉CO₂]–HFCP mixture displays a higher viscosity than the [P₆₆₆₁₄][C₄F₉CO₂]–FPPE mixture at $\chi_2 = 0.1$ even though the viscosity of FPPE is higher than HFCP. Shown in Supporting Figure S2a–f, the viscosity of these mixtures are plotted against the mass fraction (of [C₄mpyr][eFAP]), wt₂ where the IL mixtures do in fact follow the order of neat solvent viscosity. This suggests that the effect of mass (or volume) fraction of IL impacts the viscosity more strongly than the χ_2 of IL.

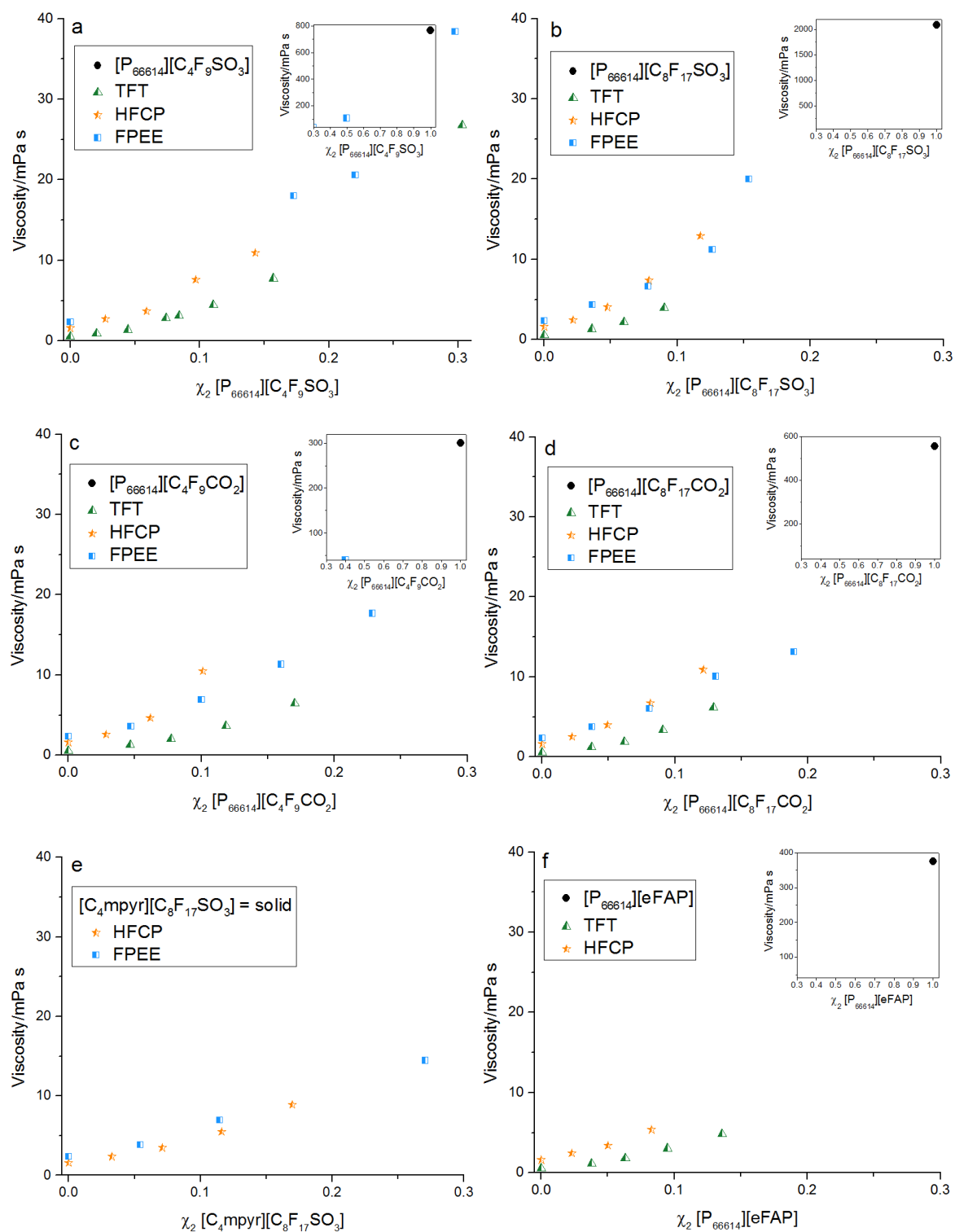


Figure 13a–f: Viscosity of IL–fluorinated solvent mixtures: a) $[P_{66614}][C_4F_9SO_3]$, b) $[P_{66614}][C_8F_{17}SO_3]$, c) $[P_{66614}][C_4F_9CO_2]$, d) $[P_{66614}][C_8F_{17}CO_2]$, e) $[C_4mpyr][C_8F_{17}SO_3]$, and f) $[P_{66614}][eFAP]$, as a function of mole fraction, χ_2 , with TFT (▲), HFCP (★), and FPEE (■) at 25 °C. Insets show the viscosity of the neat IL.

4.5.3 Walden Plot

Figure 14a—f shows the Walden plot with the neat IL itself and its IL–fluorinated solvent mixtures. It is important to note that the ionicity behaviour of some IL–fluorinated solvent mixtures is dependent on the concentration of IL and typical ion pairing/aggregation effects may not be obvious at relatively higher concentrations.²¹⁹ Nonetheless in all of the IL mixtures with HFCP, the degree of ionicity is relatively constant at all concentrations studied (i.e. all data points lie above the 10% ionisation line). This higher degree of ionicity with IL–HFCP mixtures (compared to IL–TFT and IL–FPPE mixtures) can also explain the higher ionic conductivity values observed previously. This suggests that HFCP is a better solvent in terms of screening the electrostatic attractions between the dissolved ions, resulting in better ion dissociation (and thus, higher ionic conductivity). While it would be useful to know the dielectric constants of HFCP and FPPE, they are not known in the literature and were beyond our capabilities to measure. However, based on the data from the Walden plot, HFCP likely exhibits a higher dielectric constant followed by FPPE and then TFT.

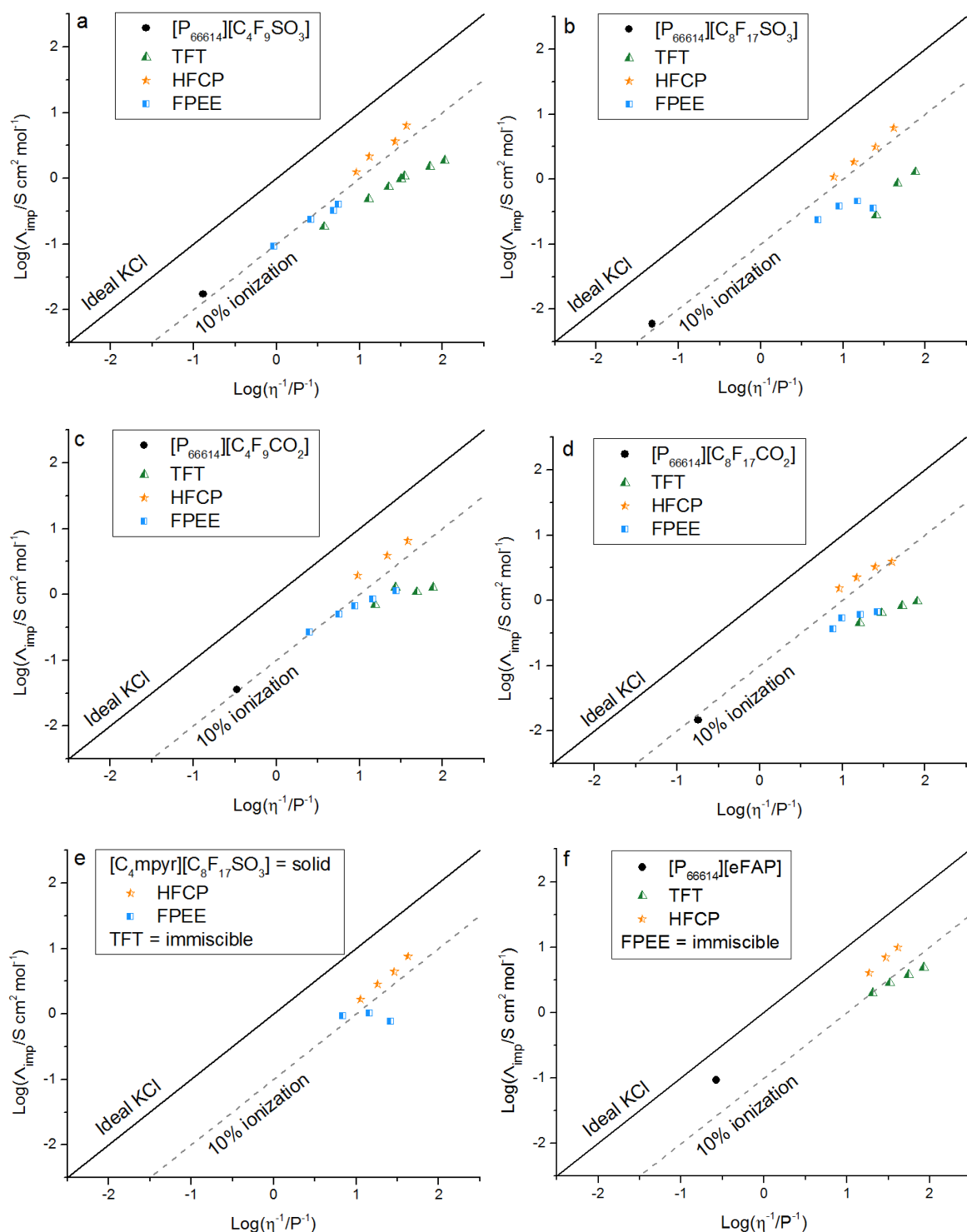


Figure 14a–f: Walden plot of IL–fluorinated solvent mixtures: a) $[P_{66614}][C_4F_9SO_3]$, b) $[P_{66614}][C_8F_{17}SO_3]$, c) $[P_{66614}][C_4F_9CO_2]$, d) $[P_{66614}][C_8F_{17}CO_2]$, e) $[C_4mpyr][C_8F_{17}SO_3]$, and f) $[P_{66614}][eFAP]$ in various compositions with TFT (\blacktriangle), HFCEP (\star), and FPEE (\blacksquare) at 25 °C.

In addition to the solvent, the ionicity of the IL itself plays a role in the ionicity of the IL–fluorinated solvent mixture. Here, $[P_{66614}][eFAP]$ displays the highest degree of ionicity compared to the perfluorosulfonate and perfluorocarboxylate–based ILs; subsequently a higher

degree of ionicity is found with [P₆₆₆₁₄][eFAP]–TFT, compared to the other IL–TFT mixtures. In some cases, IL–HFCP mixtures display a higher degree of ionicity compared to the neat IL such that HFCP aids in ion dissociation of the neat IL. In contrast, IL mixtures with TFT, and FPEE (both solvents which likely exhibit lower dielectric constants) do not show any improvement in ionicity at the concentration ranges studied.

In summary, IL mixtures with TFT, HFCP, and FPEE reduced the viscosity of ILs and enhanced ionic conductivity. These results showed that the choice of IL (cation, anion and the combination of such), the choice of solvent (based on its viscosity, dielectric constant) and the interplay between these parameters all had an effect on the transport properties of IL–fluorinated solvent mixtures. Based on the data presented in this chapter, ILs (and their mixtures) that contained the [eFAP][−] anion showed optimal mass transport behaviour.

4.6 Conclusions

This chapter described some of the requirements in the design of a fluorinated IL–based electrolyte by the selection of fluorinated solvent and the fluorinated IL. A range of solvents of different functionality, and various classes of ILs were investigated, where some of these ILs (and solid salts) were found to be miscible with fluorinated solvents (that had some degree of C–H functionality) to produce fluorinated IL–based electrolytes. The successful synthesis of novel phosphonium [eFAP][−]–based ILs resulted in two solids ([P₁₂₂₂][eFAP] which exhibits featured of plastic crystal behaviour) and two liquids at room temperature ([P_{122i4}][eFAP] which displayed excellent transport properties for an IL with high degree of fluorination). These IL electrolytes showed great potential for use in NRR and other electrochemical applications such as lithium batteries.

For the purpose of electrochemical NRR, some rational design principles were developed in order to achieve high N₂ solubility in IL electrolytes involving: i) reducing the alkyl chain length on the phosphonium cation to reduce the overall cohesive energy density of the IL (to

an optimum with $[P_{1444}]^+$) whilst increasing the volume fraction of the fluorinated domains (and possible free volume), ii) the addition of fluorinated solvents to produce a fluorinated IL-based electrolyte, and iii) the selection of a high N_2 soluble IL with an optimal volumetric composition.

The transport properties of phosphonium $[eFAP]^-$ –TFT mixtures were also examined where it was found that ILs that contained smaller sized phosphonium cations, tended to exhibit higher ionic conductivities. Moreover, the composition of IL, near the maximum in ionic conductivity, was different depending on the IL (and fluorinated solvent) itself; this was of high importance since an optimum composition of IL would ideally lie near the region where N_2 solubility is high. IL–TFT mixtures that had branched alkyl chains on the phosphonium cation displayed a higher degree of ionicity (and thus, ionic conductivity) than those with linear alkyl chains.

Lastly, the transport properties of a series of $[P_{66614}]^+$ –based IL mixtures were investigated in three fluorinated solvents: TFT, HFCE and FPEE. Trends in ionicity had shown that HFCE was the better solvent due to its higher near-optimum ionic conductivities. In terms of the fluorinated anions used in this chapter, ILs that contained the $[eFAP]^-$ anion exhibited faster mass transport, which was evident by higher ionic conductivities and a higher degree of ionicity. The study of these fluorinated IL-based electrolytes provides the fundamental knowledge to further develop fluorinated IL-based electrolytes, some of which, shown in this chapter, already show great promise for use in electrochemical NRR.

4.7 Supporting Information

4.7.1 Synthesis and Characterisation

Triisobutyl(methyl)phosphonium tris(pentafluoroethyl)trifluorophosphate $[P_{1i4i4i4}][eFAP]$

Triisobutyl(methyl)phosphonium tosylate (20% excess) was added to $[C_2mim][eFAP]$, water and dichloromethane, and stirred overnight under N_2 . After extraction of the DCM layer and drying in vacuo, afforded a white solid (96%).

^1H NMR (400 MHz, CDCl_3) δ ppm: 1.12—1.14 (18H, d), 1.81—1.84 (3H, d), 1.79—1.83 (3H, d), 1.99—2.09 (6H, m), 1.99—2.09 (3H, m). ^{19}F NMR (376 MHz, CDCl_3) δ ppm: -43.5—(-45.9) (1F, m), -80.2—(-80.1) (3F, m), -81.7—(-81.8) (6F, m), -86.8—(-86.7) (1F, m), -89.2—(-89.1) (1F, m), -116.1—(-115.4) (6F, m). ^{31}P NMR (162 MHz, CDCl_3) δ ppm: 28.1 (1P, s), -153.6—(-134.7) (1P, (q)m). ES-MS: ES+ m/z 218 P_{1444}^+ , ES- m/z 445 eFAP $^-$

Tributyl(methyl)phosphonium tris(pentafluoroethyl)trifluorophosphate [P_{1444}][eFAP]

Tributyl(methyl)phosphonium methylsulfate (20% excess) was added to $[\text{C}_2\text{mim}][\text{eFAP}]$, water and dichloromethane, and stirred overnight under N_2 . After extraction of the DCM layer and drying in vacuo, afforded a colourless liquid (95%)

^1H NMR (400 MHz, CDCl_3) δ ppm: 0.95—0.98 (9H, m), 1.46—1.50 (12H, m), 1.79—1.83 (3H, d), 1.98—2.05 (6H, m). ^{19}F NMR (376 MHz, CDCl_3) δ ppm: -43.5—(-45.9) (1F, m), -80.2—(-80.1) (3F, m), -81.7—(-81.8) (6F, m), -86.8—(-86.7) (1F, m), -89.2—(-89.1) (1F, m), -116.1—(-115.4) (6F, m). ^{31}P NMR (162 MHz, CDCl_3) δ ppm: 31.3 (1P, s), -156.4—(-138.0) (1P, (q)m). ES-MS: ES+ m/z 218 P_{1444}^+ , ES- m/z 445 eFAP $^-$

Methyl(diethyl)isobutylphosphonium tris(pentafluoroethyl)trifluorophosphate [P_{1224}][eFAP]

Methyl(diethyl)isobutylphosphonium tosylate (20% excess) was added to $[\text{C}_2\text{mim}][\text{eFAP}]$, water and dichloromethane, and stirred overnight under N_2 . Extraction and metathesis reactions were repeated several times to drive the reaction to completion, each time with the addition of methyl(diethyl)isobutylphosphonium tosylate (based on NMR integrations). After extraction of the DCM layer and drying in vacuo, afforded a colourless liquid (95%).

^1H NMR (400 MHz, DMSO) δ ppm: 1.02—1.04 (6H, m), 1.09—1.18 (6H, m), 1.79—1.83 (3H, d), 1.95—2.08 (1H, m), 2.12—2.25 (6H, m). ^{19}F NMR (376 MHz, DMSO) δ ppm: -45.6—(-42.8) (1F, m), -79.6—(-79.4) (3F, m), -81.1—(-81.0) (6F, m), -86.3—(-86.2) (1F, m), -88.7—(-88.6) (1F, m), -116.2—(-115.4) (6F, m). ^{31}P NMR (162 MHz, DMSO) δ ppm: 34.9 (1P, s), -158.7—(-140.2) (1P, (q)m). ES-MS: ES+ m/z 161 P_{1224}^+ , ES- m/z 445 eFAP $^-$

Triethyl(methyl)phosphonium tris(pentafluoroethyl)trifluorophosphate [P_{1222}][eFAP]

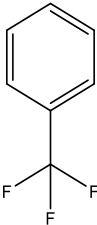
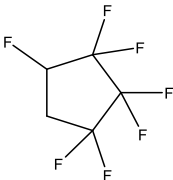
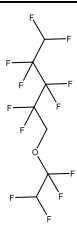
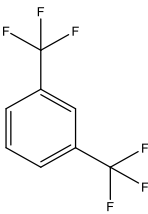
Triethyl(methyl)phosphonium dimethylphosphate (20% excess) was added to $[\text{C}_2\text{mim}][\text{eFAP}]$, water and dichloromethane, and stirred overnight under N_2 . Extraction and

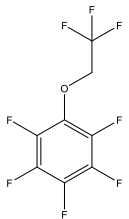
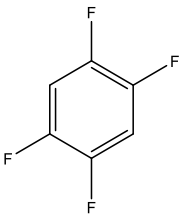
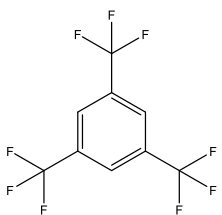
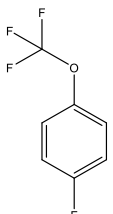
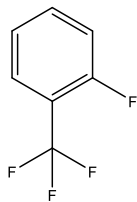
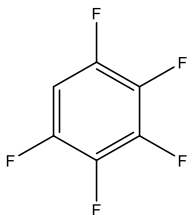
metathesis reactions were repeated several times to drive the reaction to completion, each time with the addition of methyl(diethyl)isobutylphosphonium tosylate (based on NMR integrations). After extraction of the DCM layer and drying in vacuo, afforded a white solid (79%).

^1H NMR (400 MHz, DMSO) δ ppm: 1.08—1.17 (9H, m), 1.75—1.78 (3H, d), 2.13—2.22 (6H, m), ^{19}F NMR (376 MHz, DMSO) δ ppm: -45.6—(-42.8) (1F, m), -79.6—(-79.4) (3F, m), -81.1—(-81.0) (6F, m), -86.3—(-86.2) (1F, m), -88.7—(-88.6) (1F, m), -116.3—(-115.4) (6F, m). ^{31}P NMR (162 MHz, DMSO) δ ppm: 37.9 (1P, s), -158.6—(-143.4) (1P, (q)m). ES-MS: ES+ m/z 133 P_{1222}^+ , ES- m/z 445 eFAP^-

4.7.2 Supporting Figures and Tables

Supporting Table S1: Properties of fluorinated solvents used in this study.

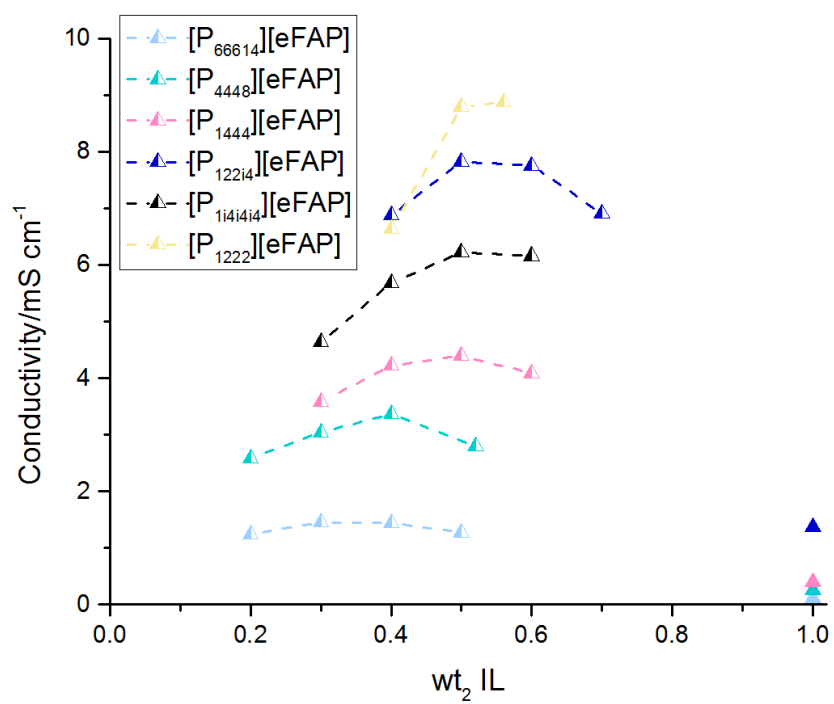
Solvent	Structure	B.P /°C	Temperature /°C	Density /g cm ⁻³	Viscosity /mPa s
σ, σ, σ -trifluorotoluene (TFT)		102	25	1.1811	0.59
			30	1.1741	0.56
			35	1.1670	0.53
			40	1.1598	0.50
			45	1.1526	0.48
			50	1.1454	0.46
1H,1H,2H- heptafluorocyclopentane (HFCP)		83	25	1.5738	1.59
			30	1.5629	1.45
			35	1.5520	1.37
			40	1.5410	1.20
			45	1.5299	1.12
			50	1.5187	1.08
1H,1H,5H-octafluoropentyl 1,1,2,2-tetrafluoroethyl ether (FPPE)		133	25	1.6433	2.36
			30	1.6328	2.11
			35	1.6223	1.90
			40	1.6117	1.72
			45	1.6011	1.57
			50	1.5904	1.43
1,3- bis(trifluoromethyl)benzene		116	25	1.3833	0.83
			30	1.3746	0.78
			35	1.3659	0.73
			40	1.3572	0.69
			45	1.3484	0.65
			50	1.3395	0.61

(2,2,2-trifluoroethoxy) pentafluorobenzene		147	25	1.6061	1.62
			30	1.5969	1.48
			35	1.5876	1.36
			40	1.5784	1.25
			45	1.5691	1.16
			50	1.5598	1.08
1,2,4,5-tetrafluorobenzene		95	25	1.4177	0.77
			30	1.4088	0.72
			35	1.3999	0.68
			40	1.3909	0.64
			45	1.3819	0.61
			50	1.3728	0.57
Tris(trifluoro)toluene		120	25	1.5142	1.47
			30	1.5044	1.32
			35	1.4946	1.22
			40	1.4846	1.13
			45	1.4745	1.05
			50	1.4643	0.95
1-Fluoro-4-(trifluoroethoxy)benzene		105	25	1.3210	0.90
			30	1.3128	0.83
			35	1.3045	0.78
			40	1.2962	0.72
			45	1.2878	0.68
			50	1.2794	0.65
2-fluoro-benzotrifluoride		115	25	1.3021	0.76
			30	1.2945	0.73
			35	1.2869	0.68
			40	1.2792	0.66
			45	1.2715	0.62
			50	1.2637	0.58
Pentafluorobenzene		85	25	1.5111	0.81
			30	1.5011	0.76
			35	1.4911	0.71
			40	1.4810	0.67
			45	1.4709	0.63
			50	1.4606	0.59

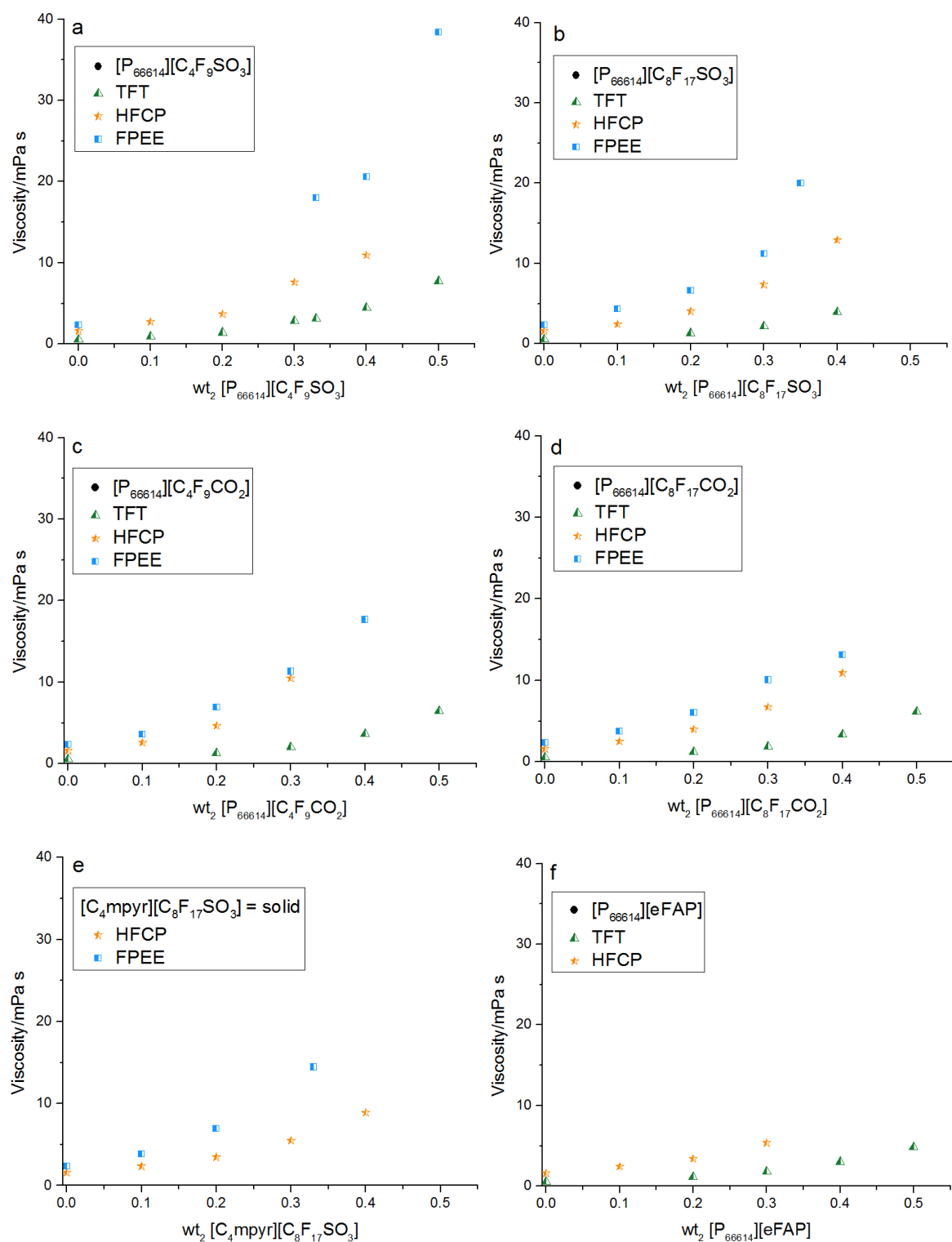
Supporting Table S2: Experimental values of N_2 solubility, corrected to a partial pressure of $p = 1$ atm where p_{eq} is the experimental equilibrium pressure, in fluorinated IL-based binary mixtures at 30°C, as a function of IL mass fraction, wt_2 , volume fraction, Φ , and mole fraction, χ_2 , expressed as molar concentration, C_{N_2} , mole fraction, χ_{2,N_2} , and molal concentration, b_{N_2} .

Sample Mixture	wt_2	Φ	χ_2	p_{eq} / 10^4 Pa	p_{sample} / 10^4 Pa	C_{N_2} /mmol L ⁻¹	χ_{2,N_2} / 10^{-3}	b_{N_2} /mmol kg ⁻¹
----------------	--------	--------	----------	-------------------------	-----------------------------	------------------------------------	-------------------------------	-------------------------------------

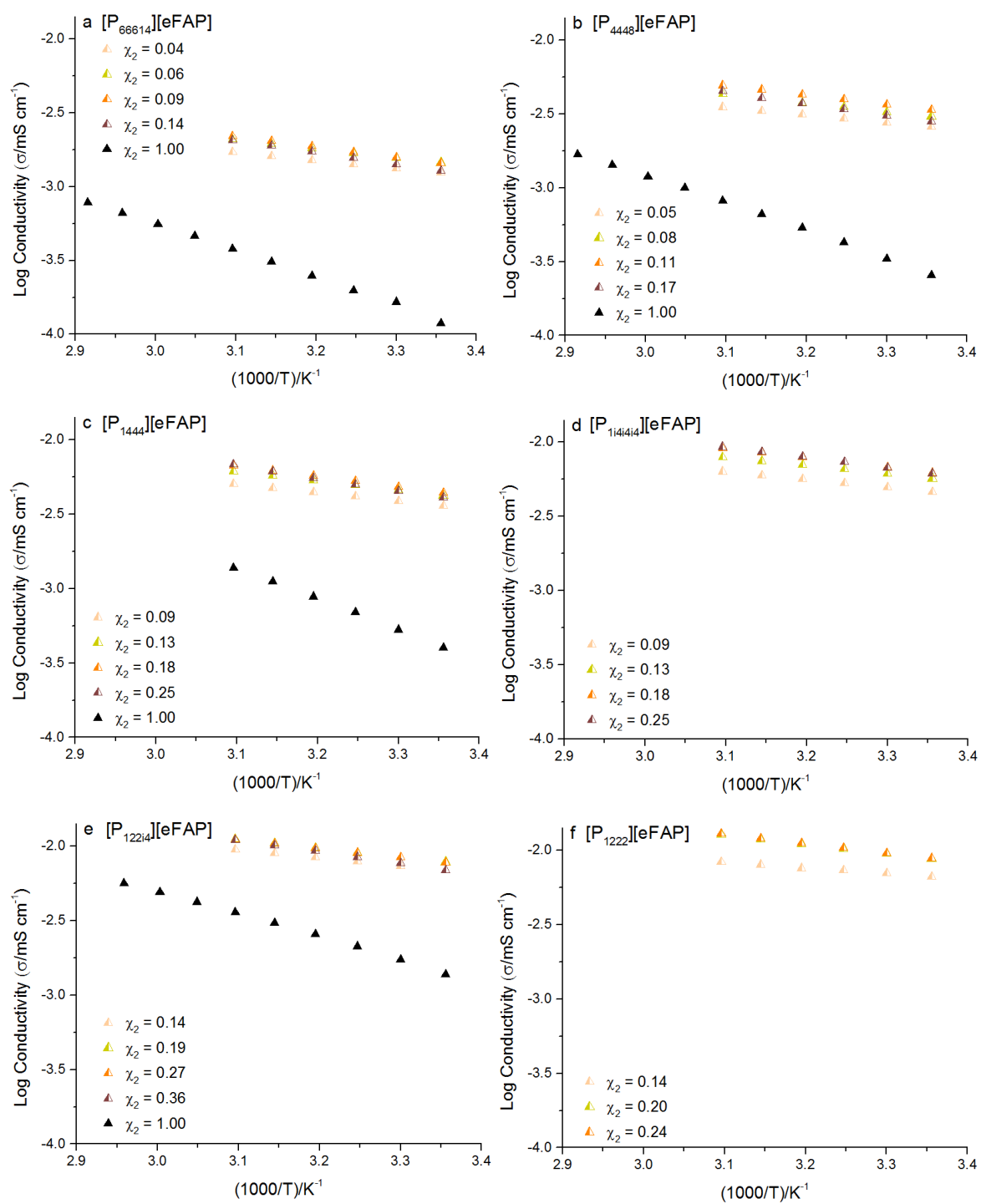
[P ₆₆₆₁₄][eFAP]	1.00	1.00	1.00	9.64	-	4.1	3.2	3.5
	1.00	1.00	1.00	9.60	-	4.4	3.4	3.7
[P ₆₆₆₁₄][eFAP]/TFT	0.50	0.49	0.14	8.96	0.61	7.8	1.7	6.5
	0.50	0.49	0.14	8.94	0.70	7.8	1.6	6.6
[P ₄₄₄₈][eFAP]	1.00	1.00	1.00	8.34	-	5.3	3.1	4.1
	1.00	1.00	1.00	9.77	-	5.2	3.1	4.0
[P ₄₄₄₈][eFAP]/TFT	0.52	0.49	0.17	9.34	0.67	7.5	1.2	6.0
	0.52	0.49	0.17	9.35	0.68	7.3	1.2	5.9
[P ₁₄₄₄][eFAP]	1.00	1.00	1.00	9.74	-	5.9	2.7	4.2
	1.00	1.00	1.00	9.77	-	5.8	2.7	4.1
[P ₁₄₄₄][eFAP]/TFT	0.54	0.49	0.21	9.00	0.62	8.1	1.6	6.2
	0.54	0.49	0.21	8.94	0.65	8.3	1.6	6.4
[P _{1i4i4i4i4}][eFAP]/TFT	0.54	0.49	0.22	9.24	0.60	7.0	1.3	5.3
	0.54	0.49	0.22	9.18	0.70	7.0	1.4	5.4
[P _{122i4}][eFAP]	1.00	1.00	1.00	10.27	-	5.4	2.2	3.6
	1.00	1.00	1.00	10.14	-	5.5	2.2	3.6
[P _{122i4}][eFAP]/TFT	0.56	0.49	0.23	9.41	0.67	6.7	1.3	4.9
	0.56	0.49	0.23	9.44	0.70	6.7	1.3	4.9
[P ₁₂₂₂][eFAP]/TFT	0.56	0.49	0.24	8.72	0.64	6.9	0.9	5.0
	0.56	0.49	0.24	8.70	0.69	6.8	0.9	4.9
[P ₆₆₆₁₄][C ₈ F ₁₇ CO ₂]	1.00	1.00	1.00	9.35	-	6.5	5.3	5.6
	1.00	1.00	1.00	8.94	-	6.6	5.3	5.6
[P ₆₆₆₁₄][C ₈ F ₁₇ CO ₂]/HFCEP	0.43	0.51	0.10	8.79	1.16	9.3	2.0	6.9
	0.43	0.51	0.10	8.74	1.14	9.7	2.1	7.2
[P ₆₆₆₁₄][C ₈ F ₁₇ SO ₃]	1.00	1.00	1.00	9.69	-	6.4	5.3	5.5
	1.00	1.00	1.00	10.15	-	6.0	5.0	5.1
[P ₆₆₆₁₄][C ₈ F ₁₇ SO ₃]/HFCEP	0.43	0.50	0.10	8.83	1.21	8.9	1.9	6.5
	0.43	0.50	0.10	8.83	1.23	8.9	1.9	6.5



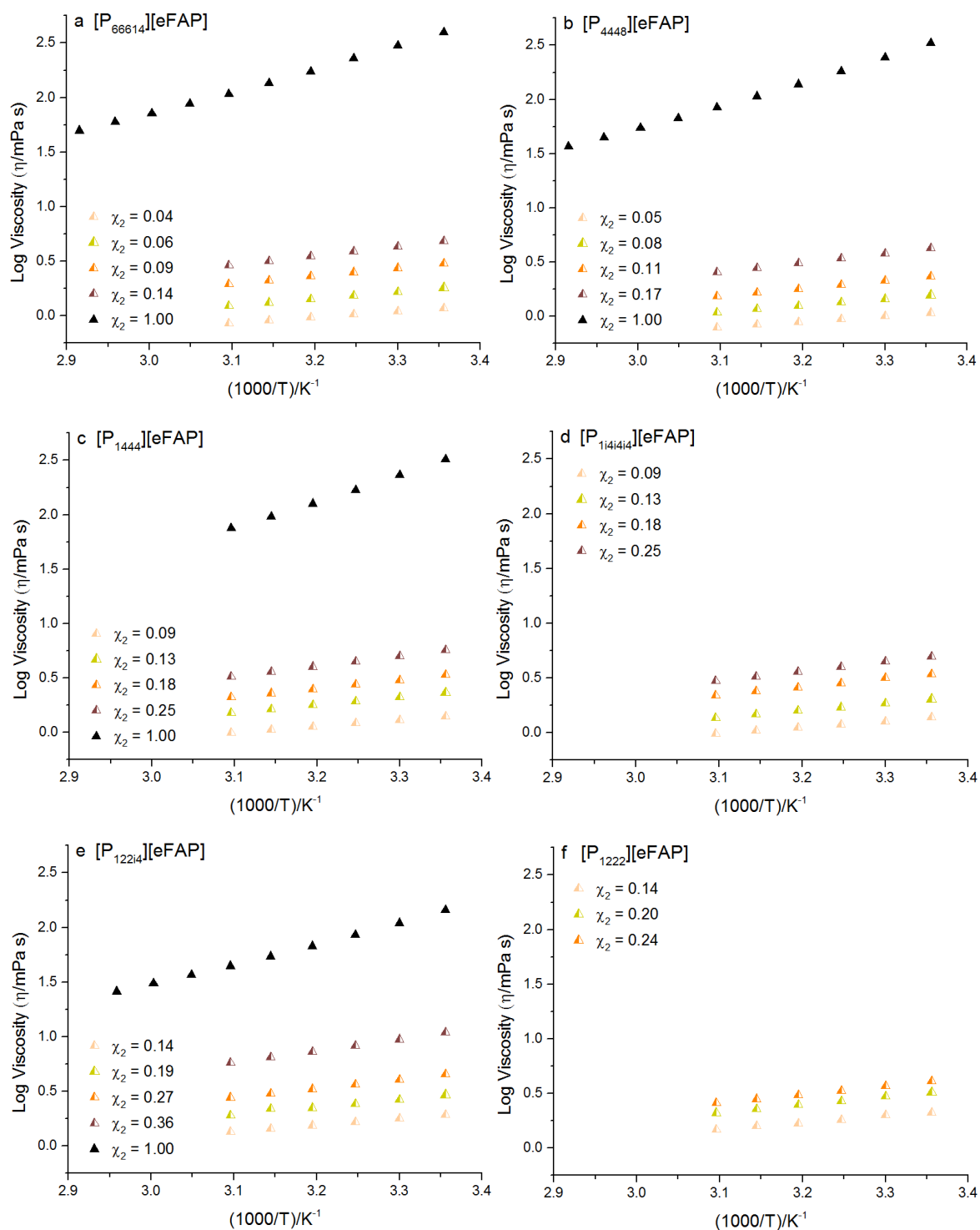
Supporting Figure S1: Ionic conductivity of IL–TFT mixtures, as a function of mass fraction, wt_2 , at 25 °C.



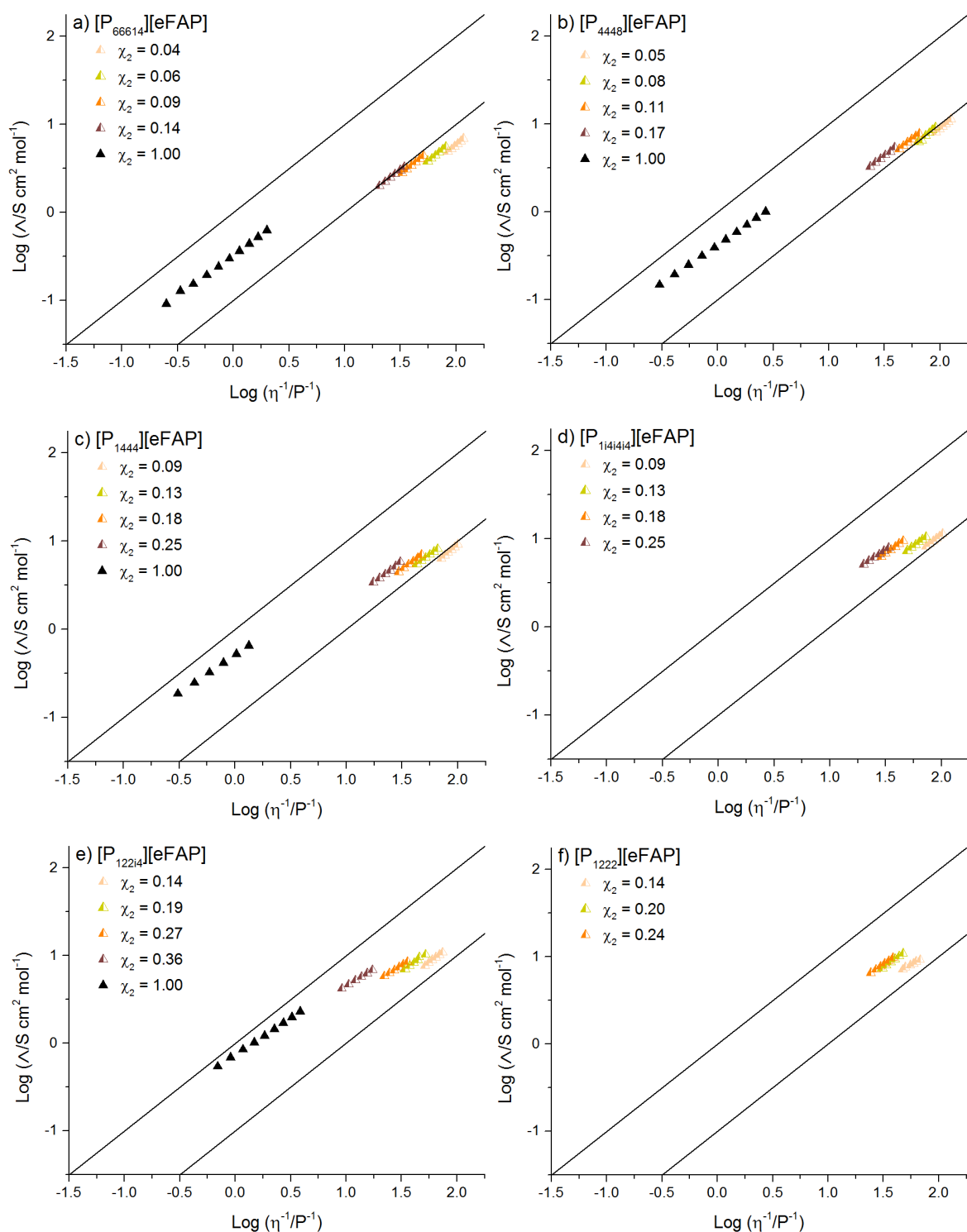
Supporting Figure S2a–f: Viscosity of IL–fluorinated solvent mixtures: a) [P₆₆₆₁₄][C₄F₉SO₃], b) [P₆₆₆₁₄][C₈F₁₇SO₃], c) [P₆₆₆₁₄][C₄F₉CO₂], d) [P₆₆₆₁₄][C₈F₁₇CO₂], e) [C₄mpyr][C₈F₁₇SO₃], and f) [P₆₆₆₁₄][eFAP], as a function of mass fraction, wt_2 , with TFT (▲), HFCEP (★), and FPEE (■) at 25 °C.



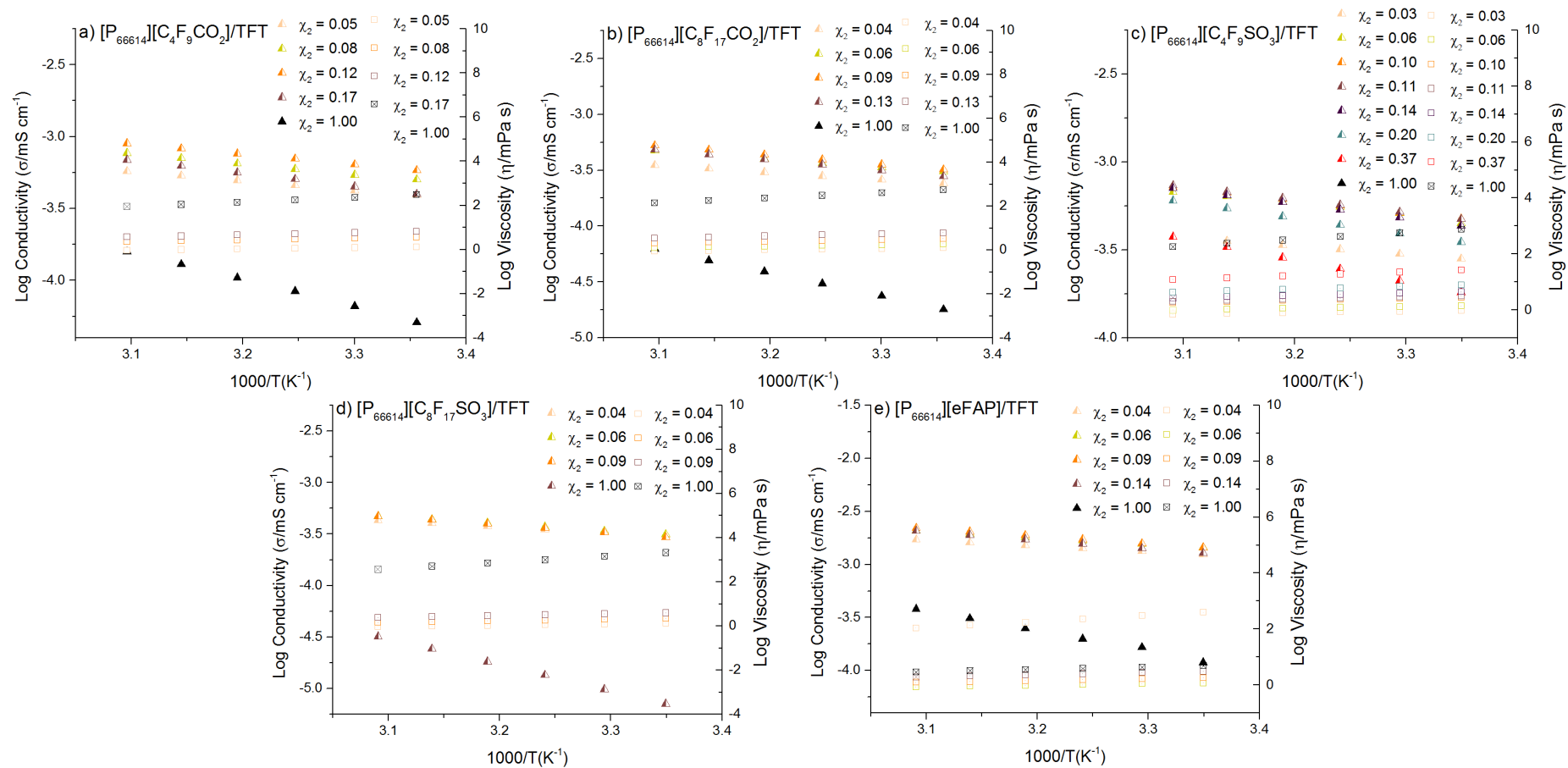
Supporting Figure 3a–f: Arrhenius plot of ionic conductivity of fluorinated IL–TFT mixtures of differing mole fraction composition with a) $[P_{66614}][eFAP]$, b) $[P_{4448}][eFAP]$, c) $[P_{1444}][eFAP]$, d) $[P_{1i4i4i4}][eFAP]$, e) $[P_{122i4}][eFAP]$, and f) $[P_{1222}][eFAP]$.



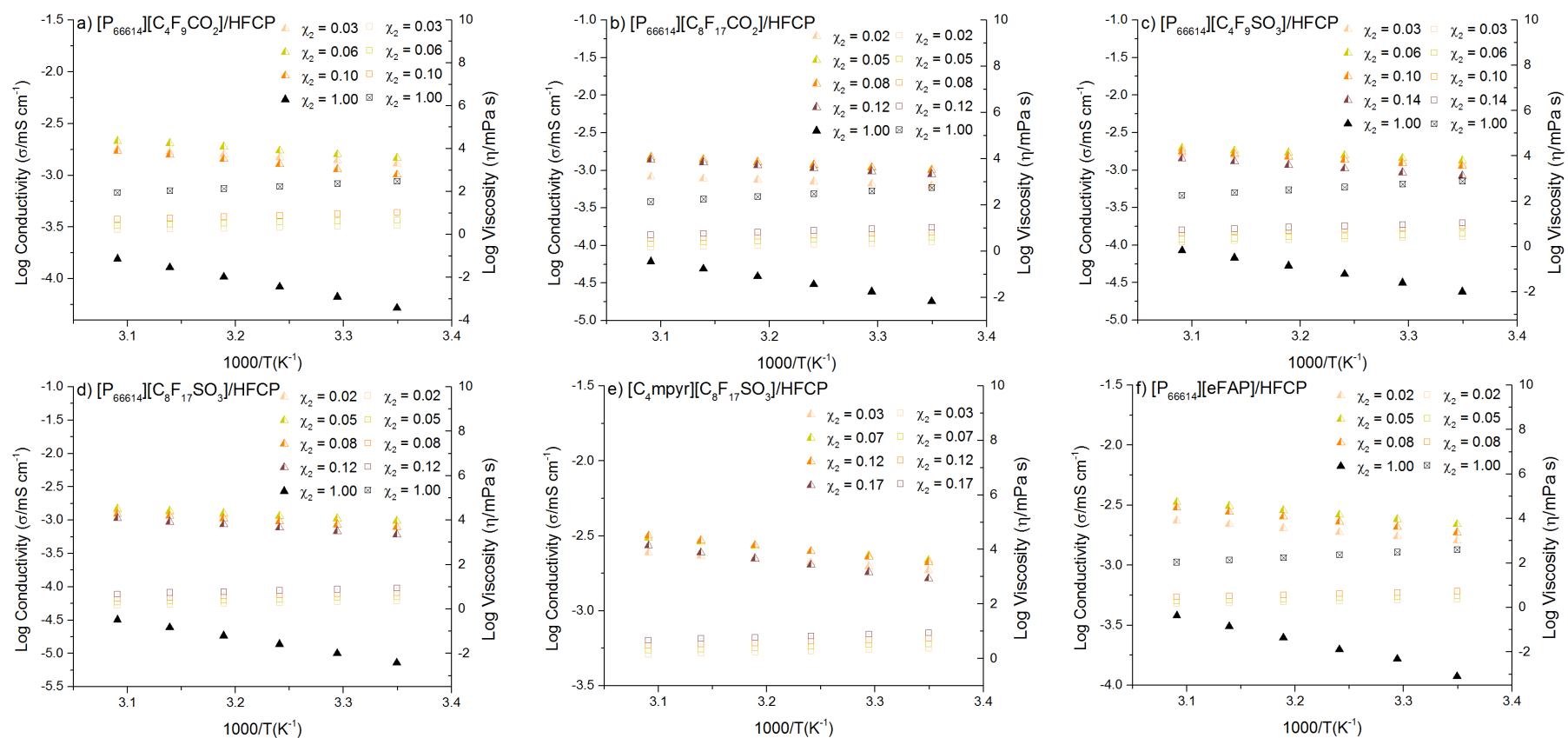
Supporting Figure 4a–f: Arrhenius plot of viscosity of fluorinated IL–TFT mixtures of differing mole fraction composition with a) $[P_{66614}][eFAP]$, b) $[P_{4448}][eFAP]$, c) $[P_{1444}][eFAP]$, d) $[P_{14i4i4}][eFAP]$, e) $[P_{122i4}][eFAP]$, and f) $[P_{1222}][eFAP]$.



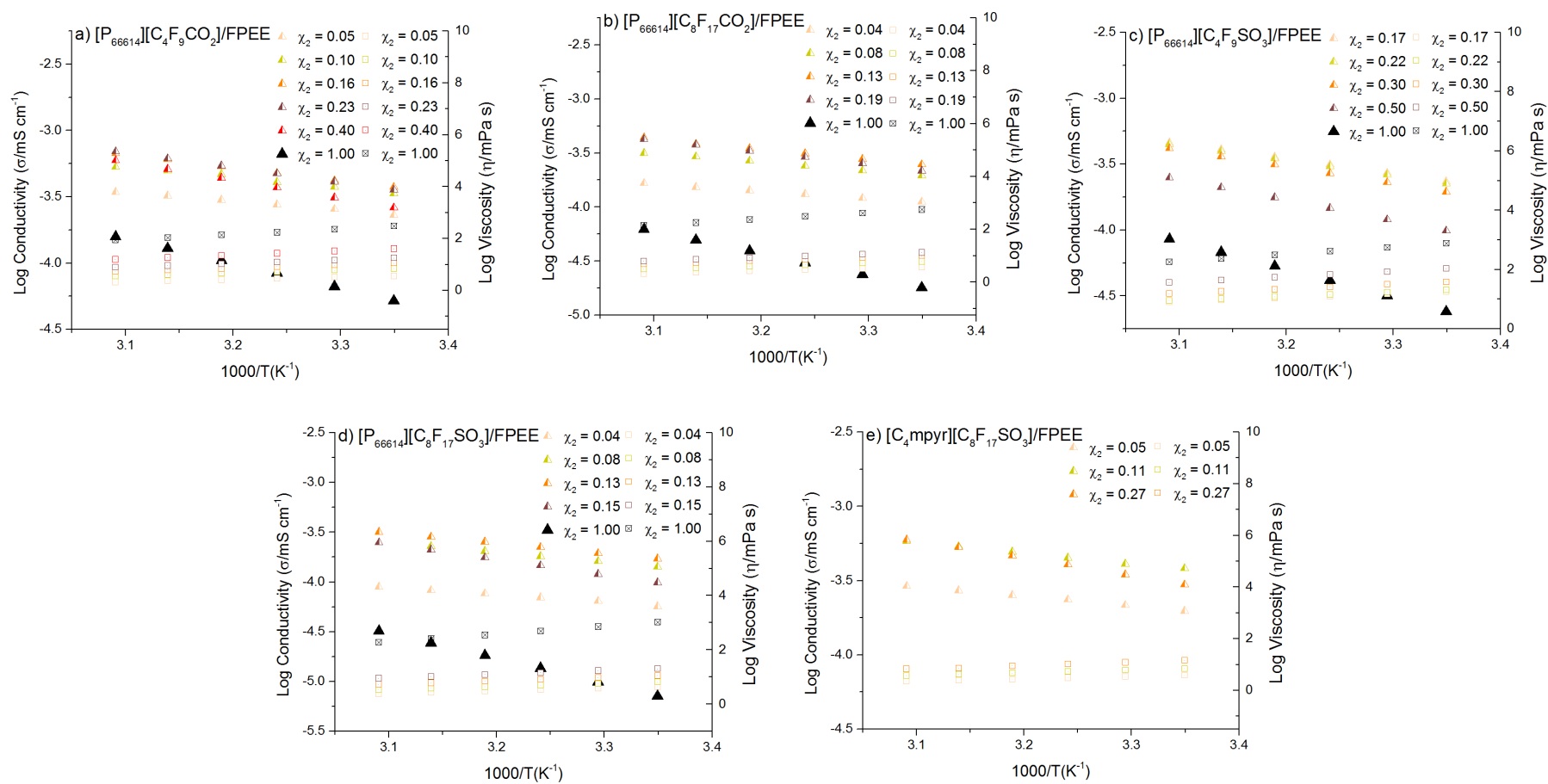
Supporting Figure 5a–f: Walden plot of fluorinated IL–TFT mixtures of differing mole fraction composition with a) $[P_{66614}][\text{eFAP}]$, b) $[P_{4448}][\text{eFAP}]$, c) $[P_{1444}][\text{eFAP}]$, d) $[P_{1i4i4i4}][\text{eFAP}]$, e) $[P_{122i4}][\text{eFAP}]$, and f) $[P_{1222}][\text{eFAP}]$ at 25 °C, 30 °C, 35 °C, 40 °C, 45 °C and 50 °C.



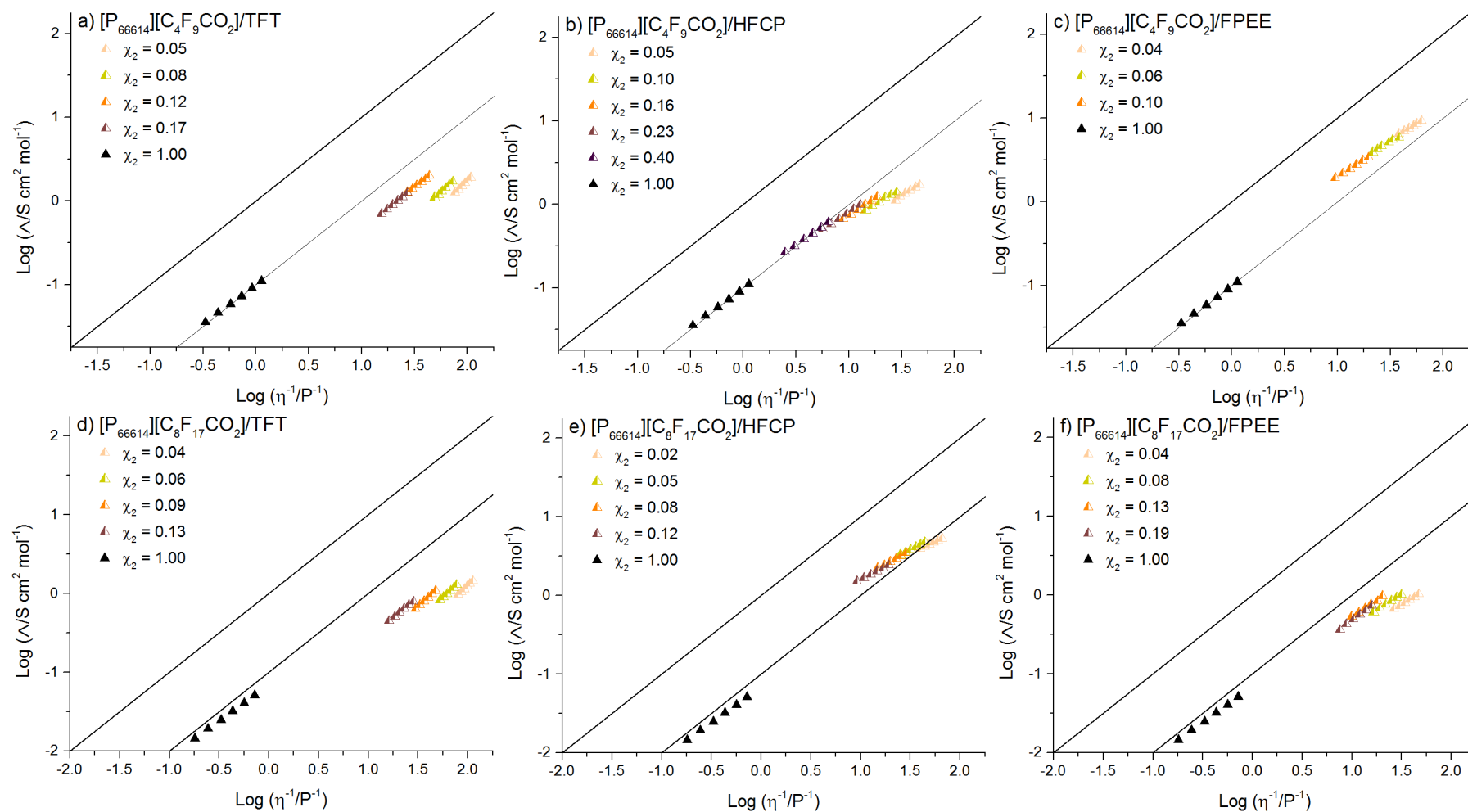
Supporting Figure 6a—e: Arrhenius plot of ionic conductivity (\blacktriangle) and viscosity (\blacksquare) of fluorinated IL-TFT mixtures of differing mole fraction composition with a) $[P_{66614}][C_4F_9CO_2]$, b) $[P_{66614}][C_8F_{17}CO_2]$, c) $[P_{66614}][C_4F_9SO_3]$, d) $[P_{66614}][C_8F_{17}SO_3]$ and e) $[P_{66614}][eFAP]$.



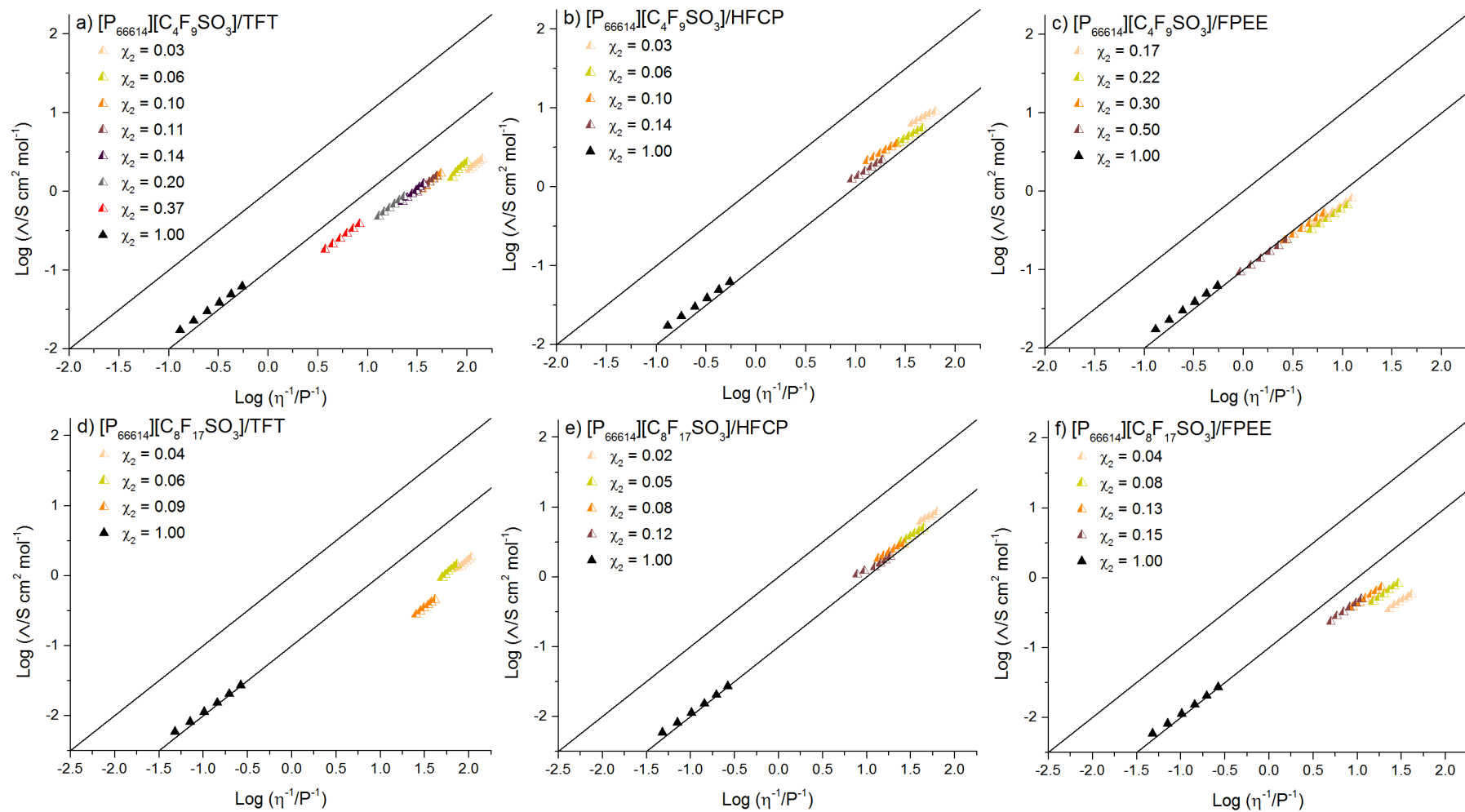
Supporting Figure 7a–f: Arrhenius plot of ionic conductivity (\blacktriangle) and viscosity (\blacksquare) of fluorinated IL–HFCP mixtures of differing mole fraction composition with a) $[P_{66614}][C_4F_9CO_2]$, b) $[P_{66614}][C_8F_{17}CO_2]$, c) $[P_{66614}][C_4F_9SO_3]$, d) $[P_{66614}][C_8F_{17}SO_3]$ and e) $[P_{66614}][eFAP]$.



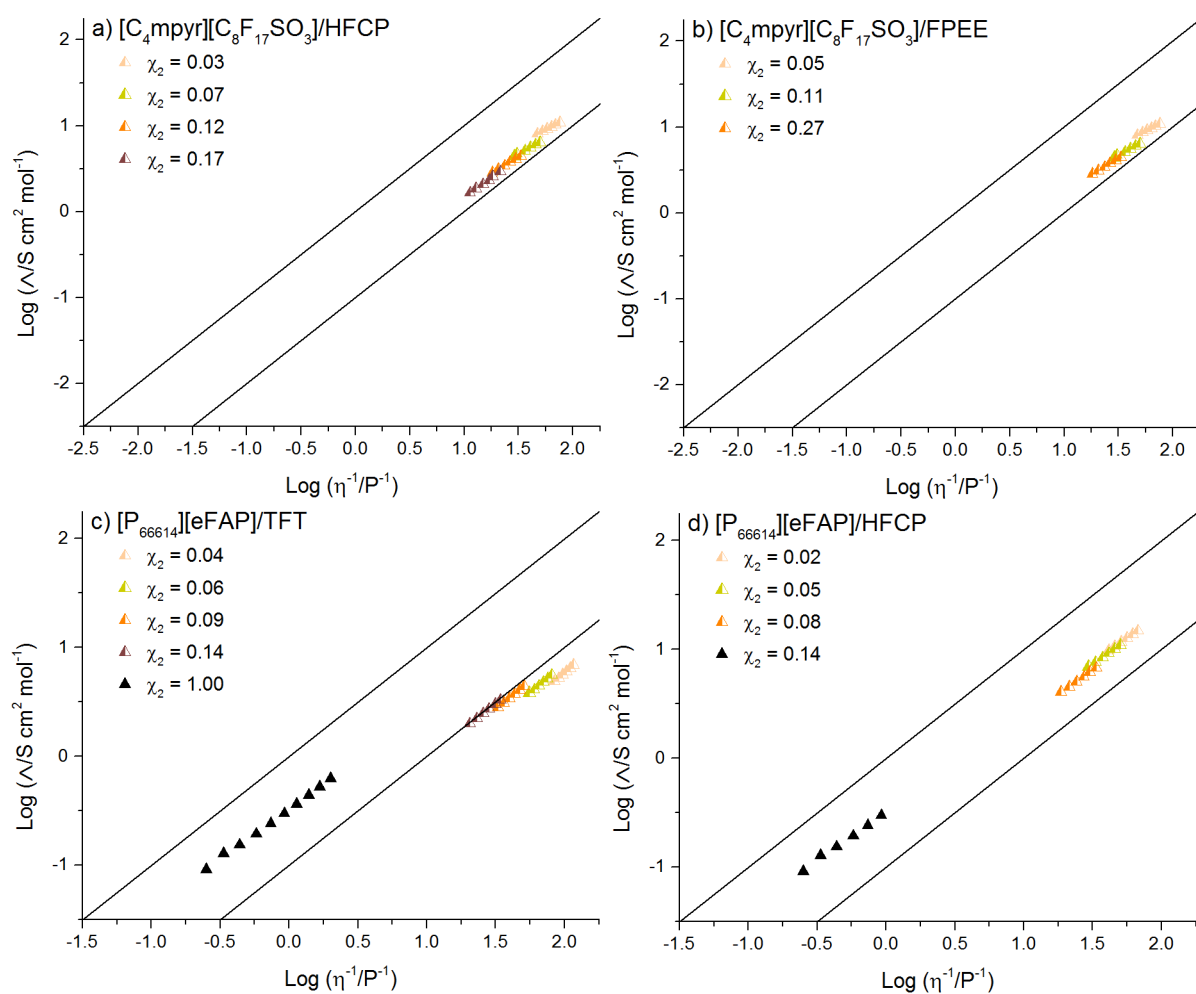
Supporting Figure 8a–e: Arrhenius plot of conductivity (\blacktriangle) and viscosity (\blacksquare) of fluorinated IL–FPEE mixtures of differing mole fraction composition with a) $[P_{66614}][C_4F_9CO_2]$, b) $[P_{66614}][C_8F_{17}CO_2]$, c) $[P_{66614}][C_4F_9SO_3]$, d) $[P_{66614}][C_8F_{17}SO_3]$ and e) $[P_{66614}][eFAP]$.



Supporting Figure 9a–f: Walden plot of fluorinated IL–fluorinated solvent mixtures of differing mole fraction composition with a) $[P_{66614}][C_4F_9CO_2]/TFT$, b) $[P_{66614}][C_4F_9CO_2]/HFCP$, c) $[P_{66614}][C_4F_9CO_2]/FPPE$, d) $[P_{66614}][C_8F_{17}CO_2]/TFT$, e) $[P_{66614}][C_8F_{17}CO_2]/HFCP$, and f) $[P_{66614}][C_8F_{17}CO_2]/FPPE$ at 25 °C, 30 °C, 35 °C, 40 °C, 45 °C and 50 °C.



Supporting Figure 10a—f: Walden plot of fluorinated IL–fluorinated solvent mixtures of differing mole fraction composition with a) $[P_{66614}][C_4F_9SO_3]/TFT$, b) $[P_{66614}][C_4F_9SO_3]/HFCEP$, c) $[P_{66614}][C_4F_9SO_3]/FPEE$, d) $[P_{66614}][C_8F_{17}SO_3]/TFT$, e) $[P_{66614}][C_8F_{17}SO_3]/HFCEP$, and f) $[P_{66614}][C_8F_{17}SO_3]/FPEE$ at 25 °C, 30 °C, 35 °C, 40 °C, 45 °C and 50 °C.



Supporting Figure 11a—d: Walden plot of fluorinated IL–fluorinated solvent mixtures of differing mole fraction composition with a) $[C_4\text{mpyr}][C_8F_{17}SO_3]/HFCEP$, b) $[C_4\text{mpyr}][C_8F_{17}SO_3]/FPEE$, c) $[P_{66614}][eFAP]/TFT$, d) $[P_{66614}][eFAP]/HFCEP$ at 25 °C, 30 °C, 35 °C, 40 °C, 45 °C and 50 °C. Fluorinated mixtures of $[P_{66614}][C_8F_{17}SO_3]/HFCEP$ and $[P_{66614}][C_8F_{17}SO_3]/FPEE$ were immiscible.

4.8 References

1. MacFarlane, D. R.; Chong, A. L.; Forsyth, M.; Kar, M.; Vijayaraghavan, R.; Somers, A.; Pringle, J. M., New Dimensions in Salt-Solvent Mixtures: A 4th Evolution of Ionic Liquids. *Faraday Discuss.* **2017**, *206*, 9—28.
2. Wilhelm, E.; Battino, R., Thermodynamic Functions of the Solubilities of Gases in Liquids at 25.Deg. *Chem. Rev.* **1973**, *73*, 1—9.
3. Welton, T., Room-Temperature Ionic Liquids. Solvents for Synthesis and Catalysis. *Chem. Rev.* **1999**, *99*, 2071—2084.
4. Stejskal, E. O.; Tanner, J. E., Spin Diffusion Measurements: Spin Echoes in the Presence of a Time-Dependent Field Gradient. *J. Chem. Phys.* **1965**, *42*, 288—292.
5. Holz, M.; Heil, S. R.; Sacco, A., Temperature-Dependent Self-Diffusion Coefficients of Water and Six Selected Molecular Liquids for Calibration in Accurate ¹H NMR PFG Measurements. *PCCP* **2000**, *2*, 4740—4742.
6. Kang, C. S. M.; Zhang, X.; MacFarlane, D. R., Synthesis and Physicochemical Properties of Fluorinated Ionic Liquids with High Nitrogen Gas Solubility. *J. Phys. Chem. C* **2018**, *122*, 24550—24558.
7. Kang, C. S. M.; Zhang, X.; MacFarlane, D. R., High Nitrogen Gas Solubility and Physicochemical Properties of [C₄mpyr][eFAP]-Fluorinated Solvent Mixtures. *J. Phys. Chem. C* **2019**, *123*, 21376—21385.
8. Wasserscheid, P.; Welton, T., *Ionic Liquids in Synthesis*; John Wiley & Sons, 2008.
9. Dunitz, J. D., Organic Fluorine: Odd Man Out. *ChemBioChem* **2004**, *5*, 614—621.
10. Hird, M., Fluorinated Liquid Crystals - Properties and Applications. *Chem. Soc. Rev.* **2007**, *36*, 2070—2095.
11. Brady, J. E.; Carr, P. W., Perfluorinated Solvents as Nonpolar Test Systems for Generalized Models of Solvatochromic Measures of Solvent Strength. *Anal. Chem.* **1982**, *54*, 1751—1757.
12. Suryanto, B. H. R.; Du, H.-L.; Wang, D.; Chen, J.; Simonov, A. N.; MacFarlane, D. R., Challenges and Prospects in the Catalysis of Electoreduction of Nitrogen to Ammonia. *Nat. Catal.* **2019**, *2*, 290—296.
13. Andersen, S. Z., et al., A Rigorous Electrochemical Ammonia Synthesis Protocol with Quantitative Isotope Measurements. *Nature* **2019**, *570*, 504—508.
14. Du, H.-L.; Gengenbach, T.; Hodgetts, R.; Macfarlane, D. R.; Simonov, A. N., Critical Assessment of the Electrocatalytic Activity of Vanadium and Niobium Nitrides for the Reduction of Dinitrogen to Ammonia. *ACS Sustain. Chem. Eng.* **2019**, *7*, 6839—6850.
15. Hu, B.; Hu, M.; Seefeldt, L.; Liu, T. L., Electrochemical Dinitrogen Reduction to Ammonia by Mo₂n: Catalysis or Decomposition? *ACS Energy Lett.* **2019**, 1053—1054.
16. Olson, E. J.; Boswell, P. G.; Givot, B. L.; Yao, L. J.; Bühlmann, P., Electrochemistry in Media of Exceptionally Low Polarity: Voltammetry with a Fluorous Solvent. *J. Electroanal. Chem.* **2010**, *639*, 154—160.
17. Pringle, J. M.; Howlett, P. C.; MacFarlane, D. R.; Forsyth, M., Organic Ionic Plastic Crystals: Recent Advances. *J. Mater. Chem.* **2010**, *20*, 2056—2062.
18. Deferm, C.; Van den Bossche, A.; Luyten, J.; Oosterhof, H.; Fransaer, J.; Binnemans, K., Thermal Stability of Trihexyl(Tetradecyl)Phosphonium Chloride. *PCCP* **2018**, 2444—2456.
19. Lo Celso, F.; Yoshida, Y.; Castiglione, F.; Ferro, M.; Mele, A.; Jafta, C. J.; Triolo, A.; Russina, O., Direct Experimental Observation of Mesoscopic Fluorous Domains in Fluorinated Room Temperature Ionic Liquids. *PCCP* **2017**, *19*, 13101—13110.
20. Lo Celso, F.; Appetecchi, G. B.; Jafta, C. J.; Gontrani, L.; Canongia Lopes, J. N.; Triolo, A.; Russina, O., Nanoscale Organization in the Fluorinated Room Temperature Ionic Liquid: Tetraethyl Ammonium (Trifluoromethanesulfonyl)(Nonafluorobutylsulfonyl)Imide. *J. Chem. Phys.* **2018**, *148*, 193816, 1—10
21. Lo Celso, F.; Appetecchi, G. B.; Simonetti, E.; Zhao, M.; Castner, E. W.; Keiderling, U.; Gontrani, L.; Triolo, A.; Russina, O., Microscopic Structural and Dynamic Features in Triphilic Room Temperature Ionic Liquids. *Front. Chem.* **2019**, *7*, 1—14.

22. Lepre, L. F.; Pison, L.; Otero, I.; Gautier, A.; Dévemy, J.; Husson, P.; Pádua, A. A. H.; Costa Gomes, M., Using Hydrogenated and Perfluorinated Gases to Probe the Interactions and Structure of Fluorinated Ionic Liquids. *PCCP* **2019**, 21, 8865—8873.
23. Walden, P., Organic Solutions-and Ionisation Means. III. Chapter: Internal Friction and Its Connection with Conductivity. *Z. Phys. Chem.* **1906**, 55, 207—249.
24. Xu, W.; Cooper, E. I.; Angell, C. A., Ionic Liquids: Ion Mobilities, Glass Temperatures, and Fragilities. *J. Phys. Chem. B* **2003**, 107, 6170—6178.
25. Armel, V.; Velayutham, D.; Sun, J.; Howlett, P. C.; Forsyth, M.; MacFarlane, D. R.; Pringle, J. M., Ionic Liquids and Organic Ionic Plastic Crystals Utilizing Small Phosphonium Cations. *J. Mater. Chem.* **2011**, 21, 7640—7650.
26. Lide, D. R., 2005 CRC Handbook of Chemistry and Physics. CRC Press, New York: 2004.
27. Battino, R.; Rettich, T. R.; Tominaga, T., The Solubility of Nitrogen and Air in Liquids. *J. Phys. Chem. Ref. Data* **1984**, 13, 563—600.
28. Stassen, H. K.; Ludwig, R.; Wulf, A.; Dupont, J., Imidazolium Salt Ion Pairs in Solution. *Chem. Eur. J.* **2015**, 21, 8324—8335.

Chapter 5: High Nitrogen Gas Solubility and Physicochemical Properties of [C₄mpyr][eFAP]–Fluorinated Solvent Mixtures

5.1 Synopsis


As the previous chapter examined a range of fluorinated IL–based electrolytes to achieve high N₂ solubility, this publication explores the physical interactions between [C₄mpyr][eFAP], and three fluorinated solvents in relation to N₂ dissolution. This study also delves into the excess molar volume of mixing these components and its effect on N₂ solubility. Moreover, the role of free volume and the effects of fluorinated domains are discussed.

Several compositions of [C₄mpyr][eFAP]:TFT/HFCP/FPEE are investigated where N₂ solubility follows an approximately linear trend from pure IL to fluorinated solvent. Furthermore, the optimal composition of IL in terms of ionic conductivity is in regard to each solvent. The N₂ solubility and transport properties of these fluorinated IL–based electrolytes indicate their potential importance in the electrochemical NRR.

High Nitrogen Gas Solubility and Physicochemical Properties of [C₄mpyr][eFAP]–Fluorinated Solvent Mixtures

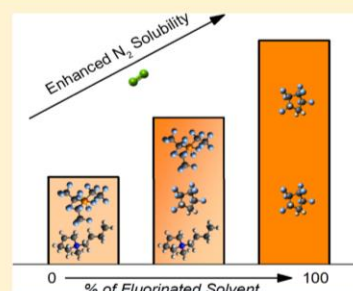
Colin S. M. Kang,¹ Xinyi Zhang,¹ and Douglas R. MacFarlane*

ARC Centre of Excellence for Electromaterials Science, School of Chemistry, Monash University, Clayton, Victoria 3800, Australia

 Supporting Information

ABSTRACT: Electrochemical ammonia synthesis at ambient temperature and pressure shows promise as a route to a carbon-free chemical fuel for renewable energy transportation and storage. However, before this process can be industrialized, issues with the low faradaic efficiencies for the nitrogen reduction reaction must be overcome. This stems from the low nitrogen (N₂) solubility in commonly used aqueous electrolytes and the hydrogen evolution reaction that is usually the more dominant process therein. On the other hand, fluorinated ionic liquid (IL)-based electrolytes can dissolve large amounts of N₂ and reduce the extent of the hydrogen evolution reaction. In this work, the IL 1-butyl-1-methylpyrrolidinium tris(pentafluoroethyl) trifluorophosphate [C₄mpyr][eFAP] was studied in binary mixtures with three fluorinated solvents: trifluorotoluene, 1H,1H,2H-heptafluorocyclopentane, and 1H,1H,5H-octafluoropentyl 1,1,2,2-tetrafluoroethyl ether, all of which

were found to have high N₂ solubility. The salt–solvent mixtures were found to be miscible in all proportions. The N₂ solubility followed an increasing trend with increasing volume fraction of the fluorinated solvent. The interactions within these binary mixtures were investigated in terms of their volumetric properties, revealing negative values of excess molar volume that were also correlated with higher than expected measured viscosity ratios. The thermodynamic properties of solvation in relation to the role of free volume and the effects of fluorine domains are discussed. At compositions around $\chi_2 \approx 0.2$, the mixtures showed a maximum in ionic conductivity and this was examined in terms of ionicity. This study demonstrates the scope for the design of fluorinated IL-based electrolytes for electrochemical nitrogen reduction, both in terms of N₂ solubility and mass transport properties.



1. INTRODUCTION

Ammonia is of increasing interest as an easily transportable hydrogen energy carrier, providing a means of accessing the abundant sources of renewables that have been identified in some remote parts of the world.¹ Currently, ammonia is produced for fertilizers via the energy-intensive Haber–Bosch process, generating millions of tonnes of CO₂ emissions and contributing 1–2% of the world's energy usage.^{2,3} An environmentally benign alternative is the electrochemical reduction of nitrogen gas (N₂) to ammonia at ambient temperature and pressure using renewable sources of energy.⁴ However, this reaction suffers from low faradaic efficiencies and requires substantially better performance before this approach can be implemented on a practical scale.⁵

One significant factor behind the low faradaic efficiencies is the hydrogen evolution reaction that is kinetically more favorable than the nitrogen reduction reaction (NRR).⁶ Part of the reason for this derives from the inherently low solubility of N₂ in aqueous electrolytes (e.g. 0.6 mmol L^{−1} in water) and many other solvents.⁷ Using ionic liquids (ILs) as electrolyte media, we have achieved high faradaic efficiencies of up to 60 and 40% using trihexyltetradecylphosphonium tris(pentafluoroethyl) trifluorophosphate ([P₆₆₆₁₄][eFAP]) and [C₄mpyr][eFAP], respectively,⁸ both of which exhibit high N₂ solubility (e.g. 4.1 mmol L^{−1} in [P₆₆₆₁₄][eFAP]).⁹ As these ILs

are otherwise excellent electrolytes (e.g., electrochemical stability, intrinsic conductivity, etc.),¹⁰ this suggests a strategy of moving away from aqueous electrolytes for NRR toward IL-based electrolytes, particularly if they display high N₂ solubility.

Fluorinated ILs can serve in a range of applications including catalysis,¹¹ biomedicine,^{12,13} surfactants,^{14,15} and so forth. Their nano-level structure has been shown to exhibit fluorine domains (in addition to polar and non-polar C–H dominated domains),^{16–18} enhancing their range of solvation properties, in particular, for gases such as N₂. In our previous work,⁹ we investigated a hypothesis that related the high N₂ solubility in an IL to the degree of fluorination of one or both of the ions (and its possible role in increasing free volume), preparing a number of novel ILs that demonstrated even higher N₂ solubility than [P₆₆₆₁₄][eFAP]. Also, Costa Gomes and co-workers have observed similar trends in increased N₂ solubility by the fluorination of the 1-methyl-3-octylimidazolium cation of the IL.^{19,20} In addition to these highly fluorinated ILs, many fluorinated solvents exhibit very high N₂ solubility (as high as 17.9 mmol L^{−1} for perfluoroheptane and 11.8 mmol L^{−1} for perfluorotributylamine).²¹ Hence, we explore here the

Received: June 24, 2019

Revised: July 23, 2019

Published: August 9, 2019

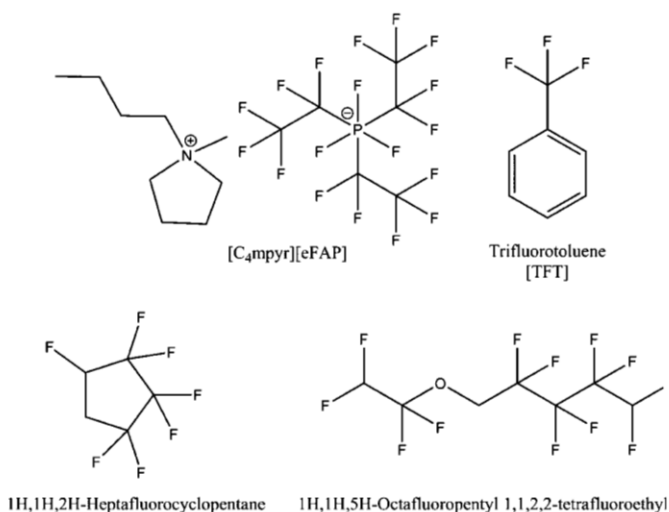


Figure 1. Chemical structures of [C₄mpyr][eFAP] and the fluorinated solvents used in this study.

potential to mix this family of solvents with ILs, where miscibility is possible, to further enhance N₂ solubility.

The addition of fluorinated solvents to an IL can offer other unique properties (e.g., tailored solvation ability, chemical inertness) and significantly change its physical properties,²² including higher ionic conductivity and reduced viscosity.^{23,24} For example, fluorinated solvent/IL-based electrolytes have recently found interest in the field of lithium–sulfur batteries^{25–27} where they display high fluidity²⁸ and also inhibit polysulfide dissolution. Hence, the transport properties of these fluorinated solvent/IL-based electrolytes present high relevance with regard to the reaction rate at which the NRR takes place. While the use, in general, of such fluorinated solvents, which are members of polyfluoroalkyl substances (PFAS) family of compounds, raises environmental concerns, it is important to recognize that their use in electrochemical devices is essentially in a hermetically closed system.

It is important to understand the nature of the interactions at play in these fluorinated IL-based electrolytes and broaden the range in which they can be utilized. Here, we examine [C₄mpyr][eFAP] dissolved in various proportions of trifluorotoluene (TFT), 1H,1H,2H-heptafluorocyclopentane (HFCP), and 1H,1H,5H-octafluoropentyl 1,1,2,2-tetrafluoroethyl ether (FPEE) and study the N₂ solubility of the binary mixtures, ranging from a slightly diluted network of ions to the other extreme of a solution of solvated ions. This particular fluorinated IL-based electrolyte system demonstrates an extensive range of miscibility, enabling the tuning of desired properties based on composition. The N₂ solubility trends in these binary mixtures are determined and discussed in terms of the excess volumes of mixing, thermodynamic properties of solvation, and free volume. Furthermore, their transport properties are examined and discussed in relation to the observed trends in ionicity.

2. EXPERIMENTAL SECTION

2.1. Materials. The chemical structures of [C₄mpyr][eFAP] and the three fluorinated solvents used in this work are shown in Figure 1. 1-Butyl-1-methylpyrrolidinium tris(pentafluoroethyl)trifluorophosphate (99%, [C₄mpyr][eFAP],

Merck), σ,σ,σ -trifluorotoluene (>99%, TFT, Synquest Laboratories), HFCP (>99%, Synquest Laboratories), and FPEE (>97%, Synquest Laboratories) were used without further purification. Nitrogen gas (N₂, ALPHAGAZ) was used as received from Air Liquide. Recognizing that the fluorinated solvents used here are members of the PFAS family of compounds, all materials were handled and disposed with all required safeguards.

2.2. Characterization. [C₄mpyr][eFAP]–fluorinated solvent mixtures were prepared immediately prior to all measurements to prevent any vapor losses and changes to composition over time. Density measurements were conducted on an Anton Paar DMA 5000 Density Meter via the “oscillating U-tube principle” with an estimated uncertainty of <0.1%. The viscosity was measured on an Anton Paar Lovis 2000M micro-viscometer using the falling ball technique with an estimated uncertainty of <2%. For conductivity measurements, the Hewlett Packard 4284 LCR meter carried out ac impedance spectroscopy over a range of 0.1 Hz to 10 MHz using a two-electrode platinum wire dip cell, calibrated using an aqueous solution of 0.01 mol L^{−1} KCl. The ionic conductivity was calculated by taking the data point closest to the x -axis in the touch down region of the impedance plane plot. The electrochemical stability of the [C₄mpyr][eFAP] binary mixtures was measured using a Princeton Applied Research VMP2 instrument and EC-Lab software (Bio-Logic Science Instruments). The three-electrode cell setup was used: a glassy carbon disk (1 mm diameter) as the working electrode, coiled platinum wire as the reference electrode, and a mixture of silver trifluoromethanesulfonate (10 mM) dissolved in [C₄mpyr][eFAP] as the reference electrode.

2.3. N₂ Solubility Measurements. The solubility of N₂ in ILs and their mixtures were measured near atmospheric pressure via the isochoric saturation method using a dual-volume apparatus, as detailed previously.⁹ In each experiment, a known volume of N₂, contained in a ballast chamber, was delivered into an equilibrium chamber which holds the degassed liquid sample. After the pressure of N₂ has reached equilibrium, between the sample and its headspace, the moles of N₂ dissolved in the sample can be determined. The overall

B

DOI: 10.1021/acs.jpcc.9b06000
J. Phys. Chem. C XXXX, XXX, XXX–XXX

calculation is shown in eq 1, where detailed calculations (including non-ideality and vapor phase corrections to ensure high accuracy of measurements) are shown in the Supporting Information

$$n_{\text{N}_2}^{\text{absorbed}} = n_{\text{N}_2}^{\text{admitted}} - n_{\text{N}_2}^{\text{headspace}} \quad (1)$$

The solubility of N_2 in a given IL or the sample mixture can be expressed as a molar concentration C_{N_2} , mole fraction χ_2 , or molal concentration b_{N_2} . N_2 solubility measurements were repeated to ensure reproducibility/high precision with tabulated data shown in Table S1 of the Supporting Information. The repeatability in N_2 solubility measurements was estimated to be within $\pm 0.2 \text{ mmol L}^{-1}$.

2.4. Diffusion NMR Measurements. Self-diffusion coefficients were measured using a pulsed gradient stimulated echo (PGSTE) pulse sequence. A Bruker DRX600 spectrometer was used to carry out diffusion NMR experiments for ^1H nuclei, and a Bruker DRX400 spectrometer for ^{19}F nuclei. Deuterium oxide (99.9%, Sigma-Aldrich) was used as the external solvent reference, to surround the inner sample tube and minimize any convection effects. The self-diffusion coefficient D was calculated by fitting data to the Stejskal–Tanner equation²⁹

$$\ln\left(\frac{S}{S_{g=0}}\right) = -\gamma^2 g^2 D \delta^2 \left(\Delta - \frac{\delta}{3}\right) \quad (2)$$

here, s is the spin-echo signal intensity, γ is the gyromagnetic ratio of the observed nucleus, g is the gradient strength, δ is the duration of the field gradient, and Δ is the time between two gradient pulses.

The self-diffusion coefficient value of Milli-Q water was measured to be $2.3 \times 10^{-9} \text{ m}^2 \text{ s}^{-1}$ at 25°C , within 1% of literature data.³⁰ The uncertainty associated with self-diffusion coefficient measurements was $\pm 5\%$.

3. RESULTS AND DISCUSSION

3.1. Miscibility of IL–Fluorinated Solvent Binary Mixtures. The mixing of two different substances as a binary mixture leads to the redistribution of intermolecular forces between the species, resulting in different physical properties. The intermolecular forces within an IL, as compared to within a fluorinated solvent can be expected to differ enormously in strength, typically resulting in low solubility of the salt. In the context of lithium battery research, a cosolvent (such as dimethoxyethane or propylene carbonate) is usually required to achieve high concentrations of dissolved lithium salt in these highly fluorinated solvents.^{25–27} However in the present case, the binary mixtures of $[\text{C}_4\text{mpyr}][\text{eFAP}]$ with TFT, HFCEP, and FPEE were all found to be miscible in all proportions without the need of a cosolvent. This allows us to study the solubility of N_2 across a wide range of compositions in the binary systems and identify any trends related to the volumetric properties such as density, excess molar volume (V^E), and partial molar volume. Lastly, the electrochemical limits of stability are shown in Figure S1, where all of these mixtures display reductive limits far beyond the reductive potentials applied in the electrochemical NRR in nonaqueous solvents (typically $\sim -1.1 \text{ V}$ vs NHE).^{8,31}

3.2. N_2 Solubility in $[\text{C}_4\text{mpyr}][\text{eFAP}]$ –Fluorinated Solvent Mixtures. The plot of N_2 solubility in $[\text{C}_4\text{mpyr}][\text{eFAP}]$ –fluorinated solvent mixtures with TFT, HFCEP, and

FPEE is presented in Figure 2. While it is common to represent gas solubility as the Henry's law constant, K_{H} , or

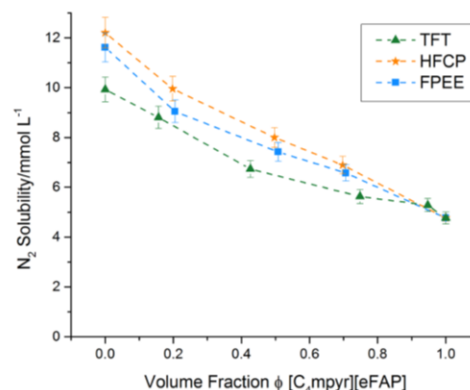


Figure 2. Solubility of N_2 (mmol L^{-1}) in $[\text{C}_4\text{mpyr}][\text{eFAP}]$ binary mixtures, as a function of volume fraction Φ , with TFT (\blacktriangle), HFCEP (\star) and FPEE (\blacksquare) at 30°C and $P = 1 \text{ atm}$. Lines serve as a guide only.

mole fraction in gas capture applications, the measured current density in electrochemical applications is typically dependent on the molar concentration of dissolved species.³² Our aim to achieve high N_2 solubility stems from the desire to improve the kinetics and selectivity in the electrochemical NRR. Hence, we report here solubility data in units of $\text{mmol}(\text{N}_2) \text{ L}^{-1}$.

All of the fluorinated solvents investigated display a higher N_2 solubility than $[\text{C}_4\text{mpyr}][\text{eFAP}]$ in the order of $\text{HFCEP} > \text{TFT} > [\text{C}_4\text{mpyr}][\text{eFAP}]$. The lack of strong interactions (i.e., from hydrogen bonding, or functional groups) within these solvents³³ contributes to a high solubility of N_2 . Though the IL itself has high N_2 solubility, the electrostatic interactions in ILs nonetheless produce a high cohesive energy density, and it is not unexpected that the fluorinated solvents display even higher N_2 solubility. Comparing the fluorinated solvents, HFCEP likely exhibits the lowest overall cohesive energy density because of its high degree of fluorination and lack of any functional groups, producing the highest N_2 solubility. With FPEE, the large number of fluorine atoms likely mitigates the polar contribution of the ether group, resulting in its relatively high N_2 solubility. TFT is not as highly fluorinated as the other solvents, as it contains only three fluorine atoms, and this may result in its relatively lower N_2 solubility. Further insight to the effect of fluorine groups is shown by comparing the N_2 solubility of these fluorinated solvents with their hydrogenated counterparts: TFT displays a two-fold increase in comparison to toluene⁷ (10 mmol L^{-1} cf. 5 mmol L^{-1} respectively) and HFCEP shows ~ 1.7 times higher N_2 solubility in comparison to, similarly structured, cyclohexane³⁴ (12 mmol L^{-1} cf. 7 mmol L^{-1} respectively). Thus, this demonstrates the capability of fluorine substituents in enhancing the N_2 solubility in these solvents.

Examining the N_2 solubility of $[\text{C}_4\text{mpyr}][\text{eFAP}]$ mixtures in Figure 2, the solubility of N_2 follows an approximately linear dependence, where the solubility appears to be simply governed by the volume fraction of each component. Furthermore, Pádua et al. carried out molecular simulations and found that the small quadrupole moment of N_2 does not

affect the calculated N_2 solubility in ILs, in contrast to CO_2 solubility.³⁵ Therefore, N_2 dissolution into these fluorinated mixtures is likely to be dominated by physical processes,^{36,37} where N_2 solubility trends are best observed as a function of IL (or solvent) volume fraction (Figure 2). Plotting the same data on a mole fraction χ_2 basis, although useful for thermodynamic analysis, results in a skewed plot (see Figures S2 and S3) from the large molecular weight of $[C_4mpyr][eFAP]$ compared to the fluorinated solvent. Further discussion on the nature of N_2 solubility in these mixtures is presented below.

3.3. Volumetric Properties. **3.3.1. Density.** The experimental densities of neat $[C_4mpyr][eFAP]$ and TFT were concordant with the literature amongst the temperature ranges included in this study,^{38–42} whilst the density of HFCEP and FPCE were not found in the literature. The densities of $[C_4mpyr][eFAP]$ mixtures in TFT, HFCEP, and FPCE at 25 °C are shown in Figure 3 (and Tables S2–S4). The addition of

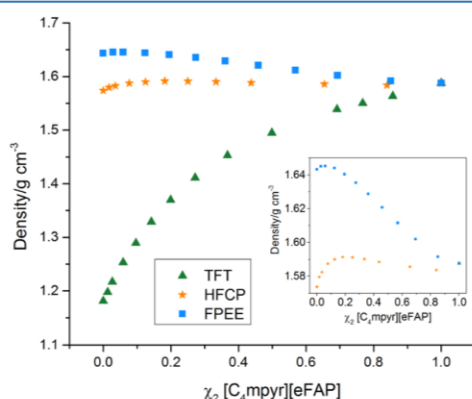


Figure 3. Densities of $[C_4mpyr][eFAP]$ binary mixtures, as a function of mole fraction χ_2 , with TFT (\blacktriangle), HFCEP (\star), and FPCE (\blacksquare) at 25 °C. Inset shows enlarged change in density with mole fraction χ_2 .

$[C_4mpyr][eFAP]$ to HFCEP (and FPCE) produces an increase in density, from the pure solvent, until a peak in density is reached (see inset). At this observed peak, there may be increased packing or attractive interactions present between the IL and the solvent, resulting in the contraction of volume and thus larger density. Subsequent addition of IL then reduces the density until it approaches that of pure $[C_4mpyr][eFAP]$. On the other hand, addition of $[C_4mpyr][eFAP]$ to TFT shows an initial increase in density until it becomes linear with further addition. Figure S3 shows the temperature dependence of density with $[C_4mpyr][eFAP]$ –fluorinated solvent mixtures. When $[C_4mpyr][eFAP]$ is mixed with HFCEP, and FPCE, a shift in the peak maximum to a higher composition of IL is observed with increasing temperature.

3.3.2. Excess Molar Volume. The calculation of the excess molar volume, V^E , allows discussion of the deviation from ideal mixing volumes, in terms of packing efficiency and the intermolecular forces between the two components (compared to each pure component). The values of V^E are calculated from the experimentally obtained density values (shown in Tables S2–S4) using eq 3

$$V^E = \frac{\chi_1 M_1 + \chi_2 M_2}{\rho_{12}} - \frac{\chi_1 M_1}{\rho_1^*} - \frac{\chi_2 M_2}{\rho_2^*} \quad (3)$$

here, χ_1 , M_1 , and ρ_1^* refer to the mole fraction, molecular weight, and density of $[C_4mpyr][eFAP]$, respectively; χ_2 , M_2 , and ρ_2^* refer to the mole fraction, molecular weight, and density of the fluorinated solvent, respectively, and ρ_{12} is the density of the mixture at a given mole fraction. The values of V^E can be fitted as a function of mole fraction χ_2 by the Redlich–Kister equation⁴³

$$V^E = x_2(1 - x_2) \sum_{n=0} A_n(1 - 2x)^n \quad (4)$$

here, A_n is adjustable parameters obtained by least squares regression.

Figure 4 shows a plot of V^E of $[C_4mpyr][eFAP]$ mixtures in TFT, HFCEP, and FPCE with increasing temperature. The calculated parameters, based on the Redlich–Kister fit and standard deviations are presented in Table S5. All three systems show a negative deviation from ideal mixing volume up to $\chi_2 \approx 0.7$, indicating a combination of greater intermolecular interactions and better volumetric packing, between the IL and fluorinated solvent. Minima are observed around a mole fraction $\chi_2 \approx 0.3$ for TFT and FPCE, and the corresponding minimum for HFCEP around a mole fraction $\chi_2 \approx 0.2$. These minima represent the optimum mole fraction of IL to the solvent, where (i) the volumetric packing is optimized and (ii) the attractive interactions between $[C_4mpyr][eFAP]$ and the solvent are strongest. These are likely to be ion–dipole interactions which may become significant compared to the weak dipole–dipole forces within the neat fluorinated solvent.

As more IL is present in the environment ($\chi_2 > 0.7$), V^E deviates toward positive values in all cases, indicating that the intermolecular interactions become weaker than those of the individual components. By comparison, Gadzuric et al. reported positive deviations of V^E across all compositions for an organic system where $[C_4mpyr][eFAP]$ was mixed with *N,N*-dimethylformamide, *N,N*-dibutylformamide, and *N,N*-dimethylacetamide.⁴¹ These differences in overall interactions suggest that the fluorinated regions of these fluorinated solvents may interact favorably with the fluorinated anion of the IL, compared to amide-based solvents. Further discussion on the parameters of the reduced V^E and partial molar volume can be found in the Supporting Information. Increasing temperature does not appear to change such trends; other than that, V^E becomes more negative with increasing temperature across all compositions. This suggests that the increasing free volume in both components with increasing temperature offers more opportunity for improved packing.

To put these values of V^E in some perspective, we have made some estimations of the likely amount of free volume that is present in these liquids, based on a comparison of their crystal structure molar volumes with their liquid-state molar volumes (details provided in the Supporting Information). From this, we estimate the free volume of TFT to be $\sim 25 \text{ cm}^3 \text{ mol}^{-1}$ ($\sim 20 \text{ vol } \%$); sufficient data are not available for $[C_4mpyr][eFAP]$; however, for $[C_2mim][BF_4]$, we estimate to be $\sim 18 \text{ cm}^3 \text{ mol}^{-1}$. Therefore, the negative V^E values appear to be relatively small compared to the expected total free volume.

3.3.3. Nature of N_2 Solubility. Returning to the N_2 solubility in $[C_4mpyr][eFAP]$ –fluorinated solvent mixtures, one could hypothesize a link between N_2 solubility and free volume, and therefore expect sensitivity to changes in the free volume available. Because V^E displays negative values up to $-2.2 \text{ cm}^3 \text{ mol}^{-1}$ at 25 °C (near $\chi_2 \approx 0.3$ in each IL–solvent system), a

D

DOI: 10.1021/acs.jpcc.9b06000
J. Phys. Chem. C XXXX, XXX, XXX–XXX

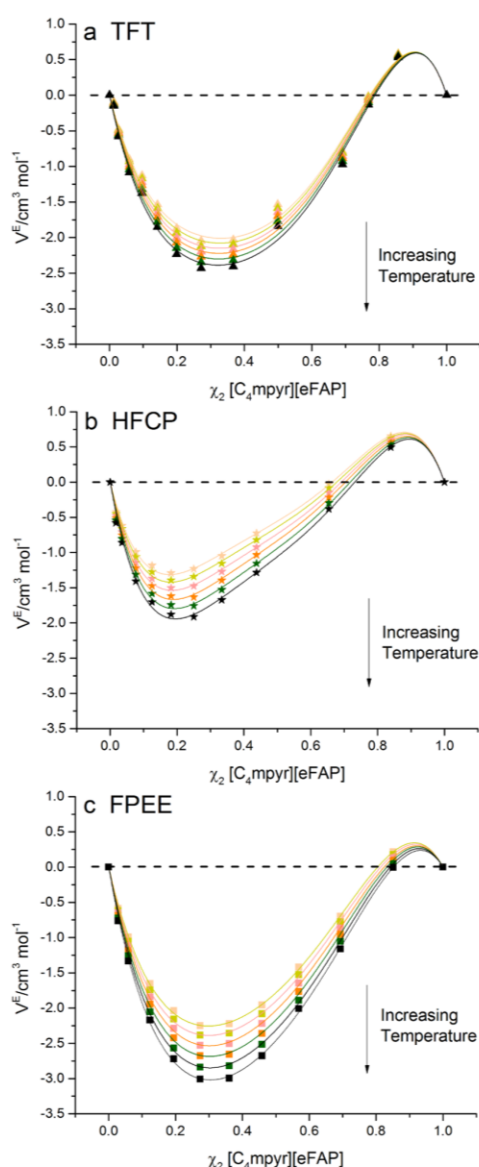


Figure 4. Excess molar volumes (V^E) of $[C_4\text{mpyr}][\text{eFAP}]$ binary mixtures, as a function of mole fraction, with (a) TFT (\blacktriangle), (b) HFCEP (\star), and (c) FPEE (\blacksquare) at 25, 30, 35, 40, 45, and 50 °C. Lines are fitted based on the Redlich–Kister equation, and dotted lines indicate the line of ideal mixing ($V^E = 0$).

decline in N_2 solubility might be expected. However, this does not appear to be the case in the solubility data presented in Figure 2. In other words, the negative values in V^E are small compared to the total free volume estimates above and therefore no correlation to N_2 solubility is observable.

To explore this further and summarize the factors that contribute to N_2 solubility, we briefly revisit the thermodynamics of gas dissolution, using

$$\Delta_{\text{sol}}G = \Delta_{\text{sol}}H - T\Delta_{\text{sol}}S$$

where T is the temperature, $\Delta_{\text{sol}}H$ and $\Delta_{\text{sol}}S$ are the enthalpy of solvation and entropy of solvation, respectively. If we separate the enthalpy term into its contributing components

$$\Delta_{\text{sol}}H = \Delta H_1 + \Delta H_2 + \Delta H_3$$

where, ΔH_1 refers to the change of solute–solute interactions, which is essentially zero for a gas-phase solute ($\Delta H_1 \approx 0$); ΔH_2 represents the disruption of solvent–solvent interactions, which is expected to be large for the IL, though increasingly less so as the IL content decreases ($\Delta H_2 > 0$); and ΔH_3 represents the energetics of N_2 –solvent interactions. Referring to the known thermodynamics of solvation of N_2 in pure $[C_4\text{mpyr}][\text{eFAP}]$, as determined by Stevanovic and Costa Gomes,³⁸ these values are calculated to be $\Delta_{\text{sol}}H = -4 \text{ kJ mol}^{-1}$ and $\Delta_{\text{sol}}S = -58 \text{ J mol}^{-1} \text{ K}^{-1}$. The overall negative $\Delta_{\text{sol}}H$ term suggests that in the pure IL, the N_2 –IL interactions, ΔH_3 , are sufficient to outweigh the disruption of IL–IL interactions, ΔH_2 . Indeed, distinct N_2 –IL interactions have been identified previously in this family of ILs by density functional theory calculations, originating in binding between the N_2 molecule and the $[\text{eFAP}]^-$ anion.⁸ The fact that the disruption of solvent–solvent interactions does not have a dominant effect in ΔH_2 may be related to the large amount of free volume available (i.e., low energy required for the necessary cavity formation) in these systems, as discussed above. To illustrate this further, we can make an estimate of the free volume in TFT as $\sim 201 \text{ cm}^3$ per liter of TFT, which is substantially larger than the estimated additional volume required to dissolve 10 mmol (N_2) $\text{L}^{-1} \cong 0.35 \text{ cm}^3$, (see the Supporting Information for calculations). We hypothesize that this relatively small amount of required cavity formation is easily accommodated by free volume rearrangement such that the disruption of IL–IL interactions (ΔH_2) is relatively small.

The entropic term $\Delta_{\text{sol}}S$ is dominated by the loss of entropy of the gaseous component and is therefore always negative and is not expected to show strong dependence on the solvent structure.³⁸

The nanostructure of the IL (or mixture) will certainly have an effect on the thermodynamic factors discussed above, especially if fluorinated domains are present. Fluorinated domains (particularly in highly fluorinated solvent mixtures) tend to be weakly interacting³³ and the chains themselves tend to be more rigid;⁴⁴ both of these factors can be expected to allow elevated levels of free volume in these domains.

To summarize, fluorinated solvent systems, such as those investigated here, exhibit a noticeable proportion of free volume ($\sim 20\%$), and this is likely to be partly occupied by N_2 upon dissolution. This reduces the enthalpic cost of the disruption of solvent–solvent interactions because of N_2 dissolution. Although negative excess molar volumes are observed here (at most compositions), these remain relatively small compared to the total free volume and no noticeable impact of this on N_2 solubility is found. This nexus between free volume and fluorinated domains may be a key in further extending N_2 solubility in IL–fluorinated solvent-based electrolytes.

3.4. Transport Properties. 3.4.1. Viscosity. Figure 5a shows the increase in viscosity as $[C_4\text{mpyr}][\text{eFAP}]$ is added to each fluorinated solvent across a range of compositions with the temperature dependence plots shown in Figure S8. The inset in Figure 5a shows that the viscosity of the binary mixtures is highly dependent on the viscosity of the neat

E

DOI: 10.1021/acs.jpcc.9b06000
J. Phys. Chem. C XXXX, XXX, XXX–XXX

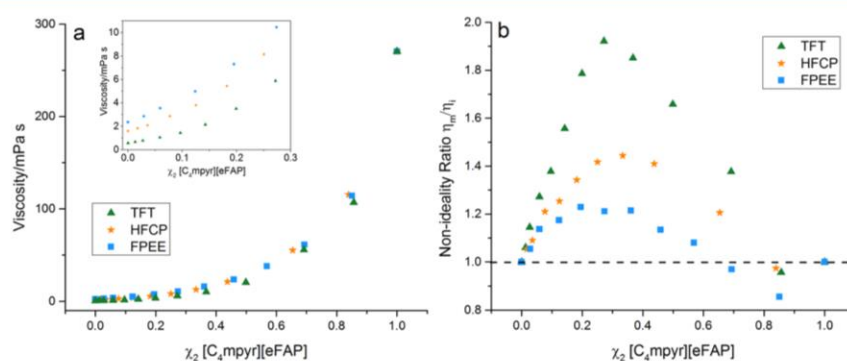


Figure 5. (a) Viscosity and (b) non-ideality ratios of $[C_4\text{mpyr}][\text{eFAP}]$ binary mixtures, as a function of mole fraction χ_2 , with TFT (\blacktriangle), HFCEP (\star), and FPEE (\blacksquare) at 25 °C. The dotted line indicates the viscosity of ideal mixtures ($\eta_m/\eta_i = 1$).

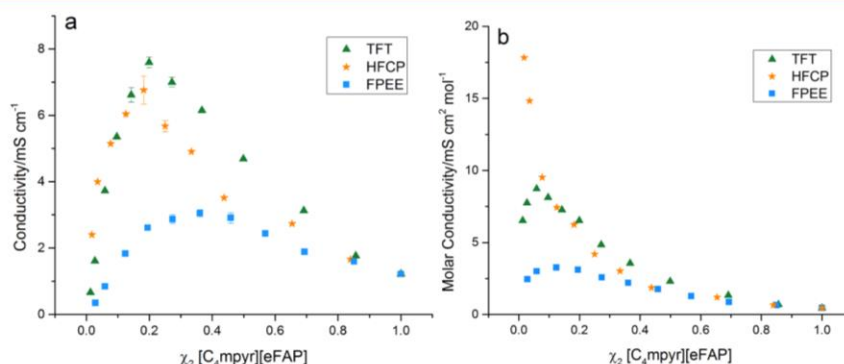


Figure 6. Plot of (a) ionic conductivity and (b) molar conductivity of $[C_4\text{mpyr}][\text{eFAP}]$ binary mixtures, as a function of mole fraction χ_2 , with TFT (\blacktriangle), HFCEP (\star), and FPEE (\blacksquare) at 25 °C (note two of the fluorinated solvents had vanishingly small ionic conductivities close to $\chi_2 = 0$).

fluorinated solvent, which follows the order FPEE > HFCEP > TFT.

Comparing the viscosity of the neat fluorinated solvents ($\chi_2 = 0$) to their hydrogenated counterparts shows that TFT is only slightly more viscous than toluene⁴⁵ (0.58 mPa s cf. 0.47 mPa s respectively) as a result of trifluoromethyl replacing the methyl group. A larger difference is found when HFCEP is compared to cyclopentane⁴⁶ (1.59 mPa s cf. 0.42 mPa s respectively), indicating that the replacement of seven hydrogen atoms with fluorine results in this larger increase in viscosity.

To describe the viscosity of the $[C_4\text{mpyr}][\text{eFAP}]$ –fluorinated solvent mixtures, the Grunberg–Nissan equation⁴⁷ can be used to describe the data and highlight non-ideality

$$\ln \eta_m = \chi_1 \ln \eta_1 + \chi_2 \ln \eta_2 + \ln \frac{\eta_m}{\eta_i} \quad (5)$$

where $\eta_i = \chi_1 \eta_1 + \chi_2 \eta_2$ describes an ideal mixture (where the viscosity is given by the weighted average viscosity of each component). Here, χ_1 and χ_2 are mole fractions of component 1 and 2, η_1 and η_2 are the viscosities of the pure molecular components 1 and 2, and η_m is the viscosity of the mixture. The non-ideality ratio η_m/η_i describes the deviation in viscosity of the mixture from the viscosity of an ideal mixture. A ratio of 1 would describe binary mixtures that exhibit ideal viscosity. This ratio, calculated from eq 5, is plotted versus $[C_4\text{mpyr}][\text{eFAP}]$ composition in Figure 5b. The mixtures display non-ideal behavior across all compositions with maxima near $\chi_2 \approx$

0.3. Positive deviations are observed at $\chi_2 < 0.8$, where the viscosity is higher than that of an ideal mixture. Conversely, when $\chi_2 > 0.8$, the mixtures exhibit lower than expected viscosities, where the non-ideality ratios are <1. This behavior is strongly correlated with the V^E trends observed in Figure 4, that is, that strong positive deviations in viscosity appear to be correlated to strong negative deviations in V^E . Clearly a reduction in free volume due to more effective packing in the mixtures, as well as intermolecular forces between the two components, will lead to increased frictional forces and higher than ideal–mixture viscosity.

3.4.2. Ionic Conductivity. The plot of ionic conductivity versus mole fraction χ_2 of $[C_4\text{mpyr}][\text{eFAP}]$ in the binary mixtures at 25 °C is shown in Figure 6a with the temperature dependence shown in Figure S9. The ionic conductivity increases as $[C_4\text{mpyr}][\text{eFAP}]$ is added to each of the three fluorinated solvents until a maximum is observed near $\chi_2 \approx 0.20$ for TFT and HFCEP and $\chi_2 \approx 0.40$ for FPEE. In terms of ionic conductivity, this peak reflects a near optimal composition of $[C_4\text{mpyr}][\text{eFAP}]$ to the fluorinated solvent for use as an electrolyte for electrochemical applications, particularly, for NRR. Further addition of IL, despite increasing the concentration of charge carriers, then lowers the ionic conductivity as a result of increased viscosity (thus slower movement of ions). The magnitude of peak ionic conductivity for $[C_4\text{mpyr}][\text{eFAP}]$ –fluorinated solvent mixtures follows the order TFT > HFCEP > FPEE.

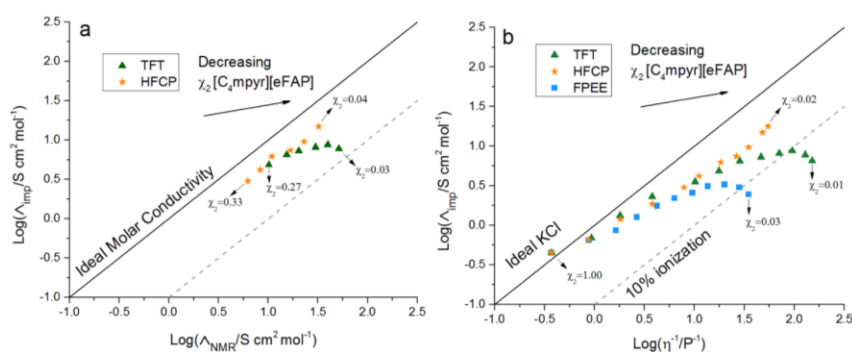


Figure 7. (a) Ionicity plot and (b) Walden plot of $[C_4\text{mpyr}][\text{eFAP}]$ binary mixtures in various compositions with TFT (▲), HFCEP (★), and FPPE (■) at 25 °C.

In addition to viscosity, such differences in ionic conductivity also arise from IL–solvent interactions where the solvent plays a significant role in the dissociation of ions within these binary mixtures. For further insight into this, the molar conductivities of these mixtures are plotted in Figure 6b. When $[C_4\text{mpyr}][\text{eFAP}]$ is dissolved in TFT and FPPE, the molar conductivity rises through a distinct maximum at the lower IL compositions before falling away toward that of the pure IL. This slightly unusual behavior is expected of very low dielectric constant solvents in which ion pairing and aggregation are strong.⁴⁸ On the other hand, when $[C_4\text{mpyr}][\text{eFAP}]$ is dissolved in HFCEP at low IL content, the molar conductivity falls away rapidly and continuously from much higher initial values; this is a more usual electrolyte behavior and likely reflects the fact that HFCEP exhibits a higher dielectric constant which is able to provide screening of the electrostatic attraction between the dissolved ions.^{48,49} Although this data show strong qualitative trends in the solvent's dielectric constant in terms of ionic associations, quantitative data were not found in the current literature and is currently beyond our capabilities to measure in our laboratories. Lastly, the temperature dependence of molar conductivity does not strongly alter any of these trends shown (see Figure S10).

3.4.3. Ionicity. To directly assess the degree of ionicity in $[C_4\text{mpyr}][\text{eFAP}]$ –fluorinated solvent mixtures, both PGSTE–NMR and impedance measurements are carried out. The self-diffusion coefficients of each component are distinguished by differing ^1H nuclei for the $[C_4\text{mpyr}]^+$ cation and ^{19}F nuclei for the $[\text{eFAP}]^-$ anion. Self-diffusion coefficients of the cation and anion in $[C_4\text{mpyr}][\text{eFAP}]$ are presented in Table S7, where the addition of the fluorinated solvent to pure IL enhances the self-diffusion coefficients by up to 2 orders of magnitude. Interestingly, in Figure 6a, the magnitude of peak ionic conductivity in $[C_4\text{mpyr}][\text{eFAP}]$ mixtures containing TFT and HFCEP are relatively similar (at $\chi_2 \approx 0.2$), yet the self-diffusion coefficients are not comparable (e.g., $2.5 \times 10^{-10} \text{ m}^2 \text{ s}^{-1}$ cf. $1.6 \times 10^{-10} \text{ m}^2 \text{ s}^{-1}$ for the $[C_4\text{mpyr}]^+$ cation in TFT and HFCEP, respectively).

To shed more light on this surprising result, the degree of ionicity is calculated from the ratio $\Lambda_{\text{imp}}/\Lambda_{\text{NMR}}$ ⁵⁰ where Λ_{imp} is the molar conductivity that is calculated from impedance measurements of ionic conductivity and Λ_{NMR} is the molar conductivity that is calculated via the self-diffusion coefficients of the IL ions ($D_{\text{cation}} + D_{\text{anion}}$) through the Nernst–Einstein equation

$$\Lambda_{\text{NMR}} = \frac{F^2(D_{\text{cation}} + D_{\text{anion}})}{RT} \quad (6)$$

here, F is Faraday's constant, T is temperature, and R is the universal gas constant.

The Nernst–Einstein equation includes the contribution of all diffusing species in calculating molar conductivity, whereas Λ_{imp} measures only the charged species responding to an electric field. As a result, any ratio less than unity indicates the presence of ion pairing and/or neutral aggregates that cannot contribute to Λ_{imp} on the time scale of the measurement.⁵¹

The degree of ionicity in $[C_4\text{mpyr}][\text{eFAP}]$ –fluorinated solvent mixtures is graphically represented in Figure 7a, with numerical data tabulated in Table S7. For comparison, a Walden plot which provides a qualitative approach to the same phenomenon by plotting Λ_{imp} versus inverse viscosity is shown in Figure 7b. In the ionicity plot, one can immediately recognize the decline in ionicity in some mixtures as IL concentration decreases. These ionicity values are compared to the simple Nernst–Einstein behavior where $\Lambda_{\text{imp}} = \Lambda_{\text{NMR}}$.⁵² Full concordance to the Nernst–Einstein relationship is not expected in concentrated electrolytes such as these for a number of reasons;^{53,54} nonetheless, the deviation from this line provides a guide as to the trends within a range of compositions. In contrast, $[C_4\text{mpyr}][\text{eFAP}]$ –HFCEP mixtures display relatively constant ionicity values at lower IL concentrations ($\chi_2 < 0.33$). This reflects the difference between TFT and HFCEP in their ability to dissociate the ions of $[C_4\text{mpyr}][\text{eFAP}]$, where HFCEP is the better solvent in this regard.

Shown in Figure 7b is the corresponding Walden plot that qualitatively compares ionicity to an “ideal” electrolyte of aqueous potassium chloride (0.01 mol L^{−1}).^{55,56} This displays similar trends to that of the ionicity plot, although the decreases in the degree of ionicity are more extreme. The temperature dependence is shown in Figure S11, where a slight decrease in ionicity with increasing temperature is observed.

The decreasing ionicity at lower concentrations of $[C_4\text{mpyr}][\text{eFAP}]$ in TFT and FPPE likely indicates ion pairing and ion aggregation in these mixtures. This suggests a structure for these mixtures that is based on fluorine domains and neutral and low-charge clusters of ions. On the other hand, the $[C_4\text{mpyr}][\text{eFAP}]$ –HFCEP mixture displays approximately constant ionicity under similar concentrations which suggest better solvation of individual ions in this case. Despite these

differences in the likely structure, the N_2 solubility trends are relatively similar. This suggests that these structural differences are not significant in the N_2 solubility mechanism.

4. CONCLUSIONS

[C₄mpyr][eFAP]–fluorinated solvent mixtures, which are miscible over a wide range of compositions, were investigated in regard to their N_2 solubility, volumetric, and physicochemical properties. The already high N_2 solubility of [C₄mpyr][eFAP] can be enhanced by the addition of the fluorinated solvents investigated. N_2 solubility was demonstrated to be dependent on the volume fraction of each component, rising to a maximum at the pure fluorinated solvent in each case. N_2 solubility was not strongly correlated to the significantly negative excess molar volumes that are observed in these [C₄mpyr][eFAP]–fluorinated solvent mixtures. However, these negative excess molar volumes were only a small fraction of the estimated total free volume present, and therefore, N_2 dissolution into this free volume remains a likely component of the solubility mechanism. Free volume is proposed as an important factor in supporting high N_2 solubility in these mixtures. Viscosity was shown to decrease rapidly with increasing solvent component in all cases. Additionally, the viscosity non-ideality ratio indicated a higher than expected mixture viscosity in the solvent-rich region and this was strongly correlated with the trends in V^E . Ionic conductivity followed the order TFT > HFCEP > FPCE where ion dissociation played a significant role. The ionicity of the [C₄mpyr][eFAP]–HFCEP mixture remained approximately constant with composition, in contrast to the TFT and FPCE mixtures where it decreased markedly at low IL content. The improved mass transport of these fluorinated IL based electrolytes compared to the neat IL demonstrates their utility for electrochemical applications, particularly for NRR because of their high N_2 solubility.

■ ASSOCIATED CONTENT

Supporting Information

The Supporting Information is available free of charge on the ACS Publications website at DOI: 10.1021/acs.jpcc.9b06000.

Fluorinated IL electrolytes data in terms of their N_2 solubility calculations with numerical data and plots, electrochemical potential windows, calculations of free volume, experimental values of density, excess molar volume, reduced excess molar volume, partial molar volumes and Redlich–Kister fitting coefficients, ionicity plot, diffusion-coefficient and ionicity data, temperature dependence plots of viscosity, ionic conductivity, molar conductivity, and Walden plot (PDF)

■ AUTHOR INFORMATION

Corresponding Author

*E-mail: douglas.macfarlane@monash.edu. Phone: +61 3 9905 4540.

ORCID

Colin S. M. Kang: 0000-0002-7697-3330

Xinyi Zhang: 0000-0003-4695-3731

Author Contributions

C.S.M.K. carried out the experiments. All authors contributed to writing of the manuscript.

Notes

The authors declare no competing financial interest.

■ ACKNOWLEDGMENTS

C.S.M.K. would like to acknowledge the Australian Government Research Training Program (RTP) Scholarship for funding and D.R.M. would like to thank the ARC for funding through Discovery Project DP170102267 and his Australian Laureate Fellowship (FL120100019).

■ REFERENCES

- (1) Soloveichik, G. Electrochemical Synthesis of Ammonia as a Potential Alternative to the Haber–Bosch Process. *Nat. Catal.* **2019**, 2, 377–380.
- (2) Smil, V. Global Population and the Nitrogen Cycle. *Sci. Am.* **1997**, 277, 76–81.
- (3) Smil, V. *Enriching the Earth: Fritz Haber, Carl Bosch, and the Transformation of World Food Production*; MIT Press: Massachusetts, USA, 2004.
- (4) Kyriakou, V.; Garagounis, I.; Vasileiou, E.; Vourros, A.; Stoukides, M. Progress in the Electrochemical Synthesis of Ammonia. *Catal. Today* **2017**, 286, 2–13.
- (5) Suryanto, B. H. R.; Du, H.-L.; Wang, D.; Chen, J.; Simonov, A. N.; MacFarlane, D. R. Challenges and Prospects in the Catalysis of Electroreduction of Nitrogen to Ammonia. *Nat. Catal.* **2019**, 2, 290–296.
- (6) Jia, H.-P.; Quadrelli, E. A. Mechanistic Aspects of Dinitrogen Cleavage and Hydrogenation to Produce Ammonia in Catalysis and Organometallic Chemistry: Relevance of Metal Hydride Bonds and Dihydrogen. *Chem. Soc. Rev.* **2014**, 43, 547–564.
- (7) Battino, R.; Rettich, T. R.; Tominaga, T. The Solubility of Nitrogen and Air in Liquids. *J. Phys. Chem. Ref. Data* **1984**, 13, 563–600.
- (8) Zhou, F.; Azofra, L. M.; Ali, M.; Kar, M.; Simonov, A. N.; McDonnell-Worth, C.; Sun, C.; Zhang, X.; MacFarlane, D. R. Electro-Synthesis of Ammonia from Nitrogen at Ambient Temperature and Pressure in Ionic Liquids. *Energy Environ. Sci.* **2017**, 10, 2516–2520.
- (9) Kang, C. S. M.; Zhang, X.; MacFarlane, D. R. Synthesis and Physicochemical Properties of Fluorinated Ionic Liquids with High Nitrogen Gas Solubility. *J. Phys. Chem. C* **2018**, 122, 24550–24558.
- (10) Welton, T. Room-Temperature Ionic Liquids. Solvents for Synthesis and Catalysis. *Chem. Rev.* **1999**, 99, 2071–2084.
- (11) Pozzi, G.; Mihali, V.; Foschi, F.; Penso, M.; Quici, S.; Fish, R. H. 3,5-Bis(N-Perfluorooctyl)Benzyltriethylammonium Bromide (F-Teba): An Efficient, Easily Recoverable Fluorous Catalyst for Solid-Liquid PTC Reactions. *Adv. Synth. Catal.* **2009**, 351, 3072–3076.
- (12) Alves, M.; Vieira, N. S. M.; Rebelo, L. P. N.; Araújo, J. M. M.; Pereira, A. B.; Archer, M. Fluorinated Ionic Liquids for Protein Drug Delivery Systems: Investigating Their Impact on the Structure and Function of Lysozyme. *Int. J. Pharm.* **2017**, 526, 309–320.
- (13) Riess, J. G. Oxygen Carriers (“Blood Substitutes”)—Raison D’être, Chemistry, and Some Physiology. *Chem. Rev.* **2001**, 101, 2797–2920.
- (14) Pereira, A. B.; Araújo, J. M. M.; Martinho, S.; Alves, F.; Nunes, S.; Matias, A.; Duarte, C. M. M.; Rebelo, L. P. N.; Marrucho, I. M. Fluorinated Ionic Liquids: Properties and Applications. *ACS Sustainable Chem. Eng.* **2013**, 1, 427–439.
- (15) Riess, J. G. Highly Fluorinated Amphiphilic Molecules and Self-Assemblies with Biomedical Potential. *Curr. Opin. Colloid Interface Sci.* **2009**, 14, 294–304.
- (16) Lo Celso, F.; Yoshida, Y.; Castiglione, F.; Ferro, M.; Mele, A.; Jafta, C. J.; Triolo, A.; Russina, O. Direct Experimental Observation of Mesoscopic Fluorous Domains in Fluorinated Room Temperature Ionic Liquids. *Phys. Chem. Chem. Phys.* **2017**, 19, 13101–13110.
- (17) Lo Celso, F.; Appetecchi, G. B.; Jafta, C. J.; Gontrani, L.; Canongia Lopes, J. N.; Triolo, A.; Russina, O. Nanoscale Organization in the Fluorinated Room Temperature Ionic Liquid:

Tetraethyl Ammonium (Trifluoromethanesulfonyl)-(Nonafluorobutylsulfonyl)Imide. *J. Chem. Phys.* **2018**, *148*, 193816.

(18) Lo Celso, F.; Appetecchi, G. B.; Simonetti, E.; Zhao, M.; Castner, E. W.; Keiderling, U.; Gontrani, L.; Triolo, A.; Russina, O. Microscopic Structural and Dynamic Features in Triphlic Room Temperature Ionic Liquids. *Front. Chem.* **2019**, *7*, 285.

(19) Almantariotis, D.; Pensado, A. S.; Gunaratne, H. Q. N.; Hardacre, C.; Pádua, A. A. H.; Coxam, J.-Y.; Costa Gomes, M. F. Influence of Fluorination on the Solubilities of Carbon Dioxide, Ethane, and Nitrogen in 1-N-Fluoro-Alkyl-3-Methylimidazolium Bis(N-Fluoroalkylsulfonyl)Amide Ionic Liquids. *J. Phys. Chem. B* **2017**, *121*, 426–436.

(20) Almantariotis, D.; Stevanovic, S.; Fandiño, O.; Pensado, A. S.; Padua, A. A. H.; Coxam, J.-Y.; Costa Gomes, M. F. Absorption of Carbon Dioxide, Nitrous Oxide, Ethane and Nitrogen by 1-Alkyl-3-Methylimidazolium (Cnmim, N = 2,4,6) Tris(Pentafluoroethyl)-Trifluorophosphate Ionic Liquids (Etap). *J. Phys. Chem. B* **2012**, *116*, 7728–7738.

(21) Wilhelm, E.; Battino, R. Thermodynamic Functions of the Solubilities of Gases in Liquids at 25.Deg. *Chem. Rev.* **1973**, *73*, 1–9.

(22) Teles, A. R. R.; Correia, H.; Maximo, G. J.; Rebelo, L. P. N.; Freire, M. G.; Pereira, A. B.; Coutinho, J. A. P. Solid–Liquid Equilibria of Binary Mixtures of Fluorinated Ionic Liquids. *Phys. Chem. Chem. Phys.* **2016**, *18*, 25741–25750.

(23) Canongia Lopes, J. N.; Costa Gomes, M. F.; Husson, P.; Pádua, A. A. H.; Rebelo, L. P. N.; Sarraute, S.; Tariq, M. Polarity, Viscosity, and Ionic Conductivity of Liquid Mixtures Containing [C4c1im]⁺[Ntf2][−] and a Molecular Component. *J. Phys. Chem. B* **2011**, *115*, 6088–6099.

(24) Zhang, S.; Zhou, Q.; Lu, X.; Song, Y.; Wang, X. *Physicochemical Properties of Ionic Liquid Mixtures*; Springer: Netherlands, 2016.

(25) Fan, X.; Chen, L.; Borodin, O.; Ji, X.; Chen, J.; Hou, S.; Deng, T.; Zheng, J.; Yang, C.; Liou, S.-C.; et al. Non-Flammable Electrolyte Enables Li-Metal Batteries with Aggressive Cathode Chemistries. *Nat. Nanotechnol.* **2018**, *13*, 715–722.

(26) Ueno, K.; Murai, J.; Ikeda, K.; Tsuzuki, S.; Tsuchiya, M.; Tatara, R.; Mandai, T.; Umebayashi, Y.; Dokko, K.; Watanabe, M. Li⁺ Solvation and Ionic Transport in Lithium Solvate Ionic Liquids Diluted by Molecular Solvents. *J. Phys. Chem. C* **2016**, *120*, 15792–15802.

(27) Zheng, J.; Ji, G.; Fan, X.; Chen, J.; Li, Q.; Wang, H.; Yang, Y.; DeMella, K. C.; Raghavan, S. R.; Wang, C. High-Fluorinated Electrolytes for Li–S Batteries. *Adv. Energy Mater.* **2019**, *9*, 1803774.

(28) Dokko, K.; Tachikawa, N.; Yamauchi, K.; Tsuchiya, M.; Yamazaki, A.; Takashima, E.; Park, J.-W.; Ueno, K.; Seki, S.; Serizawa, N.; et al. Solvate Ionic Liquid Electrolyte for Li–S Batteries. *J. Electrochem. Soc.* **2013**, *160*, A1304–A1310.

(29) Stejskal, E. O.; Tanner, J. E. Spin Diffusion Measurements: Spin Echoes in the Presence of a Time-Dependent Field Gradient. *J. Chem. Phys.* **1965**, *42*, 288–292.

(30) Holz, M.; Heil, S. R.; Sacco, A. Temperature-Dependent Self-Diffusion Coefficients of Water and Six Selected Molecular Liquids for Calibration in Accurate 1h Nmr Pfg Measurements. *Phys. Chem. Chem. Phys.* **2000**, *2*, 4740–4742.

(31) Suryanto, B. H. R.; Kang, C. S. M.; Wang, D.; Xiao, C.; Zhou, F.; Azofra, L. M.; Cavallo, L.; Zhang, X.; MacFarlane, D. R. Rational Electrode–Electrolyte Design for Efficient Ammonia Electrosynthesis under Ambient Conditions. *ACS Energy Lett.* **2018**, *3*, 1219–1224.

(32) Bard, A. J.; Faulkner, L. R.; Leddy, J.; Zoski, C. G. *Electrochemical Methods: Fundamentals and Applications*; Wiley: New York, 1980; Vol. 2.

(33) Dunitz, J. D. Organic Fluorine: Odd Man Out. *ChemBioChem* **2004**, *5*, 614–621.

(34) Gjaldbaek, J. C.; Hildebrand, J. H. The Solubility of Nitrogen in Carbon Disulfide, Benzene, Normal- and Cyclo-Hexane, and in Three Fluorocarbons. *J. Am. Chem. Soc.* **1949**, *71*, 3147–3150.

(35) Deschamps, J.; Costa Gomes, M. F.; Pádua, A. A. H. Molecular Simulation Study of Interactions of Carbon Dioxide and Water with Ionic Liquids. *ChemPhysChem* **2004**, *5*, 1049–1052.

(36) Costa Gomes, M. F.; Husson, P. Ionic Liquids: Promising Media for Gas Separations. *Ionic Liquids: From Knowledge to Application*; American Chemical Society: Philadelphia, USA, 2009; Vol. 1030, pp 223–237.

(37) Costa Gomes, M. F.; Pádua, A. A. H. Gas–Liquid Interactions in Solution. *Pure Appl. Chem.* **2005**, *77*, 653.

(38) Stevanovic, S.; Costa Gomes, M. F. Solubility of Carbon Dioxide, Nitrous Oxide, Ethane, and Nitrogen in 1-Butyl-1-Methylpyrrolidinium and Trihexyl(Tetradecyl)Phosphonium Tris-(Pentafluoroethyl)Trifluorophosphate (Etap) Ionic Liquids. *J. Chem. Thermodyn.* **2013**, *59*, 65–71.

(39) Gaciño, F. M.; Regueira, T.; Lugo, L.; Comuñas, M. J. P.; Fernández, J. Influence of Molecular Structure on Densities and Viscosities of Several Ionic Liquids. *J. Chem. Eng. Data* **2011**, *56*, 4984–4999.

(40) Jacquemin, J.; Ge, R.; Nancarrow, P.; Rooney, D. W.; Costa Gomes, M. F.; Pádua, A. A. H.; Hardacre, C. Prediction of Ionic Liquid Properties. I. Volumetric Properties as a Function of Temperature at 0.1 Mpa. *J. Chem. Eng. Data* **2008**, *53*, 716–726.

(41) Gadžurić, S.; Tot, A.; Zec, N.; Papović, S.; Vraneš, M. Volumetric Properties of Binary Mixtures of 1-Butyl-1-Methylpyrrolidinium Tris(Pentafluoroethyl)Trifluorophosphate with N-Methylformamide, N-Ethylformamide, N,N-Dimethylformamide, N,N-Dibutylformamide, and N,N-Dimethylacetamide from (293.15 to 323.15) K. *J. Chem. Eng. Data* **2014**, *59*, 1225–1231.

(42) De Lorenzi, L.; Fermeglia, M.; Torriano, G. Density and Viscosity of 1-Methoxy-2-Propanol, 2-Methyltetrahydrofuran, A,A,A-Trifluorotoluene, and Their Binary Mixtures with 1,1,1-Trichloroethane at Different Temperatures. *J. Chem. Eng. Data* **1996**, *41*, 1121–1125.

(43) Redlich, O.; Kister, A. T. Algebraic Representation of Thermodynamic Properties and the Classification of Solutions. *Ind. Eng. Chem.* **1948**, *40*, 345–348.

(44) Dias, A. M. A.; Bonifácio, R. P.; Marrucho, I. M.; Pádua, A. A. H.; Costa Gomes, M. F. Solubility of Oxygen in N-Hexane and in N-Perfluorohexane. Experimental Determination and Prediction by Molecular Simulation. *Phys. Chem. Chem. Phys.* **2003**, *5*, 543–549.

(45) Santos, F. J. V.; Nieto de Castro, C. A.; Dymond, J. H.; Dalaouti, N. K.; Assael, M. J.; Nagashima, A. Standard Reference Data for the Viscosity of Toluene. *J. Phys. Chem. Ref. Data* **2006**, *35*, 1–8.

(46) Harris, K. R.; Newitt, P. J.; Woolf, L. A. Temperature and Density Dependence of the Viscosity of Cyclopentane. *J. Chem. Eng. Data* **2004**, *49*, 138–142.

(47) Grunberg, L.; Nissan, A. H. Mixture Law for Viscosity. *Nature* **1949**, *164*, 799–800.

(48) MacFarlane, D. R.; Chong, A. L.; Forsyth, M.; Kar, M.; Vijayaraghavan, R.; Somers, A.; Pringle, J. M. New Dimensions in Salt-Solvent Mixtures: A 4th Evolution of Ionic Liquids. *Faraday Discuss.* **2018**, *206*, 9–28.

(49) Stassen, H. K.; Ludwig, R.; Wulf, A.; Dupont, J. Imidazolium Salt Ion Pairs in Solution. *Chem.—Eur. J.* **2015**, *21*, 8324–8335.

(50) Ueno, K.; Tokuda, H.; Watanabe, M. Ionicity in Ionic Liquids: Correlation with Ionic Structure and Physicochemical Properties. *Phys. Chem. Chem. Phys.* **2010**, *12*, 1649–1658.

(51) Noda, A.; Hayamizu, K.; Watanabe, M. Pulsed-Gradient Spin–Echo 1h and 19f Nmr Ionic Diffusion Coefficient, Viscosity, and Ionic Conductivity of Non-Chloroaluminate Room-Temperature Ionic Liquids. *J. Phys. Chem. B* **2001**, *105*, 4603–4610.

(52) MacFarlane, D. R.; Forsyth, M.; Izgorodina, E. I.; Abbott, A. P.; Annat, G.; Fraser, K. On the Concept of Ionicity in Ionic Liquids. *Phys. Chem. Chem. Phys.* **2009**, *11*, 4962–4967.

(53) Harris, K. R. Can the Transport Properties of Molten Salts and Ionic Liquids Be Used to Determine Ion Association? *J. Phys. Chem. B* **2016**, *120*, 12135–12147.

(54) Harris, K. R.; Kanakubo, M. Self-Diffusion Coefficients and Related Transport Properties for a Number of Fragile Ionic Liquids. *J. Chem. Eng. Data* **2016**, *61*, 2399–2411.

(55) Walden, P. Organic Solutions-and Ionisation Means. Iii. Chapter: Internal Friction and Its Connection with Conductivity. *Z. Phys. Chem.* **1906**, *55*, 207–249.

(56) Yoshizawa, M.; Xu, W.; Angell, C. A. Ionic Liquids by Proton Transfer: Vapor Pressure, Conductivity, and the Relevance of ΔpK_a from Aqueous Solutions. *J. Am. Chem. Soc.* **2003**, *125*, 15411–15419.

High Nitrogen Gas Solubility and Physicochemical Properties of [C₄mpyr][eFAP]– Fluorinated Solvent Mixtures

*Colin S. M. Kang, Xinyi Zhang and Douglas R. MacFarlane**

ARC Centre of Excellence for Electromaterials Science, School of Chemistry, Monash
University, Clayton, Victoria 3800, Australia

SUPPORTING INFORMATION

1. Detailed experimental and calculations for N₂ solubility

Details for the N₂ solubility apparatus, including instrument schematic and specifications, can be found in a previous publication.²⁰⁴ The description and calculations for N₂ solubility are shown below:

- (a) First, the number of moles of N₂ admitted into the Ec containing the degassed liquid sample is given by **equation 1**:

$$n_{N_2}^{admitted} = \frac{p_1 V_{Bc}}{RT_1 Z_1} - \frac{p_2 V_{Bc}}{RT_2 Z_2} \quad (1)$$

Here, p_1 and T_1 are the initial pressure and temperature before N₂ is admitted, and p_2 and T_2 are the pressure and temperature after thermal equilibrium respectively. V_{Bc} is the volume of the Bc, R is the universal gas constant, and Z_1, Z_2 are the compressibility factors of N₂ at the given temperature and pressure.

- (b) The number of moles of N₂ measured in the headspace of the Ec is determined by **equation 2**:

$$n_{N_2}^{headspace} = \frac{(p_3 - p_{sample})(V_{Ec} - V_{sample})}{RT_3 Z_{12}} \quad (2)$$

Here, p_3 is the total pressure (N₂ and any vapor pressure exerted by the sample mixture) contained in the headspace of the EC volume V_{Ec} , V_{sample} is the volume of the sample mixture of which the N₂ solubility is measured at temperature T_3 . p_{sample} is the vapor pressure exerted by the sample mixture that is measured before thermal equilibrium (which is usually negligible in a neat IL), Z_{12} is the compressibility factor of the vapor phase (that consists of N₂ and the vapor pressure exerted by the sample mixture) in equilibrium with the sample mixture, calculated by **equation 3**:²²⁰

$$Z_{12} = 1 + \frac{P}{RT} (y_1 B_{22} + y_2 B_{33} + y_1 y_2 \delta_{23}) \quad (3)$$

Here, y_1 and y_2 are the mole fraction of N_2 and the mole fraction of solvent contained in the vapor phase respectively, B_{22} and B_{33} are the second virial coefficients of N_2 and the respective solvent. δ_{23} is calculated using the second virial coefficient of each pure component and the crossed virial coefficient B_{23} , taken as the average between B_{22} and B_{33} ($\delta_{23} = 2B_{22} - B_{33} - B_{23}$).^{190, 220}

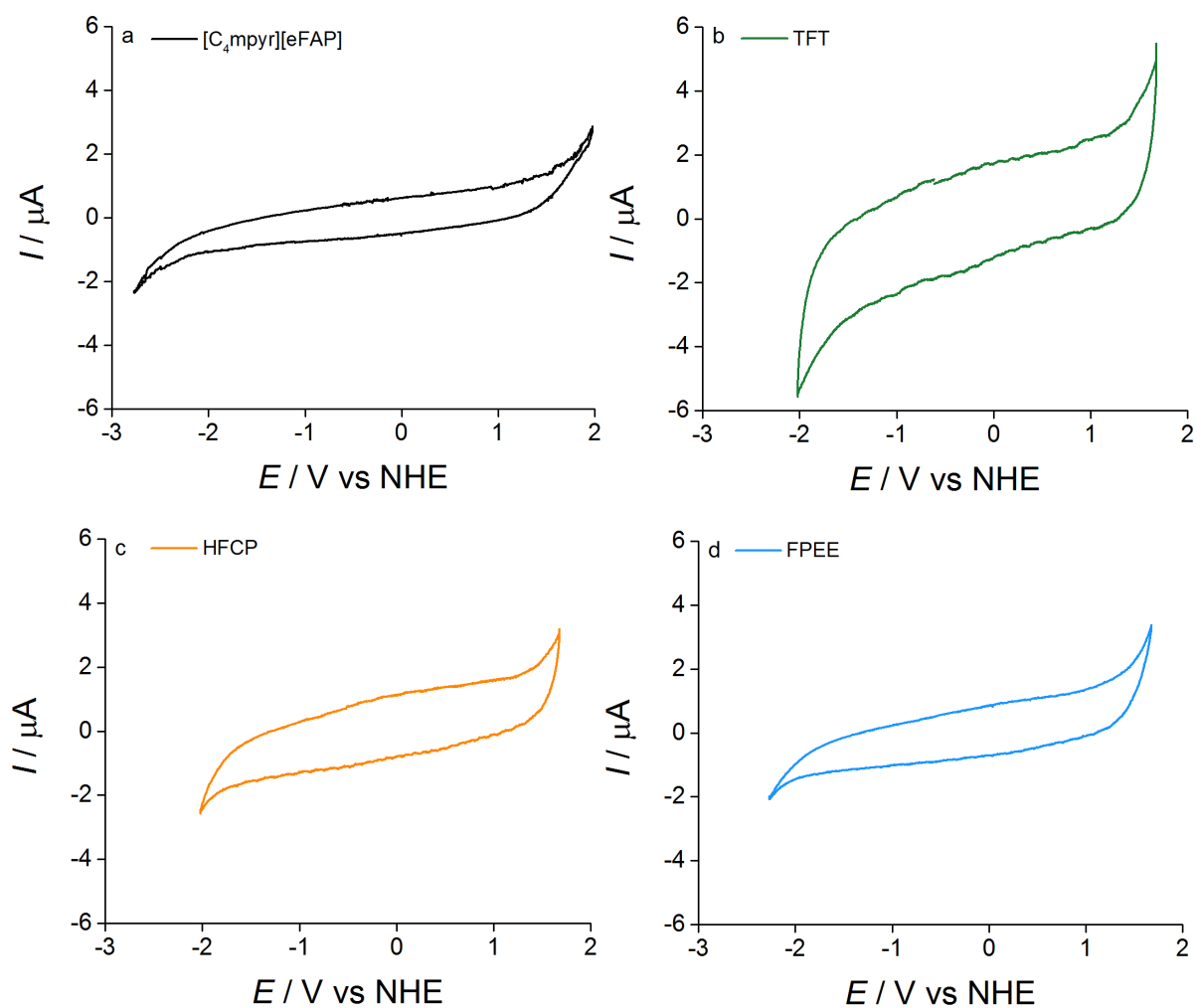
Although measurements of N_2 solubility in this study are conducted near atmospheric pressure, where such compressibility factors are not likely to be a large correction, it is still important to account for such non-ideality of gases. The final volume of sample mixture, upon mixing the IL and solvent together, is known by the exact mass and measuring the density of the final binary mixture. Furthermore, the amount of solvent that is present in the vapor phase is subtracted from the total volume of the liquid phase, although such values are substantially lower than the volume of sample mixture and hardly affects measurement accuracy.

(c) Lastly, the moles of N_2 that is dissolved in the liquid sample is determined by the difference of N_2 admitted, and N_2 in the headspace:

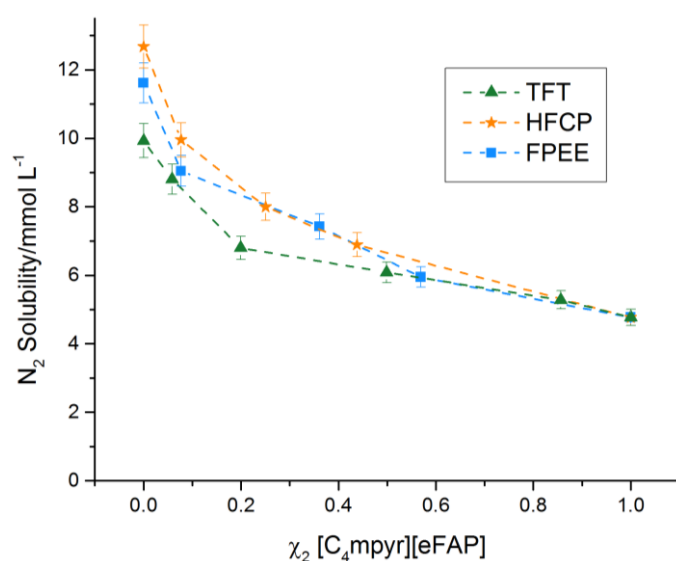
$$n_{N_2}^{absorbed} = n_{N_2}^{admitted} - n_{N_2}^{headspace} \quad (4)$$

Supporting Table S1. Experimental values of N_2 solubility, corrected to a partial pressure of $p = 1$ atm where p_{eq} is the experimental equilibrium pressure, in $[C_4mpyr][eFAP]$ binary mixtures at $30^\circ C$, as a function of $[C_4mpyr][eFAP]$ mass fraction wt_2 , volume fraction Φ , and mole fraction χ_2 , expressed as molar concentration C_{N_2} , mole fraction χ_{2N_2} , and molal concentration b_{N_2} .

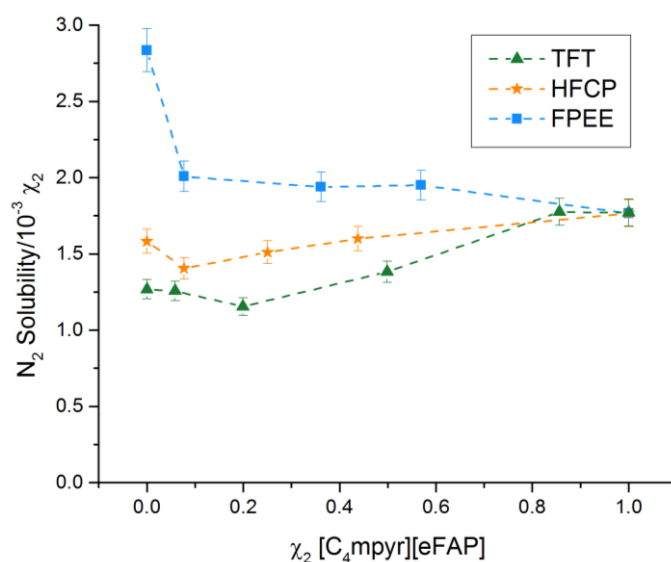
Sample Mixture	wt_2	Φ	χ_2	p_{eq} / 10^4 Pa	p_{sample} / 10^4 Pa	C_{N_2} / $mmol\ L^{-1}$	χ_{2N_2} / 10^{-3}	b_{N_2} / $mmol\ kg^{-1}$
$[C_4mpyr][eFAP]$	1.00	1.00	1.00	9.79	-	4.8	1.8	3.0
	1.00	1.00	1.00	9.67	-	4.7	1.7	3.0
$[C_4mpyr][eFAP]/$ TFT	0.96	0.95	0.86	10.04	0.32	5.5	1.8	3.5
	0.96	0.95	0.86	9.82	0.33	5.6	1.9	3.6
	0.80	0.75	0.50	9.60	0.51	5.7	1.4	3.8
	0.80	0.75	0.50	9.78	0.58	5.5	1.4	3.7
	0.80	0.75	0.50	9.57	0.63	5.5	1.4	3.7
	0.50	0.43	0.20	9.72	0.67	6.8	1.2	5.0
	0.50	0.43	0.20	9.43	0.78	6.7	1.1	4.9
	0.20	0.16	0.06	8.70	0.82	8.8	1.2	7.1
	0.20	0.16	0.06	8.95	0.80	8.8	1.2	7.1
	0.00	0.00	0.00	8.24	0.81	9.9	1.2	8.4
	0.00	0.00	0.00	8.99	0.82	9.9	1.2	8.5
	0.00	0.00	0.00	8.73	0.77	10.2	1.3	8.7
$[C_4mpyr][eFAP]/$ HFCP	0.70	0.70	0.44	9.49	0.76	6.9	1.6	4.4
	0.70	0.70	0.44	9.45	0.83	6.9	1.6	4.3
	0.50	0.50	0.25	9.10	1.10	8.1	1.5	5.0
	0.50	0.50	0.25	9.08	1.10	8.1	1.5	5.1
	0.20	0.20	0.08	8.55	1.30	10.0	1.4	6.2
	0.20	0.20	0.08	8.54	1.35	9.9	1.4	6.3
	0.00	0.00	0.00	7.75	1.41	12.2	1.6	7.8
	0.00	0.00	0.00	8.14	1.49	12.3	1.6	7.8
$[C_4mpyr][eFAP]/$ FPPE	0.70	0.71	0.57	9.81	0.27	6.5	1.9	4.1
	0.70	0.71	0.57	9.82	0.24	6.6	2.0	4.1
	0.50	0.51	0.36	9.39	0.23	7.4	1.9	4.6
	0.50	0.51	0.36	9.38	0.26	7.5	1.9	4.6
	0.20	0.21	0.08	9.18	0.26	9.0	2.0	5.5
	0.20	0.21	0.08	9.16	0.26	9.1	2.0	5.6
	0.00	0.00	0.00	8.68	0.24	11.6	2.4	7.1
	0.00	0.00	0.00	8.71	0.25	11.6	2.4	7.1



Supporting Figure S1: Electrochemical potential ranges vs. NHE of a) $[C_4\text{mpyr}][\text{eFAP}]$, and binary mixtures in a 1:1 volumetric ratio of b) $[C_4\text{mpyr}][\text{eFAP}]$ –TFT, c) $[C_4\text{mpyr}][\text{eFAP}]$ –HFCP, and d) $[C_4\text{mpyr}][\text{eFAP}]$ –FPEE. Cyclic voltammetry was conducted on a 1 mm glassy carbon working electrode at a scan rate of 100 mV s^{-1} under N_2 atmosphere.



Supporting Figure S2: N_2 solubility (mmol L^{-1}) of $[C_4\text{mpyr}][\text{eFAP}]$ binary mixtures, as a function of mole fraction χ_2 , with TFT (\blacktriangle), HFCP (\star) and FPEE (\blacksquare) at 30°C and $p = 1 \text{ atm}$. Lines serve as a guide only.



Supporting Figure S3: N_2 solubility (χ_{2N_2}) of $[C_4mpyr][eFAP]$ binary mixtures, as a function of mole fraction χ_2 , with TFT (\blacktriangle), HFCEP (\star) and FPEE (\blacksquare) at 30°C and $p = 1$ atm. Lines serve as a guide only.

Supporting Table S2: Experimental values of density (ρ), excess molar volume (V^E), reduced excess molar volume ($V^E(\chi_1\chi_2)^{-1}$), partial molar volume of TFT (\bar{V}_1) and $[C_4mpyr][eFAP]$ (\bar{V}_2) in $[C_4mpyr][eFAP]$ binary mixtures with TFT as a function of mole fraction χ_2 and weight fraction wt_2 at 25°C, 30°C, 35°C, 40°C, 45°C and 50°C.

χ_2	wt_2	ρ /g cm ⁻³	V^E /cm ³ mol ⁻¹	$V^E(\chi_1\chi_2)^{-1}$ /cm ³ mol ⁻¹	\bar{V}_1 /cm ³ mol ⁻¹	\bar{V}_2 /cm ³ mol ⁻¹
25 °C						
1.00	1.00	1.5877	-	-	-	-
0.86	0.96	1.5634	0.6	4.7	120.8	371.0
0.77	0.93	1.5504	0.0	-0.1	118.0	371.6
0.69	0.90	1.5389	-0.8	-3.7	117.9	371.6
0.50	0.80	1.4947	-1.5	-6.1	120.2	370.0
0.37	0.70	1.4529	-2.0	-8.7	121.4	368.4
0.27	0.60	1.4107	-2.0	-10.3	122.1	367.0
0.20	0.50	1.3694	-1.9	-11.7	122.5	365.4
0.14	0.40	1.3288	-1.5	-12.6	123.0	363.4
0.10	0.30	1.2893	-1.1	-13.0	123.3	361.0
0.06	0.20	1.2530	-0.9	-16.3	123.5	358.1
0.03	0.10	1.2166	-0.5	-18.1	123.7	355.0
0.01	0.05	1.1973	-0.1	-7.2	123.7	353.4
0.00	0.00	1.1811	-	-	-	-
30 °C						

x_2	wt_2	ρ /g cm ⁻³	V^E /cm ³ mol ⁻¹	$V^E(\chi_1\chi_2)^{-1}$ /cm ³ mol ⁻¹	\overline{V}_1 /cm ³ mol ⁻¹	\overline{V}_2 /cm ³ mol ⁻¹
1.00	1.00	1.5824	-	-	-	-
0.86	0.96	1.5580	0.6	4.7	120.8	371.0
0.77	0.93	1.5450	0.0	-0.1	118.0	371.6
0.69	0.90	1.5334	-0.8	-3.7	117.9	371.6
0.50	0.80	1.4890	-1.6	-6.1	120.2	370.0
0.37	0.70	1.4470	-2.1	-8.7	121.4	368.4
0.27	0.60	1.4047	-2.1	-10.3	122.1	367.0
0.20	0.50	1.3632	-1.9	-11.7	122.5	365.4
0.14	0.40	1.3224	-1.6	-12.6	123.0	363.4
0.10	0.30	1.2827	-1.2	-13.0	123.3	361.0
0.06	0.20	1.2463	-0.9	-16.3	123.5	358.1
0.03	0.10	1.2097	-0.5	-18.1	123.7	355.0
0.01	0.05	1.1904	-0.1	-7.2	123.7	353.4
0.00	0.00	1.1741	-	-	-	-
35 °C						
1.00	1.00	1.5771	-	-	-	-
0.86	0.96	1.5526	0.6	4.6	122.1	373.5
0.77	0.93	1.5395	-0.1	-0.3	119.3	374.1
0.69	0.90	1.5280	-0.9	-4.0	119.1	374.1
0.50	0.80	1.4834	-1.6	-6.6	121.5	372.4
0.37	0.70	1.4411	-2.2	-9.3	122.8	370.8
0.27	0.60	1.3987	-2.2	-11.1	123.4	369.3
0.20	0.50	1.3570	-2.0	-12.6	124.0	367.6
0.14	0.40	1.3160	-1.7	-13.5	124.4	365.4
0.10	0.30	1.2761	-1.2	-14.0	124.8	362.8
0.06	0.20	1.2396	-1.0	-17.6	125.0	359.7
0.03	0.10	1.2028	-0.5	-19.7	125.2	356.3
0.01	0.05	1.1834	-0.1	-9.0	125.2	354.6
0.00	0.00	1.1670	-	-	-	-
40 °C						
1.00	1.00	1.5719	-	-	-	-
0.86	0.96	1.5473	0.6	4.6	122.7	374.7
0.77	0.93	1.5341	-0.1	-0.4	119.9	375.3

x_2	wt ₂	ρ /g cm ⁻³	V^E /cm ³ mol ⁻¹	$V^E(\chi_1\chi_2)^{-1}$ /cm ³ mol ⁻¹	\bar{V}_1 /cm ³ mol ⁻¹	\bar{V}_2 /cm ³ mol ⁻¹
0.69	0.90	1.5225	-0.9	-4.1	119.8	375.4
0.50	0.80	1.4777	-1.7	-6.8	122.1	373.7
0.37	0.70	1.4353	-2.2	-9.6	123.4	372.0
0.27	0.60	1.3926	-2.3	-11.5	124.1	370.5
0.20	0.50	1.3507	-2.1	-13.0	124.7	368.7
0.14	0.40	1.3096	-1.7	-14.0	125.1	366.4
0.10	0.30	1.2695	-1.3	-14.6	125.5	363.7
0.06	0.20	1.2328	-1.0	-18.2	125.8	360.5
0.03	0.10	1.1959	-0.5	-20.5	125.9	357.0
0.01	0.05	1.1764	-0.1	-9.8	126.0	355.2
0.00	0.00	1.1598	-	-	-	-
45 °C						
1.00	1.00	1.5666	-	-	-	-
0.86	0.96	1.5419	0.5	4.5	123.3	376.0
0.77	0.93	1.5287	-0.1	-0.6	120.5	376.6
0.69	0.90	1.5170	-0.9	-4.3	120.4	376.6
0.50	0.80	1.4720	-1.8	-7.1	122.8	374.9
0.37	0.70	1.4294	-2.3	-10.0	124.1	373.2
0.27	0.60	1.3866	-2.3	-11.8	124.8	371.7
0.20	0.50	1.3445	-2.2	-13.5	125.4	369.8
0.14	0.40	1.3032	-1.8	-14.6	125.9	367.4
0.10	0.30	1.2629	-1.3	-15.2	126.3	364.5
0.06	0.20	1.2260	-1.0	-19.0	126.6	361.2
0.03	0.10	1.1889	-0.6	-21.3	126.7	357.6
0.01	0.05	1.1693	-0.1	-10.8	126.8	355.7
0.00	0.00	1.1526	-	-	-	-
50 °C						
1.00	1.00	1.5614	-	-	-	-
0.86	0.96	1.5366	0.5	4.3	124.0	377.3
0.77	0.93	1.5233	-0.1	-0.7	121.1	377.9
0.69	0.90	1.5115	-1.0	-4.6	121.0	377.9
0.50	0.80	1.4664	-1.8	-7.4	123.5	376.1
0.37	0.70	1.4236	-2.4	-10.4	124.8	374.4

χ_2	wt ₂	ρ /g cm ⁻³	V^E /cm ³ mol ⁻¹	$V^E(\chi_1\chi_2)^{-1}$ /cm ³ mol ⁻¹	\bar{V}_1 /cm ³ mol ⁻¹	\bar{V}_2 /cm ³ mol ⁻¹
0.27	0.60	1.3805	-2.4	-12.3	125.6	372.8
0.20	0.50	1.3383	-2.2	-14.0	126.1	370.9
0.14	0.40	1.2967	-1.9	-15.2	126.6	368.4
0.10	0.30	1.2563	-1.4	-15.8	127.1	365.4
0.06	0.20	1.2192	-1.1	-19.7	127.3	361.9
0.03	0.10	1.1819	-0.6	-22.3	127.5	358.1
0.01	0.05	1.1622	-0.2	-11.8	127.6	356.1
0.00	0.00	1.1454	-	-	-	-

Supporting Table S3. Experimental values of density (ρ), excess molar volume (V^E), reduced excess molar volume ($V^E(\chi_1\chi_2)^{-1}$), partial molar volume of HFCE (\bar{V}_1) and [C₄mpyr][eFAP] (\bar{V}_2) in [C₄mpyr][eFAP] binary mixtures with HFCE as a function of mole fraction χ_2 and weight fraction wt₂ at 25 °C, 30 °C, 35 °C, 40 °C, 45 °C and 50 °C.

χ_2	wt ₂	ρ /g cm ⁻³	V^E /cm ³ mol ⁻¹	$V^E(\chi_1\chi_2)^{-1}$ /cm ³ mol ⁻¹	\bar{V}_1 /cm ³ mol ⁻¹	\bar{V}_2 /cm ³ mol ⁻¹
25 °C						
1.00	1.00	1.5877	-	-	-	-
0.84	0.94	1.5837	0.7	4.9	123.5	370.9
0.65	0.85	1.5857	0.0	-0.1	122.0	371.2
0.44	0.70	1.5884	-0.7	-2.9	122.7	370.7
0.33	0.60	1.5901	-1.0	-4.7	122.7	370.7
0.25	0.50	1.5912	-1.2	-6.6	122.8	370.2
0.18	0.40	1.5914	-1.3	-8.7	123.2	368.7
0.13	0.30	1.5900	-1.2	-10.8	123.7	366.0
0.08	0.20	1.5875	-1.0	-14.0	124.2	361.9
0.04	0.10	1.5825	-0.6	-18.0	124.5	356.8
0.02	0.05	1.5796	-0.4	-24.8	124.6	353.8
0.00	0.00	1.5738	-	-	-	-
30 °C						
1.00	1.00	1.5824	-	-	-	-
0.84	0.94	1.5782	0.6	4.7	124.1	372.1
0.65	0.85	1.5799	-0.1	-0.4	122.7	372.5
0.44	0.70	1.5821	-0.8	-3.3	123.4	371.9
0.33	0.60	1.5834	-1.2	-5.2	123.4	371.9
0.25	0.50	1.5840	-1.3	-7.2	123.6	371.4

x_2	wt_2	ρ /g cm ⁻³	V^E /cm ³ mol ⁻¹	$V^E(\chi_1\chi_2)^{-1}$ /cm ³ mol ⁻¹	\bar{V}_1 /cm ³ mol ⁻¹	\bar{V}_2 /cm ³ mol ⁻¹
0.18	0.40	1.5836	-1.4	-9.4	124.0	369.7
0.13	0.30	1.5816	-1.3	-11.6	124.6	366.8
0.08	0.20	1.5784	-1.1	-15.0	125.0	362.5
0.04	0.10	1.5726	-0.7	-19.2	125.3	357.1
0.02	0.05	1.5693	-0.4	-26.5	125.4	354.0
0.00	0.00	1.5629	-	-	-	-
35 °C						
1.00	1.00	1.5771	-	-	-	-
0.84	0.94	1.5727	0.6	4.5	124.8	373.4
0.65	0.85	1.5741	-0.1	-0.7	123.3	373.7
0.44	0.70	1.5757	-0.9	-3.8	124.1	373.1
0.33	0.60	1.5766	-1.3	-5.7	124.1	373.1
0.25	0.50	1.5769	-1.5	-7.9	124.4	372.5
0.18	0.40	1.5758	-1.5	-10.1	124.8	370.7
0.13	0.30	1.5732	-1.4	-12.5	125.4	367.6
0.08	0.20	1.5693	-1.1	-16.0	125.9	363.1
0.04	0.10	1.5627	-0.7	-20.5	126.2	357.4
0.02	0.05	1.5590	-0.5	-28.2	126.3	354.1
0.00	0.00	1.5520	-	-	-	-
40 °C						
1.00	1.00	1.5719	-	-	-	-
0.84	0.94	1.5673	0.6	4.2	125.5	374.6
0.65	0.85	1.5684	-0.2	-1.0	124.1	374.9
0.44	0.70	1.5694	-1.0	-4.2	124.8	374.4
0.33	0.60	1.5698	-1.4	-6.3	124.8	374.3
0.25	0.50	1.5699	-1.6	-8.7	125.1	373.6
0.18	0.40	1.5680	-1.6	-10.9	125.6	371.6
0.13	0.30	1.5647	-1.5	-13.4	126.2	368.3
0.08	0.20	1.5601	-1.2	-17.2	126.8	363.5
0.04	0.10	1.5527	-0.8	-21.9	127.1	357.5
0.02	0.05	1.5485	-0.5	-30.0	127.2	354.1
0.00	0.00	1.5410	-	-	-	-
45 °C						

χ_2	wt ₂	ρ /g cm ⁻³	V^E /cm ³ mol ⁻¹	$V^E(\chi_1\chi_2)^{-1}$ /cm ³ mol ⁻¹	\bar{V}_1 /cm ³ mol ⁻¹	\bar{V}_2 /cm ³ mol ⁻¹
1.00	1.00	1.5666	-	-	-	-
0.84	0.94	1.5619	0.5	4.0	126.1	375.9
0.65	0.85	1.5626	-0.3	-1.3	124.8	376.2
0.44	0.70	1.5631	-1.2	-4.7	125.5	375.6
0.33	0.60	1.5631	-1.5	-6.9	125.6	375.5
0.25	0.50	1.5625	-1.8	-9.4	125.9	374.7
0.18	0.40	1.5601	-1.7	-11.7	126.5	372.6
0.13	0.30	1.5562	-1.6	-14.5	127.1	369.1
0.08	0.20	1.5509	-1.3	-18.4	127.7	364.0
0.04	0.10	1.5426	-0.8	-23.3	128.0	357.7
0.02	0.05	1.5380	-0.5	-32.0	128.1	354.1
0.00	0.00	1.5299	-	-	-	-
50 °C						
1.00	1.00	1.5614	-	-	-	-
0.84	0.94	1.5564	0.5	3.7	126.8	377.2
0.65	0.85	1.5568	-0.4	-1.7	125.5	377.4
0.44	0.70	1.5567	-1.3	-5.2	126.3	376.8
0.33	0.60	1.5563	-1.7	-7.5	126.4	376.7
0.25	0.50	1.5553	-1.9	-10.2	126.7	375.8
0.18	0.40	1.5522	-1.9	-12.6	127.3	373.6
0.13	0.30	1.5477	-1.7	-15.6	128.0	369.8
0.08	0.20	1.5417	-1.4	-19.8	128.6	364.4
0.04	0.10	1.5324	-0.9	-24.9	129.0	357.7
0.02	0.05	1.5274	-0.6	-34.1	129.1	353.9
0.00	0.00	1.5187	-	-	-	-

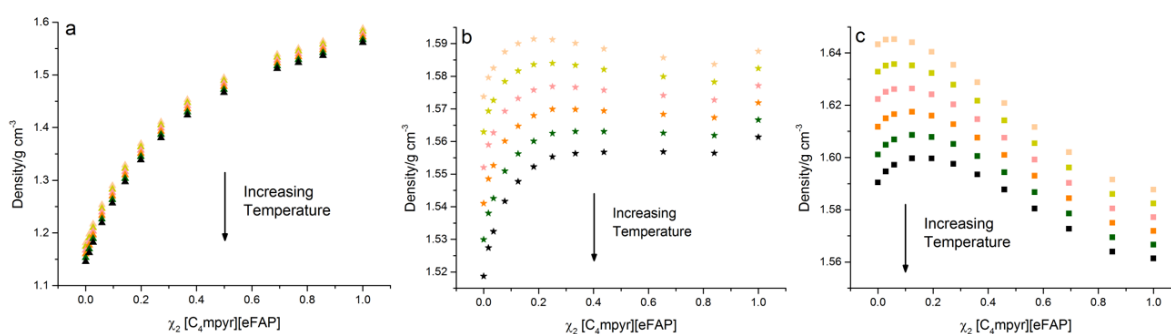
Supporting Table S4. Experimental values of density (ρ), excess molar volume (V^E), reduced excess molar volume ($V^E(\chi_1\chi_2)^{-1}$), partial molar volume of FPEE (\bar{V}_1) and [C₄mpyr][eFAP] (\bar{V}_2) in [C₄mpyr][eFAP] binary mixtures with FPEE as a function of mole fraction χ_2 and weight fraction wt₂ at 25°C, 30°C, 35°C, 40°C, 45°C and 50°C.

χ_2	wt ₂	ρ /g cm ⁻³	V^E /cm ³ mol ⁻¹	$V^E(\chi_1\chi_2)^{-1}$ /cm ³ mol ⁻¹	\bar{V}_1 /cm ³ mol ⁻¹	\bar{V}_2 /cm ³ mol ⁻¹
25 °C						

x_2	wt_2	ρ /g cm ⁻³	V^E /cm ³ mol ⁻¹	$V^E(x_1x_2)^{-1}$ /cm ³ mol ⁻¹	\bar{V}_1 /cm ³ mol ⁻¹	\bar{V}_2 /cm ³ mol ⁻¹
1.00	1.00	1.5877	-	-	-	-
0.85	0.91	1.5915	0.2	1.7	199.1	370.7
0.69	0.80	1.6020	-0.7	-3.3	196.9	371.2
0.57	0.70	1.6116	-1.4	-5.8	197.6	370.8
0.46	0.60	1.6208	-2.0	-7.9	198.5	369.9
0.36	0.50	1.6288	-2.2	-9.6	199.3	368.7
0.27	0.40	1.6354	-2.3	-11.3	200.0	367.1
0.20	0.30	1.6404	-2.0	-13.0	200.8	364.8
0.12	0.20	1.6441	-1.7	-15.3	201.4	361.3
0.06	0.10	1.6452	-1.0	-17.9	201.9	356.3
0.03	0.05	1.6451	-0.6	-20.9	202.0	353.2
0.00	0.00	1.6433	-	-	-	-
30 °C						
1.00	1.00	1.5824	-	-	-	-
0.85	0.91	1.5860	0.2	1.4	200.1	371.9
0.69	0.80	1.5961	-0.8	-3.7	197.9	372.4
0.57	0.70	1.6054	-1.5	-6.2	198.6	372.0
0.46	0.60	1.6142	-2.1	-8.4	199.6	371.1
0.36	0.50	1.6217	-2.4	-10.2	200.5	369.8
0.27	0.40	1.6279	-2.4	-12.0	201.2	368.1
0.20	0.30	1.6323	-2.2	-13.7	202.0	365.7
0.12	0.20	1.6352	-1.7	-16.1	202.7	362.0
0.06	0.10	1.6357	-1.1	-18.9	203.2	356.8
0.03	0.05	1.6351	-0.6	-22.1	203.3	353.5
0.00	0.00	1.6328	-	-	-	-
35 °C						
1.00	1.00	1.5771	-	-	-	-
0.85	0.91	1.5805	0.1	1.0	201.1	373.1
0.69	0.80	1.5903	-0.9	-4.1	199.0	373.7
0.57	0.70	1.5992	-1.6	-6.7	199.7	373.2
0.46	0.60	1.6076	-2.2	-8.9	200.7	372.2
0.36	0.50	1.6146	-2.5	-10.9	201.6	371.0
0.27	0.40	1.6203	-2.5	-12.7	202.4	369.2

x_2	wt ₂	ρ /g cm ⁻³	V^E /cm ³ mol ⁻¹	$V^E(x_1x_2)^{-1}$ /cm ³ mol ⁻¹	\bar{V}_1 /cm ³ mol ⁻¹	\bar{V}_2 /cm ³ mol ⁻¹
0.20	0.30	1.6241	-2.3	-14.6	203.2	366.6
0.12	0.20	1.6264	-1.8	-17.0	203.9	362.7
0.06	0.10	1.6261	-1.1	-20.1	204.5	357.2
0.03	0.05	1.6251	-0.7	-23.3	204.6	353.7
0.00	0.00	1.6223	-	-	-	-
40 °C						
1.00	1.00	1.5719	-	-	-	-
0.85	0.91	1.5750	0.1	0.8	202.2	374.4
0.69	0.80	1.5844	-1.0	-4.5	200.0	374.9
0.57	0.70	1.5930	-1.8	-7.2	200.8	374.4
0.46	0.60	1.6009	-2.4	-9.5	201.9	373.4
0.36	0.50	1.6076	-2.7	-11.5	202.8	372.1
0.27	0.40	1.6127	-2.7	-13.5	203.6	370.2
0.20	0.30	1.6160	-2.4	-15.4	204.5	367.4
0.12	0.20	1.6175	-1.9	-17.9	205.2	363.3
0.06	0.10	1.6165	-1.2	-21.3	205.8	357.5
0.03	0.05	1.6150	-0.7	-24.5	206.0	353.9
0.00	0.00	1.6117	-	-	-	-
45 °C						
1.00	1.00	1.5666	-	-	-	-
0.85	0.91	1.5694	0.0	0.4	203.2	375.7
0.69	0.80	1.5785	-1.1	-5.0	201.1	376.2
0.57	0.70	1.5867	-1.9	-7.7	201.9	375.6
0.46	0.60	1.5943	-2.5	-10.1	203.0	374.6
0.36	0.50	1.6005	-2.8	-12.2	204.0	373.2
0.27	0.40	1.6051	-2.8	-14.3	204.9	371.2
0.20	0.30	1.6078	-2.6	-16.4	205.8	368.3
0.12	0.20	1.6086	-2.1	-18.9	206.6	364.0
0.06	0.10	1.6069	-1.3	-22.6	207.2	357.9
0.03	0.05	1.6048	-0.7	-25.8	207.3	354.0
0.00	0.00	1.6011	-	-	-	-
50 °C						
1.00	1.00	1.5614	-	-	-	-

χ_2	wt ₂	ρ /g cm ⁻³	V^E /cm ³ mol ⁻¹	$V^E(\chi_1\chi_2)^{-1}$ /cm ³ mol ⁻¹	\overline{V}_1 /cm ³ mol ⁻¹	\overline{V}_2 /cm ³ mol ⁻¹
0.85	0.91	1.5639	0.0	0.0	204.3	376.9
0.69	0.80	1.5727	-1.2	-5.5	202.2	377.4
0.57	0.70	1.5804	-2.0	-8.2	203.1	376.9
0.46	0.60	1.5877	-2.7	-10.8	204.2	375.8
0.36	0.50	1.5935	-3.0	-13.0	205.2	374.4
0.27	0.40	1.5975	-3.0	-15.1	206.1	372.3
0.20	0.30	1.5996	-2.7	-17.3	207.1	369.2
0.12	0.20	1.5997	-2.2	-20.0	207.9	364.6
0.06	0.10	1.5972	-1.3	-24.0	208.6	358.1
0.03	0.05	1.5946	-0.8	-27.3	208.7	354.1
0.00	0.00	1.5904	-	-	-	-



Supporting Figure S4: Density of [C₄mpyr][eFAP] binary mixtures, as a function of mole fraction χ_2 , in a) TFT (▲), b) HFCEP (★) and c) FPEE (■) at 25 °C, 30 °C, 35 °C, 40 °C, 45 °C and 50 °C.

Supporting Table S5. Redlich–Kister fitting coefficients A_n of the excess molar volumes of [C₄mpyr][eFAP] binary mixtures in TFT, HFCEP, FPEE at 25 °C, 30 °C, 35 °C, 40 °C, 45 °C, and 50 °C, and the associated fitting deviation calculated by equation 5.

T/°C	A0	A1	A2	A3	σ
TFT					
25	-6.861	-7.192	4.987	-9.091	0.101
30	-7.071	-7.437	4.903	-9.228	0.102
35	-7.312	-7.621	4.791	-9.425	0.103
40	-7.545	-7.841	4.714	-9.631	0.103
45	-7.817	-8.008	4.613	-9.923	0.103

$T/^{\circ}\text{C}$	A_0	A_1	A_2	A_3	σ
50	-8.106	-8.235	4.474	-10.125	0.104
HFCE					
25	-2.224	-5.733	-0.354	-10.895	0.048
30	-2.557	-6.021	-0.658	-11.194	0.052
35	-2.940	-6.346	-0.927	-11.533	0.055
40	-3.327	-6.792	-1.360	-11.608	0.061
45	-3.764	-7.042	-1.670	-12.154	0.064
50	-4.236	-7.410	-2.064	-12.546	0.069
FPEE					
25	-7.138	-8.598	1.453	-6.021	0.025
30	-7.612	-8.925	1.284	-6.129	0.027
35	-8.138	-9.237	1.071	-6.298	0.028
40	-8.676	-9.588	0.912	-6.537	0.029
45	-9.252	-9.962	0.662	-6.664	0.032
50	-9.843	-10.413	0.351	-6.694	0.037

The standard deviation of the polynomial fit is calculated by the following expression:

$$\sigma V^E = \left[\frac{\sum (V_{exp}^E - V_{calc}^E)^2}{N-n} \right]^{1/2} \quad (5)$$

Where N is the number of data points, n is the order of fitting Redlich–Kister polynomial equation.

10. Reduced Excess Molar Volume

The reduced V^E , calculated from $V^E/\chi_1\chi_2$, aids in describing non-ideal interactions between the IL and solvent, particularly as it is more sensitive at lower concentrations.²²¹ Papović and co-workers²²² studied the reduced V^E of IL mixtures containing imidazolium cations of varying alkyl chain length and γ -butyrolactone. For the cations of alkyl chain length > 4 , the reduced V^E changes upon addition of IL which was attributed due to imperfect packing and free volume. On the other hand, for ILs with cation alkyl chain length < 4 , the reduced V^E was constant

across the studied composition range between $\chi_2 = 0.1$ — 0.9 ; this suggested that a smaller extent of free volume is present when the IL exhibits a higher degree of order. In our [C₄mpyr][eFAP]–fluorinated solvent systems shown in **Figure S5**, the reduced V^E values are changing across all compositions, suggesting the presence of such free volume within the IL and solvent.

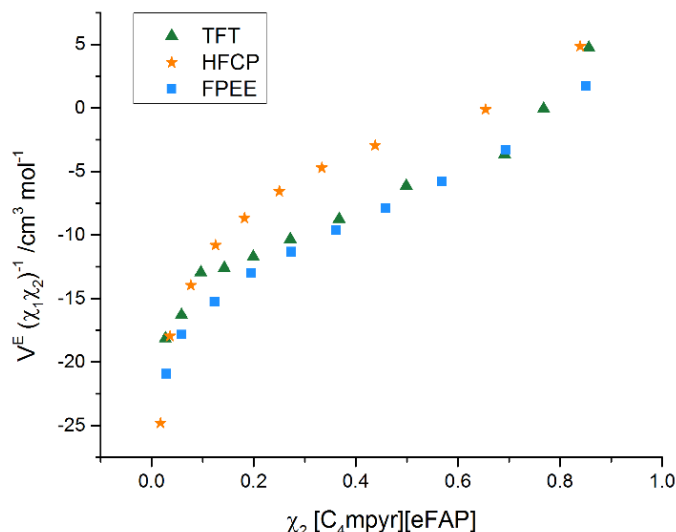
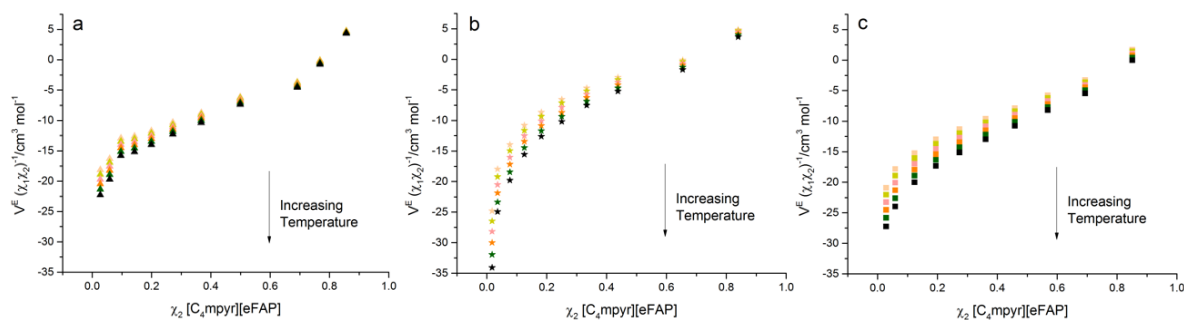


Figure S5: Reduced excess molar volumes ($V^E (\chi_1\chi_2)^{-1}$) of [C₄mpyr][eFAP] binary mixtures, as a function of mole fraction χ_2 , with TFT (\blacktriangle), HFCEP (\star) and FPEE (\blacksquare) at 25°C.

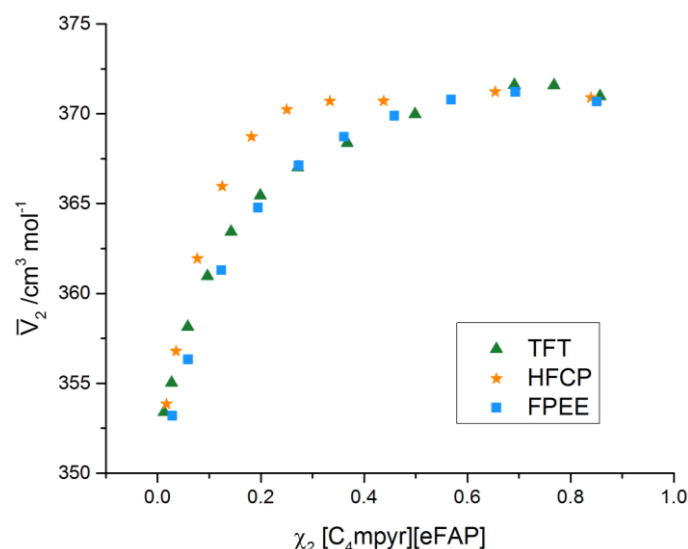
However, at very low concentrations of either IL or fluorinated solvent, a steep change in the magnitude of $V^E/\chi_1\chi_2$ values below $\chi_2 < 0.1$ (and $\chi > 0.8$) is observed for all three [C₄mpyr][eFAP]–solvent mixtures. This may reflect the different nature of [C₄mpyr][eFAP] compared to the fluorinated solvent (in terms of their interactions), and at either extreme, the complete solvation of each component is likely to be unfavorable. In contrast to this behavior, the reduced V^E of water and dioxane,²²³ where the two liquids share similar interactions, display a minimum of $-5 \text{ cm}^3 \text{ mol}^{-1}$. Our fluorinated IL electrolyte system, of dissimilar interactions, display minima values of $< -17 \text{ cm}^3 \text{ mol}^{-1}$ at $\chi_2 < 0.05$. Lastly, temperature does not appear to affect such trends other than the increase in magnitude of the reduced V^E (see **Figure S6**).



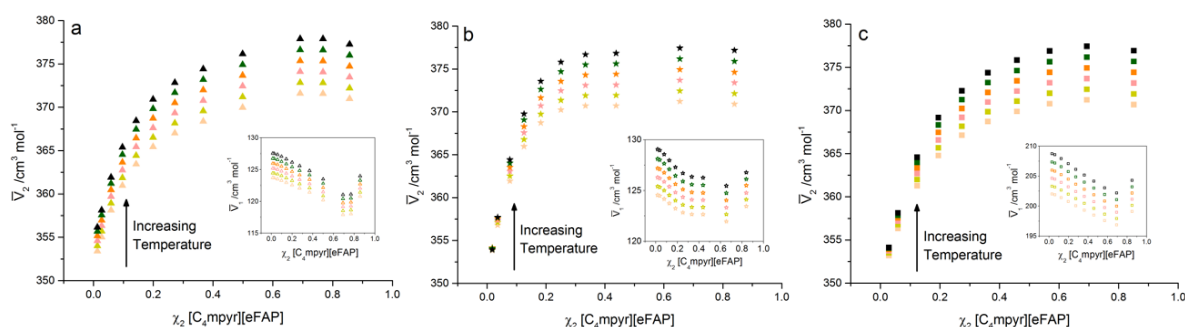
Supporting Figure S6: Reduced excess molar volume ($V^E(\chi_1\chi_2)^{-1}$) of $[C_4\text{mpyr}][\text{eFAP}]$ binary mixtures, as a function of mole fraction χ_2 , with a) TFT (\blacktriangle), b) HFCEP (\star) and c) FPEE (\blacksquare) at 25°C, 30°C, 35°C, 40°C, 45°C and 50°C.

11. Partial Molar Volume

Comparison of the partial molar volume of $[C_4\text{mpyr}][\text{eFAP}]$ in TFT, HFCEP, and FPEE mixtures across a range of compositions at 25°C are shown in **Supporting Figure S7**. With subsequent addition of $[C_4\text{mpyr}][\text{eFAP}]$, the partial molar volume initially rises sharply and then slowly increases toward the pure IL molar volume. The sharp differences in partial molar volume can reflect a change in the intermolecular interactions between the IL and fluorinated solvent due to the variation in environment as described before. The insets in **Supporting Figure S8** show the partial molar volume of the fluorinated solvents TFT, HFCEP and FPEE decreases upon initial addition of $[C_4\text{mpyr}][\text{eFAP}]$ and similarly follows the inverse trend of the IL partial molar volume corresponding to each solvent. Again, an increase in temperature does not appear to greatly affect such trends with regard to the partial molar volumes of either component as shown in **Supporting Figure S8**.



Supporting Figure S7: Comparison of partial molar volume of $[C_4\text{mpyr}][\text{eFAP}]$ in a binary mixture, as a function of mole fraction χ_2 , with TFT (\blacktriangle), HFCEP (\star) and FPEE (\blacksquare) at 25°C.



Supporting Figure S8: Partial molar volume of $[C_4\text{mpyr}][\text{eFAP}]$ in a binary mixture, as a function of mole fraction χ_2 , with a) TFT (\blacktriangle), b) HFCEP (\star) and c) FPEE (\blacksquare) at 25°C, 30°C, 35°C, 40°C, 45°C and 50°C. Insets show the partial molar volume of the respective fluorinated solvent in the binary mixture.

12. Free Volume Calculations of TFT and Toluene

To investigate the difference in attributed N_2 solubility, the free volume of TFT and toluene is estimated by the difference in molar volume, from the crystal structure to liquid. The molar volumes are calculated from the density at its crystal structure state, and the liquid density measured at 30 °C. We assume the crystal structure will exhibit a free volume close to zero, compared to the liquid form at which the crystalline packing structure is broken and free volume exists between such molecules. **Supporting Table S6** shows the estimated free

volume, from the density and molar volume, of TFT, toluene and [C₂mim][BF₄] at the crystalline and liquid state.

Supporting Table S6. The estimated free volume (FV) and % change in TFT, toluene, and [C₂mim][BF₄] calculated from the molecular weight (MW), density (ρ) and molar volume (V_m) of the crystal structure and liquid at 30 °C.

Sample	MW /g mol ⁻¹	ρ (crystal) /g cm ⁻³	V_m (crystal) /cm ³ mol ⁻¹	ρ (30 °C) /g cm ⁻³	V_m (liquid) /cm ³ mol ⁻¹	FV /cm ³ mol ⁻¹	FV%
TFT	146.1	1.473 (at - 60 °C) ²²⁴	99.2	1.176	124.2	25.0	20.2
Toluene	92.1	1.070 (at - 123 °C) ²²⁴	86.1	0.858	107.4	21.3	19.8
[C ₂ mim][BF ₄]	198.0	1.450 (at - 173 °C) ²²⁵	136.5	1.280 ²²⁶	154.7	18.2	11.8

* FV $\cong V_m$ (liquid) – V_m (crystal)

Calculations for the free volume required to dissolve N₂

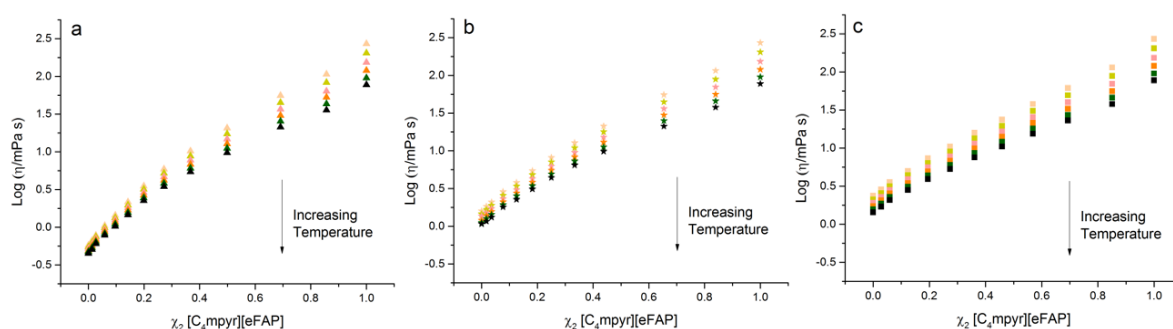
The amount of free volume present in one mole of TFT is 25 cm³ mol⁻¹ compared to a total molar volume of 124.2 cm³ mol⁻¹ (see Table S6 above). Therefore, in one liter of TFT, the amount of free volume present is:

$$\text{FV} = 25 \text{ cm}^3 (\text{FV}) \text{ mol}^{-1} \times 1000 \text{ cm}^3 / 124.2 \text{ cm}^3 (\text{TFT}) \text{ mol}^{-1} = 201.3 \text{ cm}^3$$

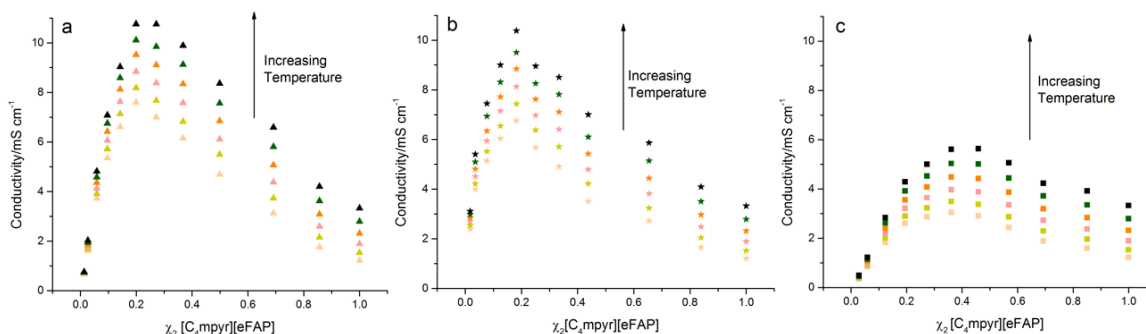
If we consider the molar volume of N₂ as a liquid:

$$28 \text{ g mol}^{-1} / 0.808 \text{ g cm}^{-3} = 34.7 \text{ cm}^3 \text{ mol}^{-1}$$

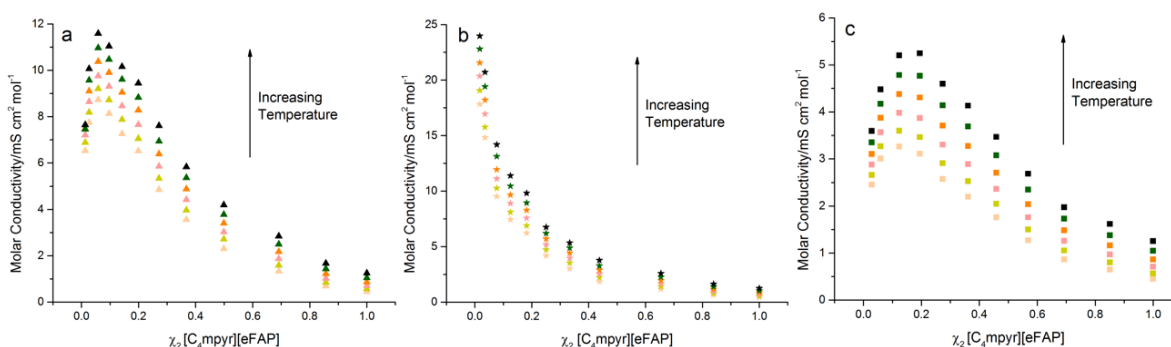
And given the N₂ solubility in TFT is measured to be 10 mmol L⁻¹, the molar volume that is required to dissolve this amount of N₂ is ~0.35 cm³.



Supporting Figure S9: Log viscosity of [C₄mpyr][eFAP] binary mixtures, as a function of mole fraction χ_2 , with a) TFT (▲), b) HFCE (★) and c) FPEE (■) at 25°C, 30°C, 35°C, 40°C, 45°C and 50°C.



Supporting Figure S10: Ionic conductivity of $[C_4\text{mpyr}][\text{eFAP}]$ binary mixtures, as a function of mole fraction χ_2 , with a) TFT (\blacktriangle), b) HFCP (\star) and c) FPEE (\blacksquare) at 25°C, 30°C, 35°C, 40°C, 45°C and 50°C.

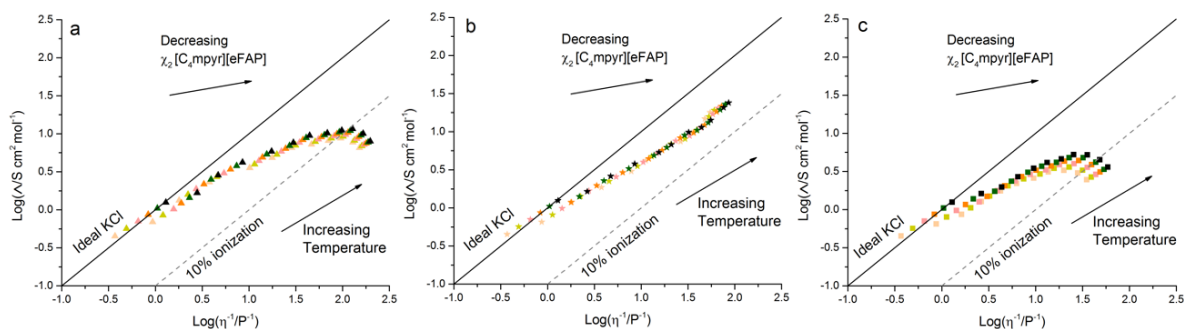


Supporting Figure S11: Molar conductivity of $[C_4\text{mpyr}][\text{eFAP}]$ binary mixtures, as a function of mole fraction χ_2 , with a) TFT (\blacktriangle), b) HFCP (\star) and c) FPEE (\blacksquare) at 25°C, 30°C, 35°C, 40°C, 45°C and 50°C.

Supporting Table S7: Self-diffusion coefficients (m^2s^{-1}) of the cation, anion and solvent in $[C_4\text{mpyr}][\text{eFAP}]$ mixtures with TFT and HFCP, as a function of mole fraction χ_2 and mass fraction wt_2 , and the degree of ionicity, at 25°C

Binary Mixture	χ_2	wt_2	D_{cation} / $10^{-10} \text{ m}^2\text{s}^{-1}$ $\pm 5\%$	D_{anion} / $10^{-10} \text{ m}^2\text{s}^{-1}$ $\pm 5\%$	D_{solvent} / $10^{-10} \text{ m}^2\text{s}^{-1}$ $\pm 5\%$	$\Lambda_{\text{imp}}/\Lambda_{\text{NMR}}$ $\pm 10\%$
$[C_4\text{mpyr}][\text{eFAP}]$	1.00	1.00	0.074	0.049	-	0.97
$[C_4\text{mpyr}][\text{eFAP}]/$ TFT	0.27	0.60	1.6	1.1	5.2	0.48
	0.20	0.50	2.5	1.5	7.5	0.42
	0.14	0.40	3.2	2.2	9.9	0.36
	0.10	0.30	4.9	3.1	14	0.27
	0.06	0.20	6.3	4.3	16	0.22
	0.03	0.10	8.5	5.2	20	0.15
	0.00	0.00	-	-	24	-
$[C_4\text{mpyr}][\text{eFAP}]/$ HFCP	0.33	0.60	0.99	0.67	2.0	0.48
	0.25	0.50	1.3	0.95	2.5	0.50
	0.18	0.40	1.6	1.3	3.1	0.57
	0.13	0.30	2.7	1.7	4.3	0.45
	0.08	0.20	3.9	2.3	5.4	0.42
	0.04	0.10	5.6	3.0	6.7	0.46

0.00	0.00	-	-	8.6	-
------	------	---	---	-----	---



Supporting Figure S12: Walden plot of $[C_4\text{mpyr}][\text{eFAP}]$ binary mixtures, in various compositions* with a) TFT (\blacktriangle), b) HFCEP (\star) and c) FPEE (\blacksquare) at 25°C, 30°C, 35°C, 40°C, 45°C and 50°C.

*The range of χ_2 compositions of $[C_4\text{mpyr}][\text{eFAP}]$ mixtures shown above:

$[C_4\text{mpyr}][\text{eFAP}]$ –TFT, $\chi_2 = 1.00, 0.86, 0.77, 0.69, 0.50, 0.37, 0.27, 0.20, 0.14, 0.10, 0.06, 0.03, 0.01$

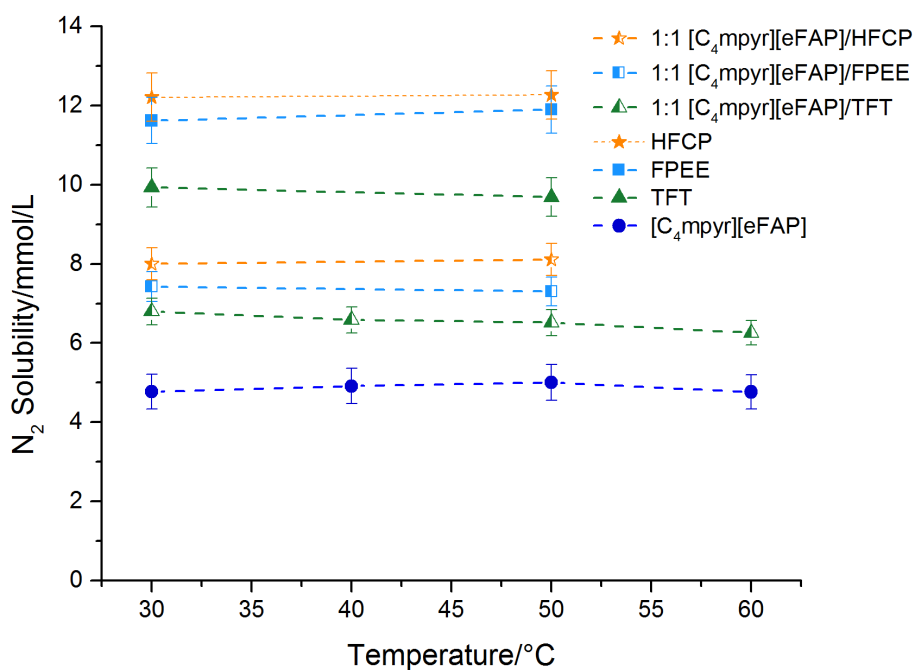
$[C_4\text{mpyr}][\text{eFAP}]$ –HFCEP, $\chi_2 = 1.00, 0.84, 0.65, 0.44, 0.33, 0.25, 0.18, 0.13, 0.08, 0.04, 0.02$

$[C_4\text{mpyr}][\text{eFAP}]$ –FPEE, $\chi_2 = 1.00, 0.85, 0.69, 0.57, 0.46, 0.36, 0.27, 0.20, 0.12, 0.06, 0.03$

Additional Supporting Information

N₂ solubility with temperature

The N₂ solubility plot of [C₄mpyr][eFAP]–fluorinated solvent mixtures at various temperatures are displayed in Supporting Figure 13, where numerical values are shown in Table S8. In chapter 2, it was found that most organic solvents displayed slightly increased N₂ solubility with temperature. In the case of fluorinated solvents, a very small temperature dependence was observed with two of the fluorinated solvents HFCEP and FPCE. However, this change in N₂ solubility with temperature was within the errors of the experiment, such that further analysis of the thermodynamic properties of solvation would yield large uncertainties. Nevertheless, these results showed that a large increase/decrease would not be expected over the given temperature range.



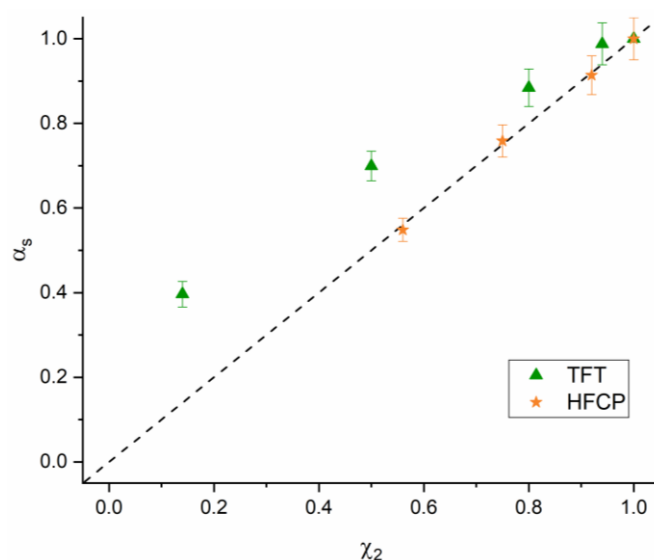
Supporting Figure S13: Solubility of N₂ (mmol L⁻¹) in [C₄mpyr][eFAP] binary mixtures, as a function of temperature (°C), with TFE (▲), HFCEP (★) and FPCE (■) at *p* = 1 atm.

Table S8. Experimental values of N_2 solubility, corrected to a partial pressure of $p = 1$ atm in $[C_4\text{mpyr}][\text{eFAP}]$ binary mixtures at various temperatures, as a function of mass fraction wt_2 , volume fraction Φ and mole fraction χ_2 , expressed as molar concentration C_{N_2} and mole fraction χ_{2,N_2} .

Sample Mixture	T / $^{\circ}\text{C}$	wt_2	Φ	χ_2	C_{N_2} / mmol L^{-1}	χ_{2,N_2} / 10^{-3}
$[C_4\text{mpyr}][\text{eFAP}]$	30	1.00	1.00	1.00	4.8	1.8
	30	1.00	1.00	1.00	4.7	1.7
	40	1.00	1.00	1.00	4.9	1.8
	50	1.00	1.00	1.00	5.0	1.9
	60	1.00	1.00	1.00	4.8	1.8
	60	1.00	1.00	1.00	4.6	1.7
$[C_4\text{mpyr}][\text{eFAP}]/\text{TFT}$	30	0.50	0.43	0.20	6.8	1.2
	30	0.50	0.43	0.20	6.7	1.1
	40	0.50	0.42	0.20	6.6	1.1
	40	0.50	0.42	0.20	6.6	1.1
	50	0.50	0.42	0.20	6.5	1.1
	60	0.50	0.42	0.20	6.3	1.1
$[C_4\text{mpyr}][\text{eFAP}]/\text{FPEE}$	30	0.5	0.51	0.36	7.4	1.9
	30	0.5	0.51	0.36	7.5	1.9
	50	0.5	0.50	0.36	7.3	1.9
	50	0.5	0.50	0.36	7.3	1.9
$[C_4\text{mpyr}][\text{eFAP}]/\text{HFCEP}$	30	0.5	0.50	0.25	7.9	1.5
	30	0.5	0.50	0.25	8.1	1.5
	50	0.5	0.49	0.25	8.1	1.5
	50	0.5	0.49	0.25	8.1	1.5
TFT	30	0	0	0	9.9	1.2
	30	0	0	0	9.9	1.2
	30	0	0	0	10.2	1.3
	50	0	0	0	9.7	1.2
FPEE	30	0	0	0	11.6	2.4
	50	0	0	0	11.6	2.4
HFCEP	30	0	0	0	12.3	1.5
	30	0	0	0	12.2	1.5
	50	0	0	0	12.2	1.6
	50	0	0	0	12.3	1.6

The vapour pressure of pure TFT was measured to be within 12% of experimental error (Ind. Eng. Chem. 1947, 39, 4, 517-540). In the case of the other fluorinated solvents, the vapour pressure values were not present in current literature. As expected, the vapour pressure with each of the pure fluorinated solvents follow the order of FPPE > TFT > HFCE, which are inversely proportional to their boiling temperature (due to the strength of their intermolecular forces).

The activity coefficients are calculated via the measured vapour pressure of the ionic liquid/fluorinated solvent mixture compared to the vapour pressure of the saturated solvent at a given mole fraction. Due to the low vapour pressure of FPPE, the differences in vapour pressure were not large enough to differentiate between varying mole fractions due to the uncertainty error. Supporting Figure S14 shows the plot of activity of TFT and HFCE mixtures with [C₄mpyr][eFAP] compared to the ideal line. The mixture of HFCE in [C₄mpyr][eFAP] behaves closer to an ideal mixture in comparison to [C₄mpyr][eFAP] in TFT, which behaves closer to a non-ideal mixture.



Supporting Figure S14: Plot of activity α_s of TFT and HFCE mixtures (with [C₄mpyr][eFAP]) as a function of mole fraction χ_2 of fluorinated solvent at 30 °C. Dotted line indicates an ideal mixture.

Supporting Information References

1. Kang, C. S. M.; Zhang, X.; MacFarlane, D. R., Synthesis and Physicochemical Properties of Fluorinated Ionic Liquids with High Nitrogen Gas Solubility. *J. Phys. Chem. C* **2018**, 122, 24550—24558.
2. Poling, B. E.; Prausnitz, J. M.; O'Connell, J. P., *The Properties of Gases and Liquids*; McGraw-Hill: New York, 2001; Vol. 5.
3. Dymond, J. H., *The Virial Coefficients of Gases: A Critical Compilation*; Clarendon Press: Oxford, 1969; Vol. 2.
4. Desnoyers, J. E.; Perron, G., Treatment of Excess Thermodynamic Quantities for Liquid Mixtures. *J. Solution Chem.* **1997**, 26, 749—755.

5. Papović, S.; Gadžurić, S.; Bešter-Rogač, M.; Jović, B.; Vraneš, M., A Systematic Study on Physicochemical and Transport Properties of Imidazolium-Based Ionic Liquids with Γ -Butyrolactone. *J. Chem. Thermodyn.* **2018**, *116*, 330—340.
6. Ouerfelli, N.; Barhoumi, Z.; Besbes, R.; Amdouni, N., The Reduced Redlich–Kister Excess Molar Gibbs Energy of Activation of Viscous Flow and Derived Properties in 1,4-Dioxane + Water Binary Mixtures from 293.15 to 309.15 K. *Phys. Chem. Liq.* **2011**, *49*, 777—800.
7. Merz, K.; Evers, M. V.; Uhl, F.; Zubatyuk, R. I.; Shishkin, O. V., Role of CHF₂- and CF₃-Substituents on Molecular Arrangement in the Solid State: Experimental and Theoretical Crystal Structure Analysis of CH₃/CHF₂/CF₃-Substituted Benzene. *Cryst. Growth Des.* **2014**, *14*, 3124—3130.
8. Matsumoto, K.; Hagiwara, R.; Mazej, Z.; Benkič, P.; Žemva, B., Crystal Structures of Frozen Room Temperature Ionic Liquids, 1-Ethyl-3-Methylimidazolium Tetrafluoroborate (EmimBF₄), Hexafluoronioate (EmimNBF₆) and Hexafluorotantalate (EmimTAF₆), Determined by Low-Temperature X-Ray Diffraction. *Solid State Sci.* **2006**, *8*, 1250—1257.
9. Neves, C. M. S. S.; Kurnia, K. A.; Coutinho, J. A. P.; Marrucho, I. M.; Lopes, J. N. C.; Freire, M. G.; Rebelo, L. P. N., Systematic Study of the Thermophysical Properties of Imidazolium-Based Ionic Liquids with Cyano-Functionalized Anions. *J. Phys. Chem. B* **2013**, *117*, 10271—10283.

Chapter 6: Conclusions and Future Work

6.1 Conclusions

Electrochemical ammonia synthesis at ambient conditions has attracted much attention over the last five years. Although small improvements to the Faradaic efficiency have been shown in aqueous electrolytes (~20%), results as high as 60% had been achieved with IL electrolytes (whilst also implementing rigorous control protocols). The work in this dissertation presents a vast suite of fluorinated IL-based electrolytes, with high N₂ solubility and comparable transport properties, which display huge potential as high performing electrolytes for the electrochemical nitrogen reduction reaction. Additionally, in-depth physicochemical studies of these fluorinated IL-based electrolytes provide fundamental insight into the molecular origins of N₂ solubility. The conclusions gathered from each chapter of this doctoral thesis are described as follows:

Chapter 2 delved into the construction of the custom-designed N₂ solubility apparatus and provided a description of the design aspects and control experiments involved with the isochoric saturation method. The construction process consisted of two different types of apparatus: Mark I involved the use of a single pressure transducer, whilst Mark II utilised a dual-transducer mode that was found to produce a stable, leak-free system. After the series of control experiments and protocols were established, high-precision measurements of N₂ solubility in common solvents were determined to be in satisfactory agreement to literature data, which enabled reliable measurements of N₂ solubility in the fluorinated IL electrolytes throughout this thesis.

The work carried out in chapter 3 detailed the synthesis of novel fluorinated ILs and a study of their physicochemical properties. While [eFAP]⁻-based ILs had displayed faster transport properties (e.g. conductivity, diffusivity, ionicity, viscosity etc.), ILs with perfluorosulfonate and perfluorocarboxylate anions were shown to display higher N₂ solubility. One key trend that

was discovered in this work was the additional increase in N₂ solubility when the perfluoroalkyl chain was extended, where the size of fluorinated domains may play a role in N₂ dissolution.

Chapter 4 described the design and optimisation of fluorinated IL-based electrolytes to be used for electrochemical ammonia synthesis. The miscibility of ILs and fluorinated solvents was studied, where some functionality on the solvent was required as perfluorinated solvents were completely immiscible in all of the ILs tested. Through measurements of N₂ solubility in newly synthesised ILs and a range of IL-fluorinated solvent combinations, some design principles to achieve high N₂ solubility were established. These ranged from the addition of fluorinated solvents to high N₂ soluble ILs through to the usage of shorter alkyl chains on the IL cation. Additionally, small phosphonium [eFAP]⁻-based electrolytes displayed better transport properties (up to five times higher ionic conductivity) than perfluorosulfonate, and perfluorocarboxylate-based electrolytes.

In chapter 5, the study of physical interactions within [C₄mpyr][eFAP]-fluorinated solvent mixtures revealed negative excess molar volumes of mixing that correlated with higher than expected viscosity values. The reduction of free volume was estimated to be a fraction of the total free volume in [C₄mpyr][eFAP]-fluorinated mixtures, such that N₂ solubility was not largely affected by these association interactions. The N₂ solubility was measured over a range of [C₄mpyr][eFAP]:fluorinated solvent compositions, which showed an approximately linear trend from neat [C₄mpyr][eFAP] to the neat fluorinated solvent (of TFT, HFCEP, and FPPEE). Finally, [C₄mpyr][eFAP]-TFT mixtures displayed the highest ionic conductivities, at $\chi_2 \sim 0.20$.

6.2 Future Work

The research work in this dissertation can be further extended in several directions:

Electrochemical Ammonia Synthesis

Further work on the electrochemical nitrogen reduction reaction can be carried out using the fluorinated IL-based electrolytes described here. Although preliminary studies had been carried out, contamination issues of NO_x species were found to affect results such that erratic results were obtained. Such NO_x species pose a significant problem as they may likely have been present in the atmosphere and potentially absorbed onto the electrode surface of iron (electrodeposited) on stainless steel. Hence, careful control of NO_x species and the use of larger electrodes is needed to produce more ammonia (above the background) to enable a thorough electrochemical study with various electrolytes. Using the fluorinated ionic liquid-based electrolytes discussed in this thesis, the following series of experiments can be conducted for the application of electrochemical ammonia synthesis:

- I. Using an active and stable catalyst for nitrogen reduction, conduct cyclic voltammetry and chronoamperometry under nitrogen gas and argon gas. These experiments can be optimised as a function of applied potential, temperature, water content, time and composition of ionic liquid to solvent.
- II. Ensure reproducibility with multiple data points, thorough blank experiments involving any nitrogen containing species and possible contamination of gas cylinders and nitrate-based compounds.
- III. Since the fluorinated ionic liquid-based electrolyte of $[\text{P}_{122}\text{i}4][\text{eFAP}]/\text{HFCEP}$ was observed to display relatively high ionic conductivity values and high N_2 solubility, this electrolyte mixture would be ideal to test for the nitrogen reduction reaction to achieve faster yield rates and faradaic efficiencies.

Exploration of Solvents

Exploration of the tailored synthesis of fluorinated solvents, particularly those that are cyclic solvents, as they tend to exhibit higher dielectric constants, which are ideal for further optimising the transport properties of the fluorinated IL-based electrolytes whilst allowing a number of fluorine substituents to permit high N₂ solubility. The effect of ether substituents have been known to enhance the transport properties of ionic liquids but its effect on N₂ solubility would be informative. N₂ solubility experiments would be measured using the constructed isochoric saturation method as detailed in chapter 2. Synthesis may be carried out via Williamson ether synthetic reactions to form tailored ether-based solvents.

Ammonia Solubility

Studying the solubility of ammonia in these electrolytes would be of significant value. Whilst the focus of this work has been on N₂ solubility, ammonia is produced as the product and the study of ammonia gas solubility would be very beneficial, since it may have to be removed from the electrolyte mixture and transferred into an acid trap. Ammonia gas solubility can be measured using the developed isochoric saturation method as similar to measuring N₂ solubility over a range of fluorinated ionic liquid-based electrolytes. Experiments over a range of compositions would be helpful to determine if the gas solubility behaviour is similar to that of N₂. Differing results may arise due to the stronger dipole that exists with ammonia in addition to its possible hydrogen bonding to the cation/anion of the ionic liquid.

Fluorinated Domains

The fluorinated domains in fluorinated IL-based electrolytes may be further explored using X-ray/neutron scattering techniques and molecular dynamics simulations. These fundamental studies would allow further insight into N₂ dissolution via computational and experimental perspectives where correlations could be made with N₂ solubility data, where the size of such domains may be the key to N₂ solubility. Also the position and presence of N₂ molecules would

be of significant value and allow further tailoring and synthesis of fluorinated ionic liquids–based electrolytes. Specifically, these experimental techniques would involve Small and Wide X-Ray Scattering (SWAXS), Small Angle Neutron Scattering (SANS), both of which would require an X-Ray source at a synchrotron facility.

Other applications

The fluorinated IL–based electrolytes presented in this work could be utilised in a range of other applications such as lithium–sulfur battery electrolytes, surfactants, catalysis, biomedicine, and the application as fluorinated media for the ‘interface between two immiscible electrolyte solutions’ for biological detection studies. The dissolution of ions into fluorinated media is not common due to its usual immiscibility with charged species. As a result, these electrolytes with unique properties (such as high gas solubility and wide electrochemical windows) provides scope into these other applications. For example, the dissolution of lithium salts in fluorinated media is not trivial and generally requires additives (which may not be desirable). Lastly, fluorinated media may be useful in electrocatalysis applications due to its very low water miscibility, thus preventing by-products (or energy loss) due to the hydrogen evolution reaction.